Geographia Technica

GEOMATICS APPLICATION FOR GEOGRAPHY

Volume 16, Special Issue

Guest Editors:

Valerio BAIOCCHI and Gino DARDANELLI

C o n t e n t s

Geographia Technica

EDITORIAL FOR SPECIAL ISSUE:
"GEOMATICS APPLICATION FOR GEOGRAPHY (GAG)"
in GEOGRAPHIA TECHNICA

Valerio BAIOCCHI[1] and **Gino DARDANELLI[2]**

1. INTRODUCTION

Geomatics or Geography, that is the question!

This is how the authors' idea of merging Geomatics and Geography in this special issue begins, paraphrasing a Shakespearean citation. The common principle that unites these two scientific disciplines, which attempt to describe the territory in the most straightforward way possible. On the other hand, Geomatics and Geography derived from "gèo- "[greek γεω-], as first element of composed words in learned and scientific terminology, meaning "earth", "globe", "land surface".

Geography is the basis of all disciplines that study the territory, its characteristics and its changes over time. It includes the analysis of the forms of territorial and landscape organisation in their physical-environmental, economic and historical-cultural components and extends to skills related to the study of economic phenomena and political-administrative structures, population and settlement structures. The research has theoretical and applicative values that are functional to planning and programming, in an interdisciplinary dimension with regard to the study of resources, the use of space, the location of activities, innovation processes, as well as the repercussions on the urban and regional system with reference to the different territorial scales and the plurality of political and geopolitical scenarios. Of fundamental analytical support remains cartography, in particular thematic cartography, integrated with the construction of geographic information systems and multimedia imaging techniques. The fields of study include the various modes of human-environment interaction in terms of the territorial and landscape effects of general and site specific policies, geographical regionalisation, the distribution of settlements, the geography of productive sectors and financial flows, the network of intangible relations concerning production, the distribution of goods and resources, the spatial diffusion of innovation, territorial marketing techniques, reflection on the epistemological nature of the models used.

Geomatic is a new neo-logism based on a disciplinary scientific content that concern the acquisition, restitution, analysis and management of data of metric or thematic nature relating to the Earth's surface, or portions of it, including the urban environment, infrastructures and architectural heritage, identified by their spatial position and qualified by the accuracy of the survey. The disciplines covered with Geomatic are geodesy (physical, geometric and spatial), survey, photogrammetry (aerial and terrestrial), cartography, remote sensing (spatial, aerial and terrestrial), navigation (spatial, aerial, maritime and terrestrial) and spatial information systems.

[1] *Sapienza University of Rome, DICEA, Via Eudossiana 18, 00184 Rome, Italy*
(e-mail: valerio.baiocchi@uniroma1.it)
[2] *Department of Engineering, University of Palermo, Viale delle Scienze, 90128 Palermo, Italy (e-mail: gino.dardanelli@unipa.it)*

The fields of application are, in particular, the study of global and local reference systems, instruments and methods for surveying, controlling, monitoring the territory, structures and cultural heritage, processing of measurement data, production and updating of cartography, topographic DBs, tracking of works and infrastructures, mobile surveying systems, numerical models of terrain and surfaces, management and sharing of multidimensional and multi-temporal geographical information.

Hence, this special issue of the journal Geographia Technica (https://technicalgeography.org/), "GEOMATICS APPLICATIONS FOR GEOGRAPHY" was successfully planned, and we here publish many papers detailing novel contributions that are of relevance to these topics.

Since 2006 Geographia Technica is a journal devoted to the publication of all papers on all aspects of the use of technical and quantitative methods in geographical research. It aims at presenting its readers with the latest developments in GIS technology, mathematical methods applicable to any field of geography, territorial micro-scalar and laboratory experiments, and the latest developments induced by the measurement techniques to the geographical research. Geographia Technica is dedicated to all those who understand that nowadays every field of geography can only be described by specific numerical values, variables both of time and space which require the sort of numerical analysis only possible with the aid of technical and quantitative methods offered by powerful computers and dedicated software.

Geographia Technica is Indexed by CLARIVATE ANALYTICS, SCOPUS, GEOBASE, EBSCO, SJR, CABELL, Web of Sciences and is SCIMAGO.

In conclusion Geomatics for Geography, this is the solution!

2. GEOMATICS APPLICATIONS FOR GEOGRAPHY

In total, 19 papers were submitted to this special issue, 15 of which were accepted and published (constituting a 79% acceptance rate), 2 manuscripts were rejected before being submitted for review due to very poor quality and 2 manuscripts were rejected after review. The geographical distribution of works is essentially linked to two continents, Asia (53%), Europe (40%); Africa is present only at 7% (**Fig. 1 a**).

The presence of paper within individual countries, on the other hand, is absolutely well balanced between Indonesia (40%) and Italy (40%), while they are present equally among Kyrgyzstan (6.7%), Morocco (6.7%), Thailand (6.7%), as you see at (**Fig. 1 b**).
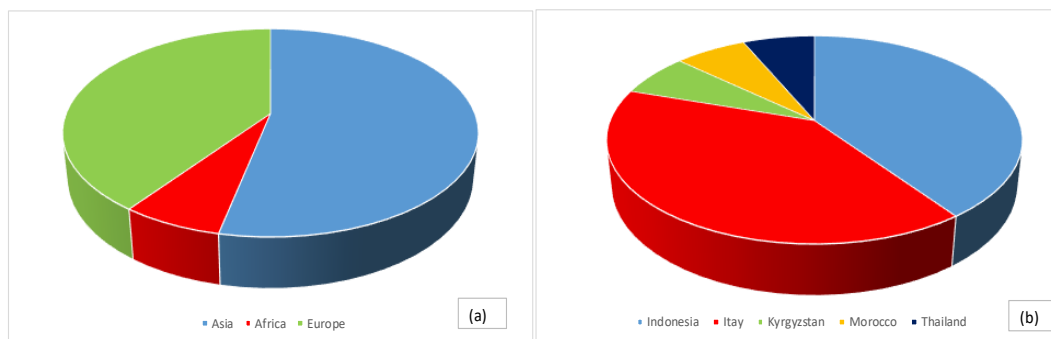
Fig. 1. Spatial distribuition of accepted paper.

The papers in this special issue cover various areas related to Geomatics Applications for Geography as cartography, GIS, remote sensing, photogrammetry and GNSS, which are typical tools used by geoinformation researchers.

A very interesting first case study has been developed by Pepe et al. in wich was identified an appropriate survey technique and numerical method for the calculation of volumes extracted in a quarry; also, the impact of the TIN (Triangulated Irregular Network) and GRID method was evaluated firstly, by the use of UAV (Unmanned Aerial Vehicle) photogrammetry and in latter the ease and speed in performing the 3D model by UAV photogrammetry was shown in the manuscript (Pepe et al. 2021).

GNSS application was used in two papers: in the work of Innac et al. was evaluate the performance assessment of a Single Point Positioning algorithm (SPP), with a Kalman filter (KF) estimator, adapted for maritime applications, in wich the algorithm is developed in Matlab environment and tested using multi-GNSS single-frequency raw data, collected by a smartphone located on board a ship (Innac et al. 2021). Dardanelli and Pipitone, on the other hand, showed the availability of Continuosly Operating Reference Station (CORS) to understand the effects of a GNSS CORS network geometry and differential corrections on the solutions. The analysis is carried out using ten different network configurations, with different inter-distances between the stations within GNSMART Geo++ software. Different surveys have been performed, including four separate session tests, with acquisitions of one hour each. The analysis has been carried out using the traditional network solutions, such as the Virtual Reference Station (VRS), the Flächen Korrektur Parameter (FKP), the nearest (Near) and the farest (Far) stations. Results confirmed the great reliability of the GNSS network, with centimetre precision in terms of coordinates (North, East and Ellipsoidal Height), whether changing the geometric configuration of the network or the corrections (Dardanelli and Pipitone, 2021).

Three papers on GIS were also presented in the Special Issue, and particularly remarkable is the one of Pesaresi et al. in wich after a contextualization about the measures used to contain the COVID-19 diffusion and the need to promote geotechnological proposals, data sharing and homogenous centralised systems for data collection and analysis. Successively, was presented the "Dynamic Space-Time Diffusion Simulator in a GIS Environment to Tackle the COVID-19 Emergency" that was elaborated on the basis of the data provided by the UOC Hygiene and Public Health Service – Local Health Unit Rome 1 (Pesaresi et al. 2021). Also Baiocchi et al. tested on a real case (the May 1999 pyroclastic flows in Campania, southern Italy) the actual possibility of implementing a model for forecasting such events using only open-source software and open data by usign GIS and Web GIS. It has been demonstrated that the entire process can be carried out using only open-source resources and it has been verified that the predictions of the hazard and risk model obtained with only input data prior to the event, give an output prediction that is significantly coincident with the events that actually occurred as documented by the authorities (Baiocchi et al. 2021). Aghad et al. showed to identify optimal sites for Rainwater harvesting (RWH) using GIS based Fuzzy Analytical Hierarchy Process (FAHP) method in the Kenitra province, NW Morocco. For preparing thematic layers, several data sources were used including remote sensing data (RS), digital elevation model (DEM), the soil and precipitation data were used to create the necessary database using ArcGIS software (Aghad et al. 2021).

Certainly, the special issue hosted numerous papers on the considerable potential offered by satellite sensors such as remote sensing, such as those related to Landsat 8, Terramodis, Sentinel-1 and 2, Spot 6/7, or Ikonos. Auntarin et al. aimed to use a split-window algorithm to retrieve the land surface temperature via Landsat-8 OLI/ TIRS data in the Roi Et province area. The research methodology included 1) separating the Landsat-8 OLI data into four types of land use, i.e. the agricultural, forest, urban and water areas and 2) the data for Landsat-8 OLI bands 4 and 5 and Landsat-8 TIRS (bands 10, 11) being analysed to retrieve the land surface temperature using a split-window algorithm (Autarin et al. 2021).

Septiangga and Mutaqin aims to analyze the spatio-temporal evolution of the Wulan Delta, in Indonesia including the shoreline and its dynamics, as well as the geomorphological processes that affect it. The shoreline change was extracted digitally from Landsat satellite images and divided into four periods, i.e., 1995-2000, 2000-2011, 2011-2015, and 2015-2020. It was used the histogram thresholding method to separate the land from the sea and produce the shoreline as the interface. This research employed field check and focus group discussion for identifying the cause and impact of shoreline dynamics in the research area (Septiangga and Mutaqin, 2021).

Considerable is the paper of Dewi et al. in wich starting for a case study located in a small island nearby Morotai Island, Indonesia, four SDB models were compared. The implementation of the SDB model was carried out by combining echo-sounding measurements and the reflectance of blue, green, red, and near infrared bands of three satellite images (World View 2, Sentinel 2A and Landsat 8). Our findings reveal that all three satellite images performed well in assessing SDB at various spatial and spectral resolution, however, the use of high-resolution imagery did not always improve accuracy, for example when using SVM (Support Vector Machine, Dewi et al. 2021). Jomsrekrayom et al. instead used Terra/Modis satellite to analyze vegetation drought variability from a vegetation phenology perspective using the vegetation condition index (VCI), in the middle of the northeast region of Thailand (Jomsrekrayom et al. 2021); it found that July, August, and September showed a coefficient of determination (r^2) equal to 0.835, 0.834, and 0 .849, respectively. The r^2 value showed that this method was reliable.

Sentinel data was used in two papers: in the work of Zholdoshbekov et al. evaluated the synthetic aperture radar (SAR) remote sensing-based approach has been used for identifying the ELA of glaciers in the Ala-Archa River catchment of Kyrgyzstan from 2015 – 2019 (Zholdoshbekov et al. 2021). Initially, the glacier radar zones were mapped using the Sentinel-1 SAR datasets of each year under consideration. It was found that mainly the middle percolation, lower percolation, and bare-ice zones along with debris cover-ice are present in the glaciers. In the second paper, Haris et al. explored the accuracy of the gray level of co-occurrence model (GCLM) textures of multitemporal Sentinel-1 data for aquaculture pond mapping in Brebes Regency, Central Java Province, Indonesia. In addition, single-date Sentinel-2 optical imagery was used to compare the results from Sentinel-1 data (Haris et al. 2021).

Still in Indonesia Rosyid et al. examined the ground surface deformation and displacement in each landslide location in terms of spatial and temporal and identifies the different types and characteristics of landslides in the Sukabumi area of West Java, Indonesia. The Small Baseline Subset Interferometric Synthetic Aperture Radar (SBAS-InSAR) methodology was used in this study, and the DinSAR method was applied. The ground surface displacement at each landslide location ranged from -10 mm/year to +34 mm/year, with most of the landslides occurring on moderate to steep slopes. These results are suitable to use for support regional development planning in reducing losses and casualties (Rosyid et al. 2021). On the other hand, regarding other satellite remote sensing, Zylshal et al. presented our results for topographic correction performed using three different DEMs on orthorectified SPOT-6/7 multispectral data. These DEMs are Shuttle Radar Topography Mission (SRTM) and ALOS World 3D 30 meters (AW3D30), as well as DEMNAS. The study was conducted on two test sites located in the mountainous region over South Sulawesi Province, Indonesia (Zylshal et al. 2021).

Last but not least, Alcaras et al. compared the results obtained from the application of eight different pan-sharpening methods, which are totally carried out by using the raster calculator in QGIS: Multiplicative, Simple Mean, Brovey Transformation, Brovey Transformation Fast, Intensity Hue Saturation (IHS), IHS Fast, Gram-Schmidt, and Gram-Schmidt Fast, with Ikonos imagery (Alcaras et al. 2021).

Finally, we hope this Special Issue will help readers to integrate Geomatics Aplication for Geography and bring us new probabilities and opportunities to our life.

ACKNOWLEDGMENT

R E F E R E N C E S

Mohamed Aghad, Mohamed Manaouch , Mohamed Sadiki , Mohcine Batchi, Jamal Al Karkouri, Identifying Suitable Sites For Rainwater Harvesting Using Runoff Model (Scs-Cn), Remote Sensing And Gis Based Fuzzy Analytical Hierarchy Process (Fahp) In Kenitra Province, Nw Morocco (2021) *Geographia Technica*, Vol 16, Special Issue, 2021, pp. 111-127.

Emanuele Alcaras, Vincenzo Della Corte , Giampaolo Ferraioli , Elena Martellato , Pasquale Palumbo , Claudio Parente , Alessandra Rotundi Comparison Of Different Pan-Sharpening Methods Applied To Ikonos Imagery (2021) *Geographia Technica*, Vol 16, Special Issue, 2021, pp. 198-210

Auntarin, C., Chunpang, P., Chokkuea, W., Laosuwan, T. Using a split-window algorithm for the retrieval of the land surface temperature via landsat-8 OLI/TIRS (2021) *Geographia Technica*, Vol 16, Special Issue, 2021, pp. 30-42

Baiocchi, V., Vatore, F., Lombardi, M., Monti, F., Onori, R. The contribution of open-source gis software and open spatial data for the re-evaluation of landslide risk and hazard in view of climate change (2021) *Geographia Technica*, Vol 16, Special Issue, 2021, pp. 153-162.

Dardanelli, G., Pipitone, C. The effects of cors network geometry and differential nrtk corrections on gnss solutions (2021) *Geographia Technica*, 16 (Special Issue), pp. 56-69.

Nurul Afdal Haris, Sandiaga Swahyu Kusuma, Sanjiwana Arjasakusuma, Pramaditya Wicaksono, Comparison Of Sentinel-2 And Multitemporal Sentinel-1 Sar Imagery For Mapping Aquaculture Pond Distribution In The Coastal Region Of Brebes Regency, Central Java, Indonesia (2021) *Geographia Technica*, Vol 16, Special Issue, 2021, pp. 128-137.

Innac, A., Angrisano, A., Dardanelli, G., Della Corte, V., Martellato, E., Rotundi, A., Ferraioli, G., Palumbo, P., Gaglione, S. A Kalman filter single point positioning for maritime applications using a smartphone (2021) *Geographia Technica*, 16 (Special Issue), pp. 15-29.

Jomsrekrayom, N., Meena, P., Laosuwan, T. Spatiotemporal analysis of vegetation drought variability in the middle of the northeast region of thailand using terra/modis satellite data (2021) *Geographia Technica*, 16 (Special Issue), pp. 70-81.

Ratna Sari DEWI , Aldino RIZALDY, Prayudha HARTANTO , Suprajaka SUPRAJAKA Assessing The Accuracy Of Shallow Water Depth Estimation By Using Multispectral Satellite Images (2021) *Geographia Technica*, Vol 16, Special Issue, 2021, pp. 180-197.

Rosyidy, M.K., Dimyati, M., Shidiq, I.P.A., Zulkarnain, F., Rahaningtyas, N.S., Syamsuddin, R.P., Zein, F.M. Landslide surface deformation analysis using sbas-insar in the southern part of the sukabumi area, Indonesia (2021) *Geographia Technica*, Vol 16, Special Issue, 2021, pp. 138-152.

Septiangga, B., Mutaqin, B.W. Spatio-temporal analysis of wulan delta in Indonesia: Characteristics, evolution, and controlling factors (2021) *Geographia Technica*, 16 (Special Issue), pp. 43-55.

Pesaresi, C., Pavia, D., De Vito, C., Barbara, A., Cerabona, V., Di Rosa, E. Dynamic space-time diffusion simulator in a gis environment to tackle the covid-19 emergency. Testing a geotechnological application in rome (2021) *Geographia Technica*, 16 (Special Issue), pp. 82-99.

Pepe, M., Costantino, D., Alfio, V.S., Zannotti, N.4D Geomatics Monitoring Of A Quarry For The Calculation Of Extracted Volumes By Tin And Grid Model: Contribute Of Uav Photogrammetry (2021) *Geographia Technica*, 16 (Special Issue), pp. 1-14.

Zholdoshbekov, E., Garg, V., Thakur, P.K., Duishonakunov, M., Voda, M. Delineation radar zones of glaciers in the ala-archa valley of Kyrgyz Republic (2021) *Geographia Technica*, 16 (Special Issue), pp. 100-110.

Zylshal, Z., Bayanuddin, A.A., Nugroho, F.S., Munawar, S.T.A. Correcting the topographic effect on Spot-6/ 7 multispectral imageries: A comparison of different digital elevation models (2021) *Geographia Technica*, Vol 16, Special Issue, 2021, pp. 163-179.

4D GEOMATICS MONITORING OF A QUARRY FOR THE CALCULATION OF EXTRACTED VOLUMES BY TIN AND GRID MODEL: CONTRIBUTE OF UAV PHOTOGRAMMETRY

*Massimiliano PEPE[1] ** ID **, Domenica COSTANTINO [1] ID , Vincenzo Saverio ALFIO[1]*,*
and Nicola ZANNOTTI[2]

ABSTRACT:
The purpose of this manuscript is to identify an appropriate survey technique and numerical method for the calculation of volumes extracted in a quarry. The impact of the TIN (Triangulated Irregular Network) and GRID method was evaluated firstly on a hypothetical stepped ground and one with a constant slope and, later, on a specific case study of a quarry of an important dimensions. In this case study, the survey at time t_0 was performed by ALS (Airborne Laser Scanning) and at time t_1 by the use of UAV (Unmanned Aerial Vehicle) photogrammetry. In the latter survey, the ease and speed in performing the 3D model by UAV photogrammetry was shown in the manuscript. Concerning the calculation of the volume over time, it has been shown how the TIN allows a calculation which is closer and more faithful to the reality than to the GRID model, in case the quarry conformation is in steps and, consequently, with important nearly vertical surfaces.

Key-words: *UAV photogrammetry, quarry, TIN, GRID, SfM.*

1. INTRODUCTION

The monitoring of the territory over time represents an important activity for the protection, management and preservation of the environment, especially in the case of consumption of non-renewable resources, such as quarries. Consequently, the choice of suitable geomatics survey techniques plays a very important role. In this context, UAV (Unmanned Aerial Vehicle) photogrammetry represents a valid tool to perform 4D monitoring of quarries. In fact, the possibility to acquire in a simple and fast way territorial information on particularly steep terrain, such as those that characterize the quarries, allows reconstructing the geometry of the study area in an accurate and detailed way. From a technological point of view, this represented a considerable step forward, since with aerial survey alone it is possible to obtain nadir and oblique images of the quarry. As a consequence of the technological progress of the aerial platform and of high performance cameras at low cost, a significant contribution to the diffusion and application of UAV photogrammetry is represented by the development of Structure from Motion (SfM) and Multi view Stereo (MVS) algorithms that have allowed to realize accurate 3D models in a simple and intuitive way (Snavely et al., 2007; Ahmadabadian et al., 2013; Furukawa and Ponce, 2010; Grünner and Dudáš, 2017; Masiero et al., 2019; Costantino et al., 2020). Given the ease of application of 3D reconstructions based on SfM/MVS, the automatism in UAV flight planning and image acquisition, UAV photogrammetry has been applied in an increasing number of fields, such as architecture, archaeology, geomorphology (Caroti et al., 2012; Gasperini et al., 2014; Baiocchi et al., 2018; Baiocchi et al., 2019; Pepe and Costantino, 2020). Over the last decade, UAV photogrammetry has become increasingly used as a method for the 3D construction of a quarry. González-Aguilera et al. 2012 describe a procedure to build a 3D modelling and accuracy assessment of granite quarry using UAV photogrammetry using

---

[1]*Politecnich of Bari, DICATECh, 70125 Bari, Italy;*

massimiliano.pepe@poliba.it, domenica.costantino@poliba.it, vincenzosaverio.alfio@poliba.it
[2]*X-Crowd srl, 80143 Napoli (Italy), nicola.zannotti@gmail.com;*

VisualSfM software. Based on the results obtained from this case study, the authors claim that the UAV technology is an effective and economical method in comparison with other remote sensing techniques, such as classical surveying and laser scanning. Raeva et al., 2017 evaluate the accuracy of UAV data for volumetric measurements to the conventional GNSS (Global Navigation Satellite Systems) techniques and highlighting, through a case study, the high performance in terms of accuracy and speed of execution of the UAV survey. Therefore, the UAV survey represents one of the best methods of survey both from the point of view of efficiency (speed, economy, simplicity) and from the point of view of accuracy to evaluate the space-time evolution of a quarry, as shown in some recent papers (Rhodes, 2017; Nguyen et al., 2019; Török et al., 2020).

For this reason, in this paper, we use UAV photogrammetry to reconstruct the 3D model of the quarry over the years and calculate the volume eroded. In particular, the aspects that we intend to investigate in this research are: i) evaluating the difference between the choice of a TIN or GRID (raster) model; ii) the influence of the cell size in raster model; iii) the impact of the point cloud density in the volume calculation.

2. CALCULATION OF THE VOLUME AND ITS UNCERTAINTY

The difference in excavation volumes measured ΔV in a quarry at two different times (t_0 and t_1) is equal to:

$$\Delta V = V_{t1} - V_{t0} \tag{1}$$

where V_{t1} is the volume of the quarry evaluated at the time t_1 while V_{t0}.

To calculate the volume changed over the years to works of anthropic actions inside the quarries, the point cloud generated by UAV photogrammetry method must be converted in Triangulated Irregular Network (TIN) or grid.

TIN model, introduced in the early 1970s (Peucker et al., 1978) represents a three-dimensional vector where the points known in the three coordinates, however distributed in space, are joined by lines in order to form flat and adjacent triangles that allow to continuously represent the surface of the territory. To establish the triangles of the points that make up the individual triangles, i.e. to organize the reference meshes, algorithms based on geometric properties are used. Starting from Dirichlet's intuition for the decomposition of a domain into several adjacent (and not overlapping) convex polygons, the Delaunay method allows defining triangles of points such that the circle circumscribing each triangle does not contain other elements of the starting series. The nodes are the same sample points and constitute the vertices of the triangles; each node has a value of altitude h. The edges are the lines representing the sides of the triangles. Triangles express the approximation of the real surface with a mathematical model where each plane (triangular) describes the course of a portion of the surface of the TIN. From the spatial coordinates of the three vertices, it is possible to obtain information such as the slope, exposure, area and perimeter of the relative surface. Finally, the topological relationships define the set of links between nodes, edges and triangles through which the data structure of the TIN is stored. In TIN environment, the relation that connecting the different elements is:

$$T = 2n - t - 2 \tag{2}$$

where:
T   number of triangles;
t   number of boundary vertices
n   number of vertexes

A raster consists of a matrix of cells organized into rows and columns (or a grid) where each cell contains a value representing information, such as elevation. Indeed, with the gridding process, the trend of a given variable (such as the altitude) is reconstructed according to a regular grid of nodes, equally spaced, starting from a series of discrete values irregularly distributed in space. There are

many interpolation methods. Some methods, implemented in the most common GIS (Geographic Information Systems) software are Inverse Distance Weighting (IDW), Kriging, Natural Neighbour and Spline (Abidine et al., 2018). In the case of dense point cloud, the grid interval is typically larger than the point spacing, and a simple average of all coordinate z-values within each raster cell is sufficient (Hartzell et al., 2015):

$$h_p = \frac{1}{m} \sum_{i=i}^{m} h_i \tag{3}$$

where:
h_i is the value of the height;
h_p mean height value evaluated on m points that is associated at each pixel.

In the representation of the quarry through the use of the raster, the volume is calculated as the product of the area of each single cell (pixel size) for the value of the pixel, naturally extended to the whole space of interest, that is:

$$V_{raster} = \sum_{p=1}^{r \cdot c} A_{cell} \cdot h_p \tag{4a}$$

where:
V total volume evaluated on a raster by a number of rows r for a number of columns c;
A_{cell} area of the single cell (or pixel).

Of course, operability is feasible if the two grids have exactly the same pitch and origin. A representation of this volume in GRID environment is shown below (**Fig.1**).
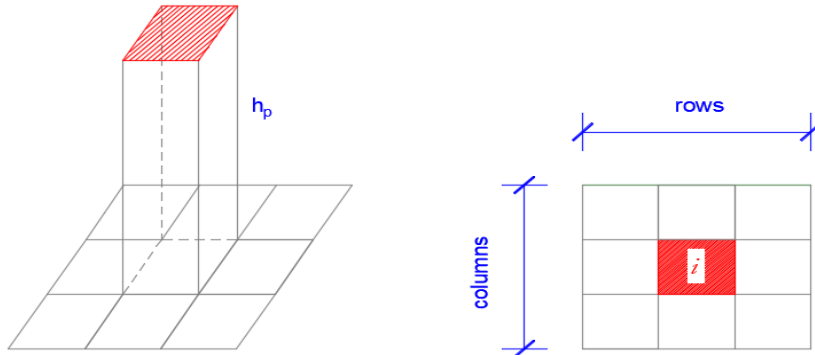
Fig. 1. Representation of the volume according to the GRID model.

Therefore, taking into account two temporal instants (time t_0 and time t_1) on which to perform the variation of volumes, it is possible to write:

$$V_{raster_{t_0}} = \sum_{p=1}^{r \cdot c} \left(A_{cell} \cdot h_p \right)_{t_0} \tag{4b}$$

$$V_{raster_{t_1}} = \sum_{p=1}^{r \cdot c} \left(A_{cell} \cdot h_p \right)_{t_1} \tag{4c}$$

If we adopt a TIN model and taking into account the volume of each prism model evaluated on u-th triangle, the total volume, i.e. extended to the whole space consisting of a number v of triangles, is:

$$V_{TIN} = \sum_{u=1}^{v} \frac{1}{3} \cdot A_u \cdot (h_1 + h_2 + h_3)_u \tag{5}$$

where:

h_1, h_2, h_3 heights of the prism measured starting from the u-th triangle;
A_u area of the prism triangular base of the u-th triangle.

A representation of the volume according the TIN model is show below (**Fig. 2**).
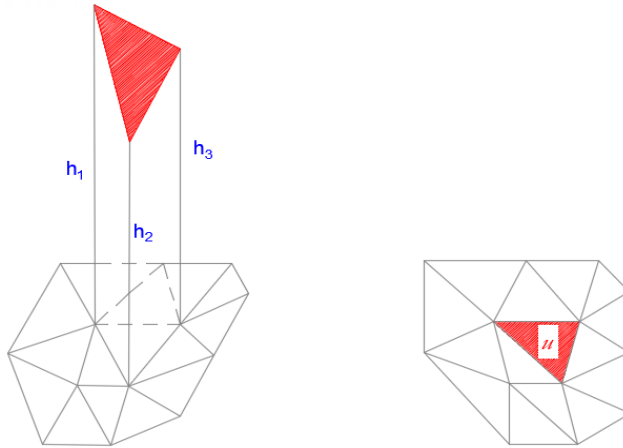
Fig. 2. Representation of the volume according to the TIN model

The calculation of the area of the u-th triangle can be performed with different methods. In GIS, the formula for calculating the area is that of Gauss, that is:

$$A_u = \frac{1}{2}[x_1(y_2 - y_3) + x_2(y_3 - y_2) + x_3(y_1 - y_2)]_u \tag{6}$$

where x and y of the three vertexes are the spatial coordinates of u-th triangle.

The above equation can also be written as:

$$V_{TIN} = \sum_{u=1}^{v} \frac{1}{3} \cdot A_u \cdot h_{1_u} + \frac{1}{3} \cdot A_u \cdot h_{2_u} + \frac{1}{3} \cdot A_u \cdot h_{3_u} \tag{7}$$

3. METHOD AND EXPERIMENTAL SETUP

The geomatics surveys allow producing accurate point clouds. Indeed, it is possible to obtain a raster o TIN model from the point cloud. In this way, by comparing raster or TIN obtained in two different epochs, it is possible to perform the calculation of the volumes.

To obtain a raster format, an interpolation of point cloud is required. Considering the high density of the points, the natural neighbour technique can be used. Natural neighbour interpolation is a method of spatial interpolation, developed by Robin Sibson and is based on Voronoi tessellation of a discrete set of spatial points (Sibson, 1981). In this way, it is possible to build a raster with a specific cell size. In order to identify the volume differences that may occur in choosing a GRID or TIN model, we will first analyse a theoretical case and then a real one. Indeed, after discussing the results obtained on hypothetical grounds (theoretical cases), a real case is taken into consideration. In addition, to evaluate the impact of geometric resolution in the calculation of volumes, three GSD (Ground Sample

Distance) values were taken into account: 0.25m, 0.5m and 1m. Once built the raster in two different epochs, it is possible to calculate the volume changed by the use of the equation (1). This task can be performed by raster calculator or by specific tool developed in GIS software. For example, in ArcMap software, which is a component of ArcGIS's suite of geospatial package developed and distributed by Esri Company, is available a tool called "Cut/Fill". This tool enables to create a map based on two input surfaces (before and after) displaying the areas and volumes of surface materials that have been modified by the removal or addition of surface material. Indeed, when the Cut/Fill operation is performed, by default a specialized renderer is applied to the layer that highlights the locations of cut and of fill. The determinant is in the attribute table of the output raster, which considers positive volume to be where material was cut (removed), and negative volume where material was filled (added) (Esri, 2020).

The TIN model, instead, is constructed by triangulating a set of vertices (point cloud). There are different methods of interpolation to form these triangles, such as Delaunay triangulation or distance ordering. ArcMap software allows building a TIN using Delaunay triangulation. The calculation of the volume changed using the TIN models (produced in the two reference periods) can be obtained from the difference of the two volumes compared to a plan. In ArcMap is implemented a tool called "Polygon Volume" which calculates the volume and surface area between a polygon and terrain or TIN surface. The output text file will store the full path to the surface, the parameters used to generate results, and the calculated area and volume measurements. Finally, calculations were performed to estimate the extracted volumes using both TIN and GRID models.

4. CALCULATION OF THE VOLUME ON HYPOTHETIC TERRAIN

To evaluate the impact of interpolation models depending on the type of terrain morphology, two terrain models have been taken into account, one with steps and another with a linear slope, as shown below (**Fig. 3b** and **3c**). The dimensions of the area of investigation are 100 m x 50 m (see **Fig. 3a**).

(a)

b)   (c)
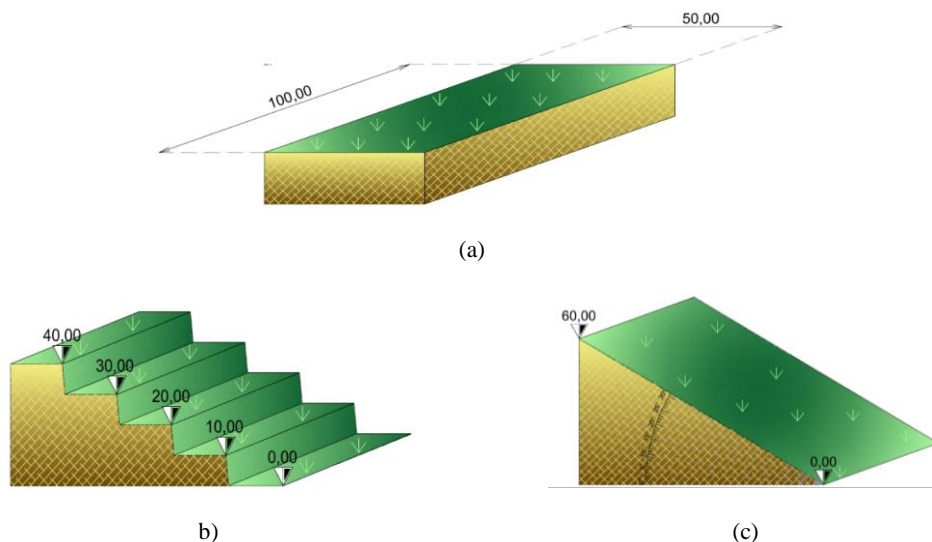
Fig. 3. Theoretical terrain models: dimension of the study area (a); stepped terrain (b) and terrain with linear slope (c)

The volume obtained by TIN model in ArcMap environment was 101,000 m^3 in the case of stepped terrain and 150,215 m^3 in terrain with linear slope. As is well known, the grid format can be obtained with several interpolating functions. In particular, the functions applied on the two case studies are: *IDW*; *Kriging* and *Natural neighbour*.

In this way, it is possible to build several GRID models, as shown below (**Fig. 4**).

(a)
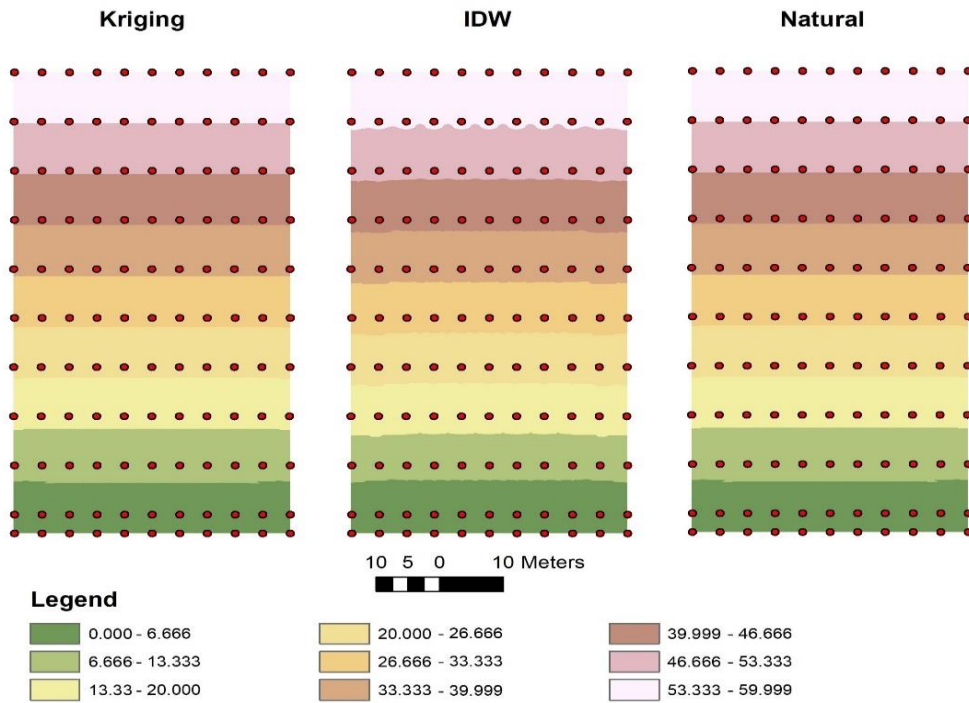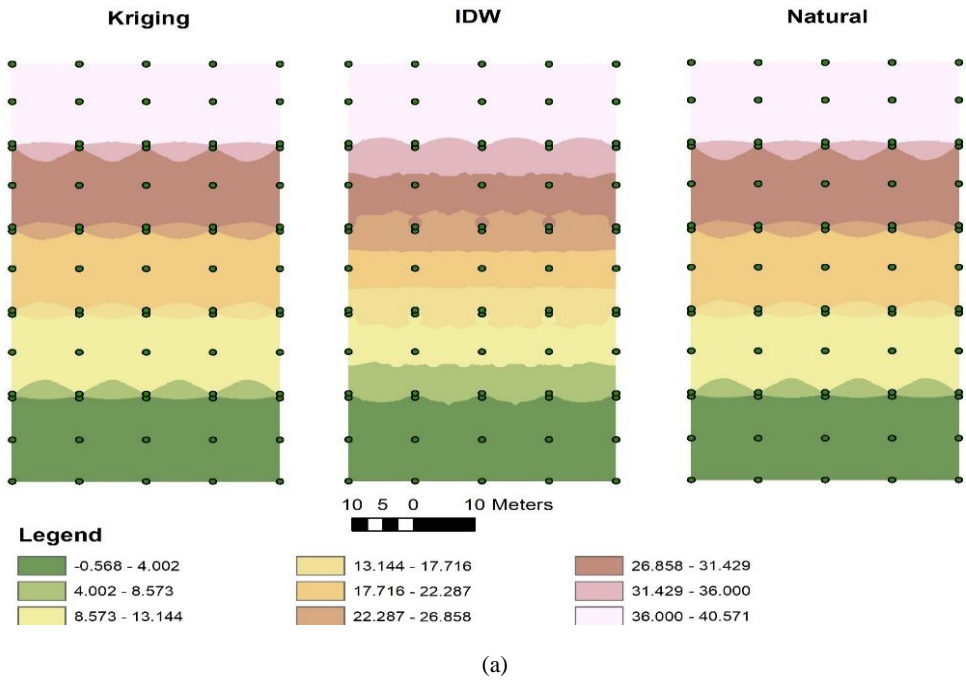
(b)

Fig. 4. GRID models (elevation in meters) obtained using stepped terrain (a) and on terrain with linear slope (b).

From the analysis of **Fig. 4**, it is easy to see that in the case of terrain with a constant slope the interpolating functions assume more or less the same value. In the case of terrain with steps, however, depending on the function used, different values were obtained. Consequently, the volumes obtained on this terrain are different, as shown in **Table 1**.

<div align="right">

Table 1.

</div>

<div align="center">

Volume calculation using GRID models.

</div>

Type of terrain	Volume (m³)			
	IDW	**Kriging**	**Natural**	**TIN**
Terrain with linear slope	149,893	150,331	150,221	150,215
Stepped terrain	99,085	99,557	99,386	101,000

The difference of the volumes between TIN models and grid model are of the order of about 2% in the case of terrain with steps ($delta_{max}$=1915 m³) while less than 1% in the case of terrain with constant slope ($delta_{max}$=322 m³).

5. CASE STUDY

5.1 Study area and geomatics surveys

Over the centuries, the exploitation of mineral resources has experienced alternating phases of more or less intense expansion that have led the Italian mining industry to a leading position at European level and recession, if not even a deterrent to mining activity. In any case, these vicissitudes have left and continue to leave their traces on our territory, as the extraction and exploitation of mineral raw materials always involves essential interactions with the natural environment, the territory, the socio-economic context. Of consequence, the monitoring of mining activities requires appropriate technological tools capable of detecting and calculating the volumes extracted from a quarry.

The quarry under investigation is located in a small town in southern Italy, located in the north-east of the city of Naples (Lat: 40°58'53.55 "N Long: 14°30'24.84 "E, RDN2008 - EPSG6706) and for its morphological conformation has a difference in height of about 180m. The geomatics surveys adopted are the ALS (Airborne Laser Scanner) sensor (at time t_0) and UAV photogrammetry (at time t_1).

5.2 Survey at time t0 by the use of ALS sensor

The survey of the investigated area was carried out using ALS sensor (Pepe et al., 2019; Zlinszky et al., 2011). The flight planning was designed in order to obtain a point density on the terrain of 10 pt/m².

To preserve the designed point density, during the flight, it has been paid much attention to respect the velocity of the project and the constant acquisition of the GPS (Global Positioning System) signal.

Once completed the flight planning, to obtain the point clouds in a specific mapping frame, it is necessary assembly the three datasets: calibration data and mounting parameters, laser distance measurements with their respective scanning angles and Position and Orientation System (POS) data. The post-processing of the ALS data was obtained using several software: Waypoint GrafNav for Differential Global Positioning System (DGPS) processing and Leica Geosystems IPAS Pro in order to manage the combination of GNSS and Inertial measurement unit (IMU).

The CORS - Continuously Operating Reference Station) (Dardanelli et al., 2020) infrastructure present in the Campania region was used in order to obtain GNSS data consisting of carrier phase in support of three-dimensional positioning (Pepe, 2018). Since the elevation coordinates produced by direct georeferencing process take into consideration the ellipsoidal height, using a suitable tool developed in Matlab environment and Italgeo05 geoid (Barzaghi et al., 2005), it was possible to obtain the orthometric height. Finally, in ArcMap software, using *Kriging* method, it was possible to obtain a Digital Elevation Model (DEM) with a geometric resolution of 0.25m x 0.25m and a TIN model of the quarry.

An altimetry representation of the quarry (**Fig. 5a**) and a profile extracted from the DEM (**Fig. 5b**) are shown below.
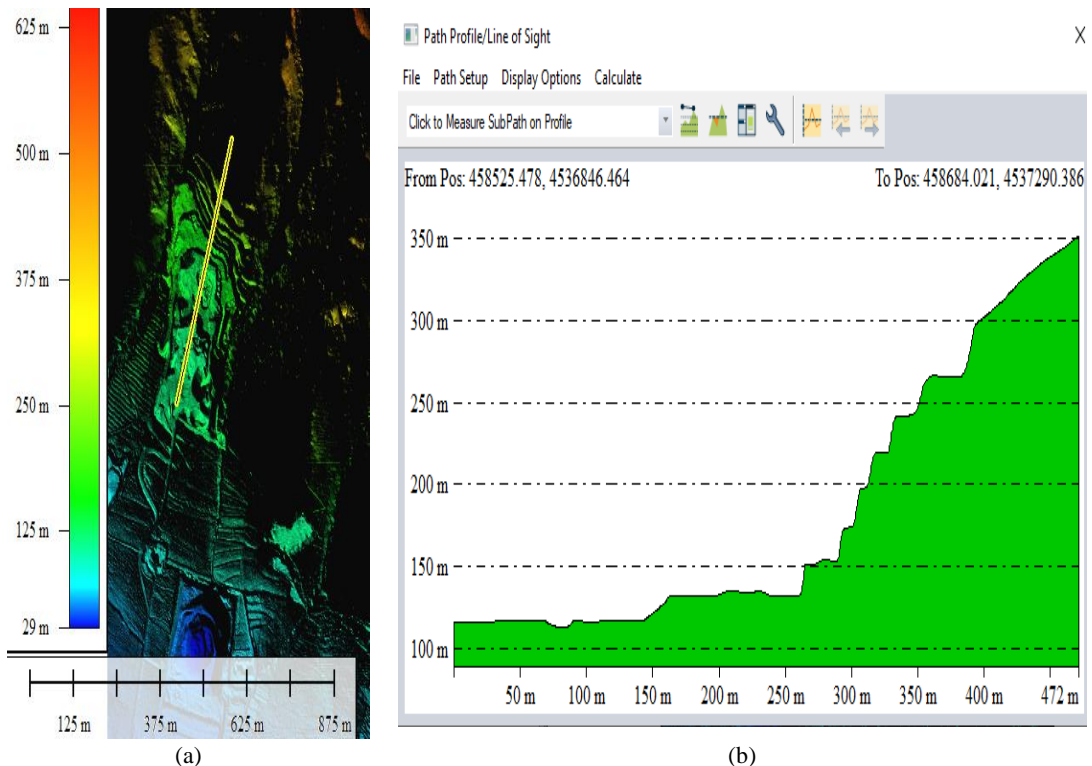
Fig. 5. Morphology of the quarry obtained by ALS survey at time t_0: DTM display in Global Mapper software (a); profile (b).

5.3. Survey at time t_1: UAV photogrammetry

5.3.1. Flight planning

The survey was performed using the Phantom 4 Pro quadcopter from the Chinese manufacturer DJI, which has a satellite assisted flight accuracy of 0.5 m vertically and 1.5 m horizontally. The UAV also has 5-way anti-collision sensors of optical and infrared type, which allow to avoid obstacles within a distance of 10 m and allow the drone to have a stable positioning even in cases where satellite coverage is not available. The main features of the UAS (Unmanned Aerial System) are reported in **Table 2**.

<div align="right">**Table 2.**</div>

<div align="center">**Technical characteristics of the UAS.**</div>

Features	Specifications
UAV Platform	
Max. take-off weight	1388 g
Maximum Speed	72 km/h / 6 m/s
Flight time	~30 min
Camera: DJI FC6310	
Sensor	Effective pixels: 20 million
Photo size	5472× 3648
Focal length	10.26 mm
Field of view	approx. 84°
Aperture	f/2.8-f/11
Shooting speed	Electronic shutter: 8–1/8000 s

In relation to the morphology of the terrain, two take-off/landing points have been identified for missions in order to guarantee the complete visibility of the UAV during the flight operations. The flight altitude adopted to acquire the images was of 30 m respect to the planned take-off/landing points.

The survey was planned through the UGCS software. This software, developed by UgCS Company (Latvia), allows to plan and fly drone survey missions providing convenient tools for areal and linear surveys and enabling direct drone control. Indeed, the software supports a wide range of UAVs, including the vehicle used to carry out the survey and two distinct types of acquisition mode, one nadir direction and the other prospective.

For a better design of flight planning, the software's ability to import custom elevation models was exploited; therefore, a DTM based on ALS data was used.

Two flight plans were designed in order to obtain an average GSD of 2 cm, using the "*terrain following*" function that allows the UAV to have a constant distance to the ground.

5.3.2. Acquisition data

The flight planning for the nadir acquisition is composed by 8 Flight Lines (FLs). A total amount of 216 frames per 216 frames, with an average overlap of 80% and sidelap of 60% was designed (**Fig. 6a**). To cover the vertical part of the steps of the quarry, a specific flight planning was designed; the inclination of the camera was adjusted with an angle of 45°. Additional 10 FLs were planned for a total of 295 frames (**Fig. 6b**).

The waypoints were uploaded into the UAS via the dedicated application (**Fig. 6c**). The correct positioning was obtained thanks to the use of integrated GNSS (Global Navigation Satellite System) receiver.

At the end of the acquisition step by UAV photogrammetry, a GNSS survey in RTK (Real Time Kinematic) with correction by CORS was carried out in order to determine the coordinates of the Ground Control Points (GCPs), which were distributed and materialized by means of high contrast markers within the area to be surveyed.

(a)

(b)
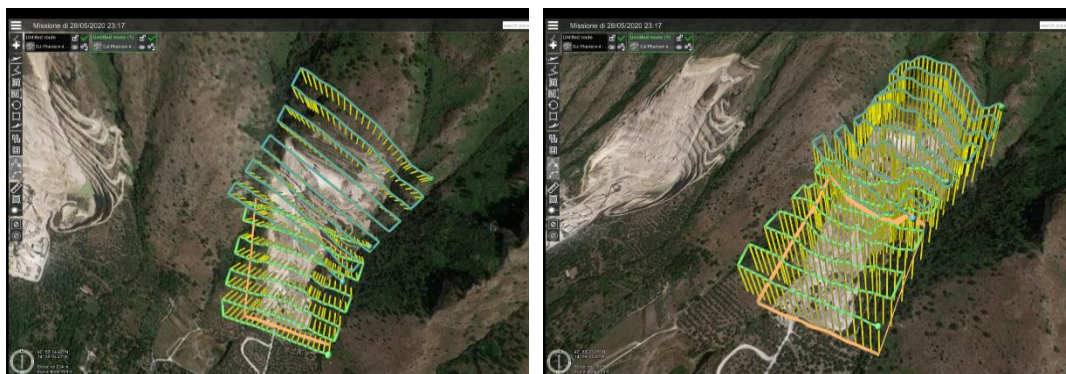
(c)

Fig. 6. Design of the flight plan on the study area: nadir acquisition (a), oblique acquisition (b) complete flight plan (c).

5.3.3. Data processing at time t1

For image processing of UAS dataset, Agisoft Metashape (2018) software was used. Recent studies on the impact of the image format in the SfM/MVS environment have shown the importance of using raw image both from the point of view of geometric accuracy and from the point of view of the quality of the dense point cloud (Alfio et al., 2020); consequently, the images were processed in the raw format.

The process of registration of image was obtained in "highest" quality setting: in this mode, the image is scaled by a factor of 4 (factor of 2 for each side) and allows for high precision in the localization of a point. A high-performance workstation was required to perform the image registration process, as the "highest" parameter requires high processing times.

Table 3 shows the error values obtained from the image recording process and the Total Error (root mean square error for East, North, and Altitude coordinates for all the cameras) on several GCPs easily recognized on images, as supplied by Agisoft Metashape software.

Table 3.

Evaluation of the accuracy on GCPs

GCP	East Error (m)	North Error (m)	Alt. Error (m)	Total Error (m)	Image Error (pix)
1001	0.010	-0.001	0.014	0.017	0.65
1002	0.001	0.021	-0.043	0.048	0.83
1003	0.029	-0.013	0,037	0.049	0.53
1005	-0.009	-0.003	-0.020	0.022	0.88
1006	-0.028	-0,012	0.004	0.031	0.60
1007	0.003	-0.003	-0.014	0.015	0.57
1008	0.002	0.004	0.004	0.007	0.52
1009	-0.009	0.007	0.016	0.020	0.49
TOTAL	*0.015*	*0.010*	*0.023*	*0.030*	*0.66*

Once the image alignment phase was finished, it was possible to process the dense cloud (see **Fig.7**) at three different quality levels, namely *Lowest, Low and Medium*. The setting Lowest mean that the images were downscaled to 6,75%, low mean downscaled to 12,5% and medium mean downscaled to 25%.

(a) (b) (c)
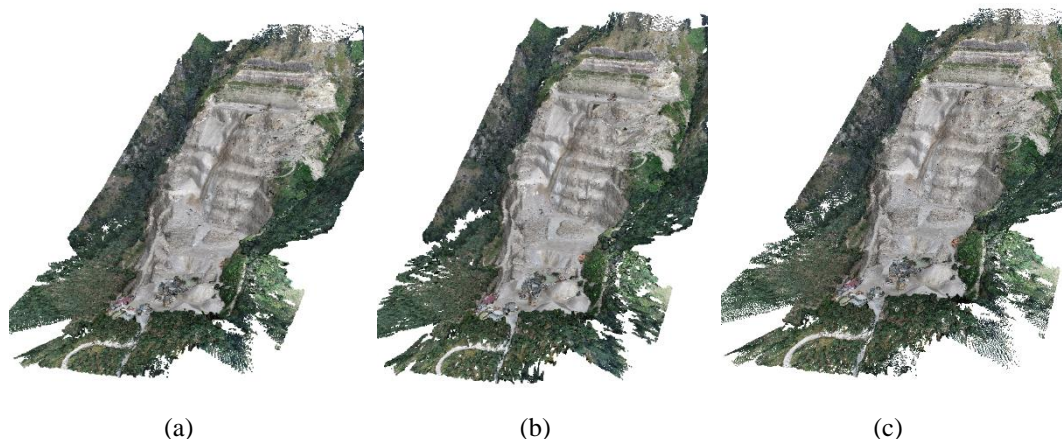
Fig. 7. Dense clouds obtained using different setting in SfM/MVS software: Lowest (a), Low (b) Medium (c).

The processing results, i.e. the number of the points generated in MVS process, using a different level of detail (lowest, low, medium) are summarized in the following **Table 4**.

Processing results using diverse settings

Quality	Tie Points	Dense Point Cloud
Lowest	930,889	3,262,349
Low	930,889	12,534,893
Medium	930,889	48,393,473

To evaluate the geometric difference between point clouds with different levels of point density, a comparison in Cloud Compare software was performed. The point cloud generated with medium setting was used as reference; the results of the comparison are shown in **Table 5**.

Point cloud comparison

Difference point cloud	Mean (m)	Standard Deviation (m)
Lowest- Medium	0.321	0.427
Low- Medium	0.104	0.201

The comparison between the point cloud processed with setting lowest and the one processed with medium shows an average difference value of 0.242m and a Standard Deviation (std) of 0.27m. The comparison between the point clouds processed in low and medium shows an average difference of 0.074m and a std of 0.116m.

6. RESULTS

As the geometrical resolution of the raster changed, it was possible to calculate the volumes in the time frame considered. The results obtained, varying the density of the point cloud, are shown in **Table 6**. In fact, the point cloud created with the setting medium required high computational performance. For this reason, it was not possible to create a TIN or GRID model with this setting.

Impact of the point cloud density and geometric resolution (GRID model) in volume calculation

Resolution (m)	Volume changes (m³)	
	Lowest	*Low*
1	493574	492838
0.5	490341	489935
0.25	485818	485174

Using the TIN as a reference surface, it is possible to obtain the volumes with respect to a reference plane, as shown in the table below (**Table 7**).

Impact of the point cloud density in volume calculations in TIN model

Volume at time to (m^3)	Volume at time t$_1$ (m^3)			Volume changes (m^3)	
	Lowest	*Low*	*Medium*	*Lowest*	*Low*
15576165	15124205	15116333	-	451960	459832

7. DISCUSSION AND CONCLUSIONS

UAV photogrammetry represents an easy, useful and accurate method to reconstruct the geometry of a quarry. Thanks to use of UAV platform, it is possible to collect a large amount of data that once analysed and processed allow to accurately representing the topographical and morphological aspects of the area under examination. The SfM/MVS algorithms allow producing very detailed point clouds of the area under investigation. The intuitive interface implemented in most commercial software based on these algorithms makes point cloud construction quick and easy.

The aim of this work was to evaluate, starting from the data obtained from the photogrammetric survey, how the decision to process a raster data or a TIN data influenced the final result; the choice between GRID and TIN model becomes important according to the morphology of the quarry.

If the quarry presents an almost regular gradient or with constant slope variations, both processing methods lead to an accurate result; on the contrary, if the quarry presents a stepped terrain or with sudden and important changes of slope, the grid model could lead to an incorrect estimation of volumes changes. Therefore, in these cases, it is preferable to adopt the TIN model to estimate volume changes. Finally, the implementation of specific tools in GIS software allows monitoring the quarries over time and, consequently, to estimate the volumes excavated in accurate and simple way.

R E F E R E N C E S

Abidine, M. M. O., El Aboudi, A., Kebd, A., Aloueimine, B. B., Dallahi, Y., Soule, A., & Vadel, A. (2018). modeling the spatial variability of the electrical conductivity of the soil using different spatial interpolation methods: case of the dawling national park in Mauritania. *Geographia Technica*, 13(2).

Ahmadabadian, A.H., Robson, S., Boehm, J., Shortis, M., Wenzel, K., Fritsch, & Fritsch, D. (2013). A comparison of dense matching algorithms for scaled surface reconstruction using stereo camera rigs. *ISPRS Journal of Photogrammetry and Remote Sensing*, 78, 157167. doi:10.1016/j.isprsjprs.2013.01.015

Alfio, V. S., Costantino, D., & Pepe, M. (2020). Influence of Image TIFF Format and JPEG Compression Level in the Accuracy of the 3D Model and Quality of the Orthophoto in UAV Photogrammetry. *Journal of Imaging*, 6(5), 30.

Agisoft, L. L. C. (2018). Agisoft metashape user manual, Professional edition, Version 1.5. Agisoft LLC, St. Petersburg, Russia, https://www.agisoft.com/pdf/metashape-pro_1_5_en.pdf (accessed February, 12, 2020).

Baiocchi, V., Napoleoni, Q., Tesei, M., Costantino, D., Andria, G., & Adamo, F. (2018). First tests of the altimetric and thermal accuracy of an UAV landfill survey. In *2018 5th IEEE International Workshop on Metrology for AeroSpace (MetroAeroSpace)*, 403-406.

Baiocchi, V., Napoleoni, Q., Tesei, M., Servodio, G., Alicandro, M., & Costantino, D. (2019). UAV for monitoring the settlement of a landfill. *European Journal of Remote Sensing*, 52(sup3), 41-52.

Barzaghi, R.; Borghi, A.; Carrion, D.; Sona, G. (2007) Refining the estimate of the Italian quasi-geoid. *Boll. Geod. Sci. Affin.*, 63, 145–158.

Caroti, G., Martinez-Espejo Zaragoza, I., & Piemonte, A. (2015). Accuracy assessment in structure from motion 3D reconstruction from UAV-born images: The influence of the data processing methods. In (Ed.), *ISPRS Archives International Archives of the Photogrammetry Remote Sensing and Spatial Information Sciences*.

Costantino, D., Pepe, M., Dardanelli, G., & Baiocchi, V. (2020). Using optical Satellite and aerial imagery for automatic coastline mapping. *Geographia Technica*, 15(2), 171-190.

Dardanelli, G., Lo Brutto, M., & Pipitone, C. (2020). GNSS CORS Network of the University of Palermo: design and first analysis of data. Geographia Technica, 15(1).

Esri (2020). https://pro.arcgis.com/en/pro-app/tool-reference/3d-analyst/cut-fill.htm (accessed January, 9, 2020.)

Furukawa, Y., & Ponce, J. (2010). Accurate, dense, and robust multiview stereopsis. *IEEE Transactions on Pattern Analysis and Machine Intelligence*, 32, 1362−1376. doi:10.1109/TPAMI.2009.161

Gasperini, D., Allemand, P., Delacourt, C., & Grandjean, P. (2014). Potential and limitation of UAV for monitoring subsidence in municipal landfills. *International Journal of Environmental Technology and Management*,17(1),1–13.

González-Aguilera, D., Fernández-Hernández, J., Mancera-Taboada, J., Rodríguez-Gonzálvez, P., Hernández-López, D., Felipe-García, B., ... & Arias-Perez, B. (2012). 3D Modelling and accuracy assessment of granite quarry using unmmanned aerial vehicle. *ISPRS Annals of the Photogrammetry, Remote Sensing and Spatial Information Sciences*, 3.

Grünner, K., & Dudáš, J. (2017). An accurate measurement of the volume of construction waste dumps by unmanned means. In *Waste Forum* (No. 5).

Hartzell, P. J., Gadomski, P. J., Glennie, C. L., Finnegan, D. C., & Deems, J. S. (2015). Rigorous error propagation for terrestrial laser scanning with application to snow volume uncertainty. *Journal of Glaciology*, 61(230), 1147-1158.

Masiero, A., Chiabrando, F., Lingua, A.M., Marino, B.G., Fissore, F., Guarnieri, A., & Vettore, A. (2019). 3d modeling of Girifalco fortress. Int. Arch. Photogramm. Remote Sens. Spatial Inf. Sci., XLII-2/W9, 473−478. doi:10.5194/isprs-archives-XLII-2-W9, 473-2019.

Nguyen, Q. L., Bui, X. N., Cao, X. C., & Le, V. C. (2019). An approach of mapping quarries in Vietnam using low-cost Unmanned Aerial Vehicles. *Inżynieria Mineralna*, 21.

Pepe, M. (2018). CORS architecture and evaluation of positioning by low-cost GNSS receiver. Geodesy and Cartography, 44(2), 36-44.

Pepe, M., & Costantino, D. (2020). Techniques, Tools, Platforms and Algorithms in Close Range Photogrammetry in Building 3D Model and 2D Representation of Objects and Complex Architectures, *Computer-Aided Design & Applications*, 18(1) 42-65.

Pepe, M., Fregonese, L., & Crocetto, N. (2019). Use of SfM-MVS approach to nadir and oblique images generated throught aerial cameras to build 2.5 D map and 3D models in urban areas. *Geocarto International*, 1-22.

Peucker, T. (1978). The triangular irregular network. *In Proc. of the Digital Terrain Models (DTM) Symposium*, American Society of Photogrammetry, 516-540.

Raeva, P. L., Filipova, S. L., & Filipov, D. G. (2016). Volume computation of a stockpile-a study case comparing GPS and UAV measurements in an open pit quarry. *International Archives of the Photogrammetry, Remote Sensing & Spatial Information Sciences*, 41.

Rhodes R.K. (2017). UAS as an inventory tool: a photogrammetric approach to volume estimation. Ph.D. Dissertation, University of Arkansas.

Sibson, R. (1981). *A brief description of natural neighbor interpolation (Chapter 2)*. In V. Barnett (ed.). Interpreting Multivariate Data. Chichester: John Wiley. 21–36.

Snavely, N., Seitz, S.M., & Szeliski, R. (2007). Modeling the world from internet photo collections. International Journal of Computer Vision, 80, 189–210. doi:10.1007/s11263-007-0107-3

Török, Á., Bögöly, G., Somogyi, Á., & Lovas, T. (2020). Application of UAV in Topographic Modelling and Structural Geological Mapping of Quarries and Their Surroundings - Delineation of Fault-Bordered Raw Material Reserves. *Sensors*, 20(2), 489.

Zlinszky, A., Tóth, V., Pomogyi, P., & Timár, G. (2011). Initial Report of the Aimwetlab Project: Simultaneous Airborne Hyperspectral, Lidar and photogrammetric survey of the full shoreline of lake Balaton, Hungary. *Geographia Technica*, 13(1), 101-117.

A KALMAN FILTER SINGLE POINT POSITIONING FOR MARITIME APPLICATIONS USING A SMARTPHONE

Anna INNAC [1],* , Antonio ANGRISANO [2] , Gino DARDANELLI [3] , Vincenzo DELLA CORTE [4] , Elena MARTELLATO [1] , Alessandra ROTUNDI [1] , Giampaolo FERRAIOLI [1] , Pasquale PALUMBO [1] and Salvatore GAGLIONE [1]

ABSTRACT
Different positioning techniques have been largely adopted for maritime applications that require high accuracy kinematic positioning. The main objective of the paper is the performance assessment of a Single Point Positioning algorithm (SPP), with a Kalman filter (KF) estimator, adapted for maritime applications. The KF has been chosen as estimation technique due to the ability to consider both the state vector dynamic and the measurements. Particularly, in order to compute an accurate vertical component of the position, suitable for maritime applications, the KF settings have been modified by tuning the covariance matrix of the process noise. The algorithm is developed in Matlab environment and tested using multi-GNSS single-frequency raw data, collected by a smartphone located on board a moving ship. The algorithm performance evaluation is carried out in position domain and the results show an enhancement of meter order on vertical component compared to the classical SPP based on Least Square estimation technique. In addition, different GNSSs configurations are considered to verify the benefits of their integration in terms of accuracy, solution availability and geometry.

Key-words: Single Point Positioning; GNSS; Vessel; Smartphone.

1. INTRODUCTION

The Global Navigation Satellite Systems (GNSS) is an essential instrument in maritime navigation, providing position, velocity and time (PVT) information. The main role of GNSS in applications like marine geodesy, offshore survey and physical oceanography is related to the ability of performing a highly precise kinematic positioning of surveying platforms such as buoys, vessels and aircrafts.

GNSS is adopted as main position system for dynamic positioning (DP) of vessels. The International Maritime Organization (IMO) and the certifying societies define a dynamically positioned vessel as a vessel that maintains its position and heading (fixed location or pre-determined track) only by means of active thrusters. Reference sensors, combined with motion sensors, gyrocompasses and wind sensors, provide information to the computer concerning the vessel's position and the amplitude and direction of environmental forces affecting its position (Sørensen, 2011).

[1]Department of Sciences and Technologies, University of Naples Parthenope, Via Ammiraglio F. Acton, 80133 Naples, Italy; anna.innac@uniparthenope.it, salvatore.gaglione@uniparthenope.it, elena.martellato@uniparthenope.it, alessandra.rotundi@uniparthenope.it, giampaolo.ferraioli@uniparthenope.it, pasquale.palumbo@uniparthenope.it

[2] University of Benevento G. Fortunato, Via R. Delcogliano, 82100 Benevento, Italy a.angrisano@unifortunato.eu

[3] Department of Engineering, University of Palermo, Viale delle Scienze, 90128 Palermo, Italy; gino.dardanelli@unipa.it

[4] IAPS – INAF, Via del Fosso del Cavaliere,100, 00133 Rome, Italy; vincenzo.dellacorte@inaf.it

Other GNSS maritime applications are related, for example, to the measures of sea level for validation/calibration of satellite radar altimetry. Information about the accurate positioning of ships and buoys, equipped with a GNSS, will contribute for the determining of the Sea Surface Height (SSH) to be used as a supplementary sensor for tsunami early warning system, combined to satellite altimetry data. GNSS measurements collected aboard a ship, for example, can be used as input parameter to algorithms computing the sea spectrum from the ship motion (IOC, 2006; Marreiros, 2013; Reinking & Härting, 2012; Alkan & Öcalan, 2013).

Different precise positioning techniques have been adopted for maritime applications, associated to accurate positioning requirements for maneuvering or anchoring floating platforms, DP vessel, sea level measurement and hydrographic surveying. GNSS precise positioning in the oceans is an attractive opportunity to be exploited. However, precise positioning of a moving ship is especially challenging due to the high dynamics of the antenna and the high reflectivity of the water (Alkan & Öcalan, 2013).

In this context, GNSS precise relative positioning techniques are widely adopted (Teunissen et al., 2011; Specht el al., 2019). The relative techniques are based on the use of a base receiver (or a network of base receivers), whose location is known, and exploit the concept of spatial correlation of several GNSS measurement errors. The classical differential GNSS technique using only pseudorange (PR) measurements provides meter level accuracy; decimeter or centimeter level accuracies can be obtained using carrier phase observable. To obtain the aforesaid performance, geodetic grade receivers and short baseline lengths are necessary. With short baseline lengths, a few kilometers, RTK (Real-Time Kinematic) is very accurate. However, as the baseline length increases, the accuracy and availability of a solution decreases. The constraint of the limited baseline lengths in RTK can be removed by using a method known as Network RTK (NRTK), whereby a network of reference stations with ranges usually less than 100 km is used (El-Mowafy, 2012). For these reasons, GNSS maritime applications are currently constrained to coastal areas and Precise Point Positioning (PPP) technique could be a valid alternative solution. In fact, PPP is increasingly becoming widespread as an absolute positioning technique since its capability to provide a precision level comparable to differential positioning through the use of a single GNSS receiver and appropriate correction models but without the support of ground stations. In addition, unlike the classical absolute positioning methods based on code measurements from four or more satellites and the broadcast ephemeris to obtain the position of the receiver, PPP has the advantage of using the most precise carrier phase observables, trying to reduce the effect of all the types of errors and biases that affect GNSS measurements.

Both RTK and PPP exploits the carrier-phase measurements, that are highly precise observations but very sensitive to signal obstruction and affected by an ambiguity which is unknown to the user and that can produce long converge time as necessary for PPP (Innac et al., 2018). The rapid development and use of combined multi-GNSS but also multi-frequency (triple and quadruple) observations may be beneficial for precise relative positioning performance. Number of new signal frequencies gives also opportunity for development of new ambiguity resolution algorithms that help to reduce the convergence time of the solution (Paziewski & Wielgosz, 2017). Furthermore, precise positioning is usually performed using high-quality, geodetic-grade GNSS receivers and antennas. These receivers are usually multi-frequency to mitigate the ionosphere influence and obtain faster ambiguity resolution, while the antennas are precisely calibrated to minimize the influence of the errors related to the antenna, and designed to reduce multipath effects. The cost of the previously mentioned equipment is very high, compared to mass-market receivers (Constantin-Octavian, 2012).

Because of technological advances, the potential of low-cost GNSS receivers and antennas has been investigated by scientific community. Low-cost GNSS hardware comprises chipsets, used also in smart devices. Indeed, the current smartphones are very advanced devices, equipped, among other things, with GNSS receivers, multi-axis accelerometers, gyroscopes and other sensors available for different applications.

Furthermore, recent smartphones receive signals from multiple GNSS systems, allowing to increase the satellite navigation performance as well-known by literature (Innac et al., 2018). In addition, the ability to access GNSS raw observables is an interesting feature since the developers are able to implement their own algorithm to compute positioning solution (Specht el al., 2019).

The opportunity of smart devices has been exploited by scientific community to carry out studies on signal quality, to develop algorithms aimed at enhancing the positioning accuracy of mass-market devices, and for several applications (Realini et al., 2017; Lachapelle et al., 2018; Robustelli et al. 2019; Paziewski, 2020).

The aim of the current work is to provide a low-cost alternative with lower performance to the common precise positioning techniques, obtained with RTK or PPP, implementing a Single Point Positioning (SPP) algorithm, with a Kalman filter (KF) estimator, able to achieve an accurate estimate of the position, especially for vertical component. The KF is a recursive algorithm based on a series of prediction and update phases to obtain an optimal state vector estimate (Angrisano et al., 2013). The KF includes a measurement model, formally identical to the one used in Least Square (LS) estimator, and a process model, representing the behavior of the state. Multi-GNSS single-frequency raw data collected by a smartphone are processed by the developed processing technique and different GNSSs combinations are considered, in order to verify the benefit of multi-GNSS integration in maritime context. The proposed algorithm can be suitable for maritime applications conducted on small boats not equipped with expensive sensors and it is especially performing in estimating the vertical component of the position, which is very useful for the analysis of the sea conditions (Montazeri et al., 2016; Piscopo et al., 2020). The positioning algorithm is tested on real data, collected by a smartphone Xiaomi Mi 8 located on board a moving ship; the receiver is a multi-GNSS, GPS, Glonass and BeiDou, device. To perform an error analysis, a ground truth trajectory is computed processing the collected dataset in differential mode.

The paper is organized as follow: section 2 describes the theoretical concepts of the developed algorithm, section 3 describes the test configuration and ground truth trajectory computation, section 4 provides a description of the experimental results and section 5 concludes the paper.

2. MULTI-GNSS SPP ALGORITHM

In this section, an overview of the adopted multi-GNSS SPP algorithm is provided. In detail, PR measurements from GPS, Glonass and BeiDou systems are processed and the KF estimation method is applied to compute position. The KF filter settings have been adapted for the considered application in order to obtain high accuracy on vertical component of the position. The EKF has the advantage to take in account, in addition to measurements information, also the dynamic model, whose uncertainty is expressed by covariance matrix of the process noise. In detail, the covariance matrix of the process noise has been configured using lower variance values for vertical component of the position in accordance with the behavior of the altitude of the moving vessel.

Even if GPS, Glonass and BeiDou are based the same operational principle, they have some differences related to signal, constellation and reference categories. These differences are largely detailed in literature (Li et al., 2015). When multi-GNSS observations are used to compute the navigation solution, the aforesaid differences are considered as detailed in (Angrisano et al., 2013). The theoretical concepts by the literature are applied in the current work as briefly described below. A customized PVT algorithm has been developed in MatLab® environment as detailed in (Angrisano et al., 2013) and belongs to a Toolbox developed by authors, who are members of PANG (PArthenope Navigation Group – http://pang.uniparthenope.it).

2.1. Multi-GNSS SPP

The standard PVT algorithm is based on PR observables, whose expression is:

$$PR = d + c\delta t_u - c\delta t_s + \Delta I + \Delta T + \varepsilon \tag{1}$$

where d is the range between the receiver and the satellite, δt_u and δt_s are the receiver and satellite clock offsets, c is the speed light, ΔT and ΔI are, respectively, the errors due to the tropospheric and ionospheric effects, and ε represents the residual errors. In detail, single-frequency raw PR measurements are corrected for the satellite clock error, using the parameters broadcast within GNSS navigation message. Furthermore, Saastamoinen and Klobuchar models are used, respectively, for the tropospheric and ionospheric delays correction (Hoffmann-Wellenhof et al., 1992; Kaplan, 2006; Angrisano et al., 2013).

Starting from nominal values of receiver clock offset and user position, indicated as $\underline{x}_0 = [x_0, y_0, z_0, c\delta t_0]^T$, the equation (1) must be linearized by a Taylor series expansion, truncated at the first order (Kaplan, 2006). The linearized measurement model describing the relationship between the state and the measurement at the current time step k is given by the following equation:

$$\underline{z}_k = H_k \cdot \underline{\Delta x}_k + \underline{\varepsilon}_k \tag{2}$$

In the above equation, the terms are defined as follows:
$\underline{z}_k$ is the measurements vector containing the differences between measured and computed PRs;
H_k is the geometry matrix;
$\underline{\varepsilon}_k$ is the measurement noise vector that is assumed to be zero-mean Gaussian with the covariance R, i.e., $\underline{\omega}_k \sim N(0, R)$;
$\underline{\Delta x}_k$ is the state vector of the linearized measurement model, containing the position and clock offsets from the linearization point.

Moreover, if multi-GNSS observations are used, the offset with respect to a time reference system, the inter-system offset, is considered for each new additional GNSS constellation.

Using an estimation method, the unknown components of the state vector $\underline{\Delta x}$ can be obtained. So, the user coordinates, the receiver clock and inter-system offsets can be obtained updating the approximate estimates as follows:

$$\underline{x}_k = \underline{x}_0 + \underline{\Delta x}_k \tag{3}$$

2.2. Extended Kalman Filter

To estimate the state vector, an Extended Kalman filter (EKF) estimator is used, that is the nonlinear type of the KF (Kalman, 1960) but able to provide the optimal solution to the linearized problem, fitting well with the considered application. In the current work, the EKF settings have been empirically tuned starting from reference values provided by literature (Kalman, 1960; Parkinson et al., 1996; Welch & Bishop, 2004). Furthermore, the measurements collected by the smartphone are characterized by higher noise than other types of receivers. In order to reduce the effects of the higher measure noise level, the covariance matrix of the process noise has been set using larger values of variance respect to the classical reference values.

The EKF estimation technique is based on knowledge about measurements and state vector dynamics adopting both measurement (2) and process models (4). The process model is given by following equation:

$$\underline{\Delta x}_{k+1} = \Phi_{k+1} \cdot \underline{\Delta x}_k + \underline{\omega}_k \tag{4}$$

where the transition matrix is indicated by Φ_{k+1} and $\underline{\omega}_k$ is the process noise vector, assumed zero-mean Gaussian with the covariance Q, i.e., $\underline{\omega}_k \sim N(0, Q)$.

KF is recursive, consisting of a series of prediction and update steps to obtain the optimal estimate of the state vector. Storing only the last filter computation result helps out in storage space issues effectively (Kalman, 1960; Parkinson et al., 1996; Welch & Bishop, 2004; Angrisano et al., 2013).

The first step of EKF is the prediction of the state vector, $\underline{\Delta x}_k$, and the associated covariance matrix, P_k , starting from the assumed process model:

$$\underline{\Delta x}_k^- = \Phi_k \cdot \underline{\Delta x}_{k-1}^+ \tag{5}$$

$$P_k^- = \Phi_k P_{k-1}^+ \Phi_k^T + Q_k \tag{6}$$

In the above expressions the superscript "-" indicates a predicted quantity (i.e. before updating the measurements) and the superscript "+" refers to the corrected quantity (i.e. after the update of the measurements). The term Q_k is the covariance matrix of the process noise and indicates uncertainty in dynamic models.

In this work, the covariance matrix of the process noise is fine-tuned in order to obtain a more accurate estimation of vertical component of position, assigning suitable values to the components of the position. In particular, lower variance values are set for Q_k element corresponding to vertical component.

After the prediction step, the update phase is used to correct the state vector and the associated covariance matrix according to the measurement model. The EKF correction equations are:

$$\underline{\Delta x}_k^+ = \mathrm{K}_k \cdot (\underline{z}_k - H_k \widehat{\underline{\Delta x}_k^-}) \tag{7}$$

$$P_k^- = \Phi_k P_{k-1}^+ \Phi_k^T + Q_k \tag{8}$$

The Kalman gain matrix K_k is defined as

$$\mathrm{K}_k = P_k^- H_k^T (H_k \, P_k^- H_k^T + R_k)^{-1} \tag{9}$$

where R_k is the measurements error covariance matrix and, in the current research, is defined as function of satellite elevation as in (Angrisano et al., 2013) for all GNSSs .

The Kalman gain matrix is a weighting factor that is multiplied to the difference between the actual measurement vector $\underline{z}_k$ and the predicted measurement vector $H_k \Delta x_k^-$ This term is referred to as innovation vector and describes the amount of information introduced by the current measurements in the system. Consequently, the Kalman gain matrix indicates how much the final state vector estimate is influenced by the new information contained in the innovation vector (Angrisano et al., 2013).

The process model must be selected according to the user dynamics, in order to obtain satisfying performance; the position states are usually modeled as random walk or Gauss-Markov processes (P model) for a stationary user located at an unknown location. Instead, velocity or acceleration states are modeled as random walk processes (PV or PVA models), respectively, for user with low or high dynamics as described in (Welch & Bishop, 2004). In the current work, PV model is used as process model to obtain the best position estimates using data collected in kinematic mode as described in sub-section 3.1.

In **Fig. 1**, an overview of the developed SPP algorithm is provided. The main inputs of the algorithm are GNSS pseudorange observables and ephemerides. The ephemerides are used to compute satellite position and clock offset; different orbital propagators are implemented for the various GNSSs considered due to the different parameterization of the ephemerides.

The raw PR measurements are corrected as described in section 2.1 and used in the EKF or Weighted Least Square (WLS) estimator techniques to estimate epoch-by-epoch the positioning solution. Finally, the error analysis is carried out in position domain comparing the computed solution to the reference.
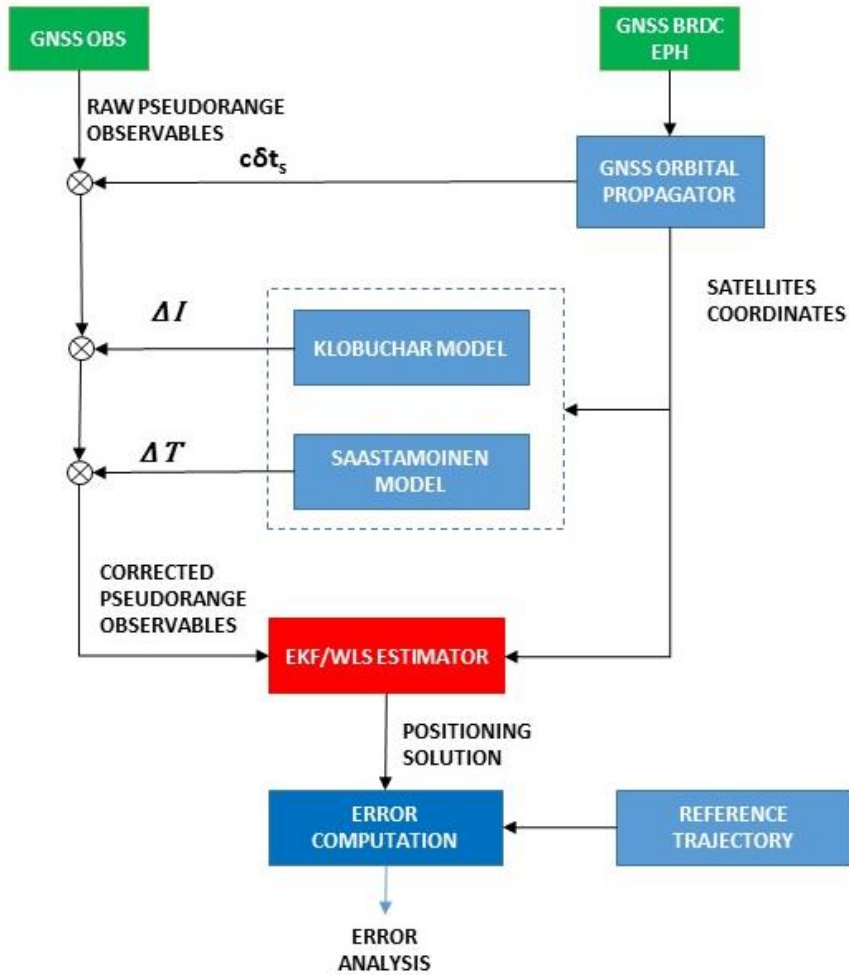
Fig. 1. SPP algorithm

3. TESTS

In this section a description of experimental setup is provided, detailing the configuration of the kinematic test in sub paragraph 3.1. To evaluate the performance of the proposed algorithm, error analysis in the position domain is carried out. Since for a kinematic test the computation of the reference trajectory is a challenging problem, in this study the data collected has been processed in differential mode, using data from a reference station as described in sub-paragraph 3.2.

3.1. Kinematic data collection

The performance of the proposed multi-GNSS SPP algorithm are evaluated processing real data in kinematic mode using a smartphone located onboard a ferry-boat travelling Mediterranean Sea on 18th of august 2019. Start and end points locations of the test are shown in **Fig. 2** and travelled distance is about 29 km.
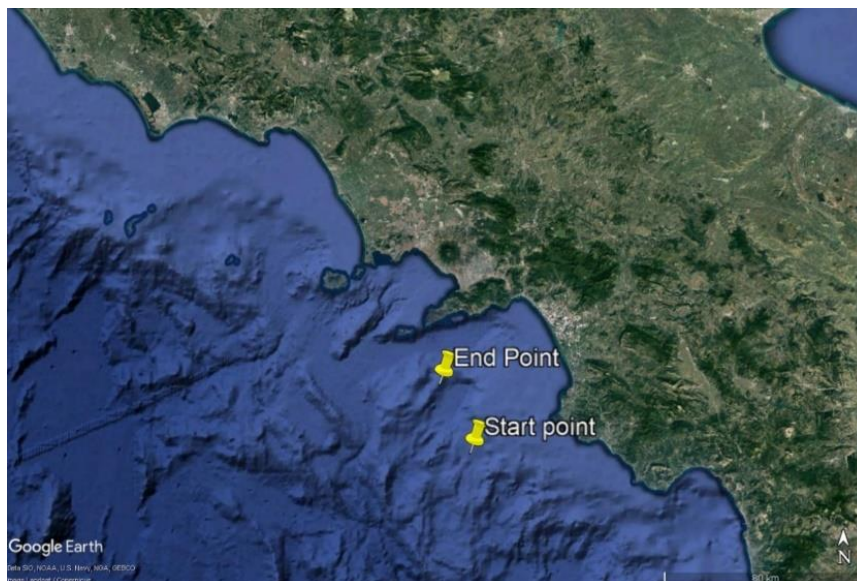
Fig. 2. Start and end points of the kinematic test performed using a smartphone onboard a ferry-boat on 18th of august 2019 (image acquired from Google Earth V. 7.3.3.7786)

One hour of 1 Hz measurements, collected on GPS L1, Glonass G1 and BeiDou B1 signals, are collected using Xiaomi Mi 8 located approximately in the centre of mass of the boat and Rinex ON application is used to store the raw observables in a RINEX (Receiver Independent Exchange Format) file. The Xiaomi Mi 8 is an Android smartphone equipped with a Broadcom BCM47755 chipset that is a dual-frequency GNSS chip able to track navigation messages, PR observables, accumulated delta ranges for GPS, Glonass, BeiDou and Galileo. However, during the considered test no Galileo satellites were tracked, probably due to a failure of the receiver or the logging application.

3.2. Reference trajectory

To perform an error analysis in position domain, a reference trajectory is obtained processing the kinematic dataset collected by the Xiaomi in differential mode using data from a permanent station located in Sorrento (SORR, Naples) and belonging to Leica ItalPoS network. Only code measurements have been used since the collected carrier phase measurements were noisy and un-continuous. It is well-known that smartphone GNSS observations are affected not only by measurement noise and multipath but also by anomalies such as gradual accumulation of phase errors and duty cycling. These phenomena limit the use of smartphone phase measurement to high-precision techniques such as RTK or PPP as described in (Paziewski et al., 2019). The analysis of smartphone signal quality confirmed the divergence between code and phase observations and poor quality of the latter.

In the present work, two different software have been used to compute the reference solution and both tools have not been able to effectively use carrier-phase measurements.

The two software used to compute the ground truth in this research, are:

- RTKlib ver. 2.4.3 b33, an open source positioning software developed by Dr. T.Takatsu (Takasu et al., 2007). Using the software Graphic User Interface, all the data and corrections are inserted as inputs. It supports standard and precise positioning algorithms with multi-GNSS (GPS, Glonass, Galileo, QZSS, BeiDou and SBAS) observations. For the aim of the paper, "DGPS/GNSS" (Code-based differential) has been chosen as positioning mode, using dual-frequency observations from GPS, Glonass and BeiDou systems. In addition, the

broadcast ionospheric and Saastamoinen tropospheric models have been applied. Navigation and observation RINEX files for both rover (smartphone) and base station (SORR) have been selected as inputs to RTKPOST (that is a RTKLIB module for post processing of GNSS data).

- Topcon Tools ver. 8.2.3, a commercial GNSS software, developed by Topcon Corporation. The software allows the processing of data from different devices such as total stations, digital levels and GNSS receivers, and it is used in many technical-scientific applications (Dawidowicz et al., 2015; Pa'suya et al., 2017). Topcon Tools uses the Modified Hopfield Model for the tropospheric corrections (Goad 1974). The employed positioning mode has been "CODE DIFF" (Code-based differential), and the time range and the cut-off angle have been set to 1 s and 10 degrees, respectively.

In the **Table 1** an overview of the settings used in the two software to obtain the positioning solution.

Table 1.

RTKlib and Topcon configurations used for the reference's computation.

Settings	RTKlib	Topcon
Positioning mode	Dual-frequency code-based differential	
Iono model	Klobuchar	Iono-free combination
Tropo model	Saastamoinen	Modified Hopfield
Mask angle	10°	
GNSS system	GPS, Glonass, BeiDou	GPS, Glonass
Base station	SORR (Sorrento, Naples) of Leica Italpos	

The ground truth has been chosen, comparing the solutions obtained with RTKlib and Topcon Tools in terms of solution availability and stability of the positioning estimates on vertical component.

The reference altitude is considered because one of the aim of the work is to provide an accurate estimation of the vertical component of the position, using the proposed SPP algorithm.

In **Fig. 3** the behavior of the two post-processed altitude values during the data collection is shown; in detail, the altitude solution computed using Topcon software is plotted in magenta line, while the altitude behavior obtained using RTKlib is represented by black line.
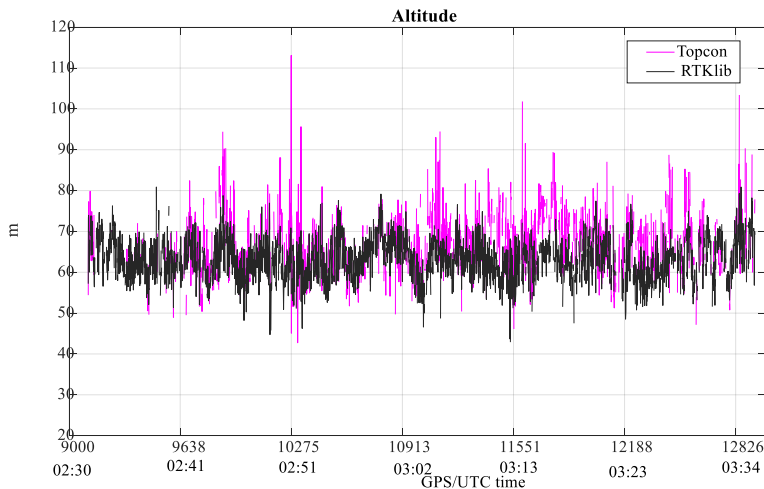
Fig. 3. comparison between altitude references obtained using RTKlib (black line) and Topcon (magenta line) software

From the figure, it can be highlighted that the altitude solution computed using RTKlib is more stable than Topcon solution. Indeed, for the altitude obtained with Topcon software, the mean value is 66.9 meters, the maximum is 113.1 meters and a standard deviation is 7.2 meters, while for the solution computed using RTKlib mean value, maximum value and standard deviation are respectively equal to 63.0, 80.9 and 5.0 meters. The altitude obtained with RTKlib has smaller peaks and less dispersion around the mean, hence it has a behavior more consistent with a ship motion.

The solution availability is the percentage of the epochs in which the software is able to provide positioning solution. Using RTKlib the solution availability is equal to 86.12 % while a lower solution availability is obtained using Topcon (52.8 %). The lower Topcon solution availability is related to the low quality of smartphone data, requiring more flexibility in the processing engine. Being Topcon Tools a professional software mainly for surveying and geodesy fields, it is designed for high quality data and based on very robust processing assumptions to deliver the most reliable solutions.

Based on these considerations, the RTKlib solution has been chosen as reference trajectory for the error analysis, with the purpose of verifying the performance of the proposed algorithm.

4. RESULTS

This section shows the experimental results obtained using the proposed SPP algorithm to process data collected during the kinematic test described in 3.1.

To verify both the benefit of GNSSs integration and the enhancement of the proposed algorithm especially on the estimation of the vertical component of position, different GNSS configurations are considered:
- GPS SPP-EKF (obtained processing only PR observables from GPS system);
- GLO (Glonass) SPP-EKF;
- BDS (BeiDou) SPP-EKF;
- GPS/GLO SPP-EKF (obtained processing only PR observables from GPS and Glonass systems);
- GPS/BDS SPP-EKF;
- BDS/GLO SPP-EKF;
- GPS/GLO/BDS SPP-EKF.

Furthermore, the SPP with WLS method is considered for comparison, using the same GNSSs combinations used for SPP-EKF approach.

After the data processing, the error analysis is carried out in position domain comparing the estimated solution with the RTKlib reference. The performance is evaluated in terms of RMS, mean and maximum error for both horizontal and vertical positioning errors.

Firstly, the improvements obtained using different GNSSs combinations in terms of satellite availability and geometry are analysed considering the number of available GNSS satellites and the satellite geometry, represented by the Position Dilution of Precision (PDOP). In **Table 2**, the minimum, maximum and mean values of PDOP and of number of visible satellites, for all the considered GNSS configurations, are shown. In addition, the solution availability is shown in the **Table 2**.

From the **Table 2**, it can be noted the improvement obtained thanks to the integration of GPS, Glonass and BeiDou satellites in terms of satellite visibility and geometry with the highest number of GNSS satellites and lowest values of PDOP. GPS-only, GPS/GLO and GPS/BDS configurations also show a good satellite geometry and high solution availability. Conversely, high PDOP values are obtained using only Glonass satellites with a maximum value of almost 30. The BDS satellites, visible diring the session, are 2 IGSO (Inclined geosynchronous orbits) and 6 MEO (Medium Earth orbits) and belongs to BDS-2 and BDS-3. BeiDou-only geometry seems better than Glonass one but is significantly worse with respect to GPS case.

The Glonass/BeiDou integration improves the satellite geometry. The best geometry is obtained, as expected, with the GPS/GLO/BDS configuration, which has PDOP values slightly lower than GPS-only case. Similarly, the solution availability of configurations including GPS is almost 100%, while the configurations without GPS are more discontinuous.

Table 2.

Statistical indicators of satellite visibility (as total number of visible satellites), geometry (as Position Dilution of Precision) and solution availability.

GNSS configuration	PDOP			Total number of SV			Solution Availability (%)
	Min	**Max**	**Mean**	**Min**	**Max**	**Mean**	
GPS	1.4	1.9	1.6	1	10	9.3	99.8
GLO	2.0	29.9	4.3	2	8	6.2	87.5
BDS	2.6	10.1	3.4	3	8	6.3	42.8
GPS/GLO	1.2	1.9	1.3	7	17	15.4	99.8
GPS/BDS	1.1	1.8	1.3	7	18	15.5	99.8
GLO/BDS	1.5	10.1	2.0	3	16	12.4	98.5
GPS/GLO/BDS	1.0	1.8	1.1	7	25	21.6	99.8

In **Fig. 4**, the number of GNSS satellites and PDOP behaviour are plotted as function of time only for GPS (green line), GLO (orange line), BDS (black line) and GPS/GLO/BDS (blue line) configurations.
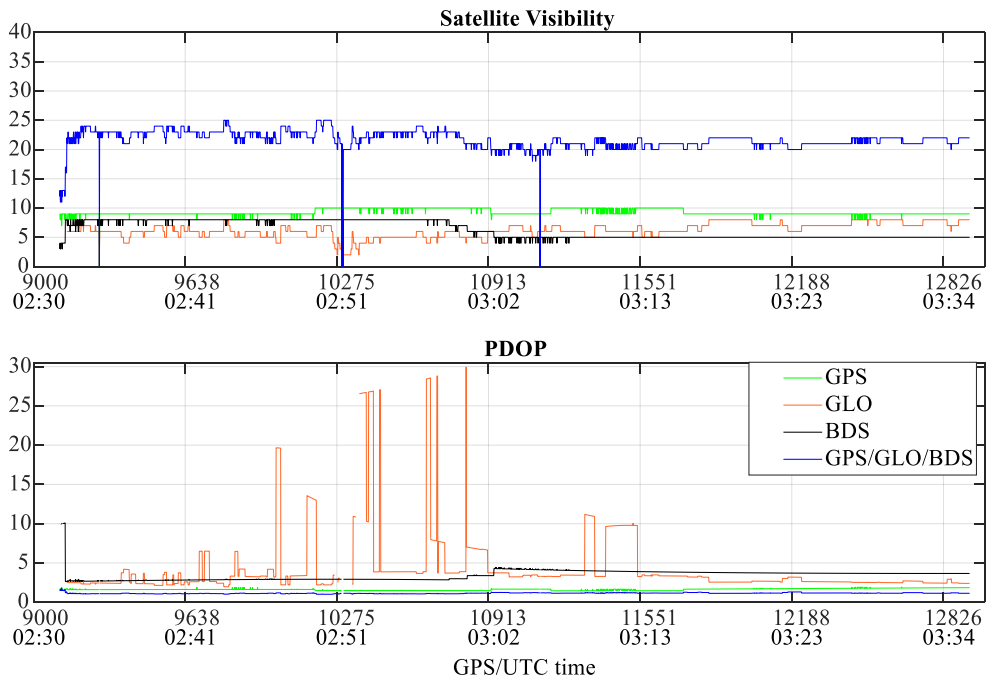
Fig. 4. Satellite visibility and PDOP behaviors for GPS (green line), GLO (orange line), BDS (black line) and GPS/GLO/BDS (blue line) configurations.

The figure confirms the results shown in **Table 2** and, in particular, the best performance of triple-GNSS constellation in terms of satellite visibility and geometry. Indeed, the number of satellites for GPS/GLO/BDS has a mean value of about 22 and PDOP mean value is equal to 1.1. However, all the

analysed GNSS configurations have shown three outages (with a duration of 1 second) due to a signal loss related to some failure of the receiver.

The **Table 3** summarizes the statistical parameters of the error analysis in the position domain for all the considered GNSS configurations and using two different estimators (EKF and WLS).

Table 1.

Summary Results for Horizontal (H) and Vertical (Up) component of the position obtained using the considered GNSS configurations and two different estimators (EKF and WLS).

PVT Algorithm	GNSS configuration	Mean Error		RMS		Max	
		H	Up	H	Up	H	Up
SPP EKF	GPS	3.39	0.03	4.00	3.87	19.27	15.82
	GLO	9.84	11.29	11.58	19.99	49.28	113.10
	BDS	8.27	4.73	9.64	18.24	32.90	72.08
	GPS/GLO	5.92	2.17	6.83	4.87	42.53	31.36
	GPS/BDS	5.87	0.81	7.51	5.52	33.66	29.00
	BDS/GLO	9.79	4.99	11.53	13.87	43.36	67.13
	GPS/GLO/BDS	6.51	0.18	7.76	5.57	31.52	27.50
SPP WLS	GPS	3.86	5.26	4.64	6.65	22.15	21.77
	GLO	11.77	12.48	14.17	28.11	88.67	269.24
	BDS	8.91	2.17	10.41	19.18	46.25	90.42
	GPS/GLO	5.77	2.49	6.73	4.97	42.55	31.16
	GPS/BDS	6.01	0.13	7.65	5.55	33.90	28.39
	BDS/GLO	9.95	4.30	11.80	14.88	57.44	93.81
	GPS/GLO/BDS	6.39	1.99	7.68	5.79	32.15	30.47

Comparing the configurations adopting different estimation techniques (EKF versus WLS), it can be noted that SPP-EKF provides significant improvement with respect to the WLS for all the analyzed figures of merit, especially on vertical component. In detail, an enhancement of meter order can be highlighted if GLO SPP-EKF is compared to GLO SPP-WLS on both vertical and horizontal component of the position. For all the other GNSS SPP-EKF configurations vertical mean error and RMS decrease by several meters compared with the corresponding GNSS SPP-WLS setting, while only an enhancement of decimeter level is evident for horizontal component of the position. The vertical errors for SPP-EKF configurations are lower than SPP-WLS due to the different adopted estimators and to the chosen setting of EKF. Indeed, EKF takes into account also the dynamic model in addition to measurements information, and the behaviour of the altitude of a ship during navigation has been taken into account choosing low variance values for the element of process noise matrix corresponding to vertical component. The same concept cannot be applied to latitude and longitude, so in EKF horizontal errors are larger than vertical ones.

About the benefit of GNSSs integration in the proposed algorithm, it can be noted that GPS-only configuration has the best performance in terms of all considered figures of merit. Conversely, GLO SPP-EKF has the worst behaviour with the highest statistical parameters' values, while a better accuracy solution is obtained using BDS SPP-EKF approach. Furthermore, the integration of Glonass satellites affects the accuracy of triple-GNSS constellation solution, that decreases with respect to GPS-only case. Considering dual-constellations, it can be noted that GPS/BDS SPP-EKF approach has better performance compared to GPS/GLO case, especially on vertical components with an enhancement of meter level. Finally, GPS/BDS SPP-EKF has statistical parameters values similar to GPS/GLO/BDS case. These results are related to the lower performance of Glonass and BeiDou systems compared to GPS in an open sky scenario.

About the expected worse performance of multi-GNSS configurations compared to GPS-only, in other work (Innac et al., 2018) the authors showed that, using multi-constellation, the enhancement in terms of accuracy is subject to the operational scenario and it is more evident in difficult environments for satellite navigation such as urban areas. However, benefits of the multi-constellation system in terms of integrity, availability and continuity are possible for any scenario, including an

open-sky scenario as confirmed by the solution availability, satellite visibility and geometry summarized in **Table 2**.

The same trend can be also highlighted for the configurations adopting WLS and comparing the several GNSS combinations: in fact, also in this case, GPS-only SPP-WLS has the best performance, especially on horizontal component. However, integrating GPS system with BeiDou or Glonass satellites, an accuracy improvement can be verified on vertical component of the position, especially for GPS/BDS integration, showing lower values of vertical mean error and RMS respect to single constellation setup. Also for SPP-WLS approach, the Glonass only configuration has the worst performance for all the figures of merit. Furthermore, considering GPS/GLO/BDS combination no evident enhancements in terms of accuracy can be seen due to the influence of Glonass measurements.

The values of horizontal and vertical RMS and mean errors for all the analysed GNSS configurations using the two SPP approaches are resumed in the **Fig. 5**. In the upper part of the plot, the statistical analysis for GNSS SPP-EKF is illustrated (where the blue bar indicating vertical mean error for GPS-only is not visible because is very low) while GNSS SPP –WLS performance are shown in the bottom.
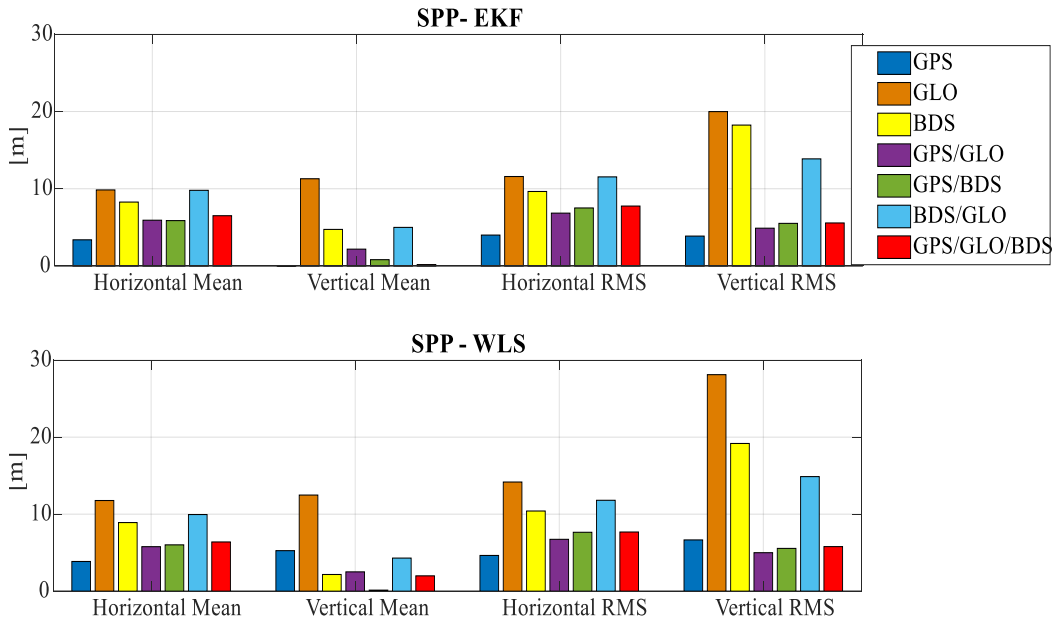
Fig. 5. RMS and Mean position errors for GPS (blue bar), Glonass (orange), BeiDou (yellow), GPS/GLO (violet), GPS/BDS (green), BDS/GLO (light blue) and GPS/GLO/BDS (red) using SPP-EKF and SPP- WLS approaches

A qualitative analysis is carried out comparing the two best solutions, obtained using the proposed SPP-EKF algorithm (GPS-only and GPS/GLO/BSD). Horizontal and vertical position errors, computed with respect to the reference solution, are plotted as a function of time in **Fig. 6** in which the green line is used for GPS SPP EKF and blue line for GPS/GLO/BDS SPP-EKF.

The figure confirms the experimental results previously described. The best configuration is GPS SPP-EKF showing the lowest positioning errors on both vertical and horizontal components. Conversely, GPS/GLO/BDS SPP-EKF solution accuracy slightly decreases in the epochs characterized by a higher satellite visibility due to the integration of BDS and GLO observables. These results are in line by literature (Angrisano et al., 2013; Innac et al., 2018) confirming that using the multi-constellation system in an open sky scenario, an enhancement in terms of availability and integrity is guaranteed but a position accuracy degradation of decimetre level could be obtained.
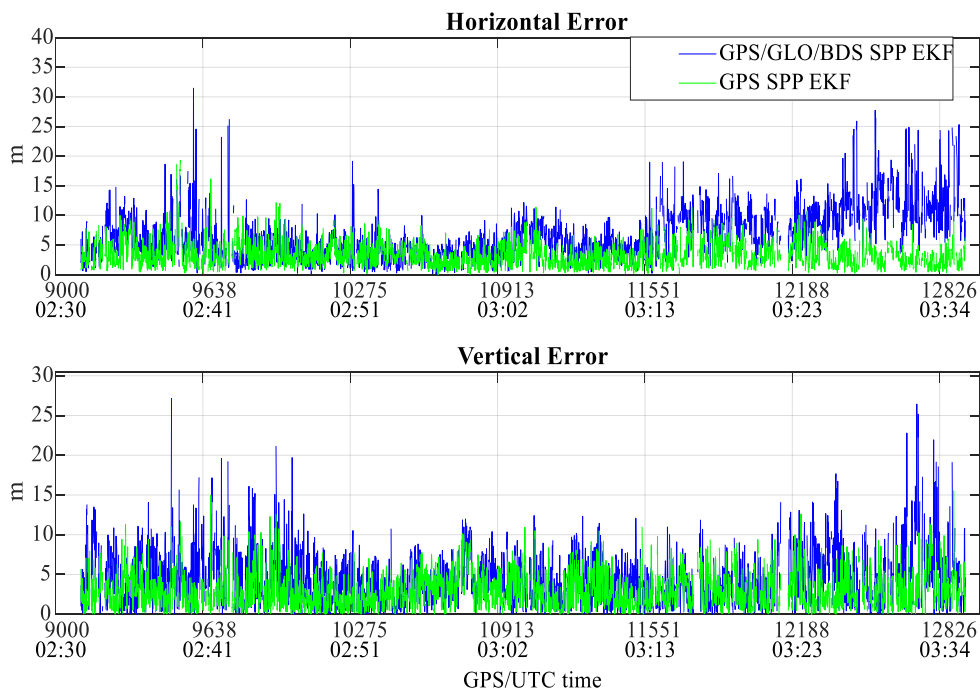
Fig. 6. Horizontal and vertical positioning errors for the considered configurations:
for GPS SPP EKF (green line) and for GPS/GLO/BDS SPP-EKF (blue line)

5. CONCLUSIONS

The precise positioning techniques (RTK or PPP), commonly used for maritime applications, are limited by different factors such as the application of corrections transmitted by stations located nearby, long convergence times due to the ambiguity resolution problem and the use of high-quality GNSS receivers and antennas. The main objective of the work is to provide a positioning technique, usable in maritime applications and based on low cost equipment.

The vertical component of the position is a key parameter for the analysis of the sea conditions, which starts from the survey of the amplitudes of the vessel motions. Therefore, for related applications, it is fundamental to estimate accurately the altitude.

A low cost positioning, which estimates accurately the altitude, is suitable for small boats (to support the navigation) or passenger of large ships (to provide information about the sea conditions).

A GNSS receiver embedded in a smartphone has been chosen for the experiment in this work.

The proposed algorithm allows global coverage for offshore applications, extending the ability to obtain acceptable accuracy even in remote areas, reducing the costs and logistic requirements necessary for maritime applications.

A SPP algorithm has been implemented using a EKF approach finely tuned to improve the altitude estimates. The proposed algorithm has been tested using a kinematic data collection performed locating a smartphone on board a ferryboat travelling Mediterranean Sea. GPS, Glonass and BeiDou PR observables have been processed using the proposed algorithm and its performance are evaluated in position domain and compared to SPP-WLS approach (that is SPP with Weighted Least Square estimator). Carrier phase measurements are not included in the processing, because of their inherent instability, typical of smartphone GNSS chips. Furthermore, different GNSSs combinations have been considered and their contribution in terms of accuracy, solution availability, satellite visibility and geometry has been analysed.

Experimental results have highlighted that SPP-EKF provides an enhancement of meter order on vertical component of the position, while a slightly improvement is evident on horizontal plane as expected from the setting of the covariance matrix of the process noise. Considering the obtained performance, based on the analysed data, the algorithm can be used for applications that need to determine the sea conditions that can cause a state of discomfort for the user on board the ship and for small boats. However, the performance of the proposed algorithm, using data collected by high grade receivers, will be analysed in future works.

About the benefit of the GNSSs integration, the results have shown that GPS-only configuration has better performance with respect to other GNSSs configurations in terms of accuracy, while an enhancement in terms of satellite availability and geometry is obtained thanks to the integration of GPS, Glonass and BeiDou observables. However, as well known, the benefit of multi-GNSS constellation in terms of accuracy could be exploited in an urban environment where the presence of obstacles creates a complex operational scenario, characterized by blocking and multipath phenomena.

A C K N O W L E D G M E N T S

R E F E R E N C E S

Alkan, R. M. and Öcalan, T. (2013). Usability of the GPS precise point positioning technique in marine applications. The Journal of Navigation, 66(4), 579–588.

Angrisano, A., Gaglione, S., Gioia, C. (2013) Performance assessment of GPS/GLONASS single point positioning in an urban environment. Acta Geodaetica et Geophysica, 48(2), 149-161.

Constantin-Octavian, A. (2012) Cost-effective precise positioning using carrier phase navigation-grade receiver. In 2012 International Conference on Localization and GNSS, 1-6. IEEE.

Dawidowicz, K., Krzan, G., Świątek, K. (2015) Relative GPS/GLONASS coordinates determination in urban areas-accuracy analysis. In Proceedings of 15th edition of SGEM GeoConferences, 2, 423-430, Bulgaria, 2015.

El-Mowafy, A. (2012) Precise real-time positioning using Network RTK. Global navigation satellite systems: signal, theory and applications, 161-189.

Goad, C. C. (1974) A modified Hopfield tropospheric refraction correction model. In Proceedings of the Fall Annual Meeting American Geophysical Union.

Hoffmann-Wellenhof, B., Lichtenegger, H., Collins, J. (1992) Global Positioning System: Theory and Practice. Springer.

Innac, A., Gaglione, S., Angrisano, A. (2018) Multi-GNSS Single Frequency Precise Point Positioning. In Proceedings of IEEE International Workshop on Metrology for the Sea, Learning to Measure Sea Health Parameters (MetroSea 2018), 222-226. IEEE.

IOC - International Oceanographic Commission, (2006) Manual on seal level measurement and interpretation, vol. IV, JCOMM technical report No 31, UNESCO.

Kalman, R.E. (1960) A new approach to linear filtering and prediction problems. Trans ASME J Basic Eng, 35–45.

Kaplan, E.D., Hegarty, (2006) C. Understanding GPS: Principles and Applications, Artech House Mobile Communications Series.

Lachapelle, G., Gratton, P., Horrelt, J., Lemieux, E., & Broumandan, A. (2018) Evaluation of a low cost hand held unit with GNSS raw data capability and comparison with an android smartphone. Sensors, 18(12), 4185.

Li, X., Ge, M., Dai, X., Ren, X., Fritsche, M., Wickert, J., & Schuh, H. (2015) Accuracy and reliability of multi-GNSS real-time precise positioning: GPS, GLONASS, BeiDou, and Galileo. Journal of Geodesy, 89(6), 607-635.

Marreiros, J.P.R. (2013) Kinematic GNSS Precise Point Positioning: Application to Marine Platforms. Ph.D. Thesis, University of Porto, Porto, Portugal.

Montazeri, N., Nielsen, U.D., Jensen, J.J. (2016) Estimation of wind sea and swell using shipboard measurements – A refined parametric modelling approach. Applied Ocean Research, 54, 73-86.

Parkinson, B. W., Enge, P., Axelrad, P., Spilker Jr, J. J. (1996) Global positioning system: Theory and applications, Volume II. American Institute of Aeronautics and Astronautics.

Pa'suya, M. F., Din, A. H. M., Amin, Z. M., Omar, K. M., Omar, A. H., & Rusli, N. (2017) Evaluation of Global Digital Elevation Model for Flood Risk Management in Perlis. In Proceedings of Global Civil Engineering Conference, 1007-1017.

Paziewski, J., Wielgosz, P. (2017) Investigation of some selected strategies for multi-GNSS instantaneous RTK positioning. Advances in Space Research, 59(1), 12-23.

Paziewski, J., Sieradzki, R., Baryla, R. (2019) Signal Characterization and Assessment of Code GNSS Positioning with Low-Power Consumption Smartphones. GPS Solution, 23, 98

Paziewski, J. (2020) Recent advances and perspectives for positioning and applications with smartphone GNSS observations. Meas. Sci. Technol, 31(091001).

Piscopo, V., Scamardella, A., & Gaglione, S. (2020). A new wave spectrum resembling procedure based on ship motion analysis. Ocean Engineering, 201, 107137.

Realini, E., Caldera, S., Pertusini, L., Sampietro, D. (2017) Precise GNSS positioning using smart devices. Sensors, Vol. 17(10), 2434.

Reinking, J., Härting, A., Bastos, L. (2012) Determination of sea surface height from moving ships with dynamic corrections. Journal of Geodetic Science, 2(3), 172-187.

Robustelli, U., Baiocchi, V., Pugliano, G. (2019) Assessment of dual frequency GNSS observations from a Xiaomi Mi 8 Android smartphone and positioning performance analysis. Electronics, 8(1), 91.

Specht, C., Pawelski, J., Smolarek, L., Specht, M., Dabrowski, P. (2019) Assessment of the positioning accuracy of DGPS and EGNOS systems in the Bay of Gdansk using maritime dynamic measurements. The Journal of Navigation, 72(3), 575-587.

Specht, C., Dabrowski, P. S., Pawelski, J., Specht, M., Szot, T. (2019) Comparative analysis of positioning accuracy of GNSS receivers of Samsung Galaxy smartphones in marine dynamic measurements. Advances in Space Research, 63(9), 3018-3028.

Sørensen, A. J. (2011) A survey of dynamic positioning control systems. Annual reviews in control, 35(1), 123-136.

Takasu, T., Kubo, N., Yasuda, A. (2007) Development, evaluation and application of RTKLIB: a program library for RTK-GPS. In Proceedings of GPS/GNSS symposium, 213-218.

Teunissen, P. J., Giorgi, G., Buist, P. J. (2011) Testing of a new single-frequency GNSS carrier phase attitude determination method: land, ship and aircraft experiments. GPS solutions, Vol. 15(1), 15-28.

Welch, G., Bishop, G. (2004) An Introduction to the Kalman Filter, University of North Carolina at Chapter Hill, Chapter Hill. TR 95-014, April 5, 2004.

USING A SPLIT-WINDOW ALGORITHM FOR THE RETRIEVAL
OF THE LAND SURFACE TEMPERATURE VIA LANDSAT-8 OLI/TIRS

Chavarit AUNTARIN [1] ⬤ *, Poramate CHUNPANG [2]* ⬤ *, Wutthisat CHOKKUEA [3]* ⬤
and Teerawong LAOSUWAN [4]* ⬤

ABSTRACT:
Climate change has worsened and has widespread impact. This is partly due to the release of greenhouse gases from human activities, which cause the greenhouse effect. This leads to the global temperature rising to an unusual level, otherwise known as global warming. This study aimed to use a split-window algorithm to retrieve the land surface temperature via Landsat-8 OLI/ TIRS data in the Roi Et province area. The research methodology included 1) separating the Landsat-8 OLI data into four types of land use, i.e. the agricultural, forest, urban and water areas and 2) the data for Landsat-8 OLI bands 4 and 5 and Landsat-8 TIRS (bands 10, 11) being analysed to retrieve the land surface temperature using a split-window algorithm. The results from the land-use separation showed that the total area of Roi Et was 8,299.46 km^2 divided into a 4,787 km^2 agricultural area, which accounted for 60.81%; a 1,555 km^2 forest area, accounting for 19.75%; a 1,212 km^2 urban area, accounting for 15.39% and a 317.44 km^2 water area, accounting for 4.03%. The land surface temperature analysis result using a split-window algorithm indicated that the average temperature of Roi Et was 34.74°C. Moreover, it was found that the land surface temperature of the urban area had the highest mean land surface temperature, followed by the forest area, the agricultural area and the water source area, respectively.

Key-words: *Remote Sensing, Land Surface Temperature, Split-Window Algorithm, Landsat-8 OLI/TIRS, Normalised Difference Vegetation Index (NDVI), Fractional Vegetation Cover (FVC)*

1. INTRODUCTION

The global environmental crises that cause the most damage and harm to humans are weather changes, which refers to the change in average weather conditions in relation to the temperature, wind, rain, etc., whether the cause is human activities or natural variation, especially when the average temperature on earth appears to be higher, which is known as global warming whereby the world cannot emit heat from solar energy in the normal way. Based on such reason, the earth average temperature seems to be higher. However, in the past century, the average temperature was higher by a small degree. The world's weather and environmental conditions have changed considerably and had a severe effect on living things (Lemke et al., 2007; IPCC, 2019). Thailand is an economic and industrial developing country that has changed agricultural land into industrial land continually within the last two to three decades (Dechaphongthana et al., 2016). Generally, the temperature of the agricultural area is higher than the forest temperature, but it is lower than the urban area full of buildings (Zhang et al., 2010; Mathew et al., 2017). Such progress has affected a growing number of communities, residences, commercial buildings and factories. Meanwhile, it has led to green areas needing to absorb sunlight and convert it into energy via a decreased photosynthesis process, contributing to warmer temperatures in urban areas and the eventual formation of the urban heat island phenomenon (Laosuwan et al., 2017; Rotjanakusol & Laosuwan, 2018).

Studying the land surface temperature is considered as another form of detecting heat on the earth's surface, and it is currently widely used to monitor the global temperature. The land surface temperature is most likely utilised in various aspects, such as studying the increasing global

---

[1,2,3,4] *Department of Physics, Faculty of Science, Mahasarakham University, Maha Sarakham, 44150,*
Thailand, chavarit.py@gmail.com, poramate_c@hotmail.com, drwutthisat@gmail.com
[*] *Corresponding author: teerawong@msu.ac.th*

temperature, which is caused by weather changes; studying weather conditions by detecting an increase in the atmospheric concentrations of green-house gases that effect the land surface temperature; studying the increase in the land surface temperature, which affects North Pole icebergs, and studying the land surface temperature, which effects plants in the ecosystem of different regions around the world (Li et al., 2013; Mukhelif et al., 2016; Miles & Esau, 2017; Khandelwal et al., 2018; Nill et a., 2019; Capodici et al., 2020). Regarding studying and searching for research papers and documents relevant to land surface temperature analysis, a lot of the research was conducted on land surface temperature analysis using satellite data, such as the land surface temperature change in urban areas (Rotjanakusol & Laosuwan, 2020), the study on the urban heat island phenomenon in atmospheric layers (Prohmdirek et al., 2020) and the detection and identification of wildfire areas using the land surface temperature (Vlassova et al., 2014).

In addition, many research studies currently focus on developing a method to detect the land surface temperature using remote sensing technology. Remote sensing technology is accepted as being modern and efficient, and it can be applied to rapidly monitor and detect global phenomena (Uttaruk & Laosuwan, 2018; Rotjanakusol & Laosuwan, 2019; Rotjanakusol & Laosuwan, 2020; Uttaruk & Laosuwan, 2020). In the meantime, many research papers have indicated using a mathematical model in conjunction with remote sensing technology to analyse the land surface temperature, such as radiative transfer equation (RTE), Mono-Window (MW), split window (SW), Dual-Angle (DA) and single-channel (SC) (Ren et al., 2011; Yu et al., 2014; Chen et al., 2015; Du et al., 2015). Furthermore, the land surface temperature from satellite data by thermal infrared emissivity can clearly show differences in land surface temperature with land use and land cover such as residential area, community area, industrial plant, open area, including the burned area in the agricultural area are relatively high land surface temperature. In addition, forests area, agricultural area, aquaculture area, wetlands, and water bodies, the land surface temperature are relatively low (Valor & Caselles, 1996). The estimation land surface temperature using a split window was first applied to the sea surface temperature estimation (Mcmillin, 1975) when two thermal infrared wavelengths were carried out at a wavelength of 10.5‑12.5 µm (band 10 and band 11), come to use it efficiently and satisfactorily. Because the influence of water vapour in the atmosphere is removed from the brightness temperature of the two wavelengths.

Due to the importance of the earlier mentioned weather change and the global temperature increase, this study aims to focus on using a split-window algorithm for the retrieval of the land surface temperature via Landsat-8 OLI/TIRS data in the Roi Et province area. The expected results will be to understand the land surface temperature and its change according to land use in Roi Et.

2. MATERIALS AND METHODS

Roi Et (**Fig. 1**) consists of 20 districts. It is located in the middle part of the northeast region of Thailand between latitudes of 15°24' to 16°19' and longitudes of 103°17' to 104°22' with a total area of 8,299.46 km², ranking it the 10th of the region and the 23rd of the country. Most of the province is covered by high plains of about 120–160 metres above mean sea level. The average temperature throughout the year is about 26.9°C, the average low temperature 22.5°C and the average maximum temperature 32.3°C. It has three seasons: the summer is hot and dry, which lasts from February to April; the rainy season lasts from May to September, but the rain is irregular, and the annual rainfall is approximately 1,200 mm/y; and it is cold in winter, which lasts from October to January.

2.1 Data

The study used Landsat-8 OLI/TIRS data (**Table 1**), which were recorded on 16 December 2018. Landsat-8 OLI/TIRS was launched on 13 February 2013 and orbits the earth every 99 minutes. The satellite travels over both the North and South Poles at an altitude of 705 km. It has bands for capturing the response of the earth's surface at discrete wavelengths, i.e. coastal aerosol, blue, green, red, NIR for one wavelength range and SWIR for two wavelength ranges. The spatial resolution of Landsat-8 OLI is 30 metres pixel size resolution in TIRS band, two wavelength ranges and 100 metres pixel size resolution, a panchromatic band, one wavelength range and 15 metres pixel size resolution.

Landsat-8 OLI/TIR bands information.

Wavelength (μm)	Sensor	Description
Band 1: 0.43–0.45	Operational Land Imager (OLI)	Coastal aerosol
Band 2: 0.45–0.51	Operational Land Imager (OLI)	Blue
Band 3: 0.53–0.59	Operational Land Imager (OLI)	Green
Band 4: 0.64–0.67	Operational Land Imager (OLI)	Red
Band 5: 0.85–0.88	Operational Land Imager (OLI)	NIR
Band 6:1.57–1.65	Operational Land Imager (OLI)	SWIR 1
Band 7: 2.11–2.29	Operational Land Imager (OLI)	SWIR 2
Band 8: 0.50–0.68	Operational Land Imager (OLI)	Panchromatic
Band 9: 1.36–1.38	Operational Land Imager (OLI)	Cirrus
Band 10:10.60–11.19	Thermal Infrared Sensor (TIRS)	TIRS 1
Band 11: 11.50–12.51	Thermal Infrared Sensor (TIRS)	TIRS 2

Fig. 1. Study area

2.2 Temperature Data from Ground Station

This study collected the daily temperature data from the Thai Meteorological Department (TMD) station located in Roi Et at the same time as the satellite data collection.

2.3 Procedures for Land-use Separation

Land use in Roi Et is separated by Landsat-8 OLI data (band 3(B) 4(G) 5(R)) into four types: the agricultural, forest, urban and water areas. The reflectance value called a digital number that the satellite recorded for categorising the layers of data to show the physical differences of the objects. A supervised classification method and a general statistical method – the maximum likelihood – were used to separate the land use (Zhang et al., 2007).

2.4 Procedures for Temperature Analysis

The land surface temperature analysis from Landsat-8 OLI/TIRS data using split-window algorithms that use a Quantum GIS (QGIS) software package can be divided, as shown in **Fig. 2**, and is detailed below:
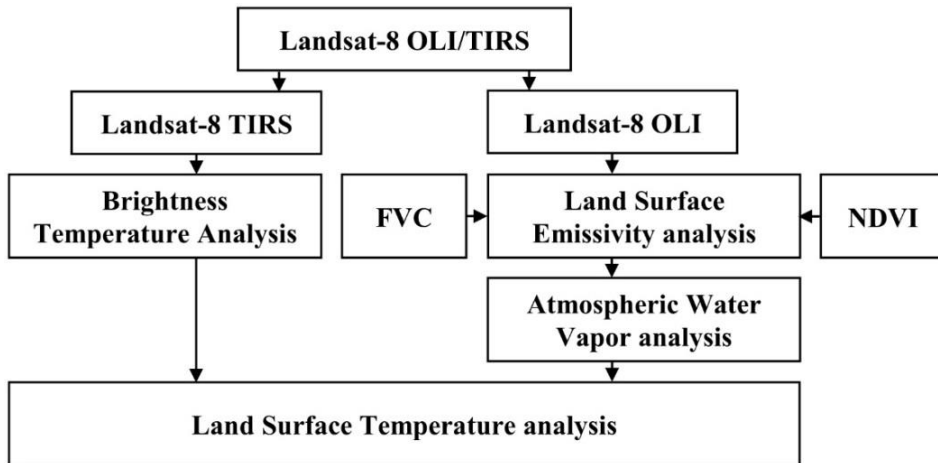
Fig. 2 Procedures for land surface temperature analysis

2.4.1 Brightness Temperature Analysis

The land surface temperature was analysed in the wavelength range of thermal infrared sensors (TIRS) (bands 10 and 11) when the radiance of the objects was equal to the black body radiation. Black body radiation determines the brightness temperature values of the objects on the earth. Furthermore, the objects' radiance will depend on the electromagnetic wavelength that interacts with the objects, and it is the proportion between the reflection, absorption and transmission. The methods of the brightness temperature analysis are shown in Equations 1 and 2 and **Table 2** (Barsi et al., 2014).

$$T = \frac{k_2}{\ln\left(\dfrac{k_1}{L_\lambda} + 1\right)} \tag{1}$$

Where:

T = The brightness temperature in Kelvin (K)

k_1 = The constant value of Landsat-8 TIRS (band 10=774.89 and band 11=480.89)

k_2 = The constant value of Landsat-8 TIRS (band 10=1321.08 and band 11=1201.14)

L_λ = The TOA spectral radiance (Watts/(m^2 * srad * μm))

$$L_\lambda = M_L Q_{cal} + A_L \tag{2}$$

Where:

M_L = The band-specific multiplicative rescaling factor from the metadata

A_L = The band-specific additive rescaling factor from the metadata

Q_{cal} = The quantised and calibrated standard product pixel values (DN)

Table 2.
Rescaling factor values.

Rescaling factor	Band 10 and Band 11
M_L	0.000342
A_L	0.1

2.4.2 Land Surface Emissivity Analysis

This is an analysis of the radiation emitted by real objects on the earth that cannot absorb all the energy, but they can emit a small amount of radiation compared to a black body. Emissivity can be estimated from the proportion of the plants that extend into the soil that is obtained from the Normalised Difference Vegetation Index (NDVI). The land surface emissivity analysis is shown in Equation 3 (Rajeshwari & Mani, 2014). Based on Equation 3, it is necessary to firstly analyse the fractional vegetation cover (FVC) value, as shown in Equation 4 (Laosuwan & Uttaruk, 2014). The NDVIs and NDVIv are values of the NDVI for bare soil (NDVIs = Minimum value of the NDVI) and pure green vegetation (NDVIv = maximum value of the NDVI). The FVC value is the plant fertility analysis, whose result is taken from the NDVI, as shown in Equation 5 (Uttaruk & Laosuwan, 2017), while p is the reflectance value of electromagnetic radiation from land cover, which depends on the wavelength and the proportion of the reflection, absorption and transmission. The analysis method is shown in Equation 6.

$$LSE = \varepsilon_s \left(1 - FVC\right) + \varepsilon_v * FVC \tag{3}$$

Where:

ε_s = The constant value of Landsat-8 (band 10=0.971 and band 11=0.977)

ε_v = The constant value of Landsat-8 (band 10=0.987 and band 11=0.989)

$$FVC = \frac{NDVI - NDVI_s}{NDVI_v - NDVI_s} \tag{4}$$

Where:

$NDVI_v$ = The maximum value of NDVI

$NDVI_s$ = The minimum value of NDVI

$$NDVI = \frac{\rho_{NIR} - \rho_{Red}}{\rho_{NIR} + \rho_{Red}} \tag{5}$$

Where:

ρ_{NIR} = The reflection value of vegetation in the near infrared wave range (NIR)

ρ_{Red} = The reflection value of vegetation in the red wave range (RED)

ρ = The reflection value of the soil cover

$$\rho_\lambda = M_\rho Q_{cal} + A_\rho \tag{6}$$

Where:

M_ρ = The reflectance multiplicative scaling factor

A_ρ = The reflectance additive scaling factor

Q_{cal} = The digital number (DN)

2.4.3 Atmospheric Water Vapour Analysis

Atmospheric water vapour analysis can be analysed from electromagnetic radiation in the thermal infrared sensors (TIRS) wavelength range, which travels through atmospheric layers with a brightness temperature value calculation on bands 10 and 11 of Landsat 8 (TIRS 1 wavelength range between 10.60–11.19µm and TIRS 2 wavelength range between 11.50–12.51µm, respectively). The analysis method is shown in Equation 7 (Ren et al., 2015).

$$WV = a + b \times \tau_j / \tau_i \tag{7}$$

Where:

$$\frac{\tau_j}{\tau_i} \approx R_{ji} = \sum_{k=1}^{N} \left(T_{i,j} - \overline{T} \right)\left(T_{i,j} - \overline{T} \right) / \sum_{k=1}^{N} \left(T_{i,j} - \overline{T} \right)^2$$

Where:

a and b are the coefficients of the model
τ = The electromagnetic wave's transmission ability through the atmosphere (bands 10 and 11)
i, j = Bands 10 and 11
$T_{i,j}$, $T_{j,k}$ = The brightness temperature of bands 10 and 11
$\overline{T_i}$, $\overline{T_j}$ = The mean brightness temperature of bands 10 and 11

2.4.4 Land Surface Temperature Analysis

In this study, the land surface temperature analysis using a split-window algorithm was conducted from (1) the brightness temperature value calculation on bands 10 and 11, (2) the land surface emissivity value of bands 10 and 11 and (3) the atmospheric water vapour analysis result. The analysis method is shown in Equation 8 and **Table 3** (Yue et al., 2007).

$$LST = \left(T_{10} + C_{10} - T_{11} \right) + \left(T_{10} - T_{11} \right)^2 C_0 + \left(C_3 + C_4 W \right)\left(1 - \varepsilon \right) + \left(C_5 + C_6 W \right)\Delta\varepsilon \tag{8}$$

Where:

T_{10}, T_{11} = The brightness temperature of bands 10 and 11
ε = The mean land surface emissivity of bands 10 and 11
$\Delta\varepsilon$ = The difference land surface emissivity of bands 10 and 11
C_0 - C_6 = The constant value (see in **Table 3**)
W = The atmospheric water vapours

Table 3.
The coefficient of the split-window algorithm.

Constant	Value
C0	-0.678
C1	1.378
C2	0.183
C3	54.30
C4	-2.238
C5	-129.2
C6	16.40

3. RESULTS AND DISCUSSIONS

The method of acquiring the land surface temperature from Landsat-8 OLI/TIRS data using the SWA method is shown below:

3.1 Result of land-use Separation

The landsat-8 OLI data were recorded on 16 December 2018 and brought to separate land use into four types: the agricultural, forest, urban and water areas, as seen in **Fig. 3**.

The result of the land-use separation using supervised classification and maximum likelihood methods revealed that Roi Et was separated into a 4,787 km^2 agricultural area, accounting for 60.81%; a 1,555 km^2 forest area, accounting for 19.75%; a 1,212 km^2 urban area, accounting for 15.39% and a 317.44 km^2 water area, accounting for 4.03%. To validate the land use accuracy in this study, the sampling point was selected using a random method, and it required every land-use group to be worth at least 10 validation points. In this case, the confidence value of 95% was assigned a number of points for the verification of 200 points. The result showed that the overall accuracy was 94%, and the kappa coefficient was 0.92. In addition, it was found that the land-use groups that obtained producer's accuracy and user's accuracy were the agriculture, urban, water and forest areas with values of 95.50, 95.30, 94.80 and 94.60, respectively. The results of the land-use validation in this study are shown in **Table 4**.

Furthermore, when the land-use separation data were analysed at a district level (**Table 5**), it was found that most lands are agricultural areas.

(1) The top three districts with the largest agricultural areas per the whole area of the districts were Kaset Wisai at 1.07 km^2, accounting for 78.24%; Mueang Suang at 0.19 km^2, accounting for 76.81% and Suwanna Phum at 0.99 km^2, accounting for 73.16%.

(2) The top three districts with the largest forest areas per the whole area of the districts were Phon Thong at 0.31 km^2, accounting for 28.52%; Nong Phok at 0.27 km^2, accounting for 30.44% and Suwanna Phum at 0.23 km^2, accounting for 17.15%.

(3) The top three districts with the largest urban areas per the whole area of the districts were Phon Thong at 0.30 km^2, accounting for 27.10%; Nong Phok at 0.27 km^2, accounting for 30.39% and Phochai at 0.15 km^2, accounting for 24.89%.

(4) The top three districts with the largest water area per the whole area of the districts were Sela Phum at 0.16 km^2, accounting for 13.26%; Phanom Phai at 0.04 km^2, accounting for 6.09% and Thawat Buri at 0.03 km^2, accounting for 5.25%.
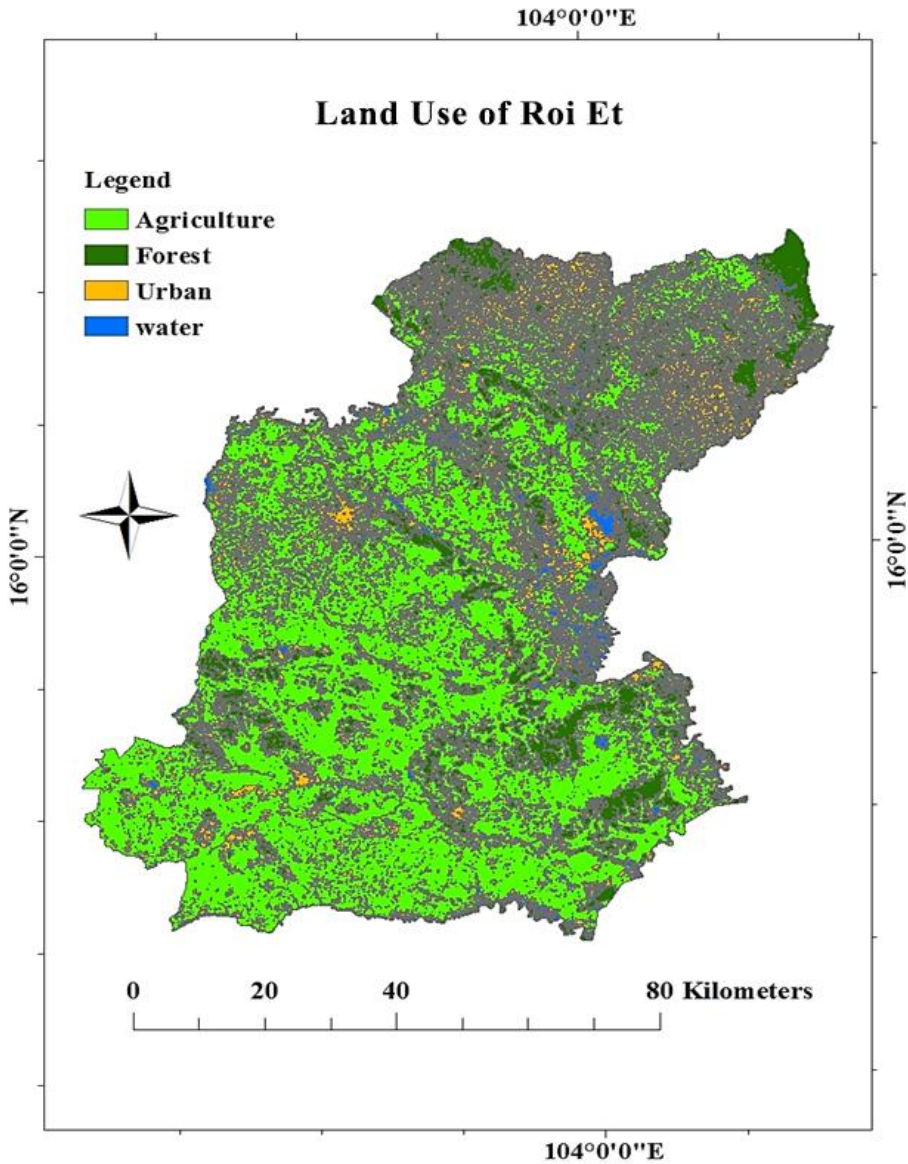
Fig. 3. Separate land use of Roi Et province.

Table 4.

Land surface temperature analysis separated by districts.

Land-use classification	Producer's accuracy	User's accuracy
Agriculture area	95.50	95.01
Forest area	94.60	94.60
Urban area	95.30	95.00
Water area	94.80	95.28
Overall accuracy	94.00 %	
Kappa coefficient	0.92	

Table 5.

Land surface temperature analysis separated by districts.

Districts	Agricultural (km²)	Urban (km²)	Forest (km²)	Water (km²)	Temperature (°C)
Atsamat	270.46	47.00	90.00	12.00	34.00
Changhan	118.07	24.17	26.71	15.24	34.00
Chaturaphak Phiman	365.60	40.25	73.50	7.32	35.27
Chiang Khwan	44.20	7.04	7.61	8.70	34.80
Kaset Wisai	667.08	88.69	83.00	13.93	36.00
Muai Wadi	85.04	41.38	41.04	2.37	33.80
Muang Roi Et	314.35	68.40	61.07	6.21	34.80
Muang Sruang	119.07	10.67	23.46	1.87	35.00
Nong Hi	95.27	10.38	44.89	4.91	34.20
Nong Phok	211.65	169.93	170.19	9.11	34.00
Pathumrat	237.45	47.06	48.87	11.68	36.00
Phanom Phai	238.35	43.01	131.88	26.89	33.40
Phochai	134.30	93.62	137.21	10.85	34.50
Phon Sai	166.57	15.76	28.50	19.84	34.24
Phon Thong	289.76	185.25	194.90	13.45	35.00
Sela Phum	429.30	90.26	130.44	99.37	33.50
Sri Somdet	108.44	39.01	12.32	4.62	35.07
Suwanna Phum	621.01	63.00	145.62	19.07	35.74
Thawat Buri	303.74	45.43	68.72	23.18	35.53
Thung Kao Luang	50.42	13.58	20.43	6.83	36.00

3.2 Land Surface Temperature Analysis Result

The analysis result of Roi Et's land surface temperature using Landsat-8 OLI/TIRS data with a split-window algorithm is shown in **Fig. 4**.

3.3 Analysis Result of Temporal Variation of Land Surface Temperature

The analysis result of the temporal variation between the land surface temperature and the types of land use in Roi Et based on Landsat-8 OLI/TIRS data is shown in **Fig. 5**. It shows that Roi Et has 20 districts, as indicated by the graph on the x-axis, which shows that there are districts whose land use was separated into four types: 1) agricultural area, 2) forest area, 3) urban area and 4) water source area. The research hypothesis was that the urban area of each district has a higher temperature than other areas in the land use. The graph on the y-axis on the left shows the area size of the land use in km², and the right side shows the temperature in °C. From **Fig. 4**, it can be seen that the temperature graph changes according to the types of land use in each district. The findings from the study revealed that the three districts with a maximum land surface temperature in urban areas were Kaset Wisai, Pathumrat and Thung Khao Luang, where the land surface temperature was 36.00°C.

The top three districts with a minimum land surface temperature in urban areas were Phanom Phrai, Sela Phum and Moei Wadee, where the land surface temperatures were 33.40°C, 33.50°C and 33.80°C, respectively. The land surface temperature analysis result was associated with land use; namely, the analysed land surface temperature in urban areas showed the maximum value, followed by the agricultural, forest and water source areas, respectively. Furthermore, in remote sensing technology, the detector measures the electromagnetic radiation that reflects from the earth's surface material. These measurements can help distinguish the type of land that is covered. Soil, water and vegetation have distinctly different reflections and absorption patterns at different wavelengths. The reflected of radiation from a surface material, such as soil, varies with the range of wavelengths in the electromagnetic spectrum. This is known as a material spectral signature.
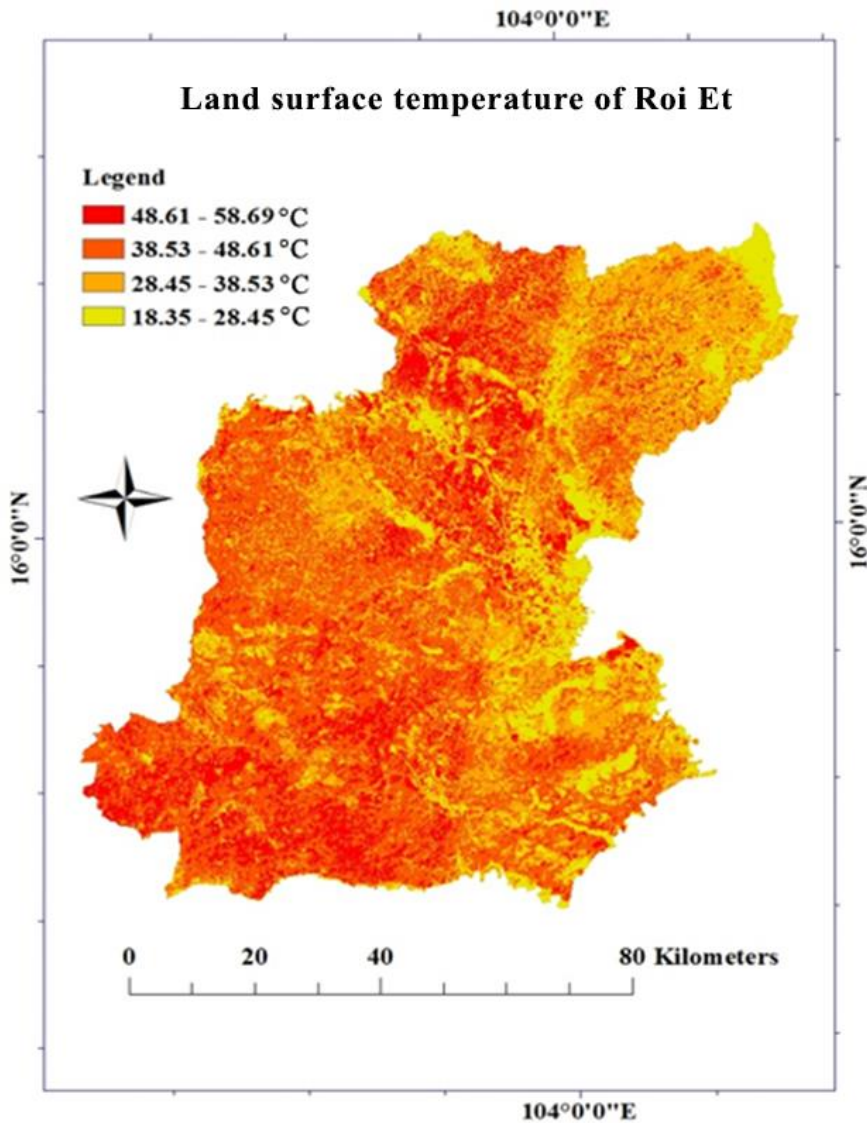
Fig. 4. Land surface temperature of Roi Et province.
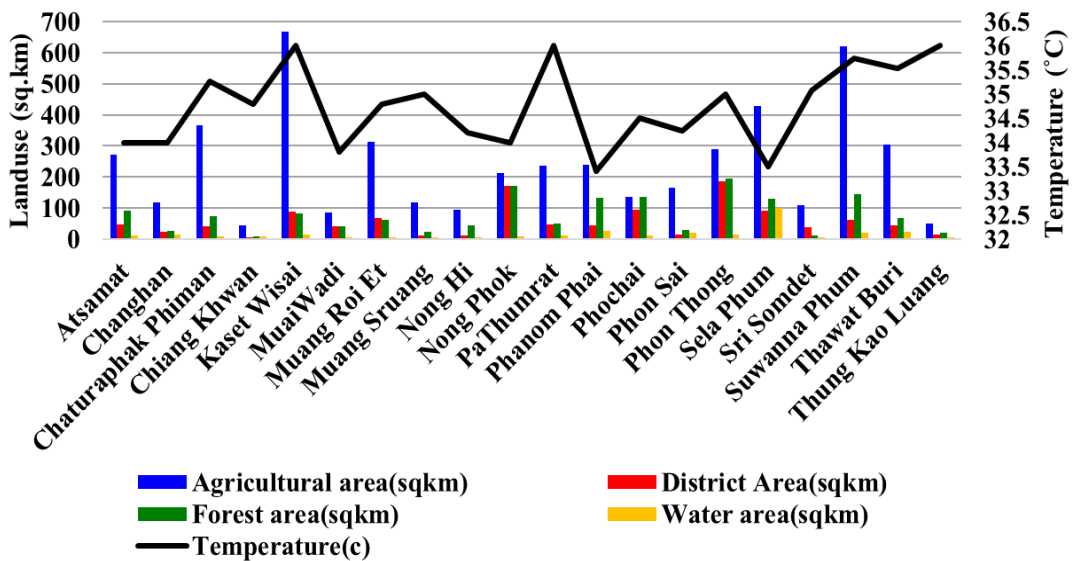
Fig. 5. Temporal variation land surface temperature of Roi Et province.

4. CONCLUSIONS

As of today, global climate has severely and frequently changed. Such change is reflected by El Nino and La Nina, which occur more frequently, including the land surface temperature, which seems to increase continuously. Through this research, the land surface temperature value analysed by the satellite data was compared to the daily temperature measured by the TMD station located in Roi Et, and an error of 4.07% was found. The value of the land surface temperature analysed by the satellite data was 34.74°C, while the temperature data from the TMD station was 32.00°C. Therefore, a hypothesis was set that the TMD temperature measurement station located in each district of Roi Et province is available for one to two stations, and the district with the maximum TMD temperature measurement stations (two stations) is Muang Roi Et (see **Fig.1**). It can be noted that the Thai Meteorological Department's temperature data from the one to two stations may not be enough to represent each district and the entire province. As for the land surface temperature data analysed by the satellite, they were analysed from every inch of the Roi Et province area.

R E F E R E N C E S

Barsi, J.A., Schott, J.R., Hook, S.J., Raqueno, N.G., Markham, B.L., & Radocinski, R.G. (2014). Landsat-8 thermal infrared sensor (TIRS) vicarious radiometric calibration. *Remote Sensing*, 6(11), 11607–11626.

Capodici, F., Cammalleri, C., Francipane, A., Ciraolo, G., La Loggia, G., & Maltese, A. (2020). Soil Water Content Diachronic Mapping: An FFT Frequency Analysis of a Temperature–Vegetation Index. *Geosciences*, 10(1), 23.

Chen, F., Yang S., Su, Z., & He, B. (2015). A new single-channel method for estimating land surface temperature based on the image inherent information: The HJ-1B case. *ISPRS Journal of Photogrammetry and Remote Sensing*, 101, 80–88.

Dechaphongthana, W., Karnchanasutham, S., Nualchawee, K., & Intarawichian N. (2016). The relationships between land surface temperature and NDVI of paddy rice areas in stages of growth from satellite data. *Journal of Geoinformation Technology of Burapha University*, 1(2), 14–30. (in Thai)

Du, C., Ren, H., Qin, Q., Meng, J., & Zhao, S. (2015). A practical split-window algorithm for estimating land surface temperature from Landsat 8 data. *Remote Sensing,* 7(1), 647–665.

IPCC. (2019). *An IPCC Special report on climate change, desertification, land degradation, sustainable land management, food security, and greenhouse gas fluxes in terrestrial ecosystems* (ISBN 978-92-9169-154-8) Retrieved from https://www.ipcc.ch/site/ assets/uploads/sites//02/2020/4SPM_Updated-Jan.20pdf

Khandelwal, S., Goyal, R., Kaul, N., & Mathew, A. (2018).Assessment of land surface temperature variation due to change in elevation of area surrounding Jaipur, India. *Egyptian Journal of Remote Sensing and Space Science*, 21(1), 87–94

Laosuwan, T., & Uttaruk, P. (2014). Estimating tree biomass via remote sensing, MSAVI 2, and Fractional Cover model. *IETE Technical Review*, 31(5), 362–368.

Laosuwan, T., Gomasathit, T., & Rotjanakusol, T. (2017). Application of remote sensing for temperature monitoring: The technique for land surface temperature analysis. *Journal of Ecological Engineering*, 18 (3), 53–60.

Lemke, P*.,* Ren, J., Alley, R.B., Allison, I., Carrasco, J., Flato, G., …Zhang*,* T. (2007). *Climate Change 2007: The Physical Science Basis. Contribution of Working Group I to the Fourth Assessment Report of the Intergovernmental Panel on Climate Change*. Cambridge University Press, Cambridge, United Kingdom and New York, NY, USA.

Li, X., Zhou, W., & Ouyang, Z. (2013). Relationship between land surface temperature and spatial pattern of greenspace: What are the effects of spatial resolution? *Landscape and Urban Planning*. 114, 1–8.

Mathew, A., Khandelwal, S., & Kaul, N. 2017. Investigating spatial and seasonal variations of urban heat island effect over Jaipur city and its relationship with vegetation, urbanization and elevation parameters. *Sustainable Cities and Society*, 35, 157–177.

McMillin, L. M. (1975). Estimation of sea surface temperature from two infrared window measurements with different absorption. *Journal of Geophysical Research*, 20, 11587–11601.

Miles, V., & Esau, I. (2017). Seasonal and Spatial Characteristics of Urban Heat Islands (UHIs) in Northern West Siberian Cities. *Remote Sensing*, 9(10), 1–15.

Mukhelif, A., Al. Ammar, K., & Al Jooburi, M. (2016). The seasonal variation of the urban heat island effect and estimating the Human Discomfort Index at the City of Hillah. *Pure and Applied Sciences*, 24(2), 423–434.

Nill, L., Ullmann, T., Kneisel, C., Sobiech-Wolf, J., & Baumhauer, R. (2019). Assessing Spatiotemporal Variations of Landsat Land Surface Temperature and Multispectral Indices in the Arctic Mackenzie Delta Region between 1985 and 2018. *Remote Sensing*, 11(19), 2329.

Prohmdirek, T., Chunpang, P., & Laosuwan, T. (2020). The Relationship between Normalized Difference Vegetation Index and Canopy Temperature that affects the urban heat island phenomenon. *Geographia Technica*, 15(2), 222–234.

Rajeshwari, A. & Mani, N.D. (2014). Estimation of land surface temperature of Dindigul district using Landsat 8 data. *International Journal of Research in Engineering and Technology*, 3 (5), 122–126.

Ren, H., Du, C., Liu, R., Qin, Q., Yan, G., Li, Z. & Meng, J. (2015). Atmospheric water vapor retrieval from Landsat 8 thermal infrared images. *Journal of Geophysical Research Atmospheres*, 120(5), 1723–1738.

Ren, H., Yan, G., Chen, L., & Li, Z.L. (2011). Angular effect of MODIS emissivity products and its application to the split-window algorithm. *ISPSR J. Photogramm*, 66, 498–507.

Rotjanakusol, T., & Laosuwan, T. (2018). Estimation of land surface temperature using Landsat satellite data: A case study of Mueang Maha Sarakham district, Maha Sarakham province, Thailand for the years 2006 and 2015. *Scientific Review Engineering and Environmental Sciences*, 27 (4), 401–409.

Rotjanakusol, T., & Laosuwan, T. (2019). An Investigation of drought around Chi Watershed during ten-year period using Terra/MODIS data. *Geographia Technica,* 14(2), 74–83.

Rotjanakusol, T., & Laosuwan, T. (2020). Model of relationships between land surface temperature and urban built-up areas in Mueang Buriram district, Thailand. *Polish Journal of Environmental Studies*, 29(5), 3783–3790.

Rotjanakusol, T., & Laosuwan, T. (2020). Surface water body extraction using Landsat 8 images and different forms of physical models. *The Scientific Journal of King Faisal University, Basic and Applied Sciences*, 21(2), 218–223.

Uttaruk, Y., & Laosuwan, T. (2017). Drought detection by application of remote sensing technology and vegetation phenology. *Journal of Ecological Engineering*, 18(6), 115–121.

Uttaruk, Y., & Laosuwan, T. (2018). Community forest for global warming mitigation: The technique for estimation of biomass and above ground carbon storage using remote sensing method. *Agriculture and Forestry*, 64(3), 47–57.

Uttaruk, Y., Laosuwan, T. (2020). Comparison of carbon storage measurement methods on Agroforestry Systems in Sakon Nakhon province, Northeast Thailand. The Scientific *Journal of King Faisal University, Basic and Applied Sciences*, 21(2), 95–99.

Valor, E., & Caselles, V. (1996). Mapping land surface emissivity from NDVI: Application to European, African, and South American areas. *Remote Sensing of Environment*, 57 (3), 167–184.

Vlassova, L., Pérez-Cabello, F., Mimbrero, M., Llovería, R., & García-Martín, A. (2014). Analysis of the relationship between land surface temperature and wildfire severity in a series of Landsat images. *Remote Sensing*, 6(7), 6136–6162.

Yue, W., Xu, J., Tan., W., & Xu, L. (2007). The relationship between land surface temperature and NDVI with remote sensing: Application to Shanghai Landsat 7 ETM+ data. *International Journal of Remote Sensing*, 28(15), 3205–3226.

Yu, X., Guo, X., & Wu, Z. (2014). Land surface temperature retrieval from Landsat 8 TIRS-Comparison between Radiative Transfer Equation-based method, split window algorithm and single channel method. *Remote Sensing,* 6(10), 9829–9852.

Zhang, X.X., Wu, P.F., & Chen, B. (2010). Relationship between vegetation greenness and urban heat island effect in Beijing City of China. *Procedia Environmental Sciences*, 2, 1438–1450.

Zhang, Y., Gao, J., Wang. J. (2007). Detailed mapping of a salt farm from Landsat TM imagery using neural network and maximum likelihood classifiers: A comparison. *International Journal of Remote Sensing*, 28(10), 2077–2089.

SPATIO-TEMPORAL ANALYSIS OF WULAN DELTA IN INDONESIA: CHARACTERISTICS, EVOLUTION, AND CONTROLLING FACTORS

*Bagus SEPTIANGGA[1], Bachtiar W. MUTAQIN[2]**

ABSTRACT:
The evolution of the Wulan Delta began after the construction of the Wulan River Canal in 1892. It alters the shoreline erosion and accretion that affect the land dynamics of the coastal area. This study aims to analyze the spatio-temporal evolution of the Wulan Delta, including the shoreline and its dynamics, as well as the geomorphological processes that affect it. The shoreline change was extracted digitally from Landsat satellite images and divided into four periods, i.e., 1995-2000, 2000-2011, 2011-2015, and 2015-2020. We used the histogram thresholding method to separate the land from the sea and produce the shoreline as the interface. This research employed field check and focus group discussion for identifying the cause and impact of shoreline dynamics in the research area. The results show that land loss and accumulation over 25 years (1995-2020) are -7.16 km^2 and +6.58 km^2, respectively. In Wulan Delta, the erosion is due to high waves and sedimentation due to mangrove planting and high sediment from the rivers. The development rates of the Wulan Delta for the period of 1995-2020 were 73,200 m^2/year.

Key-words: *coastal, morphodynamics, histogram thresholding, Wulan Delta, Indonesia.*

1. INTRODUCTION

The coastal area has high productivity of available resources and an essential role in supporting human lives (UNISDR/UNDP, 2012; Mutaqin, 2020; Marfai et al., 2020; Mutaqin et al., 2020). Hence, the coastal area is essential for human existence since almost all major cities are located in this area. Furthermore, one-third of the world population was living in the coastal area, and the numbers always increase year by year. This situation can inflict an increasing hazard level in the coastal areas since this area is very dynamic due to its natural and human processes (Mujabar and Chandrasekar, 2013; Mutaqin, 2017; Mutaqin et al., 2019; Arjasakusuma et al., 2021).

Delta evolutions due to sedimentation are one example of the dynamics phenomenon in the coastal area (Chen et al., 2020; Collins et al., 2021). Wulan Delta (**Fig. 1**), as one of the most dynamics delta in Indonesia, has been experiencing rapid evolutions since the construction of the Wulan Canal in 1892 (Bird and Ongkosongo, 1980; Fadlillah et al., 2018; Fadlillah et al., 2019). The canal dredging generates intensive sedimentation that is transported through the Serang River and deposited in the estuarine. This condition has accelerated the formation and evolution of the Wulan Delta. As Fadlillah et al. (2018) state, aside from massive sediment transport, human construction in aquaculture and housing on Wulan Delta's body also contributes to its development, including its water environment. Although the tidal patterns in Wulan Delta are categorized as micro-tidal with a mean of 0.8 m, flat morphology in this area leads to the tidal run-up that can reach far ashore, up to 8 km upstream during floods, and in other hands also making this area as an area which vulnerable to sea-level rise (Marfai, 2014; Fadlillah et al., 2019). The evolution of the Wulan Delta provides several benefits to the local community. The community has utilized a broader land in Wulan Delta to build fishponds. Furthermore, the local community also competes to mark the new lands emerging in the estuarine during low tides to be recognized as their own (Ruswanto and Adisaputra, 1990). Simultaneously, several settlements and fishponds in three villages in the north of Wulan Delta (Semat, Tanggultlare, and Bulak Village) have been destroyed and sink in due to the erosion. Most residents in that three

[1]Ministry of Public Works and Housing, Directorate General of Water Resources, Jakarta, Indonesia, septianggabagus@gmail.com

[2] Universitas Gadjah Mada, Faculty of Geography, Coastal and Watershed Research Group, 55281 Yogyakarta, Indonesia, mutaqin@ugm.ac.id

villages were forced to move, about 250-m inland from their previous settlements. In 1984, some of the remaining buildings, e.g., houses, mosques, and water reservoirs, were still seen. However, in 1993 all of the buildings were disappeared due to erosion (Ruswanto and Adisaputra, 1990).
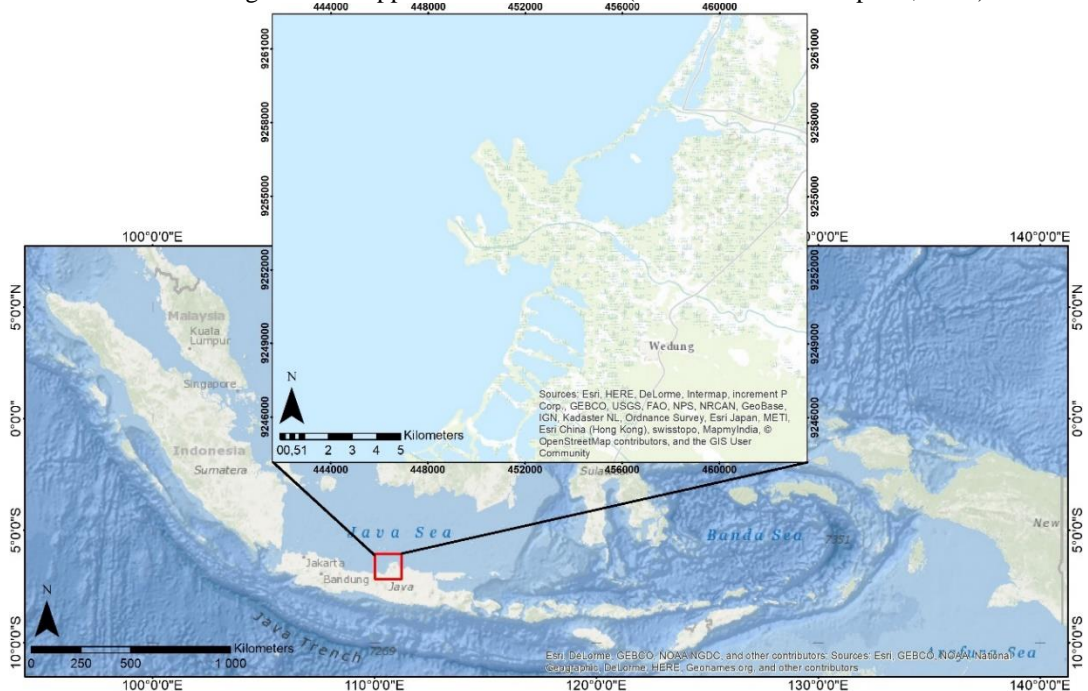
Fig. 1. Wulan Delta, one of the most dynamics delta in Indonesia.

Sunarto (2005) has described Wulan Delta's morphology from 1925 to 1992; Wulan Delta's dynamics are further analyzed in this study, i.e., from 1995 to 2020. Marfai et al. (2016) also has explained the Wulan Delta's morphodynamics but focuses more on social impacts. Furthermore, this study aims to analyze the spatio-temporal evolution of the Wulan Delta, including the shoreline and its dynamics, as well as the geomorphological processes that affect it. The research results in the form of the spatio-temporal map of Wulan Delta during 1995-2020, calculation of land loss and land accumulation, as well as the assessment of the annual rate of the Wulan Delta evolutions, can use as an input for disaster mitigation strategy in this area and its surroundings.

2. DATA AND METHODS

2.1. Laboratory and computational analysis

We used multi-temporal images of Landsat 5 TM (1995, 2000, and 2011) and Landsat 8 OLI/TIRS (2015 and 2020) from USGS (https://earthexplorer.usgs.gov/) as the database to recognize the evolution of Wulan Delta (**Table 1**). The spatio-temporal monitoring in the coastal area using remote sensing data could help understand the erosion distribution and quickly predict coastal evolution trends with extensive coverage area (Wahyunto et al., 1995; Cracknell, 1999; Zhang, 2011; Mutaqin, 2017; Wicaksono and Wicaksono, 2019; Costantino et al., 2020; Arjasakusuma et al., 2021).

Under normal conditions, the water favorably reflects the green wavelengths, i.e., Band 2 on Landsat 5 TM and Band 3 on Landsat 8 OLI/TIRS. The water also absorbs the energy at wavelengths that are longer than near-infrared. Near-infrared (Band 4 on Landsat TM and Band 5 on Landsat OLI/TIRS) is very well known in shoreline analysis since it distinguishes water from land (Tong et al., 2014; Al-Mansoori and Al-Marzouqi, 2016; Pardo-Pascual et al., 2018; Zhang and Hou, 2020). Therefore, this research's band ratios were 2/4 for Landsat TM and 3/5 Landsat OLI/TIRS. We used several steps to get better results during the satellite image processes (e.g.,interpretation and analyses),

such as image cropping, radiometric correction, histogram thresholding, and mean erosion distance (MED). We used Dark Object Subtraction (DOS) technique to fix the images' visual quality and fix the pixel values that did not correspond to the reflection values for radiometric image correction. This technique assumes that the digital value of the darkest objects on the Earth's surface is zero.

Table 1.

The types of satellite images used in this research.

Images	Censors	Paths/rows	Time acquired		Resolution (m)
			Dates	Clock	
Landsat 5	TM	120/65	May 22, 1995	13:55	30
Landsat 5	TM	120/65	July 6, 2000	14:24	30
Landsat 5	TM	120/65	June 19, 2011	14:37	30
Landsat 8	OLI/TIRS	120/65	June 14, 2015	14:47	30
Landsat 8	OLI/TIRS	120/65	August 30, 2020	14:48	30

The shoreline information was identified digitally based on the satellite images' pixel values (Maglione et al., 2017; Zhang and Hou, 2020). The identification used ENVI 4.7 software with the assistance of histogram threshold feature on interactive stretching (**Fig. 2a**). Histogram thresholding is the process of separating land from the sea-based on pixel values. The thresholding includes dividing the histogram into two visually separated parts by graphical valleys seen in the histogram (Marfai et al., 2008; Aedla et al., 2015; Nassar et al., 2018; Ghorai and Mahapatra, 2020). Moreover, the tabulated histogram is described of frequency distributions, and to interpret land and water from it, a density slice was applied. Thresholding was done by shifting the line threshold step by step until the gap between water (max value) and land (min value) was reached minimum gap and feature distinction were clear (Tong et al., 2014). The thresholding results are binary images that have two values; value 0 for water and value 1 for land. These images are processed further to generate a shoreline. This histogram separation produces a minimum value that indicates the water body and a maximum value that indicates land. Pixel values from thresholding separation for each image have been generated, as shown in **Table 2** that inform pixel values (minimum and maximum) for each feature. Moreover, the maximum water value gap and the minimum land value are where shorelines potentially emerge.

Table 2.

Pixel value for each feature.

Images	Year	Water threshold		Land threshold	
		Min	Max	Min	Max
Landsat 5 TM	1995	0.552	0.792	0.795	2.896
Landsat 5 TM	2000	0.074	0.527	0.530	3.926
Landsat 5 TM	2011	0.194	0.519	0.521	3.500
Landsat 8 OLI/TIRS	2015	0.552	0.743	0.744	2.670
Landsat 8 OLI/TIRS	2020	0.554	0.749	0.751	2.625

The shoreline erosion and accretion from 1995 to 2020 were identified using the image processing method results, which were performed and analyzed quantitatively with the Mean Erosion Distance (MED) technique. With the MED technique, we also can obtain and determine the average land loss and land accumulation in the research area. The scenario and the equation used in MED are shown in **Fig. 2b** and **Eq. 1**. The MED equation used in shoreline monitoring was according to Tong et al. (2014). The spatio-temporal evolutions of the Wulan Delta were identified quantitatively from the equation and then analyzed in a qualitative descriptive manner.

To determine the processes that occurred in the shoreline, we establish four sections as an observed shoreline based on the existing main processes. Sections A and D were selected to identify the primary morphodynamics processes and their influence on the Wulan Delta evolution. In contrast, Sections B and C were selected to determine the evolution of the delta. The section analysis aimed to obtain detailed information on the processes occurring in each section.

(a)   (b)
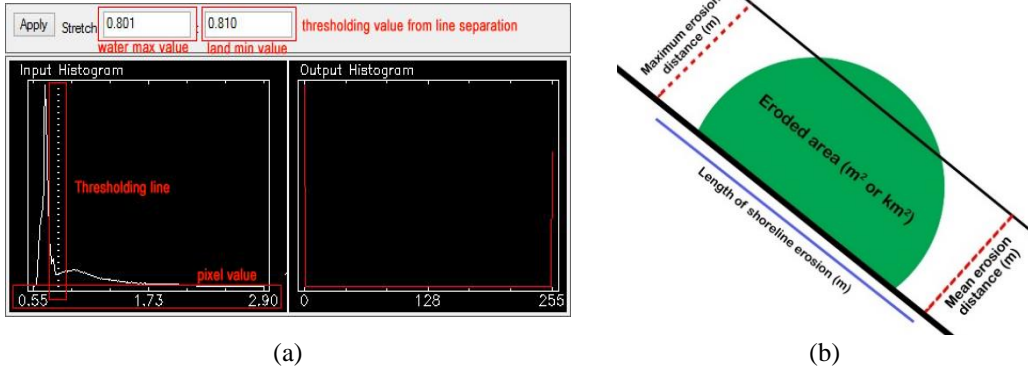
Fig. 2. (a) An example of a histogram thresholding technique to separate the land and the water; and (b) Mean Erosion Distance (MED) scenario.

$$\text{Mean Erosion Distance (m)} = ES/L \qquad (1)$$

where: ES -eroded or accreted area (m^2);
    L -length of shoreline erosion/accretion (m)

2.2. Field observations

We conduct a Focus Group Discussion (FGD) with the local community, especially the fishpond owners in Wulan Delta and its surrounding areas (**Fig. 3a**). The FGD aimed to gather the information and identify the cause and impact of the erosion and accretion in the Wulan Delta according to the local communities' perspectives through a discussion. Furthermore, validation of shoreline extraction results has been done during field observations by ground checking for some sample points to prove the existence of morphodynamics processes that occur by looking for evidence (**Fig. 3b**).
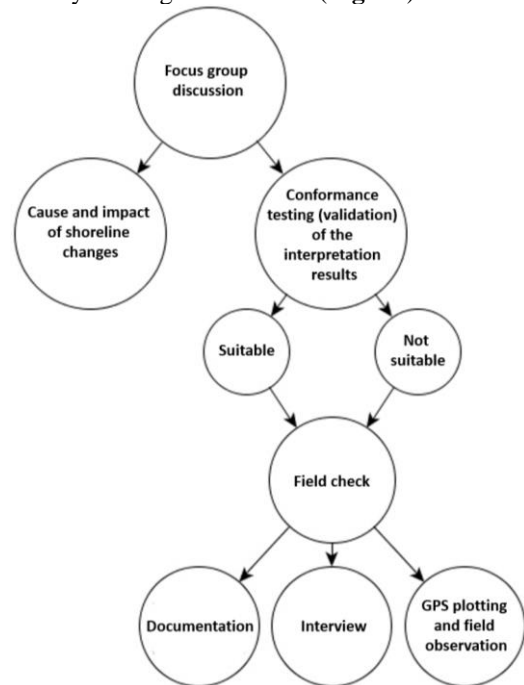
(a)   (b)

Fig. 3. (a) Focus Group Discussion with the local community in Wulan Delta; and (b) Validation of shoreline extraction results during field measurements.

3. RESULTS AND DISCUSSIONS

3.1. Shoreline change

Detailed monitoring can show a clear description of the morphodynamics processes along the shoreline. As mentioned before, we divided the study area into four sections (A, B, C, and D). Section A consists of Purworejo, Betahwalang, and Wedung Village; Section B consists of Berahan Kulon Village; Section C consists of Berahan Kulon and Berahan Wetan Village; and Section D consists of Kedungmalang, Kalianyar, Surodadi, Panggung, Bulakbaru, and Tanggultlare Village. This research divided the years 1995-2020 into four periods, namely 1995-2000, 2000-2011, 2011-2015, and 2015-2020. During 1995-2000, the shoreline in the study area shifted both seaward and landward (**Fig. 4a**). We used 11 years (from 2000 to 2011) due to limited data available on the website of the United States Geological Survey (USGS). The year 2005 was initially a time limit in the second period. However, the only available 2005 image was from Landsat 7 ETM+, which experienced a string. A string is a malfunction appearing in the image pixels, resulting in diagonal black stripes on the image. Even though the string is repairable, the pixel value correction is not good enough for shoreline extraction. Moreover, the diagonal black stripes are also found on Landsat 7 ETM+ images from 2005 to 2010. Therefore, this research used the 2011 image of Landsat 5 TM as a substitute.

(a)   (b)

(c)   (d)
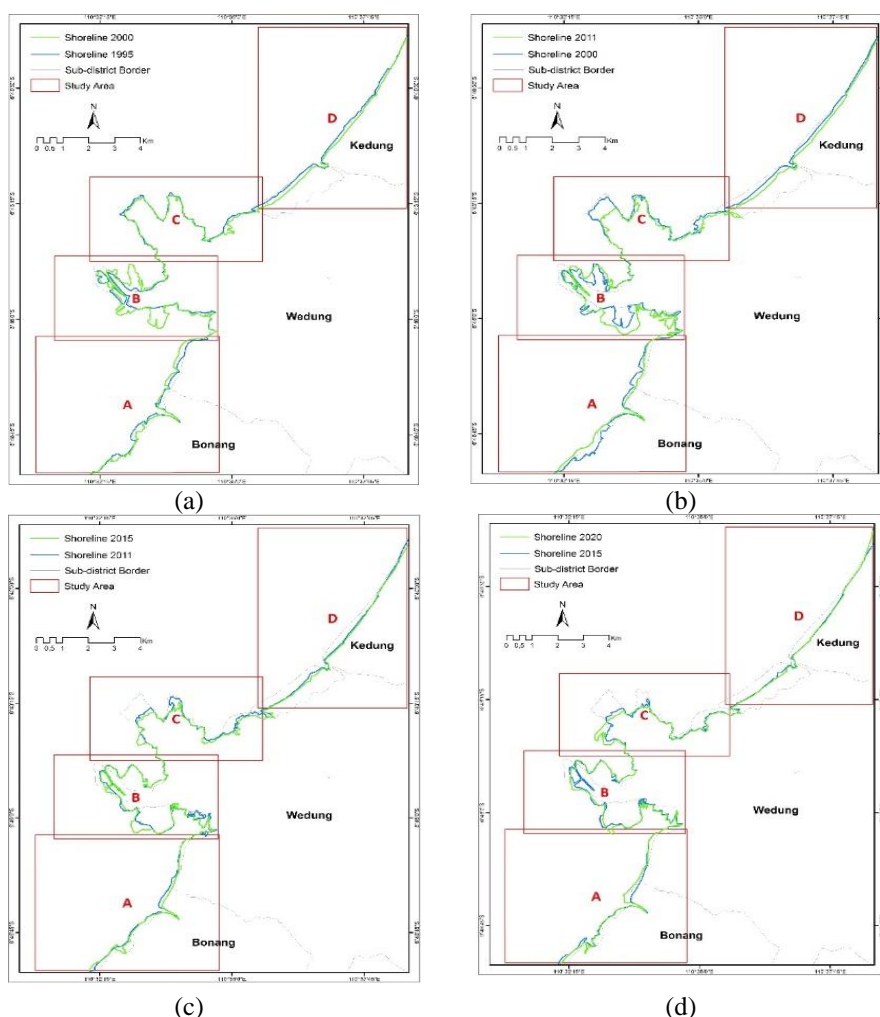
Fig. 4. The shoreline changes in Wulan Delta and its surrounding area during: (a) 1995-2000; (b) 2000-2011; (c) 2011-2015 and (d) 2015-2020.

The shoreline change analysis during 2000-2011 (**Fig. 4b**) used the same regional section as the analysis during 1995-2000. The shoreline change during 2011-2015 (**Fig. 4c**) was most significant than the shoreline change in the previous years or during 2015-2020 (**Fig. 4d**). This is due to the less deposited shoreline length during 2011-2015 (17.76 km) compared to other years, i.e., between 22.98-29.83 km. The shoreline change rate in this area during 25 years is more significant than what has happened in Yogyakarta and East Java (Mutaqin, 2017; Arjasakusuma et al., 2021).

Field observation was done by selecting 11 sample points (**Fig.5**) based on the most dynamic process that has occurred. Furthermore, this observation ensures the process generated from the laboratory by taking documentation and field observation. Locals accompanied this checking, so a locals interview was also conducted along with the observation to emphasize the results. According to Fadlillah et al. (2018), fishponds are the most dominant landuse; they expanded from 82.94% (2008) to 91.55% (2016) of major landuse in the Wulan Delta. Field observation strengthens this claim, and our observation found that from 11 ground points, 8 points were fishponds predominantly (**Table 3**). In addition, Mangrove plants were also found in 9 out of 11 points. As Marfai et al. (2016) assert that Wulan Delta morphodynamic causes landuse conversion from mangroves to fishponds; this condition will continue to happen in the future due to the extent of mangrove vegetation and fishponds as a local primary livelihood source.
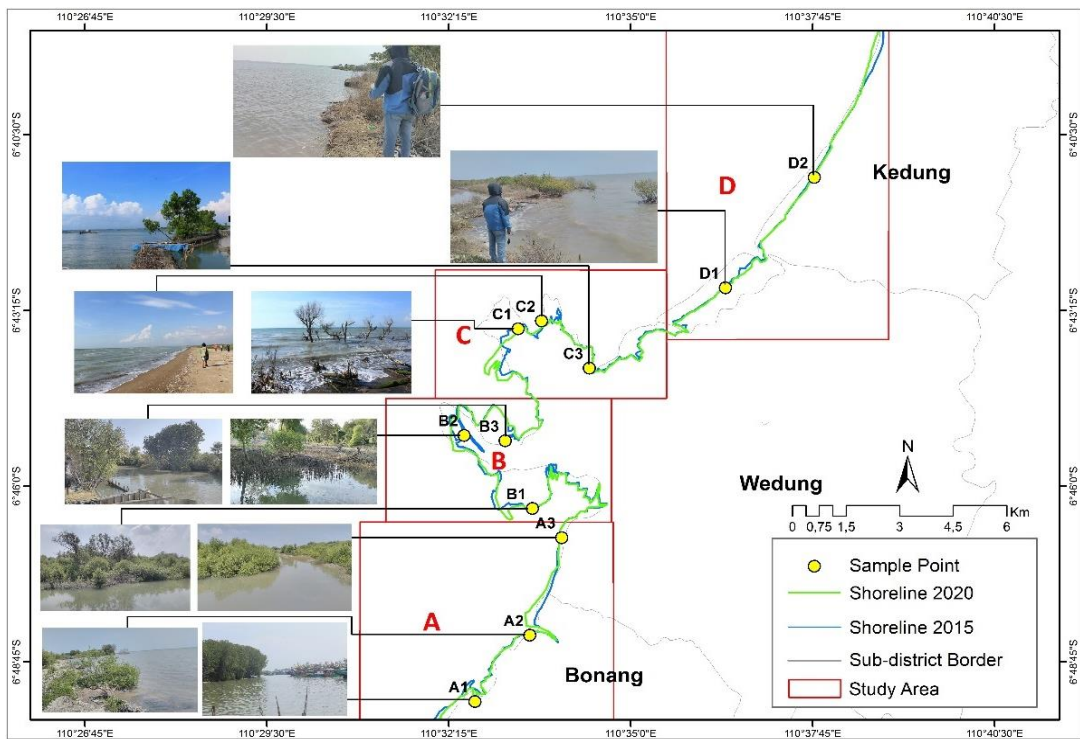
Fig 5. Field observation samples to ensure the process generated from laboratory.

Based on local explanation through focus group discussion (**Table 4**), shoreline deposition on points A1 and A2 was caused by mangroves planting along the coast around the 2000s. Meanwhile, at point A3, there has been erosion since the 2000s and caused many fishponds to be damaged, and it was proven by the remains of wooden stakes near the shore. All sample points in area B show the land deposition process due to the massive sediment load from the Wulan River. According to the locals (**Table 4**), accretion has been going for a long time, and the mangrove zone has made the accretion faster and often triggers land ownership conflicts. There have been deposition in points B1,

B2, and B3, which began to form around 1990. Moreover, calm waves make the process more dominant and faster.

Table 3.

Validation result from field observation and interview.

Sample point	Dominant process (tentative map)	Interview validation		Vegetation	Land use
		Process	Note		
A1	Deposition	Confirmed	The deposition had occurred since the 2000s	Mangrove	Fishpond, settlement, port
A2	Deposition	Confirmed	The little deposition had occurred since the 2000s	Mangrove	Fishpond
A3	Erosion	Confirmed	Erosion had occurred since the 2000s	Mangrove	Fishpond
B1	Deposition	Confirmed	The massive deposition has occurred since 1990	Mangrove	-
B2	Deposition	Confirmed	The massive deposition has occurred since 1990	Mangrove	Fishpond
B3	Deposition	Confirmed	The massive deposition has occurred since 1990	Mangrove	Fishpond
C1	Erosion	Confirmed	Massive erosion has occurred since the 1990s	Mangrove	-
C2	Erosion	Confirmed	Massive erosion has occurred since the 1990s, emergence of spit landforms in early 2000	-	Empty land
C3	Erosion	Confirmed	Erosion has occurred since the 2000s	Mangrove	Fishpond
D1	Erosion	Confirmed	Erosion has occurred before 1995	Mangrove	Fishpond
D2	Erosion	Confirmed	Erosion has occured before 1995	-	Fishpond

Table 4.

Focus Group Discussion (FGD) result.

| Sample point	Process confirmed	Focus Group Discussion		
		Cause	Effect	Local adaptation
A1	Deposition	Mangrove planting	New land	New land used for fishponds
A2	Deposition	Mangrove planting	New land	New land used for fishponds
A3	Erosion	High waves	Fishponds damage	Mangrove planting
B1	Deposition	Calm waves, sediment from the river	New land, land claim conflict	New land used for fishponds
B2	Deposition	Sediment from river	New land, land claim conflict	New land used for fishponds
B3	Deposition	Calm waves, sediment from the river	New land, land claim conflict	New land used for fishponds
C1	Erosion	High waves	Mangrove damage	Mangrove planting
C2	Erosion	High waves	The emergence of the natural barrier since the 2000s	Mangrove planting
C3	Erosion	High waves	Fishponds damage	Mangrove planting
D1	Erosion	High waves	Fishponds damage, irregular beach	Build shore protector from wood
D2	Erosion	High waves	Fishponds damage, irregular beach	Build shore protector from wood

Point C1 is located in the forefront area at the delta's foot and directly faces the open sea. Large waves have caused this area to experience shoreline erosion from 1995 until now. In addition, massive

damage to mangrove plants and fishponds has also occurred in this area. Point C2 is the location of Spit landform, and according to the local community (**Table 4**), it is also called 'Tirang', which stretches like an arrow along the coast around delta's foot, and it emerged around the 2000s. This landform becomes a natural barrier to prevent further erosion. Uniquely, this landform stretch and covers seawater trapped on the land and formed a lagoon. Likewise, Point C3 has experienced erosion since the 2000s and damaged many fishponds. The shoreline erosion in area D also continues from 1995 until these days. However, the shoreline retreat is not as intensive as before because the community started to make wave protectors from wood along the shore. Shoreline erosion at points D1 and D2 caused irregular shoreline form. The erosion makes the community's fishponds continue to be threatened, whereas aquaculture is still the local communities' main livelihood.

3.2. Land loss and land accumulation

The morphodynamics assessment emphasizes more on land loss and land accumulation during 1995-2020. According to Sunarto (2005), Wulan Delta experienced positive growth continuously from 1925 to 1995. It changed from 1.9 km^2 to 9.15 km^2 over 70 years at a growth rate of 0.39 km^2/year. Shoreline change accompanied the evolution during 1995-2020 on the south and the north of the delta. The land loss and land accumulation in the south varied uniquely. However, the coastal area on the north experienced land loss progressively.

The morphodynamics map, which shows the land loss and land accumulation in Wulan Delta and its surroundings during 1995-2020, is presented in **Fig. 6**. The map shows land loss distribution and land accumulation in 1995-2000, 2000-2011, 2011-2015, and 2015-2020. Aside from land loss and land accumulation, this map provides information on mean distance erosion and deposition, which are useful for determining the average distances of shoreline retreats and advances. **Table 5** shows the land development and mean erosion or deposition distance.

(a)   (b)

(c)   (d)
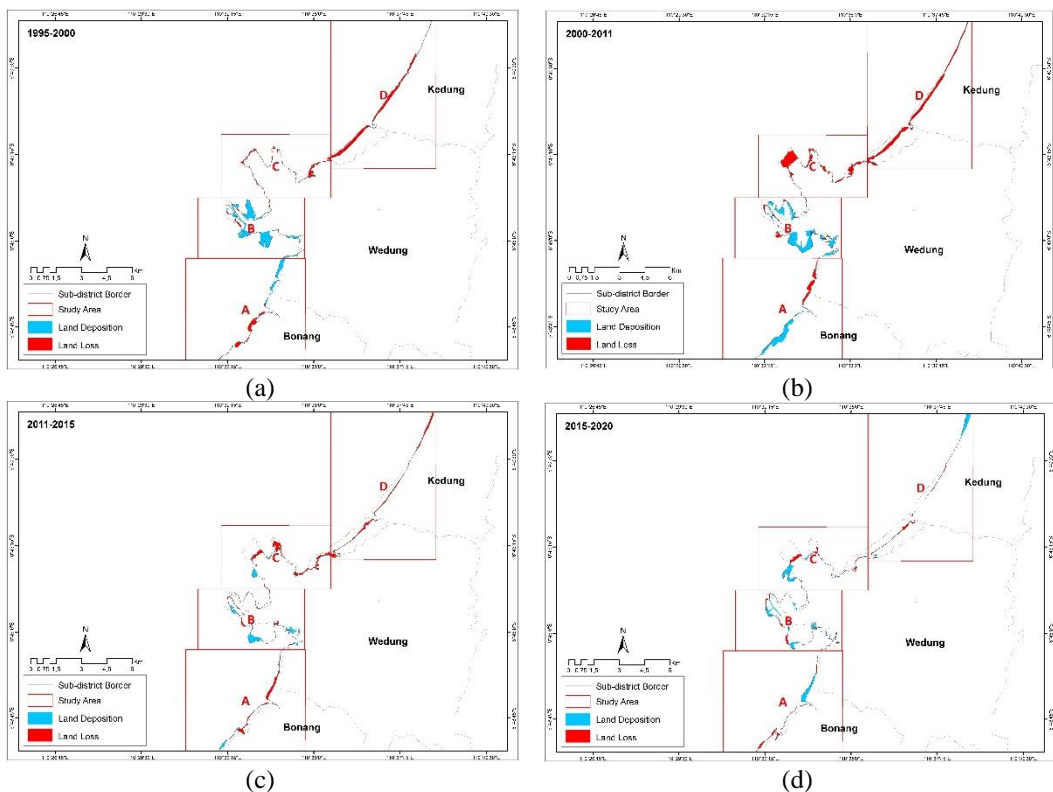
Fig. 6. Map of the spatio-temporal evolution of Wulan Delta and its surrounding during: (a) 1995-2000; (b) 2000-2011; (c) 2011-2015; (d) 2015-2020.

The shoreline in Section-A experienced moderate land loss during 1995-2000, i.e., 0.35 km^2, and continuously increased until the period of 2011-2015, which reach 0.38 km^2. However, the land loss had declined in the following years, i.e., 0.18 km^2 in the period of 2015-2020. Meanwhile, this section's shoreline accretion fluctuated and peaked during 2000-2001, causing the most massive land accumulation, i.e., 0.71 km^2. Coastal erosion leads to shoreline retreats by an average of 64.76 m. Meanwhile, due to accretion, the shoreline shifts with an average as far as 68.24 m seaward.

The land loss and the land accumulation in Section-B are imbalanced. Land accretion tends to be higher since it is located in the river estuary (Arjasakusuma et al., 2021). The most extensive land accumulation was 1.62 km^2 during 2000-2011, whereas the severest land loss was 0.16 km^2 during 2000-2011 and 2011-2015. The shoreline in this section has retreated by an average of 24.29 m and advanced by 72.12 m.

Table 5.
Morphodynamics and the mean erosion or deposition distances in Wulan Delta and its surroundings.

Sections	Periods	Morphodynamics (km^2)		Eroded shoreline length (km)	Deposited shoreline length (km)	Mean erosion distance (m)	Mean deposition distance (m)
		Land loss	Land deposition				
Section A	1995-2000	-0.35	0.38	-4.15	6.63	84.34	57.32
	2000-2011	-0.36	0.71	-3.99	6.76	90.23	105.03
	2011-2015	-0.38	0.09	-7.32	2.18	51.91	41.28
	2015-2020	-0.18	0.33	-5.53	4.76	32.55	69.33
Section B	1995-2000	-0.09	1.57	-3.51	12.69	25.64	123.72
	2000-2011	-0.16	1.62	-5.33	18.23	30.02	88.86
	2011-2015	-0.16	0.54	-12.66	11.57	12.64	46.67
	2015-2020	-0.15	0.49	-5.20	16.76	28.85	29.24
Section C	1995-2000	-0.44	0.02	-11.49	2.03	38.29	9.85
	2000-2011	-1.11	0.01	-12.45	1.24	89.16	8.06
	2011-2015	-0.57	0.13	-9.81	2.75	58.10	47.27
	2015-2020	-0.27	0.35	-8.03	4.32	33.62	81.02
Section D	1995-2000	-0.99	0.02	-9.95	1.63	99.50	12.27
	2000-2011	-1.22	0.00	-12.75	0.00	95.69	0.00
	2011-2015	-0.55	0.01	-11.49	1.26	47.87	7.94
	2015-2020	-0.18	0.31	-17.72	3.99	10.16	77.69

A contrary phenomenon has been found in Section-C, where the land loss was dominant. Shoreline erosion created a land loss of 2.39 km^2 over 25 years, whereas the land deposition reaches 0.51 km^2 with the highest land accretion is 0.35 km^2 during 2015-2020. The length of the shoreline in Section-C continues to decline. The shoreline in this section has retreated with an average of 54.79 m and advanced by 36.55 m. The land loss in Section-D, lying administratively on Jepara Regency, is the most severe. Over 25 years, total land loss in this section reaches 2.94 km^2, with the most significant land loss was during 2000-2011, which reach up to 1.22 km^2. Meanwhile, the most massive land accumulation was only 0.31 km^2 during 2015-2020. The severe land loss reduces the length of the shoreline in Section-D progressively. On average, the shoreline in this section has retreated by 63.31 m and advanced merely by 24.46 m.

The shoreline morphodynamics was analyzed comparatively with the wind and wave data of Demak and Jepara. The analysis aimed to identify the relationship between the cause and impact of the shoreline with the coastal morphodynamics.

Wind speed and direction influence the direction and magnitude of sea waves proportionally. During the west monsoon, the wind speed tends to become stronger, and the wave tends to become higher and more destructive (Muskananfola et al., 2020). This situation is different from the southern part of Java, where the high and extreme waves happened during the east monsoon (Mutaqin, 2017). Destructive waves erode the shoreline in Demak and Jepara (Muskananfola et al., 2020). On the contrary, during the east monsoon, the wind speed tends to be weaker, and the wave tends to be lower.

The intensity of the eastern sea wave is reduced by Muria Peninsula, causing land accretion along Demak and Jepara's shoreline.

The local community's adaptation is more to structural adaptation, such as making protective stakes and mangrove planting. Despite the loss, the positive side has been obtained by the fishermen. Fishers in area C are lucky because they can build the floating fish cage close to the beach because of the coastal erosion process, this evidenced by the discovery of several floating fish cage in area C.

3.3. Evolution of Wulan Delta

The delta initially had grown into a straight shape (strand plain) before it developed into a bird-foot shape (digitate). According to Setiawan (2014), the shoreline accretion in Wulan Delta is due to Muria Volcano's presence that supplies abundant obsolete materials to the Wulan River. As a result, the Wulan River estuary experiences progradation continuously, and the Wulan Delta area widens. **Fig. 7** shows Wulan Delta's development from 1995 to 2020, which also depicts image interpretation and field survey results.
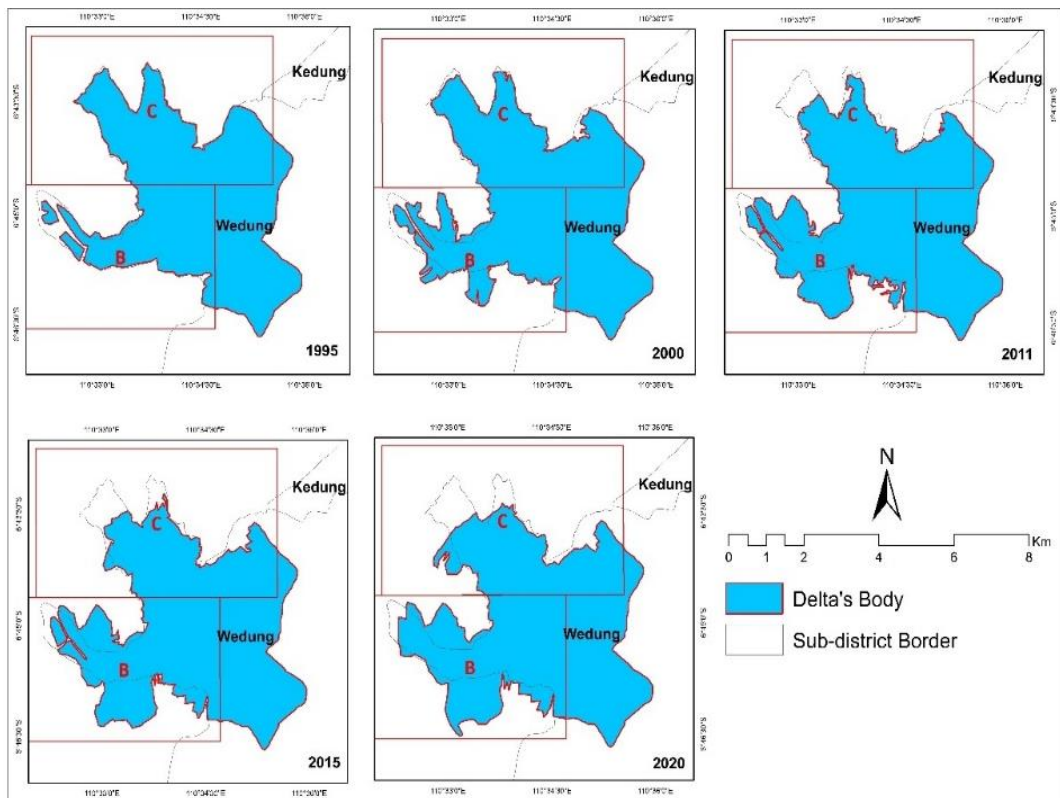
Fig. 7. The development of Wulan Delta during 1995–2020.

Wulan Delta has a bird-foot shape because the Wulan River bifurcates into two rivers, i.e., northward and northwestward, causing shoreline accretion to occur on these two distributary channels. Also, these river channels develop differently. According to Sunarto (2005), the main development initially occurred on the northwestern channel. However, in 1972, the northern channel began to form. Therefore, the shape of the delta changes to arcuate, cuspate, and digitate. Based on the Wulan Delta development presented in **Fig. 7**, we identify the extensive development and delta growth rate during 1995-2020 (**Table 6**).

Table 6.
The development and the growth rate of Wulan Delta during 1995 – 2015.

Years	Size of Delta (km^2)	Total growth (km^2)	Growth rate (km^2/year)	Growth percentage (%)
1995	21.19	-	-	-
2000	22.27	1.08	0.216	4.85
2011	22.62	0.35	0.032	1.55
2015	22.60	-0.02	-0.005	-0.09
2020	23.02	0.42	0.084	0.02

The Wulan Delta area always experienced extensive accumulation during 1995-2020, as seen in **Table 6**. It accumulated from 21.19 km^2 in 1995 to 23.02 km^2 in 2020. The most extensive land growth over 25 years happened during 1995-2000, which reach 1.08 km^2. It was enormously more significant than the land growth during 2011-2015 since the Wulan Delta area was reduced by 0.02 km^2. The growth rate in **Table 6** was obtained from the division of total growth by the length of the period. The highest growth rate was during 1995-2000, i.e., 216,000 m^2/year, while the lowest one was during 2011-2015, i.e., 5,000 m^2/year. The growth percentage describes the percentage of accumulated land to the total area of the Wulan Delta. It is proportional to total growth.

4. CONCLUSIONS

Over the years of 1995-2020, the shoreline change in Wulan Delta and its surroundings varied widely. An inconsistency is found in the southern part of the delta, representing shoreline retreats and advances. However, the shoreline continuously retreats in the northern part of the delta due to high waves. Wulan Delta has divided into two parts, i.e., southern and northern, which experience various changes. The northern shoreline retreats, while the southern one advances due to mangrove planting and high sedimentation from the rivers. During 1995-2020, the total land loss and accumulation in the study area were -7.16 km^2 and +6.58 km^2, respectively. The growth rates of the Wulan Delta over 25 years (1995-2020) were 73,200 m^2/year.

R E F E R E N C E S

Aedla R., Dwakarish G.S., Reddy D.V. (2015). Automatic Shoreline Detection and Change Detection Analysis of Netravati-GurpurRivermouth Using Histogram Equalization and Adaptive Thresholding Techniques. *Aquatic Procedia*, 4, 563-570. https://doi.org/10.1016/j.aqpro.2015.02.073.

Al-Mansoori S. and Al-Marzouqi F. (2016). Coastline Extraction using Satellite Imagery and Image Processing Techniques. *International Journal of Current Engineering and Technology*, 6(4), 1245-1251.

Arjasakusuma S., Kusuma S.S., Saringatin S., Wicaksono P., Mutaqin B.W., Rafif R. (2021). Shoreline Dynamics in East Java Province, Indonesia from 2000 to 2019 Using Multi-sensor Remote Sensing Data. *Land*. 10(2), 100. https://doi.org/10.3390/land10020100.

Bird E., and Ongkosongo O.S.R. (1980). *Environmental Changes of the Coasts of Indonesia*. Tokyo: United Nations University. 510p.

Chen D., Li X., Saito Y., Liu J.P., Duan Y., Liu S., Zhang L. (2020). Recent evolution of the Irrawaddy (Ayeyarwady) Delta and the impacts of anthropogenic activities: A review and remote sensing survey. *Geomorphology*, 365, 107231. https://doi.org/10.1016/j.geomorph.2020.107231.

Collins D.S., Nguyen V.L., Ta T.K.O., Mao L., Ishii Y., Kitagawa H., Nakashima R., Vo T.H.Q., Tamura T. (2021). Sedimentary evolution of a delta-margin mangrove in Can Gio, northeastern Mekong River delta, Vietnam. *Marine Geology*, 433, 106417. https://doi.org/10.1016/j.margeo.2020.106417.

Costantino D., Pepe M., Dardanelli G., Baiocchi V. (2020). Using Optical Satellite and Aerial Imagery for Automatic Coastline Mapping. *Geographia Technica*, 15(2), 171-190. http://doi.org/10.21163/GT_2020.152.17.

Cracknell A.P. (1999). Remote Sensing Techniques in Estuaries and Coastal Zones. *International Journal of Remote Sensing*, 20(3), 1–9. https://doi.org/10.1080/014311699213280.

Fadlillah L.N., Sunarto., Widyastuti M., Marfai M.A. (2018). The impact of human activities in the Wulan Delta Estuary, Indonesia. *IOP Conf. Ser: Earth Environ Sci*, 148, 012032. https://doi.org/10.1088/1755-1315/148/1/012032.

Fadlillah L.N., Widyastuti M., Geottongsong T., Sunarto, Marfai M.A. (2019). Hydrological Characteristics of Estuary in Wulan Delta in Demak Regency, Indonesia. *Water Resources*, 46, 832-843. https://doi.org/10.1134/S0097807819060101.

Ghorai D. and Mahapatra M. (2020). Extracting Shoreline from Satellite Imagery for GIS Analysis. *Remote Sensing in Earth Systems Sciences*, 3, 13–22. https://doi.org/10.1007/s41976-019-00030-w.

Maglione P., Parente C., Vallario A. (2017). Coastline extraction using high resolution WorldView-2 satellite imagery. *European Journal of Remote Sensing*, 47(1), 685-699. https://doi.org/10.5721/EuJRS20144739.

Marfai M.A., Almohammad H., Dey S., Susanto B., and King L. (2008). Coastal dynamic, and shoreline mapping: multi-sources spatial data analysis in Semarang Indonesia. *Environ Monit Assess*, 142, 297-308. https://doi.org/10.1007/s10661-007-9929-2.

Marfai M.A. (2014). Impact of sea level rise to coastal ecology: a case study on the northern part of Java Island, Indonesia. *Quaestiones Geographicae*, 33(1), 107–114. https://doi.org/10.2478/quageo-2014-0008.

Marfai M.A., Tyas D.W., Nugraha I., Ulya A.F., Riasasi, W. (2016). The Morphodynamics of Wulan Delta and its impact on the coastal community in Wedung Subdistrict, Demak Regency, Indonesia. *Journal of Environmental Protection*, 7. 60-71.

Marfai M.A., Ahmada B., Mutaqin B.W., Windayati R. (2020). Dive Resort Mapping and Network Analysis: Water Resources Management in Pemuteran Coastal Area, Bali Island, Indonesia. *Geographia Technica*. 15(2), 106-116. http://doi.org/10.21163/GT_2020.152.11.

Mujabar P.S. and Chandrasekar N. (2013). Shoreline change analysis along the coast between Kanyakumari and Tuticorin of India using remote sensing and GIS. *Arabian Journal of Geosciences*, 6, 647-664. https://doi.org/10.1007/s12517-011-0394-4.

Muskananfola M.R., Supriharyono, Febrianto S. 2020. Spatio-temporal analysis of shoreline change along the coast of Sayung Demak, Indonesia using Digital Shoreline Analysis System. *Regional Studies in Marine Science*, 34, 101060. https://doi.org/10.1016/j.rsma.2020.101060.

Mutaqin B.W. (2017), Shoreline Changes Analysis in Kuwaru Coastal Area, Yogyakarta, Indonesia: An Application of the Digital Shoreline Analysis System (DSAS). *International Journal of Sustainable Development and Planning* 12(7), 1203-1214. https://doi.org/10.2495/SDP-V12-N7-1203-1214.

Mutaqin B.W., Lavigne F., Hadmoko D.S., Malawani M.N. (2019), Volcanic Eruption-Induced Tsunami in Indonesia: A Review, *IOP Conf. Ser.: Earth Environ. Sci*. 256 012023. https://doi.org/10.1088/1755-1315/256/1/012023.

Mutaqin B.W. (2020). Spatial Analysis and Geomorphic Characteristics of Coral Reefs on the Eastern Part of Lombok, Indonesia. *Geographia Technica*. 15(2), 202-211. http://doi.org/10.21163/GT_2020.152.19.

Mutaqin B.W., Marfai M.A., Helmi M., Rindarjono M.G., Windayati R., Sunarto (2020), Spatio-temporal Mapping of Ecotourism Activities in Buleleng Conservation Zone: A Methodological Review, *IOP Conf. Ser.: Earth Environ. Sci*. 451 012095. https://doi.org/10.1088/1755-1315/451/1/012095.

Nassar K., Fath H., Mahmod W.E., Masria A., Nadaoka K., Negm A. (2018). Automatic detection of shoreline change: case of North Sinai coast, Egypt. *Journal of Coastal Conservation*, 22, 1057–1083. https://doi.org/10.1007/s11852-018-0613-1.

Pardo-Pascual J.E., Sanchez-Garcia E., Almonacid-Caballer J., Palomar-Vazquez J.M., de los Santos E.P., Fernandez-Sarria A., and Balaguer-Beser A. 2018. Assessing the Accuracy of Automatically Extracted Shorelines on Microtidal Beaches from Landsat 7, Landsat 8 and Sentinel-2 Imagery. *Remote Sensing*, 10(2), 326. https://doi.org/10.3390/rs10020326.

Ruswanto and Adisaputra K. (1990). *Perkembangan Garis Pantai Welahan–Jepara Jawa Tengah*. Geologi Indonesia: Bandung.

Setiawan M.A., Rahayu E., and Sulistyaningrum Y. (2014). Dinamika Lingkungan Daerah Aliran Sungai dan Pesisir. In Sunarto, Marfai M.A., Setiawan M.A. *Geomorfologi dan Dinamika Pesisir Jepara*. 77-116. Yogyakarta: Gadjah Mada University Press.

Sunarto. (2005). Perubahan Fenomena Geomorfik Daerah Kepesisiran di Sekeliling Gunungapi Muria Jawa Tengah. *Dissertation*. Yogyakarta: Fakultas Geografi UGM.

Tong S.S., Pham T.L., Gunasekara K., Nguyen T.N., and Deroin J.P. (2014). Monitoring Coastal Morphological Changes Using Remote Sensing and GIS in the Red River Delta Area, Vietnam. *Photo Interpretation European Journal of Applied Remote Sensing*, 2, 51-97.

UNISDR/UNDP. (2012). *A Toolkit for Integrating Disaster Risk Reduction and Climate Change Adaption into Ecosystem Management of Coastal and Marine Areas in South Asia*. New Delhi: UNDP.

Wahyunto, Djohar H.H., and Marsoedi D.S. (1995). Analisis Data Penginderaan Jauh untuk Mendukung Identifikasi dan Inventarisasi Lahan Sawah di Daerah Jawa Barat. In Pusat Penelitian Tanah dan Agroklimat, Bogor (Eds.) *Proceedings of Pertemuan Teknis Penelitian Tanah dan Agroklimat*. 37-49.

Wicaksono A. and Wicaksono P. (2019). Geometric Accuracy Assessment for Shoreline Derived from NDWI, MNDWI, and AWEI Transformation on Various Coastal Physical Typology in Jepara Regency using Landsat 8 OLI Imagery in 2018. *Geoplanning J. Geomat. Plan*. 6(1), 55–72. https://doi.org/10.14710/geoplanning.6.1.55-72.

Zhang, Y. (2011). Coastal Environmental Monitoring Using Remotely Sensed Data and GIS Techniques in the Modern Yellow River Delta, China. *Environ Monit Assess*, 179(1-4), 15-29. https://doi.org/10.1007/s10661-010-1716-9.

Zhang Y. and Hou X. (2020). Characteristics of Coastline Changes on Southeast Asia Islands from 2000 to 2015. *Remote Sensing*. 12(3), 519. https://doi.org/10.3390/rs12030519.

THE EFFECTS OF CORS NETWORK GEOMETRY AND DIFFERENTIAL NRTK CORRECTIONS ON GNSS SOLUTIONS

Gino DARDANELLI [1] , *Claudia PIPITONE* [1]

ABSTRACT:
The widespread availability of Continuosly Operating Reference Station (CORS) all over the world, allows to improve more scientific and technical studies on the use of satellite positioning techniques. The aim of this paper is to understand the effects of a GNSS CORS network geometry and differential corrections on the solutions. The analysis is carried out using ten different network configurations, with different inter-distances between the stations within GNSMART Geo++ software. The coordinates of one control point placed on the top of the Department of Engineering (University of Palermo, Italy) have been used to perform several static positioning mode test within fourthy hours. Different surveys have been performed, including four separate session tests, with acquisitions of one hour each. The analysis has been carried out using the traditional network solutions, such as the Virtual Reference Station (VRS), the Flächen Korrektur Parameter (FKP) and other two more recent techniques, which use the satellite corrections from the nearest (Near) and the farest (Far) stations. Results confirmed the great reliability of the GNSS network, with centimetre precision in terms of coordinates (North, East and Ellipsoidal Height), whether changing the geometric configuration of the network or the corrections.

Key-words: GNSS, CORS, Network configuration, NRTK, VRS, FKP, Geo++.

1. INTRODUCTION

In the last few decades, the high performances of the real-time satellite positioning allowed the increasing of the number of the Network Real Time Kinematic (NRTK)-GNSS stations worldwide. Indeed, the use of GNSS networks allows reducing the problems occurred with the RTK approach, mainly connected to the distance between the master and rover receivers. Indeed, the latter needs to be less than 20 kilometers, for the ambiguity-phase resolution using the "*on-the-fly*" mode to obtain the centimeter level of precision (Zhang and Teunissen, 2011).

Recently, several studies have been performed by Universities, Research Center, Public or Private Institutions, to test the precision and the reliability of NRTK-GNSS positioning, focusing on the repeatability of the experiments. The Department of Geomatics, *University of Calgary* (Canada), performed one of the earliest experiments. The MultiRef approach has been tested to analyze the influence of the network geometry configuration on the achievable precision. The analysis demonstrated that best results can be achieved when the reference stations are distributed at the same distance along the configuration scheme; also, the CORS outside the analysed network do not increase the precision achievable anyway (Fortes et al., 2003, Pugliano and Lachapelle, 2005).

At the *Ohio State University* (USA), the analyses developed by Grejner-Brzezinska provided a great contribution to the research. The effects of the network geometric configuration and the reliability of the differential corrections, using 24 hours data, but also the horizontal and vertical achievable precision are discussed in Grejner-Brzezinska et al. in 2005. Other studies focused on the network calibration for adverse reference-rover geometry in RTK network-based (Grejner-Brzezinska et al., 2009), the high-accuracy Differential Global Position System (DGPS) and precise point

---

[1] *Department of Engineering, University of Palermo, 90128 Palermo, Italy, gino.dardanelli@unipa.it; claudia.pipitone02@unipa.it*

positioning (PPP) based on CORS networks (Wielgosz et al., 2005) and the efficiency and reliability of ambiguity resolution in network-based real-time kinematic GPS (Grejner-Brzezinska et al., 2011). Also, Rizos and Satirapod discussed in 2011 the main role of GPS/GNSS setup (as CORS Networks) by creating the Global Geodetic Observing System (GGOS), managed by the International Association of Geodesy (IAG). Since 2005, in Australia, the analyses were focused on the distance between the stations, ranging from 50 to 200 kilometers, within GNSS CORS networks, such as *GPSnet ™*. Results have shown that the use of NRTK solutions provides high performances in terms of precision, accuracy and repeatability of the final coordinates (Gordini et. al., 2006, Hope et al., 2008, Hausler and Collier, 2013). Other studies involved the analysis of the network based geometry-free models for Three Carrier Ambiguity Resolution (TCAR) and phase bias estimation with DD and ZD code and phase measurements (Feng and Rizos, 2009).

In Great Britain, static and cinematic surveys have been conducted to evaluate the accuracy, the precision and the availability of NRTK commercial services, like *SMARTnet*. In both cases, centimeter precisions have been reached. Also, the influence of the number of visibile satellites, the Dilution of Precision (DOP) and the ambiguity-phase resolution time have been analysed (Aponte et al., 2009). The NRTK stations located on the border between Spain and Portugal but also those on the border between regions (Lombardia and Piemonte) of the same country (Italy) have been used for scientific purposes (Garrido et al., 2012, Dabove et al., 2016). Other studies also involved the use of NRTK stations for archaeological settlements (Inal et al., 2017, Fazio et al., 2019, Ebolese et al., 2019). In 2018, Pepe investigated the performance of the NTRK approach using several types of corrections (VRS, Nearest, FKP, MAC) with a low cost GNSS receiver equipped with Arduino jumper wires, power bank and a smartphone, employing the stop-and-go kinematic technique (Pepe, 2018).

Finally, in Poland, several tests have been also performed to evaluate the quality of the network-based GNSS positioning services provided by all available CORS networks, using 20 reference points of the first-order geodetic network (Prochniewicz et al. 2020). The international works, already discussed, involved different methodologies and mathematical approaches to compute the network corrections. The size of the network, the number of GNSS stations and the geometric configurations have been deeply analysed in their studies. Periodically, in Australia, the improvements connected to the use of GPS-GNSS CORS networks have been analysed. As an example, in 2013, the *Department of Industry, Innovation, Climate Change, Science, Research and Tertiary Education*, demonstrated that the GPS-GNSS CORS network positioning allows increasing the economic benefits in terms of the Australian Gross Domestic Product (GDP). The increasing estimation of the GDP goes from $2.3 billion and $3.7 billion in 2012, to $7.8 billion and $13.7 billion in 2020 (ACIL Allen Consulting, 2013).

Focusing more deeply on this work, since 2005, the UNIPA GNSS CORS network is available in the central-western part of Sicily, Italy (**Fig. 1**). The design, the geodetic framework and the preliminary results of the network have been discussed in Dardanelli et al. (2020). In recent times, the UNIPA GNSS CORS network had the scientific acknowledgment through many tests in different application fields. Ammoscato et al. (2008) used data to design a GPS-GIS integrated system for electromagnetic pollution; Dardanelli et al. (2017) showed the results of technical criticalities for GIS modelling in an urban noise map; Catania et al. (2020) evaluated the positioning accuracy by comparing GNSS receivers used for mapping and guidance of agricultural machines.

Other studies referred to the use of data from UNIPA network to collect performance assessment of Precise Point Positioning (PPP) surveys using the GNSS GPS–GLONASS–Galileo Constellations. Specifically, the GNSS configurations involved were seven: GPS only, GLONASS only, Galileo only, GPS+GLONASS, GPS+Galileo, GLONASS+Galileo, and GPS+GLONASS+Galileo. The results showed significant performance improvement of the GNSS combinations compared to single GNSS constellations (Angrisano et al., 2020). Over the last couple of years, Kenyeres et al. (2019) also used data of UNIPA GNSS CORS for a European regional integration of long-term national dense network solutions, with positions and velocities for 3192 stations. Other applications involving the UNIPA GNSS CORS network have been analyzed and discussed. Dardanelli et al. (2015) and

Dardanelli and Carella (2013) applied network corrections to trajectories calculation of MMS (Mobile Mapping System).

Fig. 1. Geographical position of the study area, by digital orthophoto from Italian National Geoportal, scale 1:6000000, reference system UTM-WGS8433N (ETRF2000).

Stocchi et al. (2017) used RINEX file to geodetic measurements of the stalactite elevation in geological analyses, meanwhile Dardanelli and Pipitone (2017), Dardanelli et al. (2014) and Pipitone et al. (2018) focused on dams monitoring with integrated geomatics and GNSS technique. Finally, Barreca et al. (2020) used UNIPA CORS dataset from 2008-2016 to monitor the active faulting in southwestern Sicily, with an integrated geodetic and InSAR technique.

The aim of this paper is to understand the effects of the geometric configuration and the differential corrections of a GNSS CORS network on the solutions. The analysis is carried out using ten different network configurations, with different inter-distances between the stations computed with *GNSMART Geo++* software. The coordinates of one control point placed on a concrete pillar on the rooftop of the Department of Engineering have been used to perform several static positioning mode tests within fourthy hours. Different surveys have been performed, including four separate session tests, with acquisition of one hour each.

The analysis has been carried out using the traditional network solutions, such as the *Virtual Reference Station* (VRS) approach (Wanninger, 2003), the *Flächen Korrektur Parameter* (FKP) (Keenan et al. 2002, Kim et al. 2017) and other two more recent techniques, which use the satellite corrections from the nearest (Near) and the farest (Far) stations. Results confirmed the great reliability of the GNSS network, with centimetre precision in terms of coordinates (North, East and Ellipsoidal Height), whether changing the geometric configuration of the network or the corrections.

The paper is organized as follows: the description of Materials, Software used and Methods is discussed in Section 2; the Results and the Discussion of the analyses are presented in Section 3. Finally, the Conclusions and future applications are reported in Section 4.

2. MATERIALS, SOFTWARE USED AND METHODS

In this work, the data set (of two months) used was collected at the Engineering Department for the geodetic survey operations carried out during the first step of network setup and consists of all available GPS/GLONASS data from UNIPA GNSS CORS, as showed in Dardanelli et al. 2020 with 8 CORS, installed on the top of a building at the: University of Palermo (PALE), Termini Imerese (TERM), Trapani (TRAP), Agrigento (AGRI), Caltanissetta (CALT), Partinico (PART), Campobello di Mazara (CAMP) and Prizzi (PRIZ) including also the external CORS of Alcamo. In **table 1** list of geographical coordinates in ETRS89 of all CORS.

Table 1.

Geographical coordinates of UNIPA CORS Network in ETR89.

CORS	Latitude	Longitude	UP (m)
AGRI	37°19'13.00674N	13°36'04.19433E	297.355
ALCA	37°58'24.64002N	12°57'20.77357E	354.154
CALT	37°29'35.40220N	14°03'18.35414E	633.969
CAMP	37°37'45.32620N	12°44'41.57530E	146.089
PALE	38°06'19.94099N	13°20'54.42250E	113.508
PART	38°02'25.49135N	13°06'35.29019E	247.601
PRIZ	37°43'08.31149N	13°26'12.80031E	961.984
TERM	37°58'59.71290N	13°42'07.77880E	55.31
TRAP	38°00'45.43112N	12°32'28.04159E	61.985

The GNSS *Topcon Hiper-Pro* double-frequency receivers equipped with FC-100 controller and *Nokia N70* mobile phone have been used for the static survey. The control point, in the ETRS89 framework, is placed on a concrete pillar on the rooftop of Palermo University, according to other studies, recently published (Angrisano et al., 2020).

The three-commercial software, used to compute the ground truth in this research, are:

- *Topcon Tools* ver. 8.2.3, developed by Topcon Corporation. The software allows the data processing from different devices such as total stations, digital levels and GNSS receivers, and it is used in several technical-scientific applications (Uradziński and Bakuła, 2020, Dawidowicz et al., 2015). Topcon Tools uses the Modified Hopfield Model for the tropospheric corrections. The employed positioning mode was Code-based differential ("CODE DIFF"), the time range and the cut-off angle were set to 1 s and 10 degrees, respectively;

- *GNSMART*, developed by *Geo++ GNSMART* was one of the earliest systems to guarantee the uniform coverage for the absolute positioning with centimeter precision in real time (Wubbena et al. 2005). The GNSS observations (GPS and GLONASS in this study) at high resolution are in RTCM 2.3 format, able to send the differential corrections (VRS, FKP, Near, Far);

-*Meridiana* ver. 2011, developed by Topcon Corporation, for recording data from the different corrections (VRS, FKP, Near, Far).

Preliminary, the coordinates of the control point, used to compare other measurements in real time (NRTK), have been determined with a relative static survey, obtaining high precision, and processed by Topcon Tools. The scheme involved three baselines connecting the control Point and other three CORS, specifically those of Alcamo, Prizzi, and Termini Imerese.
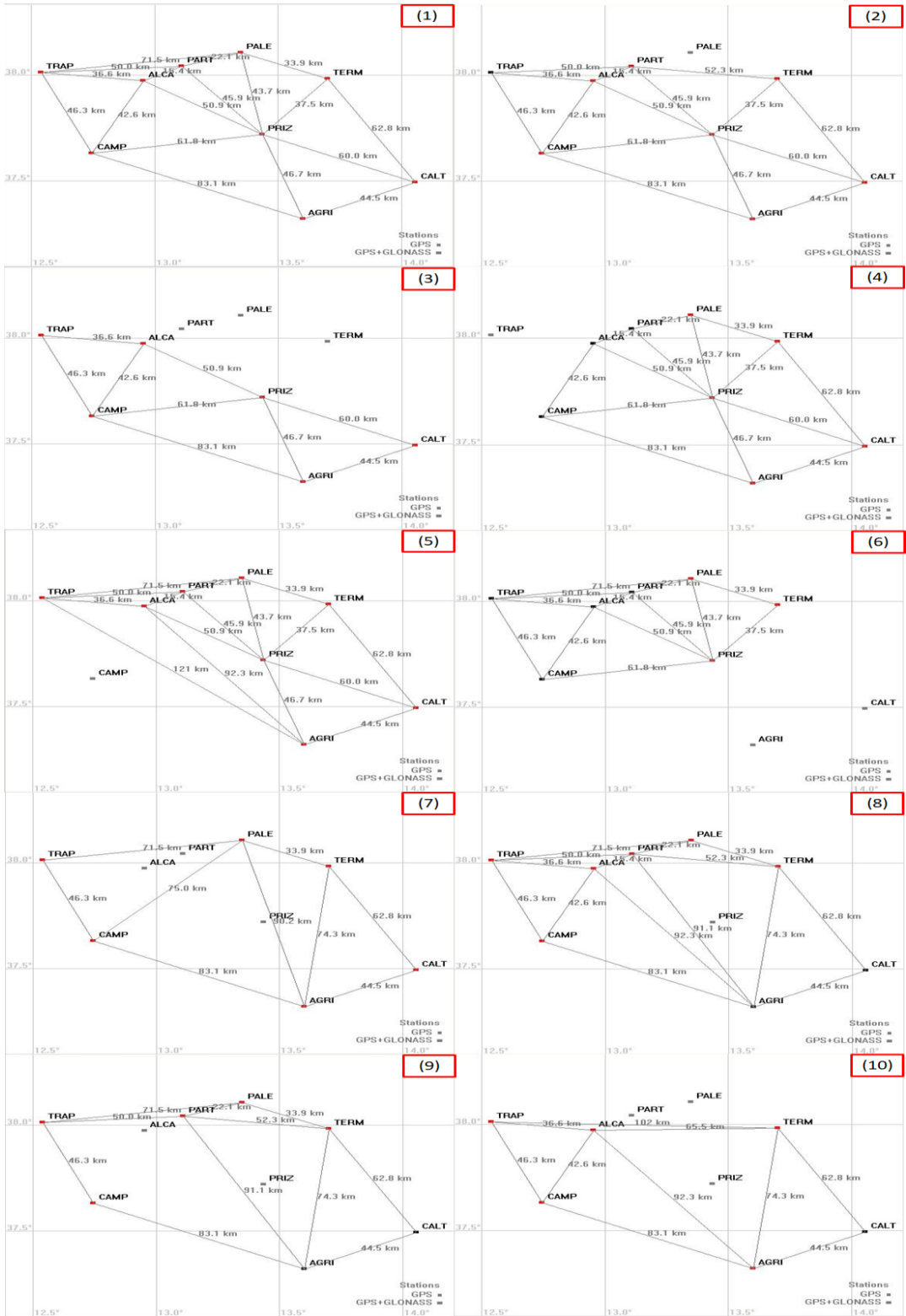
Fig. 2. GNSMART screenshot of UNIPA CORS geometry.

Then, some CORS belonging to UNIPA network have been randomly disconnected to simulate different schemes within the GNSMART software with different inter-distances between the stations. The experiments involved many sessions, with acquisition of 40 hours without interruptions with four hours of occupation planning during the static surveys and four different connections to the stream (VRS, FKP, Near, Far) (**Fig. 2**).

For NRTK measurements, an experimental procedure based on different projects by *Politecnico di Milano* (Benciolini et al., 2006) has been performed. Specifically:

1) the measurements have been carried out during the weekdays from 8:00 am to 6:00 pm, without a preliminary check about the geometric configuration of the satellite constellations or the existence of active connected stations within the network;

2) two separate sessions, in different time over the day, have been recorded for each point aiming to obtain independent satellite configurations;

3) for each session, four independent tests (including the start up, the connection to CORS network, the ambiguity-phase fixing, the data recording, the turning off and the relight of the instruments during the tests) for each network solution are analyzed (VRS, FKP, Near, Far);

4) rate of 1 sec;

5) cut-off angle of 10 degrees;

6) the recording of the results at the fifth epoch with fixed phase solution and ambiguity phase are fixed;

7) the reject of the solution when the ambiguity phase fixing does not occur within five minutes since the connection with the software is established (float or stand-alone solution).

4. RESULTS AND DISCUSSION

In **table 2**, all results of this work are summarized, reporting for each scheme the difference between the values of the coordinates obtained from the static survey and the solutions using the differential corrections (VRS, FKP, Near, Far). The empty spaces are due to the missing differential corrections within the fixed time span in the analysis, according with experimental procedure by *Politecnico di Milano* (five minutes since the connection with the software is established).

Table 2.
Standard deviation of the residuals for each network solution: VRS, FKP, Near, Far (mm).

| Scheme	VRS			FKP			Near			Far		
N.	ΔN	ΔE	ΔU	ΔN	ΔE	ΔU	ΔN	ΔE	ΔU	ΔN	ΔE	ΔU
1	3	2	5	5	3	7	3	3	7	33	16	35
2	6	8	12	-	-	-	5	4	17	119	54	48
3	-	-	-	6	6	15	22	7	51	-	-	-
4	3	3	7	-	-	-	3	3	6	29	21	33
5	4	3	9	7	3	6	4	3	7	-	-	-
6	5	4	7	5	6	14	4	3	6	13	10	50
7	5	3	7	6	3	9	4	2	8	13	6	16
8	4	3	7	8	4	10	3	3	6	-	-	-
9	4	3	6	6	4	8	4	3	9	-	-	-
10	-	-	-	7	10	19	-	-	-	-	-	-

The results (**Fig. 3-9**) are discussed separately as follows:

3.1 Full network with all CORS (scheme 1);

3.2 Original full network without one CORS (schemes 2-4-5-8);

3.3 Original full network without two CORS (schemes 6-9);

3.4 Original full network without three CORS (schemes 3-7-10);
3.5 Reference Point outside the network (schemes 2-3-10);
3.6 Reference Point within the network (schemes 1-4-5-6-7-8-9);
3.7 Original full network considering reduced inter-distances (schemes 1-2-3-4-6);
3.8 Original full network considering high inter-distance (schemes 5-7-8-9-10).

3.1 Full network with all CORS (scheme 1)

All CORS and all network solutions are considered in this configuration, as reported in **Fig. 3**. Results show (in red) that the standard deviation of the residuals of the coordinates is ±3 mm and ±2-3 mm for the East and North components, respectively, while it is ±5-7 mm for the Up component. This means that VRS, FKP and Near solutions provide similar results, in terms of standard deviation. The value for the last solution (Far), instead, is higher than the previous ones.
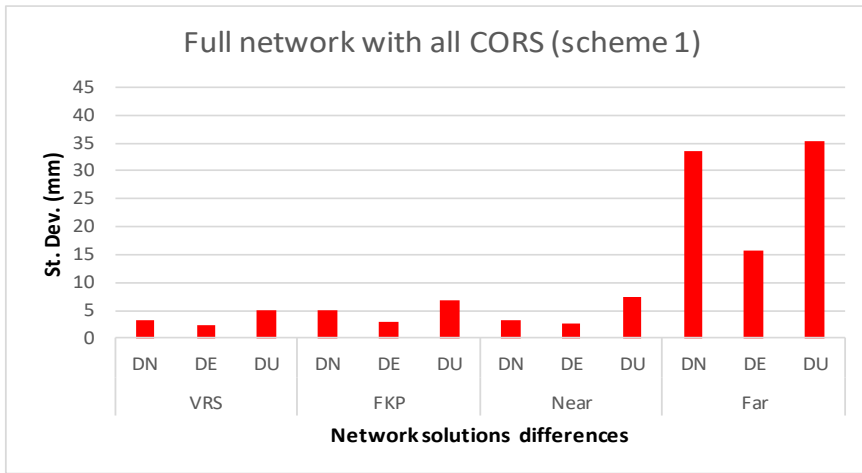
Fig. 3. Standard deviation of the residuals for each network solution: VRS, FKP, Near, Far (mm) for the full network.
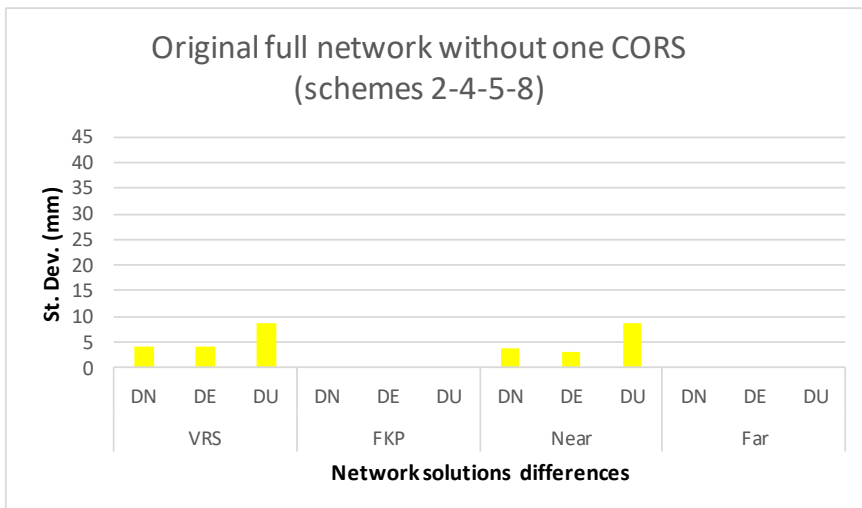

Fig. 4. Standard deviation of the residuals for each network solution: VRS, FKP, Near, Far (mm) for the original full network without one CORS.

3.2 Original full network without one CORS (schemes 2-4-5-8)

In this configuration, the FKP and the Far solutions are missing for some schemes. In particular, the FKP corrections are missing in the schemes 2 and 4, but also the results of scheme 5 are not correct due to the outliers; the Far corrections are missing for schemes 5 and 8, as reported in **Fig. 4**.
The standard deviation for VRS and Near corrections are comparable for the two solutions (in yellow); in particular for the East and North components the values are ±4 mm and ±3-4 mm, respectively, and for the Up component the value is ±9 mm. Obviously the results for the FKP and the Far solutions can not be discussed.

3.3 Original full network without two CORS (schemes 6-9)

In this configuration, in scheme 9 the Far solution was not obtained as reported in **Fig. 5**.
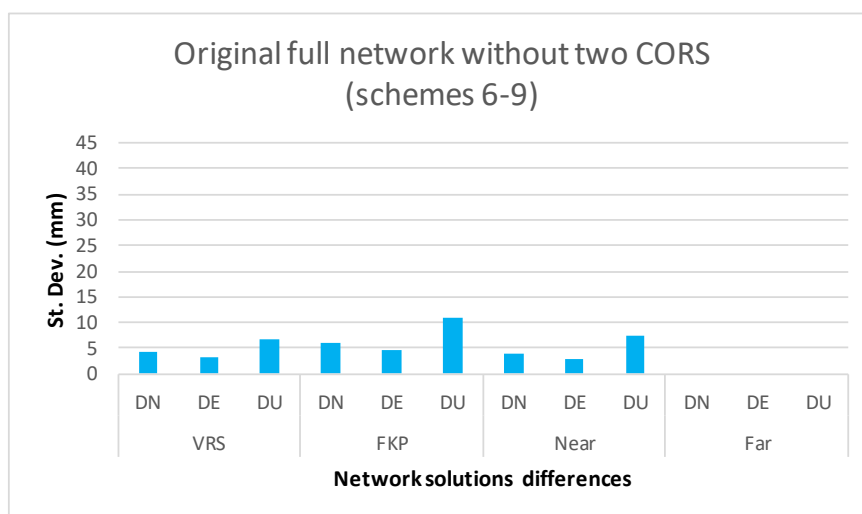
Fig. 5. Standard deviation of the residuals for each network solution:
VRS, FKP, Near, Far (mm) for the original full network without two CORS.

Results show (in light blue) that for VRS e Near solutions the average of the standard deviation is ±4 mm and ±3 mm for the East and North components, respectively, and ±7 mm for the Up component, thus the two methods are comparable. The FKP correction shows higher values of standard deviation, but with the same magnitude (±6 mm and ±5 mm for the East and North components, respectively and ±11 mm for the Up component).

3.4 Original full network without three CORS (schemes 3-7-10)

In this configuration, the VRS and the Far solutions are missing for schemes 3 and 10. While the Near corrections are missing only for schemes 10, as reported in **Fig. 6** (in black).
The limited geometric configuration influenced the results computed with GNSMART (the software needs 5 stations minimum), especially for stream corrections as VRS, Near and Far, but it

does not affect the FKP solution for which the standard deviation is ±7 mm and ±6 mm for the East and North components and ±14 mm for the Up component.
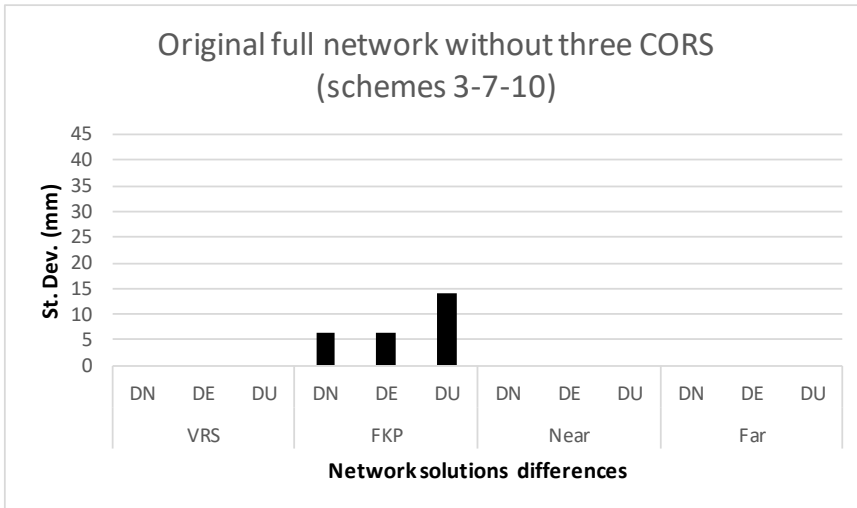
Fig. 6. Standard deviation of the residuals for each network solution:
VRS, FKP, Near, Far (mm) for the original full network without three CORS.

3.5 Reference Point outside the network (schemes 2-3-10)

In this configuration, it is not possible computing the average of the standard deviation of the residuals, because the the corrections can not be estimated due to the impossibility to reach the minimum average value, as reported in **table 3**.

Table 3.

Standard deviation of the residuals for each network solution:
VRS, FKP, Near, Far (mm) for the reference point outside the network.

Scheme	VRS			FKP			Near			Far		
N.	ΔN	ΔE	ΔU	ΔN	ΔE	ΔU	ΔN	ΔE	ΔU	ΔN	ΔE	ΔU
2	6	8	12	-	-	-	5	4	17	119	54	48
3	-	-	-	6	6	15	22	7	51	-	-	-
10	-	-	-	7	10	19	-	-	-	-	-	-

3.6 Reference Point within the network (schemes 1-4-5-6-7-8-9)

For this configuration, results are reported (in green) in **Fig. 7**.
According to VRS and Near solutions the values of the standard deviation are ±4 mm and ±3 mm

for the East and North components, ±7 mm for the Up component. As previously reported for scheme 1 the two methodologies are equivalent. Also, for the FKP solutions the values are ±6 mm and ±4 mm for the East and North components respectively and ±9 mm for the Up component, but in this case the average of the standard deviation has been computed on six solutions instead of seven. Also, in this case the scheme 5 is affected by outliers as previously reported for other configurations.
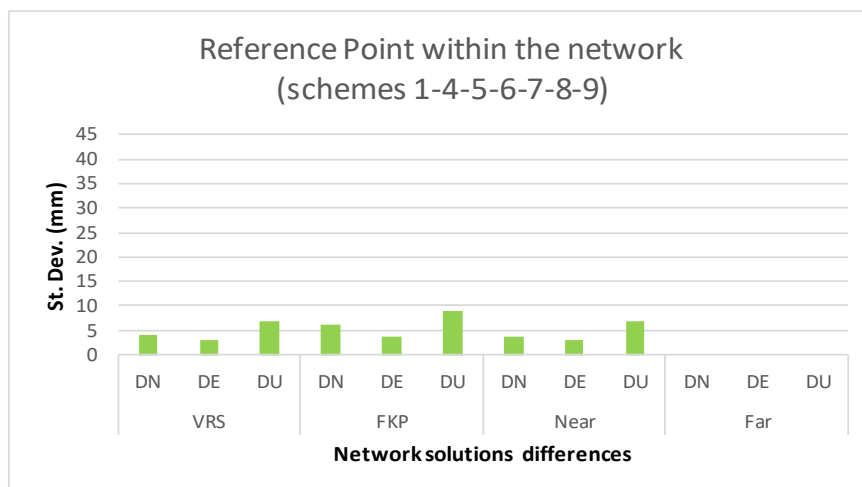
**Fig. 7.** Standard deviation of the residuals for each network solution:
VRS, FKP, Near, Far (mm) for the reference point within the network.

3.7 Original full network considering reduced inter-distances (schemes 1-2-3-4-6)

In this configuration (in orange), FKP solution are missing, meanwhile only the Near solution is completely evaluated, while the VRS and the Far corrections are computed on 4 solutions of the 5 schemes, as reported in **Fig. 8**.

In this configuration, referring to the Near solutions, the values of the standard deviation are ±7 mm and ±4 mm for the East and North components, ±17 mm for the Up component. The VRS solutions show that the standard deviation is ±4 mm for the East and North components and ±8 mm for the Up component; the magnitude for the Far solutions is higher, with ±39 mm and ±20 mm of the standard deviation for the East and North components, ±33 mm for the Up component. Anyway, the average of the standard deviation for the VRS and Far corrections are based only on four solutions.

3.8 Original full network considering high inter-distance (schemes 5-7-8-9-10)

In this configuration (in purple), only the FKP solution is correctly computed (based on all solutions), while the VRS and the Near corrections are computed on 4 solutions, as reported in the following **Fig. 9**.

Referring to the FKP solution, the values of the standard deviation are ±7 mm and ±5 mm for the East and North components, respectively, and ±10 mm for the Up component. The VRS and Near corrections, instead, show ±4 mm and ±3 mm of the residual of the standard deviation for or the East and North components, respectively, and ±7 mm for the Up component. However, also in this case for both VRS and Near corrections, the average of the standard deviation is computed on 4 solutions and the scheme 5 is affected by outliers as for the other configurations.
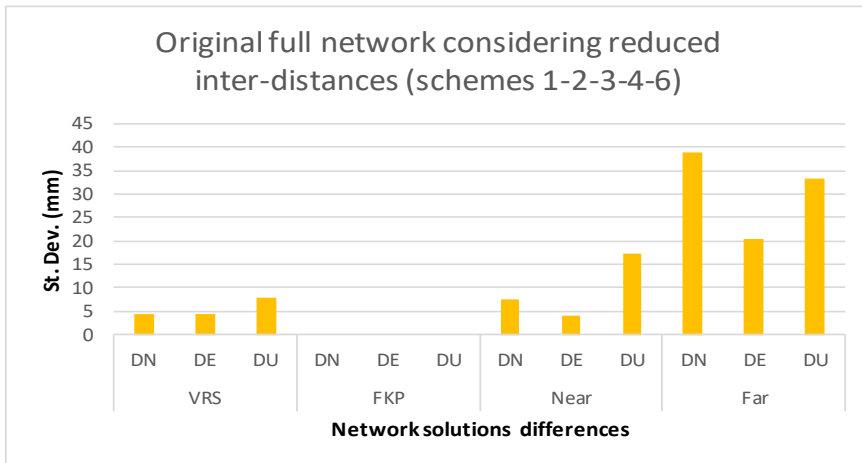
Fig. 8. Standard deviation of the residuals for each network solution:
VRS, FKP, Near, Far (mm) for reduced inter-distances within the network.
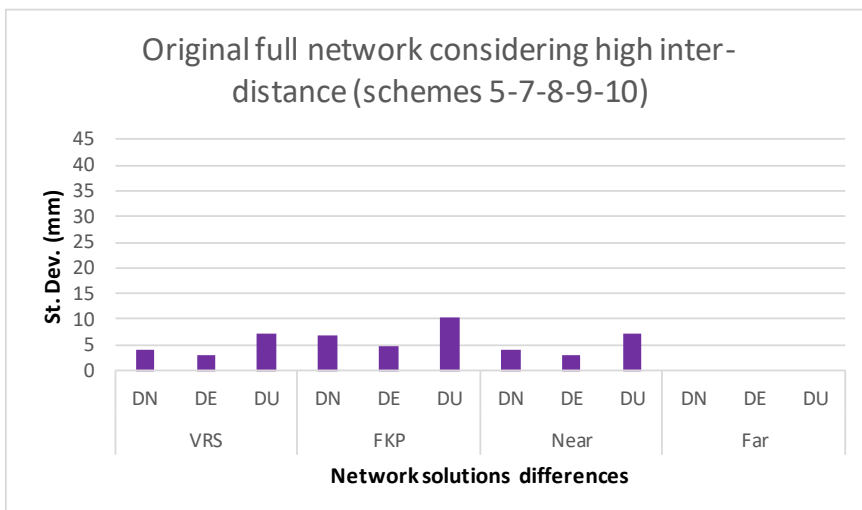
Fig. 9. Standard deviation of the residuals for each network solution:
VRS, FKP, Near, Far (mm) for high inter-distances within the network.

5. CONCLUSIONS

Preliminary results of this work highlighted the great performances of the differential corrections used for the purpose (VRS, FKP, Near and Far) in terms of precision and accuracy. The work is based on the combined use of NRTK and static surveys over 40 hours on a control point located on a pillar on the rooftop of Palermo University.

Specifically, using the full network with all CORS and different geometric configurations, the solutions obtained for VRS, FKP and Near corrections are equivalent, while the magnitude of the Far solution is one order higher.

Without one or two CORS, in the other configurations, the results for VRS, Near and FKP corrections are similar, especially in the configuration without two CORS; for the limited geometric

configuration without three CORS, only the FKP solution achieves high precisions. The latter solution is also influenced by the GNSMART software that generally works with 5 stations minimum.

When the reference point is located outside the network, none of the corrections, in the configuration, reaches the minimum number to compute the average of the standard deviation; on the contrary, when the point is located within the network the solutions are similar to those found for the full network and specifically, the results for VRS and Near corrections are comparable.

Finally, in the configuration with reduced inter-distance between the CORS, best results are associated to the differential corrections, especially for the Near solution; while in the other with high inter-distance, the FKP solution shows best results.

Anyway, this works does not aim to judge the capability of the well-known *GNSMART* software by *Geo++*, which undoubtedly is one among of the most useful GNSS processing software available, but aims to show the experimental results of this research. Future works will exploit the influence of different geometric configurations on larger networks on regional scale and the contribution of the *Galileo*/*Beidou3* configuration on the single satellite corrections.

ACKNOWLEDGMENT

R E F E R E N C E S

ACIL Allen Consulting. 2013. "The Value of Augmented GNSS in Australia.". Available online: http://www.acilallen.com.au/cms_ files/ACIL_GNSS_positioning.pdf. [Accessed Feb. 2021].

Ammoscato, A., Corsale, R., Dardanelli, G., Scianna, A., Villa, B. (2008) "GPS-GIS integrated system for electromagnetic pollution" International Archives of the Photogrammetry, Remote Sensing and Spatial Information Sciences - *ISPRS Archives*, 37, 491-497.

Angrisano, A., Dardanelli, G., Innac, A., Pisciotta, A., Pipitone, C., Gaglione, S. (2020) "Performance assessment of PPP surveys with open source software using the GNSS GPS-GLONASS-Galileo constellations". *Applied Sciences Switzerland*, 10 (16): art. no. 5420

Aponte, J., Meng, X., Hill, C., Moore, T., Dodson, A., Burbidge, M. (2009) "Quality assessment of a network-based RTK GPS service in the UK". *Journal of Applied Geodesy*, 3 (1): 25-34.

Barreca, G., Bruno, V., Dardanelli, G., Guglielmino, F., Lo Brutto, M., Mattia, M., Pipitone, C., Rossi, M. (2020) "An integrated geodetic and InSAR technique for the monitoring and detection of active faulting in southwestern Sicily". *Annals of Geophysics*, 63, art. no. EP03.

Benciolini, B., Biagi, L., Crespi, M., Manzino, A., Roggero, M. (2006) "Linee guida per la realizzazione di reti di stazioni permanenti di servizio". *Bollettino di Geodesia e Scienze Affini*, 65 (2), 90-121

Catania, P., Comparetti, A., Febo, P., Morello, G., Orlando, S., Roma, E., Vallone, M. (2020) "Positioning accuracy comparison of GNSS receivers used for mapping and guidance of agricultural machines". *Agronomy,* 10 (7): art. no. 924.

Dabove, P., Cina, A., Manzino, A.M. (2016) "How reliable is a Virtual RINEX?" Proceedings of the IEEE/ION Position, Location and Navigation Symposium, PLANS 2016, art. no. 7479709, 255-262.

Dardanelli, G., Carella, M. (2013) "INTEGRATED SURVEYNG WITH MOBILE MAPPING SYSTEM, EGNOS, NTRK AND LASER TECHNOLOGIES IN THE PARK "NINNI CASSARA IN PALERMO". *ISPRS Annals of the Photogrammetry, Remote Sensing and Spatial Information Sciences*, 2 2W1., 95-100.

Dardanelli, G., La Loggia, G., Perfetti, N., Capodici, F., Puccio, L., Maltese, A. (2014) "Monitoring displacements of an earthen dam using GNSS and remote sensing". *Proceedings of SPIE* - The International Society for Optical Engineering, 9239, art. no. 923928.

Dardanelli, G., Lo Brutto, M., Pipitone, C. (2020) "GNSS cors network of the University of Palermo: Design and first analysis of data". *Geographia Technica*, 15 (1): 43-69.

Dardanelli, G., Marretta, R., Santamaria, A.S.; Streva, A.; Lo Brutto, M., Maltese, A. (2017) "Analysis of technical criticalities for GIS modelling an Urban noise map". *Geographia Technica*, 12 (2): 41-61.

Dardanelli, G., Paliaga, S., Allegra, M., Carella, M., Giammarresi, V. (2015) "Geomatic applications tourban park in Palermo". *Geographia Technica*, 10 (1): 28-43.

Dardanelli, G., Pipitone, C. (2017) "Hydraulic models and finite elements for monitoring of an earth dam, by using GNSS techniques". *Periodica Polytechnica Civil Engineering*, 61 (3): 421-433.

Dawidowicz, K., Krzan, G., Świątek, K. (2015) "Relative GPS/GLONASS coordinates determination in urban areas-accuracy analysis". In 15th edition of SGEM GeoConferences, Bulgaria, Albena Resort, Vol. 2, 423-430.

Ebolese, D., Lo Brutto, M., Dardanelli, G. (2019) "Uav survey for the archaeological map of lilybaeum Marsala, Italy". *ISPRS Annals of the Photogrammetry, Remote Sensing and Spatial Information Sciences*, 42 2/W11., 495-502.

Fazio, L., Lo Brutto, M., Dardanelli, G. (2019) "Survey and virtual reconstruction of ancient roman floors in an archaeological context". *ISPRS Annals of the Photogrammetry, Remote Sensing and Spatial Information Sciences*, 42 2/W11., 511-518.

Feng, Y., Rizos, C. (2009) "Network-based geometry-free three carrier ambiguity resolution and phase bias calibration". *GPS Solutions*, 13 (1): 43-56.

Fortes, L.P., Cannon, M.E., Lachapelle, G., Skone, S. (2003) "Optimizing a network-based RTK method for OTF positioning". *GPS Solutions*, 7 (2): 61-73.

Garrido, M., Giménez, E., Armenteros, J., Lacy, M.,, Gil, A. (2012) "Evaluation of NRTK positioning using the RENEP and rap networks on the southern border region of Portugal and Spain". *Acta Geodaetica et Geophysica Hungarica*, 47 (1): 52-65.

Gordini, C., Kealy, A.N., Grgich, P.M., Hale, M.J. (2006) "A performance analysis of sparse GNSS CORS network for real time centimetric level positioning: A case study in Victoria, Australia ". Proceedings of the Institute of Navigation - 19th International Technical Meeting of the Satellite Division, ION GNSS 2006, 2, 1196-1207.

Grejner-Brzezinska, D.A., Arslan, N., Wielgosz, P., Hong, C.-K. (2009) "Network calibration for unfavorable reference-rover geometry in network-based RTK: Ohio cors case Study". *Journal of Surveying Engineering*, 135-3, 90-100.

Grejner-Brzezinska, D.A., Kashani, I., Wielgosz, P. (2005) "On accuracy and reliability of instantaneous network RTK as a function of network geometry, station separation, and data processing strategy". *GPS Solutions*, 9 (3): 212-225.

Grejner-Brzezinska, D.A., Kashani, I., Wielgosz, P., Smith, D.A., Spencer, P.S.J., Robertson, D.S., Mader, G.L. (2011) "Efficiency and reliability of ambiguity resolution in network-based real-time kinematic GPS CORS and OPUS for Engineers: Tools for Surveying and Mapping Applications", 133-142.

Hausler, G., Collier, P. (2013) "National Positioning Infrastructure: identifying and evaluating high accuracy GNSS service coverage across Australia". *Journal of Spatial Science*, 58 (2): 191-214.

Hope, S., Gordini, C., Kealy, A. (2008) "Positional accuracy improvement: Lessons learned from regional Victoria, Australia". *Survey Review*, 40 (307): 29-42.

Inal, C., Kocak, O., Esen, O., Bulbul, S.; Kizgut, R. (2017) "Surveying and mapping using mobile phone in archaeological settlements". *Geographia Technica*, 12 (2): 82-96.

Keenan, C.R.; Zebhauser, B.E.; Euler, H.-J.; Wübbena, G. Using the Information from Reference Station Networks: A Novel Approach Conforming to RTCM V2.3 and Future V3.0.; 2002; pp. 320–327.

Kenyeres, A., Bellet, J.G., Bruyninx, C., Caporali, A., De Doncker F., Droscak, B., Duret, A., Franke, P., Georgiev, I., Bingley, R., Huisman, L., Jivall, L., Khoda, O., Kollo, K., Kurt, A.I., Lahtinen, S., Legrand, J., Magyar, B., Mesmaker, D., Morozova, K., Nágl, J., Özdemir, S., Papanikolaou, X., Parseliunas, E., Stangl, G., Ryczywolski, M., Tangen, O.B., Valdes, M., Zurutuza, J., Weber, M. (2019) "Regional integration of long-term national dense GNSS network solutions". *GPS Solutions*, 23 (4): art. no. 122.

Kim, J.; Song, J.; No, H.; Han, D.; Kim, D.; Park, B.; Kee, C. (2017) Accuracy Improvement of DGPS for Low-Cost Single-Frequency Receiver Using Modified Flächen Korrektur Parameter Correction. *ISPRS International Journal of Geo-Information*, 2017, 6

Pepe, M. (2018) Cors architecture and evaluation of positioning by low-cost gnss receiver. *Geodesy and Cartography*, 44 (2), pp. 36-44.

Pipitone, C., Maltese, A., Dardanelli, G., Lo Brutto, M., Loggia, G.L. (2018) "Monitoring water surface and level of a reservoir using different remote sensing approaches and comparison with dam displacements evaluated via GNSS". *Remote Sensing*, 10 (1): art. no. 71.

Prochniewicz, D., Szpunar, R., Kozuchowska, J., Szabo, V., Staniszewska, D., Walo, J. (2020) "Performance of Network-Based GNSS Positioning Services in Poland: A Case Study". *Journal of Surveying Engineering*, 146 (3): art. no. 05020006,

Pugliano, G., Lachapelle, G. (2005) La collocazione nel posizionamento GPS network RTK [The least-squares collocation method applied to the network RTK GPS positioning] *Bollettino di Geodesia e Scienze Affini*, 64 (2): 93-106.

Rizos, C., Satirapod, C. (2011) Contribution of GNSS CORS infrastructure to the mission of modern geodesy and status of GNSS CORS in Thailand. *Engineering Journal,* 15 (1), pp. 25-42.

Stocchi, P., Antonioli, F., Montagna, P., Pepe, F., Lo Presti, V., Caruso, A., Corradino, M., Dardanelli, G., Renda, P., Frank, N., Douville, E., Thil, F., de Boer, B., Ruggieri, R., Sciortino, R., Pierre, C. (2017) "A stalactite record of four relative sea-level highstands during the Middle Pleistocene Transition". *Quaternary Science Reviews*, 173, 92-100.

Uradziński, M., Bakuła, M. (2020) "Assessment of Static Positioning Accuracy Using Low-Cost Smartphone GPS Devices for Geodetic Survey Points' Determination and Monitoring". *Applied Sciences Switzerland*, 10, 5308.

Wielgosz, P., Grejner-Brzezinska, D., Kashani, I. (2005) "High-accuracy DGPS and precise point positioning based on Ohio CORS network Navigation", *Journal of the Institute of Navigation*, 52 (1): 23-28.

Wübbena, G., Schmitz, M., Bagge, A. (2005) "PPP-RTK: Precise Point Positioning using state-space representation in RTK networks". Proceedings of the 18th International Technical Meeting of the Satellite Division of The Institute of Navigation, ION GNSS 2005, 2005, 2584-2594

Wanninger, L. (2003) Virtual Reference Stations (VRS). *GPS Solutions* 2003, 7, 143–144

Zhang, B., Teunissen, P.J.G., Odijk, D. (2011). "A novel un-differenced PPP-RTK concept." *Journal of Navigation*, 64 SUPPL. 1., S180-S191.

SPATIOTEMPORAL ANALYSIS OF VEGETATION DROUGHT VARIABILITY IN THE MIDDLE OF THE NORTHEAST REGION OF THAILAND USING TERRA/MODIS SATELLITE DATA

Nanthawat JOMSREKRAYOM [1], Pattanapol MEENA [2] , Teerawong LAOSUWAN [3] *

ABSTRACT:
Drought is one of Thailand's most common catastrophes and causes a considerable amount of damage, especially to farming, in the northeast of the country. The objective of this study is to analyze vegetation drought variability from a vegetation phenology perspective using the vegetation condition index (VCI) from Terra/MODIS satellite data in the middle of the northeast region of Thailand .The MOD09A1 dataset from Terra/MODIS satellites was analyzed using the normalized difference vegetation index (NDVI), and the results were analyzed with the VCI to examine vegetation drought variability in July, August, and September 2009–2019. The study found that in August 2013, the drought was most severe and accounted for 47.71% coverage (22,456.76 km^2), and in September 2013, the drought was the least severe at 55.55% coverage (17,456.42 km^2) Moreover, using simple linear regression analysis, the VCI results for each month of the 11-year period were used to find the statistical correlation with rainfall data from ground monitoring stations. It found that July, August, and September showed a coefficient of determination (r^2)equal to 0.835, 0.834, and 0.849, respectively. The r^2 value showed that this method was reliable. Furthermore, the analyzed VCI averages can be used as a very good indicator of drought in the middle of the northeast region of Thailand.

***Key-words*:** *Remote sensing, Vegetation drought variability, NDVI, VCI*

1. INTRODUCTION

Drought is a natural disaster that occurs in many areas and is a devastating and detrimental problem for national development . Areas that experience drought often also experience water shortages for consumption and agriculture. Thai farming relies mainly on natural rainwater, and when there is insufficient water, the crop yield decreases, which, in turn, causes a shortage of agricultural and process products for domestic consumption and exports (Laosuwan et al., 2016). Drought has a direct impact on the economy and an indirect impact on society and culture, which has resulted in the abandonment of agriculture and people migrating to work in the city when normal farming is not possible.Additionally, extremely dry conditions can also cause forest fires, which is another environmental problem (Uttaruk & Laosuwan, 2017). The development of drought is a gradual process, the severity of which is constantly increasing. This makes the process difficult to understand. Drought conditions are generally estimated by decreasing rainfall, resulting in water shortages for some activities (Malo & Nicholson, 1990). To accurately determine drought is challenging because it is a natural disaster that progresses slowly. Drought has different intensities due to rainfall imbalances in a particular area, which makes it difficult to make comparisons at any one time, as one area may be drier than another (Rotjanakusol & Laosuwan, 2018). Nevertheless, weather data, especially rainfall data, can be considered the most widely used primary information for drought tracking . However, there are relatively few weather station networks in the northeastern region of Thailand; therefore, weather data is often incomplete, and the weather data logging model is not usually readily

[1,2,3] *Department of Physics, Faculty of Science, Mahasarakham University, Maha Sarakham, 44150, Thailand* *bomnantawat1995@gmail.com, pattanapol.m@msu.ac.th,* **Corresponding author teerawong@msu.ac.th*

available for immediate analysis; thus, monitoring drought and assessing the influence of weather conditions on farmland is sometimes unreliable (Gebrehiwot et al., 2011; Lines et al., 2017).

The application of satellite-based remote sensing technology to monitor periods of unusually dry conditions is another method quickly detect droughts because satellite data is re-recorded continuously, so it can be used to monitor the area in near real-time over different periods (Kogan, 1997; Gu et al., 2007; Zhang et al., 2013; Rotjanakusol & Laosuwan, 2019a; Rotjanakusol & Laosuwan, 2019b). To use satellite data to estimate drought, derivative data from earth-observing satellites are often analyzed as they can reflect the drought conditions of the area. This is because the different biological characteristics of vegetation cover are related to the spatial and temporal patterns of drought as the plants respond to dehydration, such as withering and leaf drop; this occurs because Thailand is in a region with distinct wet and dry seasons (Uttaruk & Laosuwan, 2019).

Although satellite data suggest that changes in vegetation in arid regions appear to have different reflectance values, studies have found that the data may need to be adjusted so that it is fit for the research purpose or enhanced to make the topic of study clearer, which is referred to as indexing (Tucker, 1979). As drought is such a complex phenomenon, it is difficult to use just one index to cover studies in terms of quantity, density, and severity as well as the possibility of their impact on each group (Fensham & Holman, 1999). Therefore, a drought study with remote sensing technology has applied wave indices related to the physical conditions of vegetation, plant water content, and soil water content to examine and study drought with multiple indices, such as the NDVI (Tarpley et al., 1984), the soil-adjusted vegetation index (SAVI; Huete, 1988), the vegetation condition index (VCI; Kogan, 1995), the normalized difference water index (NDWI; Gao, 1996), the enhanced vegetation index **(**EVI; Huete et al., 2002), and the standardized vegetation index (SVI; Peters et al., 2002). For this reason, the objective of this study is to analyze vegetation drought variability from a vegetation phenology perspective using vegetation condition index - VCI from Terra/MODIS satellite data in the middle of the northeast region in July, August, and September 2009–2019.

2. MATERIALS AND METHODS

The middle of the northeast region of Thailand (**Fig. 1**) is located between latitude 17–25° N and longitude 101–103° E, covering the provinces of Kalasin, Khon Kaen, Maha Sarakham, and Roi Et.
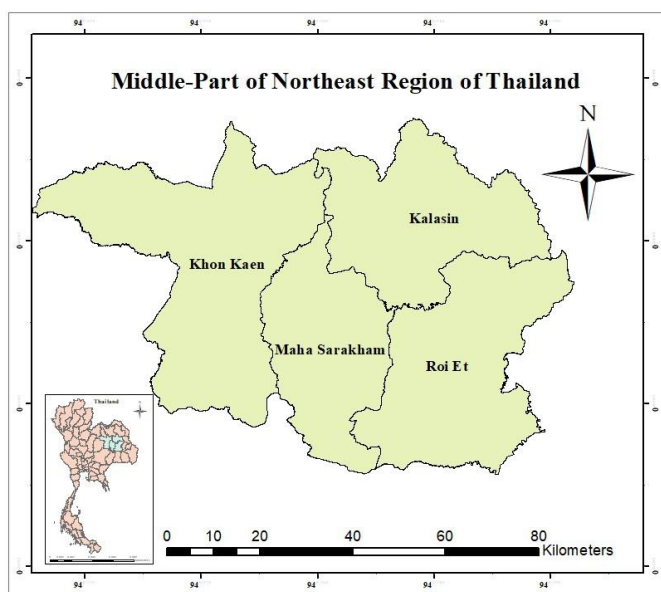
Fig.**1.** Study area.

The total area of the provincial clusters is 31,423.87 km^2, accounting for 6.18% of the total country area and 18.61% of the northeastern region. Agricultural areas equal 21,736.708 km^2 or 69.17% of the province's area; Khon Kaen is the largest area, followed by Roi Et Province, Kalasin Province, and Maha Sarakham Province, respectively. The overall topography is lowland and is approximately 200 meters above sea level. Climate characteristics are classified as rain alternating with drought. The average maximum temperature is 36.35 °C, and there are three seasons: summer, rainy, and winter.

2.1. Terra/MODIS data

Terra/MODIS is designed to track and monitor natural resources. It is approximately 2,330 km wide with a spatial resolution ranging from 250 to 1000 m and 36 wavelength data logging, which covers the entire globe in two days. Therefore, data from Terra/MODIS satellites are ideal for tracking spatial changes. In this operation, the MOD09A1 product suite was used to collect data from satellites between July and September 2009–2019 at h27v07 and h28v07. In this study, Mosaic Image was used to concatenate the two datasets to cover the entire study area. Then, the geometric correction was adjusted using the WGS84-UTM zone 47 N reference coordinate system by evaluating the pixels using the nearest neighbor method.

2.2. Rainfall data

This study was based on the average monthly rainfall data from July to September 2009–2019 from the Thailand Meteorological Department's terrestrial rainfall monitoring station.

2.3. Procedures for analysis

Multi-period data from Terra/MODIS satellites was applied to the VCI to examine the vegetative drought in the middle of the northeast region of Thailand.

2.3.1. NDVI analysis

The VCI uses a value to indicate the proportion of vegetation covering the earth's surface and can be calculated by the proportion of related wavelengths of vegetation to each other. A popular method is the NDVI (Prohmdirek et al., 2020), which is a surface reflectance measure that provides quantitative estimates of plant growth and biomass (Jingyong et al., 2003; Pettorelli et al., 2005). The difference in surface reflection between the near-infrared (NIR) wavelength and red wavelength is proportional to the sum of the two wavelengths to adjust the normal distribution characteristics can be adjusted. This results in an NDVI between –1 and +1, which will help translate the results more easily. A value of 0 means that there are no green leafy plants in the survey area, while a value of 0.8 or 0.9 suggests very dense green vegetation in the area.

In the case of vegetation-covered surfaces, the reflectance in the NIR wavelength is higher than the red wavelength, making the NDVI positive, while the terrestrial surface has a similar reflection between the two wavelengths, so the NDVI value is close to 0. If the water surface has a reflection in the NIR wavelength below the red wavelength, the NDVI is negative. Usually, this value only ranges from 0.1 to 0.7. Equation 1 calculates the vegetation values for NDVI (Peters et al., 2002):

$$\text{NDVI} = \frac{\text{NIR-RED}}{\text{NIR+RED}} \tag{1}$$

where
NIR = reflection in the NIR wavelength of the spectrum
RED = reflection in the red wavelength of the spectrum
2.3.2. VCI analysis

The VCI is an index derived from remote sensing data. It compares the current NDVI with a range of values observed for the same period in the previous year. Droughts mostly affect the agricultural sector; therefore, plant growth and conditions are affected. VCI is an alternative to looking at vegetation conditions and characterizing agricultural drought. The principle of the VCI is a standard range analysis that determines the state of the NDVI at the current time of interest where it is positioned in the lowest and highest NDVI ranges for a particular area. The equation and table showing the plant values of VCI are shown in Equation 2 and **Table 1** (Kogan, 1995; Quiring et al., 2010):

$$VCI = \frac{NDVI - NDVI_{min}}{NDVI_{max} - NDVI_{min}} \times 100 \tag{2}$$

where
$NDVI_{max}$ = maximum NDVI at the study time of each pixel
$NDVI_{min}$ = minimum NDVI at the study time of each pixel

Table. 1.
VCI drought levels.

Level	VCI
00.00–20.00	very high drought
21.00–40.00	high drought
41.00–60.00	moderate drought
61.00–80.00	low drought
81.00–100.00	very low drought

2.4. Statistical correlation analysis

In this study, VCI results and average monthly rainfall data for July to September 2009–2019 were taken from the ground rain measurement station of the Thai Meteorological Department to find statistical relationships in the form of linear regression analysis.

$$y = ax + b \tag{3}$$

where
x = independent variable
y = dependent variable

3. RESULTS AND DISCUSSION

3.1. NDVI analysis results

The monthly NDVI analysis in July showed an average of 0.47, with the lowest of 0.42 in 2019, and the highest of 0.53 in 2018. In August, the mean was 0.54, with the lowest of 0.44 in 2013, and the highest of 0.60 in 2014; in September, the mean was 0.63, with the lowest of 0.43 in 2011, and the highest of 0.70 in 2016. The results of the NDVI analysis that were mean for the three months across 11 years is shown in **Fig. 2**, with the curves showing the variance of NDVI for each year; the lowest value of 0.47 occurred in 2011, the highest value of 0.60 occurred in 2016, and the 11-year average was 0.55 (**Fig. 3**).
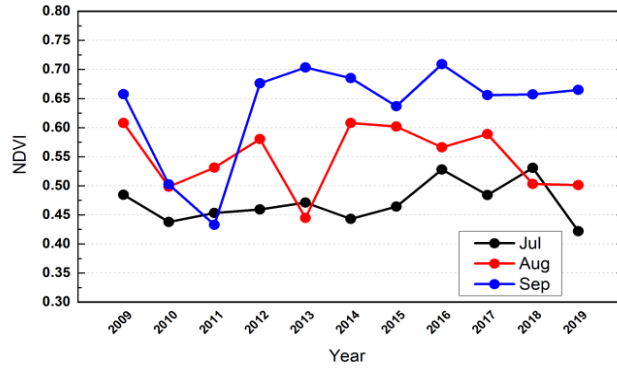
Fig. **2.** NDVI analysis results.
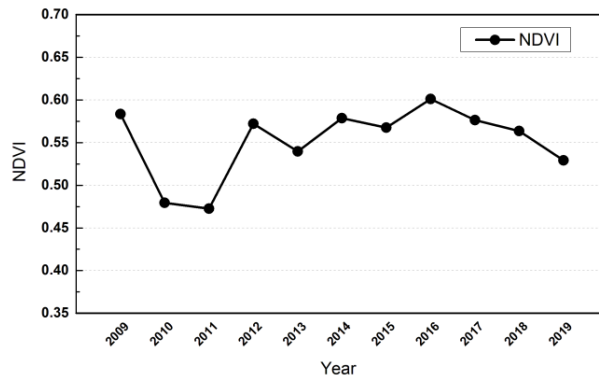
Fig. **3.** NDVI analysis average over three months.

3.2. VCI analysis results

Three months of different VCI analyses in July showed different plant conditions in the 0–100 range, which were theoretical values, with the average indicating vegetation conditions or drought for each year. The average was 53.99 the lowest was 38.46 in 2019, and the highest was 70.31 in 2016.

The August VCI results showed different plant conditions in the 0–100 range, with the mean value of 60.41 the lowest value of 42.56 in 2013, and the maximum value of 77.01 in 2014. The results of the September VCI calculation showed different plant conditions in the 0–100 range, with the average being 67.50 the lowest was 30.59 in 2011, and the highest was 78.83 in 2013.
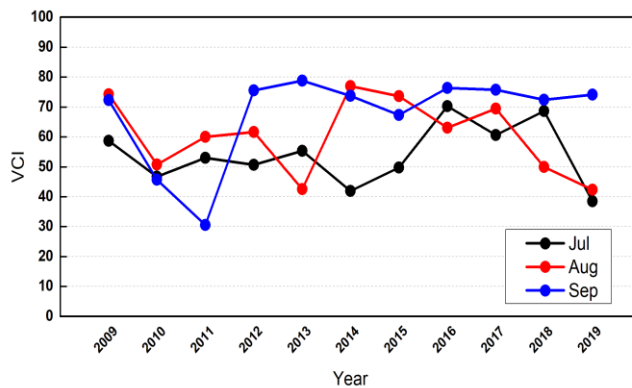
Fig. **4.** VCI analysis results.

The average VCI analysis for all three months throughout the 11 years is shown in **Fig. 4** the curve shows the VCI variance for each year with the lowest in 2010 at 47.70 the highest in 2009 at 68.41 and the 11-year average was 60.63 (**Fig. 5**)
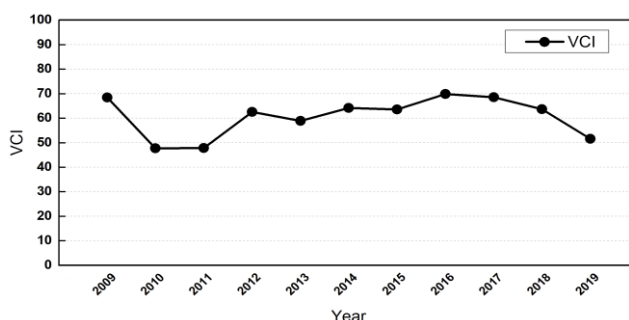
Fig. **5.** NDVI analysis average over three months.

3.3. VCI drought classification results

VCI analysis can be inferred from the maximum, minimum, mean, and standard deviation of VCI for July, August, and September (2009–2019), with each period revealing different plant conditions. The results of the VCI analysis determined the condition of plants or annual droughts. VCI drought classification for each three-month period over the 11 years is shown in **Figs. 6a**, **b**, and **c**.

Fig. 6a shows that the drought was most severe in 2019, accounting for 70.82% of the area or 22,250.31 km^2 (the very high level of drought was 12.61% or 3,961.18 km^2, high-level drought was 29.51% or 36,9,271 km^2, moderate-level drought was 28.70% or 77,9,017 km$^{2.}$).
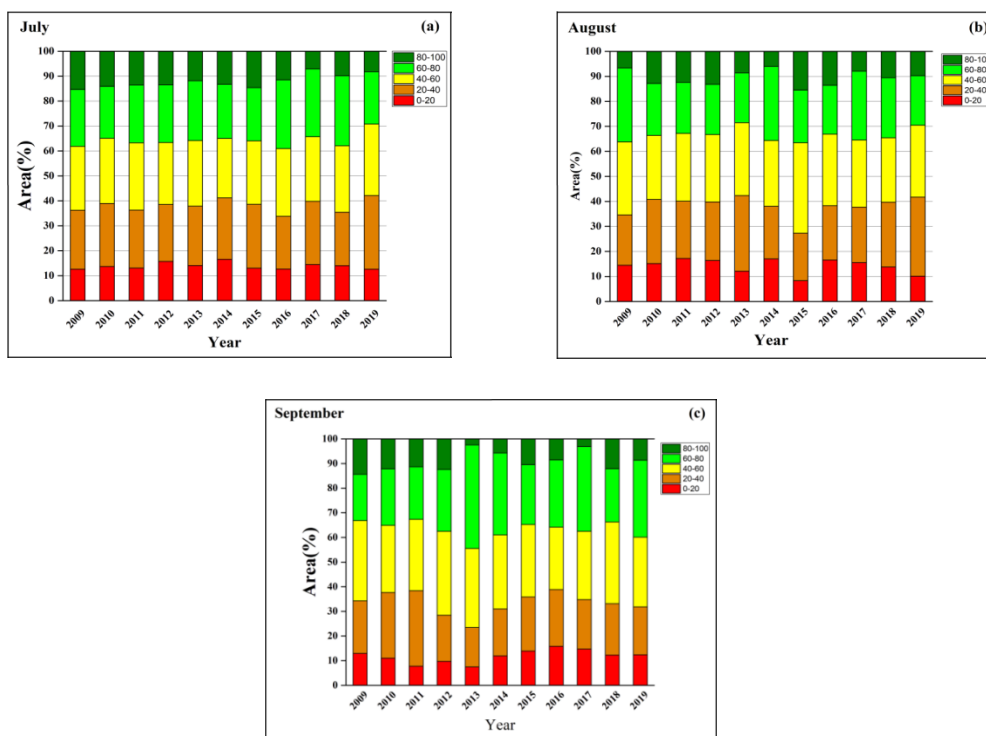
Fig. **6a, b, and c:** Three-month VCI drought classification.

In 2016, the drought covered a minimum of 60.93% of the area or 19,147.29 km^2 (very high-level drought covered 12.66% or 3,978.47 km^2, high-level drought covered 21.16% or 42.6,649 km^2, moderate drought covered 27.11% or 40.8,519 km^2).

Fig. 6b displays the August VCI drought classification results, which were classified by the VCI level each year. The results show that in 2013, the drought was most severe, accounting for 71.47% of the area or 22,456.76 km^2 (very high-level drought was 12.11% or 3,805.64 km^2, high-level drought was 30.21% or 9,493.20 km^2, moderate drought levels were 29.14% or 9,157.92 km^2).In 2015, the least drought covered 63.45% of the area or 19,938.21 km^2 (very high-level drought covered 8.29% of the area or 2,603.40 km^2, high-level drought covered 19.03% or 5,980.74 km^2, moderate drought covered 36.13% or 11,354.07 km^2).

Fig. 6c shows the September VCI drought classification results with the most drought in 2011, accounting for 67.33% of the area or 21,157.42 km^2 (very high-level drought covered 7.73% or 2,430.25 km^2, high-level drought covered 30.68% or 9,641.20 km^2, moderate drought covered 28.92% or 9,085.96 km$^{2.}$) . In 2013, drought covered a minimum of 55.55% of the area or 17,456.42 km^2 (very high-levels drought covered 7.47% or 2,347.30 km^2, high-level drought covered 15.96 % or 5,015.74 km^2, moderate drought covered 32.12% or 10,093.38 km^2).

To get a clearer picture of the drought, we analyzed drought levels and classified them spatially with the VCI for July, August, and September for the entire 11 years. The results of this spatial VCI analysis are shown in **Figs. 7, 8,** and **9**.
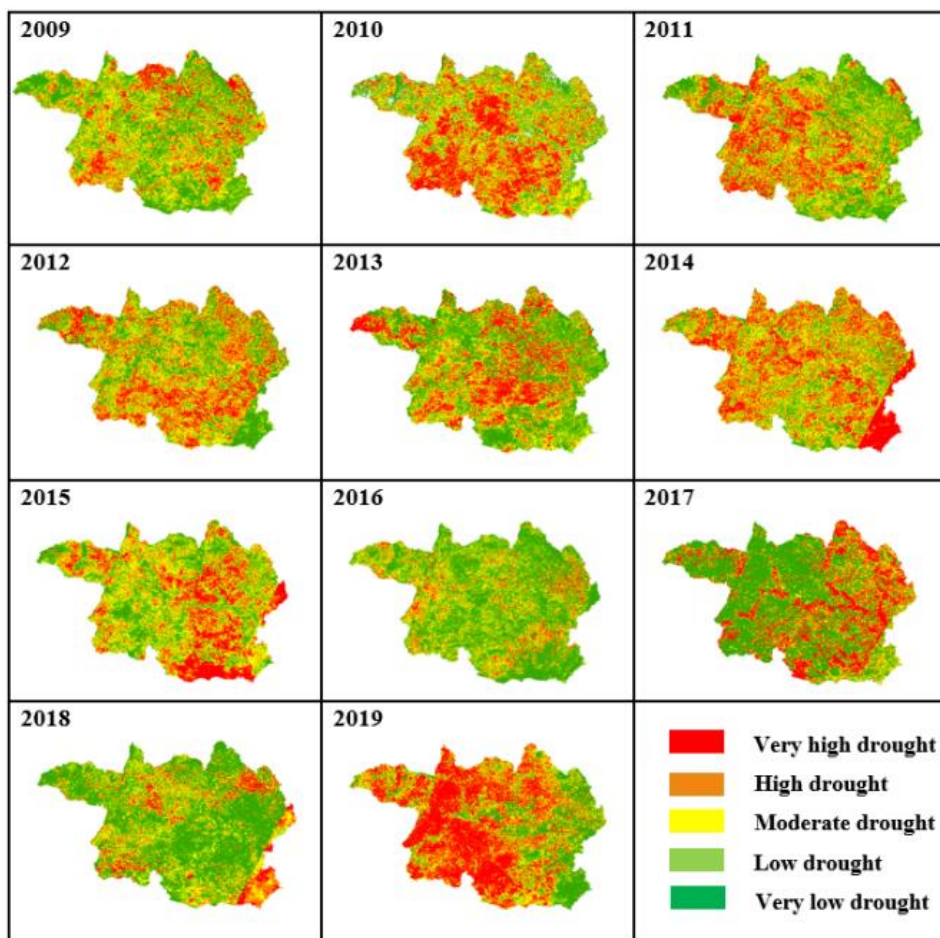
Fig. **7.** Spatial analysis of VCI in July.
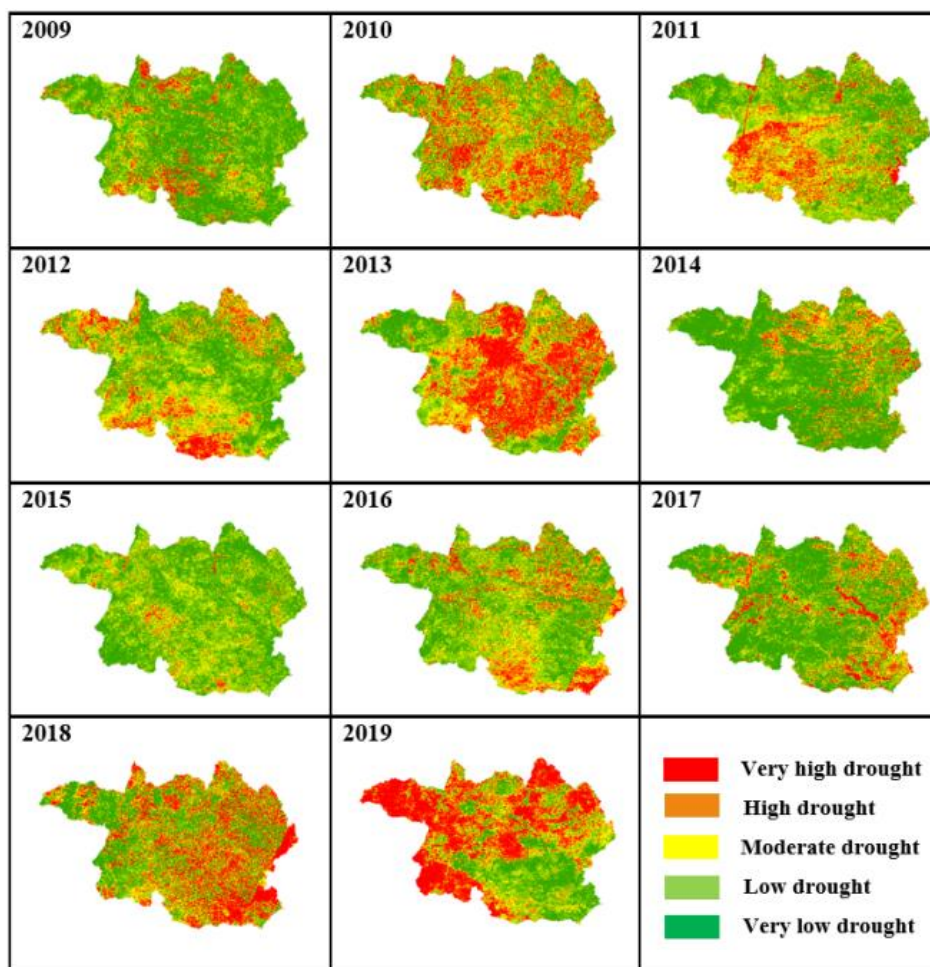
Fig. **8.** Spatial analysis of VCI in August.

Figs. 7 to 9 show five drought levels that were classified according to the VCI criteria. These five levels of drought are consistent with **Fig. 4** in terms of the maximum drought and minimum drought in each month of the year. In **Figs .7 to 9**, the yellow, orange, and red areas indicate those that experience much drought. The light and dark green areas indicate those with less drought.

3.4. Statistical correlation results

A statistical correlation analysis was performed using linear regression analysis from the monthly mean of the VCI for the three months of the 11 years studied. Results showed that the VCI and rainfall from ground monitoring stations were related, and this is demonstrated in **Figs. 8 to 10** . In **Figs .10 to 12**, there was a high statistical correlation, and the decision coefficients for all three months in the 11 years were $R^2 = 0.835$, $R^2 = 0.834$, and $R^2 = 0.849$, respectively.
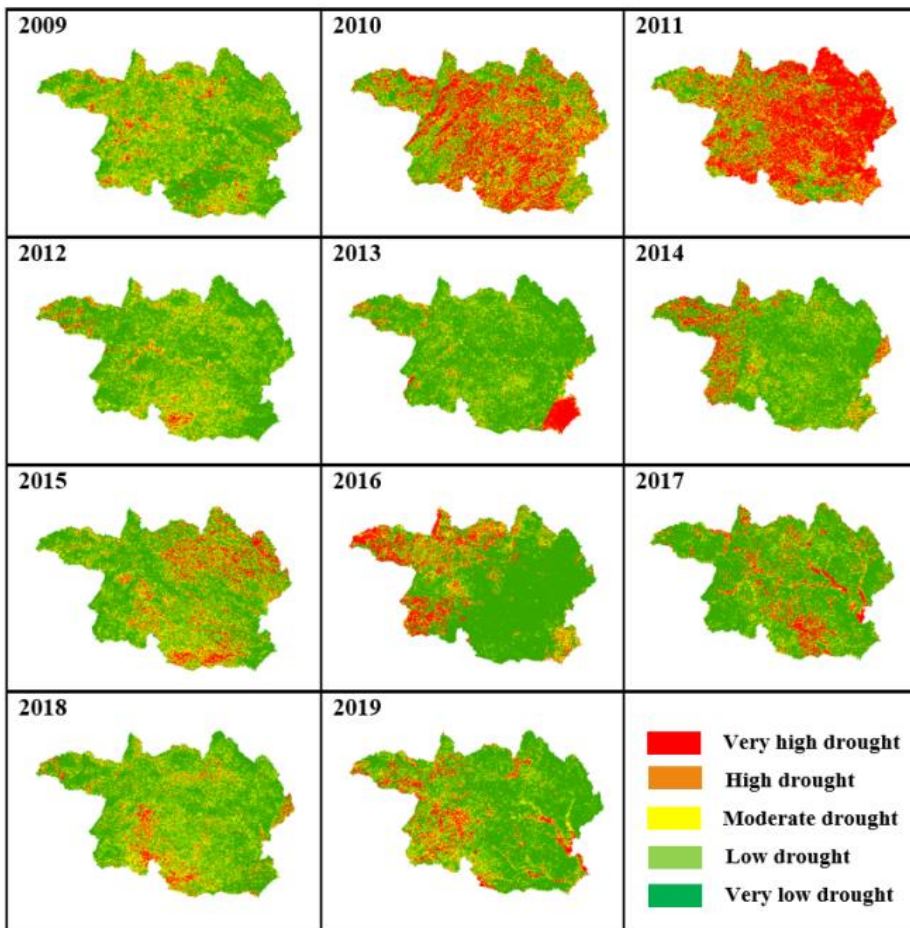
Fig. **9.** Spatial analysis of VCI in September.
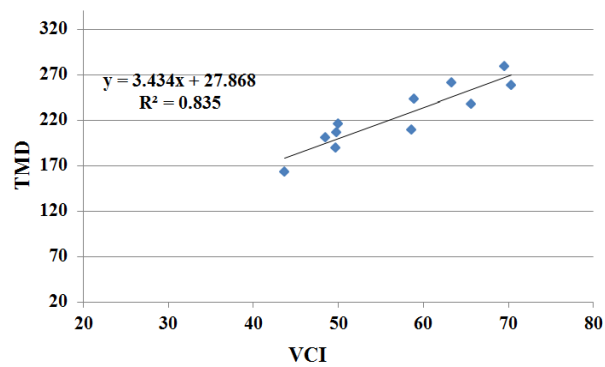
Fig. **10.** Relationship between the VCI and rainfall statistics in July.
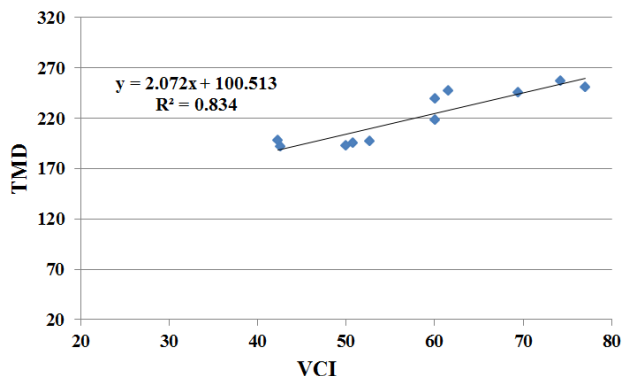
Fig. **11.** Relationship between the VCI and rainfall statistics in August.
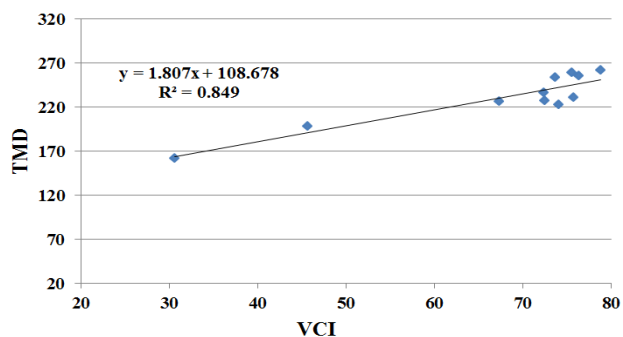
Fig. **12.** Relationship between the VCI and rainfall statistics in September.

4. CONCLUSIONS

During the past decade, the most severe natural disasters in Thailand have been drought caused by less rainfall than usual or longer seasonal rain that covers a wide area .On the one hand, analyzing the VCI in this study demonstrated that the closer the VCI is to 0, the greater the area lacks moisture, and drought is very severe .On the other hand, if the VCI was closer to 100, the area had plenty of moisture, and there was less drought. Furthermore, when there was a high level of rainfall, the VCI was high, but if the rainfall level was low, the VCI was also low. Changes in VCI may be slightly slower than rainfall because vegetation grows and produces green leaves after sufficient water. Additionally, the results of this study aligned with those of three similar studies by Jiao et al. (2016) , Zambrano et al. (2016), and Rousta et al. (2020). The methods and results of this study should serve as criteria for a rational examination of vegetative drought in the northeastern region of Thailand. It is also possible to perform a quick and reliable inspection and assessment of the drought area. Both governmental and non-governmental agencies can apply the methods of this study to analyze expected drought areas and use the results to formulate sustainable drought prevention and mitigation plans in other areas of Thailand.

ACKNOWLEDGMENTS

REFERENCES

Fensham, R., & Holman, J. (1999). Temporal and spatial patterns in drought-related tree dieback in Australian savanna. *Journal of Applied Ecology*, 36(6), 1035-1050.

Furtuna, P. & Holobaca, I. (2013). Forest fires study using remote sensing and meteorological indicators. Case study. *Geographia Technica*, 8(2), 23-37.

Gao, B.C. (1996). NDWI - A normalized difference water index for remote sensing of vegetation liquid water from space. *Remote Sensing of Environment,* 58, 257-266.

Gebrehiwot, T., Veen, A. V., & Maathuis, B. (2011). Spatial and temporal assessment of drought in the Northern highlands of Ethiopia. *International Journal of Applied Earth Observation and Geoinformation*, 13(3), 309-321.

Gu, Y., Brown, J.F., Verdin, J. P. & Wardlow, B. (2007). A five-year analysis of MODIS NDVI and NDWI for grassland drought assessment over the central Great Plains of the United States. *Geophysical Research Letters*, 34(6), 1-6

Huete, A.R. (1988). A Soil-adjusted Vegetation Index (SAVI). *Remote Sensing of Environment*, 25(3), 295–309.

Huete, A., Didan, K., Miura, T., Rodriguez, E.P., Gao, X., & Ferreira, L.G. (2002). Overview of the radiometric and biophysical performance of the MODIS vegetation indices. *Remote Sensing of Environment*, 83(1), 195–213.

Jiao, W., Zhang, L., Chang, Q., Fu, D., Cen, Y., & Tong, Q. (2016). Evaluating an enhanced vegetation condition index (VCI) based on VIUPD for drought monitoring in the continental United States. *Remote Sensing*, 8(3), 224.

Jingyong, Z., Wenjie, D.,Congbin, F.,Lingyun, W. (2003). The influence of vegetation cover on summer precipitation in China: A statistical analysis of NDVI and climate data. *Adv. Atmos. Sci*., 20, 1002–1006.

Kogan, F.N. (1995). Application of Vegetation Index and Brightness Temperature for Drought Detection. *Advances in Space Research*, 15(11), 91–100.

Kogan, F.N.(1997). Global drought watch from space .Bulletin of the American Meteorological Society, 78, 621–636 .

Laosuwan, T., Sangpradid, S., Gomasathit, T., & Rotjanakusol, T. (2016). Application of Remote Sensing Technology for Drought Monitoring in Mahasarakham Province, Thailand. *International Journal of Geoinformatics*, 12(3), 17-25.

Lines, D., Werner, M., & Bastiaanssen, W. (2017). The predictability of reported drought events and impacts in the Ebro Basin using six different remote sensing data sets. *Hydrol. Earth Syst. Sci*., 21, 4747-4765.

Malo, A. & Nicholson, S. E. (1990). A Study of Rainfall and Vegetation Dynamics in the African Sahel Using Normalized Difference Vegetation Index. *Journal of Arid Environments*, 19, 1–24.

Peters, J.A., Walter-Shea, E.A., Ji, L., Andres, V., Michael, H., Svoboda, M.D. (2002). Drought Monitoring with NDVI Based Standardized Vegetation Index. *Photogrammetric Engineering & Remote Sensing*, 68(1), 71–75.

Pettorelli, N., Vik, J.O., Mysterud, A., Gaillard, J.M., Tucker, C.J., Stenseth, N.C. (2005). Using the satellite-derived NDVI to assess ecological responses to environmental change. *Trends Ecol. Evol*., 20, 503–510.

Prohmdirek, T., Chunpang, P & Laosuwan, T. (2020). The relationship between normalized difference vegetation index and canopy temperature that affects the urban heat island phenomenon. Geographia Technica, 15(2),222-234.

Quiring, S .M ., and S .Ganesh) . (2010). Evaluating the utility of the Vegetation Condition Index (VCI) for monitoring meteorological drought in Texas, *Agric .For .Meteorol*., 150 (3), 330–339 .

Rotjanakusol, T. & Laosuwan, T. (2018). Remote Sensing Based Drought Monitoring In The MiddlePart of Northeast Region of Thailand. *Studia Universitatis Vasile Goldis Arad, Seria Stiintele Vietii*, 28(1), 14-21.

Rotjanakusol, T., & Laosuwan, T. (2019a). Drought Evaluation with NDVI-Based Standardized Vegetation Index in Lower Northeastern Region of Thailand. *Geographia Technica*, 14(1), 118-130.

Rotjanakusol, T., & Laosuwan, T. (2019b). An Investigation of Drought around Chi Watershed during Ten-Year Period Using Terra/Modis Data. *Geographia Technica*, 14(2), 74-83.

Rousta, I., Olafsson, H., Moniruzzaman, M., Zhang, H., Liou, Y.-A., Mushore, T. D., & Gupta, A. (2020). Impacts of drought on vegetation assessed by vegetation indices and meteorological factors in Afghanistan. *Remote Sensing*, 12(15), 2433.

Uttaruk, Y., & Laosuwan, T. (2017). Drought Detection by Application of Remote Sensing Technology and Vegetation Phenology. *Journal of Ecological Engineering*, 18(6), 115-121.

Uttaruk, Y., & Laosuwan, T. (2019). Drought Analysis Using Satellite-Based Data and Spectral Index in Upper Northeastern Thailand. *Pol. J. Environ. Stud*. 28(6), 1-8.

Tarpley, J.D., Schneider, S.R., & Money, R.L. (1984). Global vegetation indices from the NOAA-7 meteorological satellite. *Journal of Climate and Applied Meteorology*, 23, 491–494.

Tucker, C.J. (1979). Red and photographic infrared linear combinations for monitoring vegetation. *Remote Sensing of Environment*, 8(2), 127–150.

Zambrano, F., Lillo-Saavedra, M., Verbist, K., & Lagos, O. (2016). Sixteen years of agricultural drought assessment of the BioBío region in Chile using a 250 m resolution vegetation condition index (VCI). *Remote Sensing*, 8(6), 530.

Zhang, Y., Peng, C., Li, W., Fang, X., Zhang, T., Zhu, Q., Chen, H. & Zhao, P. (2013). Monitoring and estimating drought-induced impacts on forest structure, growth, function, and ecosystem services using remote-sensing data: Recent progress and future challenges. *Environmental Reviews*, 21, 103-115.

DYNAMIC SPACE-TIME DIFFUSION SIMULATOR IN A GIS ENVIRONMENT TO TACKLE THE COVID-19 EMERGENCY. TESTING A GEOTECHNOLOGICAL APPLICATION IN ROME

Cristiano PESARESI[1] ⓘD *, Davide PAVIA[1]* ⓘD *, Corrado DE VITO [2]* ⓘD *, Andrea BARBARA[2,3],*
Vito CERABONA[2,3], Enrico DI ROSA[3]

ABSTRACT:
In this paper, we start from a contextualization about the measures used to contain the COVID-19 diffusion and the need to promote geotechnological proposals, data sharing and homogenous centralised systems for data collection and analysis. Successively, we present the "Dynamic Space-Time Diffusion Simulator in a GIS Environment to Tackle the COVID-19 Emergency" that we have elaborated on the basis of the data provided by the UOC Hygiene and Public Health Service – Local Health Unit Rome 1. Particularly, after describing the main technical process able to predispose the dynamic simulator, we underline the possible added value that it can provide in terms of infection surveillance and monitoring, precision preparedness, support to decision making and territorial screening. For this demonstrative application, we have extracted from the simulator some groups of four digital screenshots which are able to show synoptic photographs in temporal perspective concerning the total number of cases of COVID-19 in Rome (Italy) for the period February 25th - September 26th. Specifically we have selected: - four screenshots for the period February 25th - June 11th, to provide significant evidence about the first three months and a half; - four screenshots for the period March 1st – March 29th, to add an insight into the geographically and statistically meaningful month of March; - four screenshots for the period June 12th - September 26th, to supply an efficacious geovisualisation of the last three months and a half available; - four screenshots for the period February 25th - September 26th, to show a cumulative elaboration aimed at geolocating all the cases recorded in the seven months examined; - four screenshots for the period March 26th - September 26th, with a distinction about the first and second data sets, for a detailed (cumulative) zoom. This simulator, elaborated for the COVID-19 emergency, can be replicated in any circumstance for which specific data and information are available for the scientific community, shared and progressively updated in order to provide a productive contribution to the identification of serious infectious disease clusters, patterns and trends, and quickly respond to specific needs.

Key-words: *COVID-19, Geocoding, GIS, Sanitary emergency, Dynamic simulator.*

1. INTRODUCTION

The current pandemic of COVID-19 – declared by the WHO in March 2020 – had two epidemic waves, although a real break between the first and second waves did not occur. The WHO European region experienced its first epidemic wave in March and April 2020, which – after repeated lockdowns in many countries – seemed to be controlled during the following summer months (Kupferschmidt, 2020). The second epidemic wave started in September 2020 with a rapid escalation of cases, mainly due to government easing of restrictions and people's consequent reduction of attention to precautions (Looi, 2020).

---

[1] Department of Letters and Modern Cultures, Sapienza University of Rome, Rome, Italy
cristiano.pesaresi@uniroma1.it, davide.pavia@uniroma1.it

[2] Department of Public Health and Infectious Diseases, Sapienza University of Rome, Rome, Italy
corrado.devito@uniroma1.it, andrea.barbara@uniroma1.it, vito.cerabona@uniroma1.it

[3] UOC Hygiene and Public Health Service – Local Health Unit Rome 1, Rome, Italy
enrico.dirosa@aslroma1.it

Now we are facing the tail of the second wave, after continuous attempts to balance opening-up and lockdowns, personal freedoms and public health needs. The real turning point came with the possibility of using SARS-CoV-2 vaccines, the development of which has proceeded apace over the past year, resulting in one of the most important scientific findings and the largest mass vaccination of our century. The best comparison to the massive global vaccination effort might be the smallpox vaccination campaigns that culminated in eradicating the disease (Horton, 2021). Currently (first half of May 2021), there are 115 COVID-19 vaccine candidates; 333 are being tested in clinical trials, and 15 are approved (McGill COVID19 Vaccine Tracker Team, 2021). Globally, 8.4% of the world population has been vaccinated with the first or single-dose and 4.1% is fully vaccinated. In Italy, of the 24,502,646 people vaccinated, 7,561,566 are fully vaccinated (Ministero della Salute, 2021).

Although the available vaccines are highly effective and safe in reducing the likelihood of serious disease, we must take several variables into account before completely abandoning primary prevention measures and resuming free movement within and between states. First of all, even though COVID-19 vaccines induce higher levels of antibodies than natural infection, scientific studies, even with the short amount of time that has passed, cannot say how long the antibodies will last. Secondly, new variants of the SARS-CoV-2 virus are sprouting up that might be more transmissible and resistant to vaccines. Finally, it is not clear whether vaccines prevent infection. If not, the achievement of herd immunity would be seriously compromised (Aschwanden, 2021). In this scenario, primary prevention measures should be maintained until vaccination coverage reaches safe levels. Most countries in the world are continuing to implement mitigation strategies, using various degrees of non-pharmaceutical interventions (NPI) combined with backward and forward tracking of people infected, and tracing their contact (TTT) interventions. Repeated lockdowns are also used as a containment strategy.

Geospatial analysis, in this context, has much room for application. Geolocalisation has proved to be an essential tool for analysing the path of the virus on a global scale and to modelling scenarios of virus distribution (Valjarević et al., 2020). In other cases, GIS technology was used to identify the space-time clusters of COVID-19 in a large country at the family level (Xu et al., 2021). Moreover, GIS, spatial statistics and specific methods have been used to study the time-series spatial autocorrelation patterns and possible factors influencing the COVID-19 diffusion at different geographical scale, in order to provide important information for the disease prevention and surveillance (Xiong et al., 2020). GIS mapping has been also used to represent and analyse some key aspects and themes, as for example (de Kadt et al., 2020): COVID-19 "Index of risk factors to maintaining social distance and preventative hygiene" and "Index of risk factors that increase health and social vulnerability during an outbreak or broader shutdown".

Such technology is most useful in the early phase of a pandemic to identify and contain outbreaks, in the middle phase to identify areas at greatest risk of spreading, and in the final phase to identify critical areas and factors. And then, during the COVID-19 pandemic, the integration among GIS elaborations, web-based tools and map-based dashboards is making it possible to: offer update accessible information; feed data sharing and knowledge; show territorial discrepancies and emergency conditions; support international comparisons and decision making; evidence the need of applicative solutions based on real-time data, also having a circumstantial level of detail (Kamel Boulos & Geraghty, 2020; Dangermond et al., 2020).

After all, many recent researches have underlined the great analytical capabilities of specific techniques and methods in a GIS environment and in a perspective of interoperability i.e. in order to: identify possible risk factors and areas exposed to electromagnetic fields coming from radio base stations (Pesaresi & Pavia, 2021); model and produce the acoustic map of the vehicular traffic of an urban area (Dardanelli et al., 2017); reduce emergency department (ED) overcrowding and particularly code white (inappropriate) attendances, after having identified the zones of greatest provenance of improperly used ED access (Pesaresi et al., 2020a); select and determine the suitable locations of certain elements and components (Nistor et al., 2019; Cristea & Jocea, 2016); work towards combined approaches with machine learning and remote sensing for recognising areas strongly exposed to hazard and risk (Avand et al., 2021) and coming up with a cognitive system in response to emergencies (Atek et al., 2021).

In a similar framework and in the light of the possible added value obtainable by geotechnological applications, a dynamic space-time diffusion simulator in a GIS environment, based on official health data regarding Rome (Italy), is presented in this study.

2. THE IMPORTANCE OF GEOTECHNOLOGICAL PROPOSALS, DATA SHARING AND HOMOGENOUS CENTRALISED SYSTEMS

In a previous piece of work the importance has been evidenced of having a geotechnological tested system that (in an adequate balance with privacy aspects) can make it possible to produce detailed digital maps, applications and models able to support geospatial analysis, bringing to light crucial aspects, trends, patterns and clusters. In particular, three geotechnological proposals (**Fig. 1**) were hypothesised to tackle health emergencies starting from the present COVID-19 pandemic, with specific reference to the (Pesaresi et al., 2020b): elaboration in a GIS environment of geographical-healthcare-epidemiological models of spatial and temporal diffusion; devising of an App for data tracking, digital flow mapping and health education; realization of a geolocalised online questionnaire, for a smart survey for the identification of possible positives. One of the biggest and most common problems for the scientific community has been the lack of highly detailed accessible and continuously updated data for testing and advancing geotechnological solutions able to support interpretative analysis, intervention planning, definition of implementational measures.

The low level of data disaggregation and the absence of an open-source platform for collecting and sharing accurate data in real-time – although we are (*or should be*) in the era of big data – do not make it possible to scientifically operate and contribute to the decision making and strategic planning of sanitary actions. Therefore, the potentialities of applied geography and the GIS approach, in the interdisciplinary perspective, risk being suffocated by the absence of adequate data, with notable negative repercussions on the geospatial analysis and operative steps. In a similar situation, three geotechnological proposals were advanced on the basis of simulated data and theoretical-methodological assumptions aimed at showing the possible added value and what could be produced at application level to support emergency phases in the case of availability and sharing of real data.

Specific examples and demonstrative elaborations were presented, for conventionally selected study areas of Rome (Italy), in order to underline the potential contributions that could be provided as support to intersectoral analysis, policy making and precision preparedness.
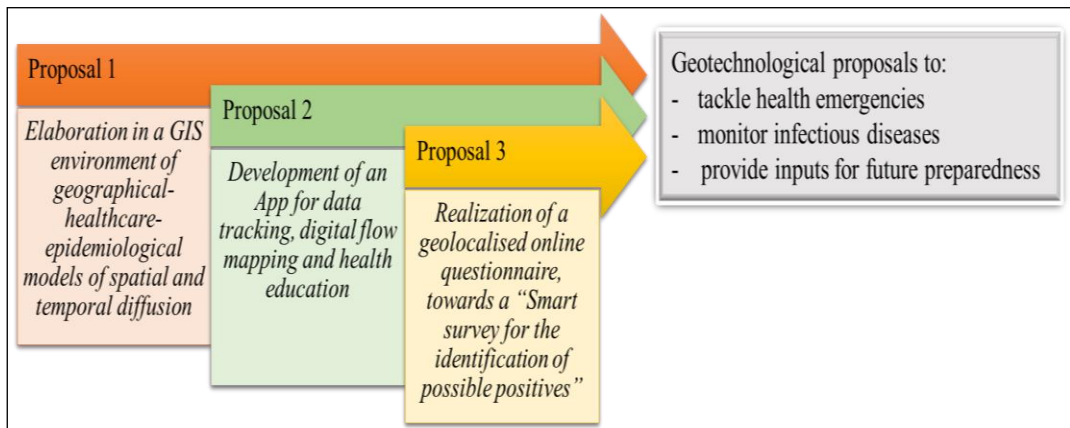

Fig. 1. Three geotechnological proposals to tackle health emergencies, monitor infectious diseases, provide inputs for future preparedness starting from the COVID-19 pandemic. Source: Authors' elaboration based on Pesaresi et al., 2020b.

After all, other studies have generally reiterated that:

- reliable disaggregated and age-disaggregated data – above all in the case of COVID-19 – are vital for epidemiological and geographical analysis, supporting specific responses and monitoring the prioritisation of different age groups in policy actions (Lloyd-Sherlock et al., 2021, 141);
- a centralised, harmonised and fully reproducible open-access and age-structured database of COVID-19 is essential to estimate the impact of the disease, allow comparisons and support scientific analysis which can provide a notable added value also for practical measures and future preparedness (Riffe et al., 2020, 1-2);
- real-time and valid information flow and reporting have a crucial role during pandemics and principles of open science and data sharing are of utmost relevance (Wolkewitz & Puljak, 2020, 2-3);
- a common insight that an invaluable benefit could come from a pooled, accurate and available dataset analysable by the scientific community in academic and research institutes is necessary (Cosgriff et al., 2020);
- it is hoped that open science will start to be considered as a "new normal" scientific method in this and future crises too, since it can greatly help to find approaches and strategies to alleviate global and individual suffering (Tse et al, 2020, 5);
- geography, GIS and an interdisciplinary approach can play a central role in monitoring and mitigating disease transmission, above all if it is possible to refer to a plethora of tested methods and functionalities which can be implemented and refined in a short timeframe to effectively interact with public health institutions, decision-makers and local officials "about spatial and space-time transmission dynamics" (Desjardins et al., 2020, 6);
- incorporating and integrating geographic information science and technology (GIS&T) into COVID-19 pandemic surveillance and modelling helps to understand and monitor the disease. Particularly, applications and elaborations "of GIS&T include 1) developing spatial data infrastructures for surveillance and data sharing, 2) incorporating mobility data in infectious disease forecasting, 3) using geospatial technologies for digital contact tracing, 4) integrating geographic data in COVID-19 modeling, 5) investigating geographic social vulnerabilities and health disparities, and 6) communicating the status of the disease or status of facilities for return-to-normal operations" (Smith & Mennis, 2020, 1).

In another contribution (Pesaresi, 2020), the prompt availability and setup of automatically updated data regarding COVID-19 – and for the future about other possible infectious diseases – have been considered as a key element in order to support accurate GIS mapping and interdisciplinary analyses able to allow the interpretation of viral and dynamic phenomena and to validate the response capacity of the healthcare facilities, hospitals, emergency departments, intensive therapies and governments. In this perspective, a common and determined effort should be necessary for the creation of a tested Homogenous Centralised System for Dynamic Geoprocessing and Geolocalised Diffusion Models in response to Emergencies (**Fig. 2**) into which to collect and merge data (involving domicile and residence of the positives, their age and sex) gathered by means of homogenous formats in order to set up reliable and superimposable databases at a regional, provincial and municipal level, such as for census sections. Emergency departments, Local Health Units and the other health facilities should in fact have recourse to a standard system and process of data collection that flows into a high-performance cloud platform, able to support geocoding and geospatial analysis, reducing time and risk of error, guaranteeing requirements of safety and confidentiality. Through geolocalised data, which make it possible to use the geocoding tool in GIS environment on the basis of domicile and residence, specific models of spatial and temporal diffusion can be elaborated and updated to recognise – on satellite images, digital street maps or other bases – critical areas and axes, also by the overlay of multiple layers. Moreover, in terms of synthetic view and to avoid confidentiality matters, from the point maps, where each point can for example represent the single ascertained case or death, it is possible to move towards aggregate scale digital mappings or geospatial and geostatistical functionalities, to identify the zones requiring ad hoc interventions and services.
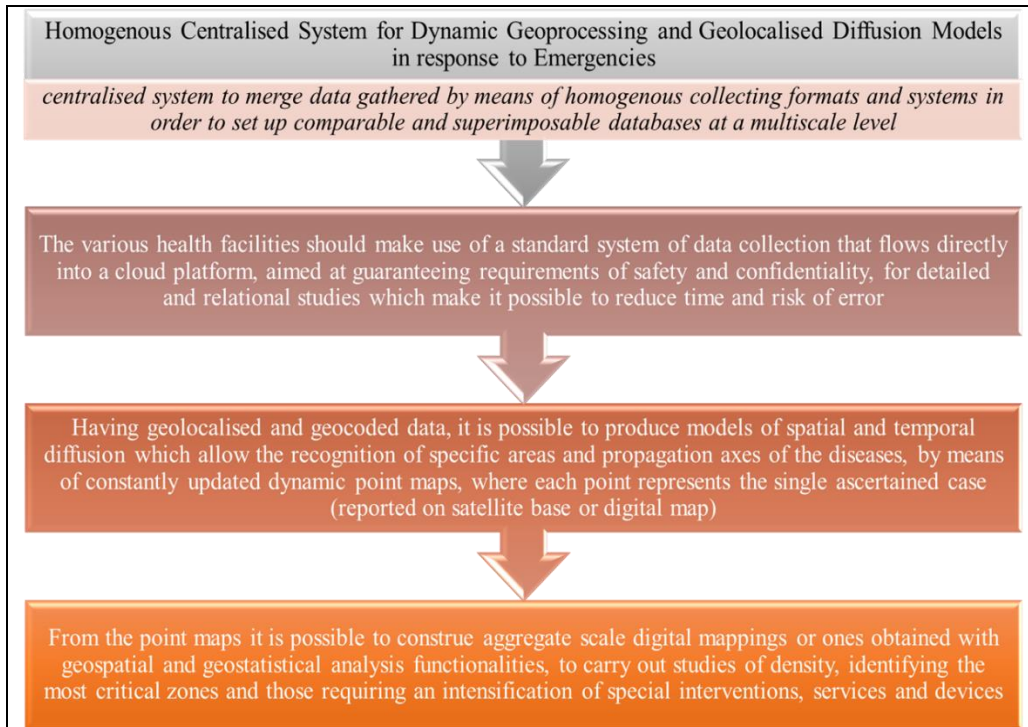
Fig. 2. The importance of having a Homogenous Centralised System for Dynamic
Geoprocessing and Geolocalised Diffusion Models in response to Emergencies.
Source: Authors' elaboration based on Pesaresi, 2020.

3. MATERIAL AND METHODS. DYNAMIC SPACE-TIME DIFFUSION SIMULATOR IN A GIS ENVIRONMENT TO TACKLE THE COVID-19 EMERGENCY

3.1. Prerequisites and basic aspects

In the group of interdisciplinary operative works aimed at highlighting how the GIS applications and digital models can prove to be of great support for research and concrete actions aimed at opposing contingent sanitary problems and social drama, through rigorous processing and analysis of data and images, we have produced and tested a "Dynamic Space-Time Diffusion Simulator in a GIS Environment to Tackle the COVID-19 Emergency" on the basis of the data collected and provided by the UOC Hygiene and Public Health Service – Local Health Unit Rome 1 (*UOC Servizio Igiene e Sanità Pubblica – ASL Roma 1*). This simulator, created specifically for the COVID-19 emergency, can be replicated in any circumstance for which accurate data and information are available, shared and progressively updated and it has been conceived to provide a significant contribution to recognise outbreaks of infectious diseases, identify clusters and distribution patterns, monitor and predict the disease's temporal and spatial evolution.

As a first foundation, the simulator, developed in a GIS environment on satellite images, digital street maps and other background templates, is based on the geocoding process, by means of which data and information, with a precise domicile and residence address available, are geolocated to show the evolution of the phenomenon, the spatial distribution of positive cases and deaths and to conduct a high-detail screening. It (potentially) makes it possible to daily monitor the progression of the disease, in terms of territorial thickening and temporal trend, through automatic and digital GIS-mapping able to auto-implement in parallel with the evolution of the phenomenon itself and with the registration of the data in a specific database.

The dynamic simulator is also characterised by an animation effect, to be interpreted like a video mode, which can make it possible to select and represent the data and their continuous evolution for specific temporal ranges, supporting advanced hypotheses on possible disease evolution and revealing, in terms of retrospective analysis useful as training for the future, which measures and interventions could have recorded with a certain level of success to tackle the sanitary emergency being studied. The role played by the simulator can be notable in different phases but above all in the early stages of an emergency, to concretely work and take decisions in order to rapidly block the spread of the disease through specific analysis, guidelines and ad hoc measures with which to intervene on the first affected areas and the ones highly exposed to contagion risk.

3.2. The source and characteristics of the data

The Public Health and Hygiene Service (SISP) is one of the Services of the Prevention Departments of the Local Health Authorities (ASL). Starting from February 2020, the SISP of ASL Rome 1 was involved in the management of the SARS-CoV-2 pandemic and set up a work team that could guarantee the tracing of positive patients permanently resident in the ASL Rome 1 territory or even temporarily present and admitted to hospitals in the area of competence.

From a procedural point of view, the multidisciplinary team activated a management system with the use of an e-mail box (Covid19@aslroma1.it) appointed to receive, from the hospitals and general practitioners of the area and from other Hygiene Services, reports of positivity to COVID-19 through the form ANNEX_3_SCHEDA_SARS_COV2_v4.1, specially modified and adapted by SERESMI for the notification of the infectious disease from SARS-CoV-2. Every day an administrative resource had the task of monitoring the e-mail address Covid19@aslroma1.it and to print the reporting forms.

For the registration of the notification forms a database in blocks was created, always accessible to all UOC SISP's staff (Doctors, Health Assistants, Environmental and Workplaces Prevention Technicians and Nurses) for the daily care of the domiciled patients and for Contact Tracing operations, which contains the following information.

- The first block contains the patient's personal information and other information useful for optimising the management of the case and specifically: progressive master is the progressive arrival number of the ANNEX_3_SCHEDA_SARS_COV2_v4.1 email address at Covid19@aslroma1.it; gender; place and date of birth; the date reported on the ANNEX_3_SHEET_SARS_COV2_v4.1 form which corresponds with the positive result of swab test carried out; date of input of the information on the database; Official Body that notified the infectious disease; indication of the place of hospitalisation or home isolation, and home address; Municipality and Local Health Authority competent for the patient's residence. Patient Tax Code, surname, first name, telephone number and e-mail address of the patients, useful for the daily activation of health surveillance and for contact tracing activities, as well as for official communications between the Local Health Authority and the patient, were removed from the dataset used for the analysis to ensure anonymity.
- The second block contains information on the evolution of the patient's clinical picture after a second control swab, and specifically: ESITO_1 which contains the swab result or the clinical evolution of the patient (Healing, Clinical Healing, Discharge, Death); Note_Esito_1 which contains information on the outcome date (date of Healing, date of Discharge, date of Death), Data Segnalazione Aggiornamento_1 which indicates the Date of notification of the update indicated on the notification form (corresponding to the second swab carried out or with the exitus date or with the discharge date from the Hospital), the data input date Aggiornamento_1, which is the date on which such notification reached the Hygiene Service and was taken charge of; the Notifying Body_1 and the new placement of the Patient through the information contained in the "Isolation / Hospitalization at_1" cell.

The subsequent blocks represent further evolutions of the clinical status or consequent to following controls with TNF.

3.3. The data cleaning and optimisation

In order to convert the COVID-19 cases into an accurate feature class – a vector spatial data format used to represent and analyse a discrete object in a GIS environment – a data cleaning and optimisation (aimed at geocoding) was at first conducted on the data sets received from the Local Health Unit Rome 1.

Basically, the operation was conducted with regard to two criteria: a temporal one, to verify the presence of the notification dates for each of the patients recorded; a spatial one, to verify the presence and the quality of the addresses of the place where patients spent their isolation. Both pieces of information were required for the creation of a simulator aimed not only at representing the location of the cases, but also their change over time, bringing together the dimensions of space and time in a 4D application devised to monitor and study the spread of the outbreak.

Since the data were provided in two different sets with the same schema (from February 25th to June 11th 2020; from June 12th to September 26th 2020), a new Excel worksheet was created to merge the relative rows in a new database, which finally contained 3,717 rows.

Then, the data cleaning and optimisation started from the temporal criteria. The date of each notification was stored in a homonym field called "Date of notification", reporting the year, the month and the day when the case was ascertained. At first, the cells of this field were filtered to detect the presence of null values, like empty cells or values in a non-date format. Thus, the operation led to the replacement of the values of 40 cells with those of the cells of the "Date of insertion" field, which stored the date when the notification was recorded into the database. Only one row was cancelled as there was no valid information in both fields, reducing the number of rows to 3,716.

These rows were then cleaned and optimised with regard to the spatial criteria. Among the spatial fields stored in the table, such as the one containing the patients' country of birth, the "Domicile" field was used as input for the geocoding process, because it contained the larger scale information available for the geocoding: the address of the places where the patients spent their isolation.

Therefore, the process has focused on reviewing both the presence and quality of these values, in order to provide the best possible input for the ESRI "ArcGIS World Geocoding Service", a cloud-based service that converts the addresses of 153 world countries into point features[4]. At first, the domicile field was filtered for empty cells to be deleted, reducing the number of rows to 3,713. The remaining cells were then filtered again with a specific formula, aimed at displaying only the addresses that did not start with the words "Via" and "Piazza" (i.e. the Italian words for street and square). Thus, the data cleaning and optimisation could have been concentrated on a smaller set of cells (297 cells, the 8% of the whole dataset), whose values were most likely not an address or a value that could be geocoded. Basically, these values were wrong for the following reasons: 31 cells reported the country of origin of the patients instead of their address of domicile; 4 cells were filled with the value "Not specified"; 7 cells mentioned the state of the person, such as homeless, soldier and tourist, without reporting any address to geocode.

Some of the remaining filtered cells reported more than one address and were rewritten by choosing the first: this has generally been the case of the cells of patients treated by more than one medical facility. The remaining 3,671 rows were cleaned from those containing addresses located outside Rome using the values of the "Municipality" field, which stored both the number of sub-municipal areas in the case of Rome addresses and the name of the municipality for the others. The numbers of the sub-municipal areas were then replaced with the word "Rome", in order to refer the addresses of the "Domicile" field to the municipality to which they belong. Finally, the "Domicile" field was reviewed in search of special characters like brackets, often used to add a note to the case, in order to leave in the cells nothing but the addresses.

---

[4] 153 countries are classified by ESRI "ArcGIS World Geocoding Service" from level 1 to 3, where level 1 means maximum accuracy for the geocoding service. The remaining countries of the world are classified with level 4, which means that the geocoding service is only available for points of interest and administrative boundaries. The service documentation is available at https://doc.arcgis.com/it/arcgis-online/reference/geocode-coverage.htm; last access on April 26th 2021.

3.4. The input data for the dynamic space-time diffusion simulator

At the end of the data cleaning and optimisation, the 3,184 remaining rows were copied onto a new database with a more simplified schema than the one of the original source, made up only of the fields that would be used by the simulator: the "Date of notification", the "Domicile" and the "Municipality" ones. The two latter fields where then used as the input ones for the "Geocode Addresses" tool of ArcGIS Pro, the latest desktop application of the ArcGIS platform. Using ESRI's "ArcGIS World Geocoding Service" as the input address locator, the "Domicile" field was referred as the Address or Place parameter of the tool, while the "Municipality" field was used as the City one. Finally, "Italy" was chosen in the Country parameter to reduce the extent of the geocode process.

Each of the points created by the geocode process was evaluated in terms of the accuracy of the geocoding: of all the addresses, 6.5% were rated as "Unmatched", which means the process could not find a perfect match for these input addresses. In most cases, these addresses did not match due to the lack of the civic number or the use of a different prefix than the one found by the address locator (i.e. "Street" instead of "Boulevard"); furthermore, they did not match because of the presence of homonymous addresses. Each of these 207 addresses was rematched every time it was possible to find an unambiguous candidate among the ones selected by the process. T

The point feature class was then added to a new ArcGIS Pro map, together with the layer of Rome sub-municipal areas downloaded from the portal of the Italian National Institute of Statistics (ISTAT)[5], in order to select and delete the points outside the city boundaries using the "Select Layer by Location" tool, reducing the number of features to 3,056. These were the points that were used as input for the time-space simulator, which used the values of the "Date of notification" field to gradually display the points based on a time slider. This feature can be applied to all temporal layers of a map, that is to say the ones that point to a dataset that stores time values in its attribute table. Using these values, the COVID-19 case layer could be turned into a temporal one and could be used to display the gradual increase of the cases via the time slider.

Using for example a frequency of two days, an animation was created based on the values of the "Date of notification" field, showing the spread of the cases in Rome from February 25th to September 26th. Due to the possibility to replay the animation with a different time interval, this tool can be particularly useful to support the study of the outbreak and its spread, slowing down the frame rate of the animation to better identify the distribution of the clusters.

Finally, the animation was exported as an independent video file, in order to reach a wider audience and effectively communicate the spread of the infection across the space and time studied.

3.5. The temporal scanning for the demonstrative application

The data used for producing and testing the simulator, originally received in two sets, cover two successive periods and make it possible to analyse the dynamics recorded in about seven months.

- From February 25th to June 11th 2020 (in terms of notification date) and involving the period of the Italian lockdown; in fact, on the basis of the DPCM dated 9th March 2020, it was declared that the urgent measures to contain the contagion would have been extended throughout the whole national territory (Official Gazette General Series No. 62; https://www.gazzettaufficiale.it/eli/id/2020/03/09/20A01558/sg), and the lockdown period continued until May 18th, the day of the end of the enforcement of all restrictive measures on circulation within the regional territory on the basis of Decree-Law No. 33 dated 16th May 2020, (https://www.normattiva.it/uri-res/N2Ls?urn:nir:stato:decreto.legge:2020-05-16;33!vig=).

---

[5] https://www.istat.it/storage/cartografia/basi_territoriali/aree-subcomunali-xls-shp/ASC2011_WGS84.zip; last access on May 1st 2021.

- From June 12th to September 26th 2020 and involving the period of the second wave inflated during the summer holidays, the recovery of touristic flows sometimes without respect for the rules and the easing off of the containment measures.

For the demonstrative application shown here we have focussed the attention on the cases of positivity for each period and the cumulative cases, representing the number of positives ascertained in one of the healthcare facilities of Local Health Unit Rome 1.

Particularly:
- for the period from February 25th to June 11th 2020, we have used orange points to represent each positive ascertained, using a satellite image as background template;
- for the period from June 12th to September 26th 2020, we have used red points to represent each positive ascertained, using a digital street map as background template;
- for the period from February 25th to September 26th 2020, we have used overlayed orange and red points to show each positive ascertained, using Light Gray Canvas as background template in order to better highlight the notable number of cumulative points which also have two different colours. The first screenshot, dated June 12th, is here due to the sum of the cases recorded from February 25th to June 11th plus the cases recorded on June 12th.

4. RESULTS AND DISCUSSIONS

4.1. The digital screenshots extracted by the simulator

For the demonstrative application and analysis we extracted by the simulator – displayable and to be seen online in a simplified and exemplificative mode at http://geolab.uniroma1.it/geolab/it/simulatorecovid19 – some groups of four digital screenshots which are able to provide synoptic photographs in temporal perspective regarding the number of cases of COVID-19, on the basis of the data available and subject to data cleaning and optimisation and then to geocoding.

Specifically, we have selected the following.
- Four screenshots for the period February 25th - June 11th (**Fig. 3a**), represented over a satellite image (and with sub-municipal areas of Rome), to provide incisive evidence about the first three months and a half available with the cadence: February 25th, April 11th, May 11th, June 11th.
- Four screenshots for the period March 1st – March 29th (**Fig. 3b**), over a satellite image, to give an insight into the month of March (geographically and statistically very meaningful and not graphically covered in the previous elaboration) with the cadence of March 1st, March 8th, March 22nd, March 29th.
- Four screenshots for the period June 12th - September 26th (**Fig. 4**), over a digital street map, to provide an efficacious geovisualisation of the last three months and a half available with the cadence: June 12th, July 26th, August 26th, September 26th.
- Four screenshots for the period February 25th - September 26th (**Fig. 5a**), over a Light Gray Canvas as background template, to produce a cumulative elaboration aimed to show all the cases recorded in the seven months examined, with a distinction regarding the first and the second data sets and with the cadence: June 12th (starting from February 25th), July 26th, August 26th, September 26th.
- Four screenshots for the period March 26th - September 26th (**Fig. 5b**), over a Light Gray Canvas, with a focus on a zone of Rome centre, with a distinction regarding the first and the second data sets, to evidence at a detailed geographical scale the potentialities of a similar application in terms of accurate territorial screening and surveillance, on the basis of the bimonthly cadence March 26th, May 26th, July 26th, September 26th.
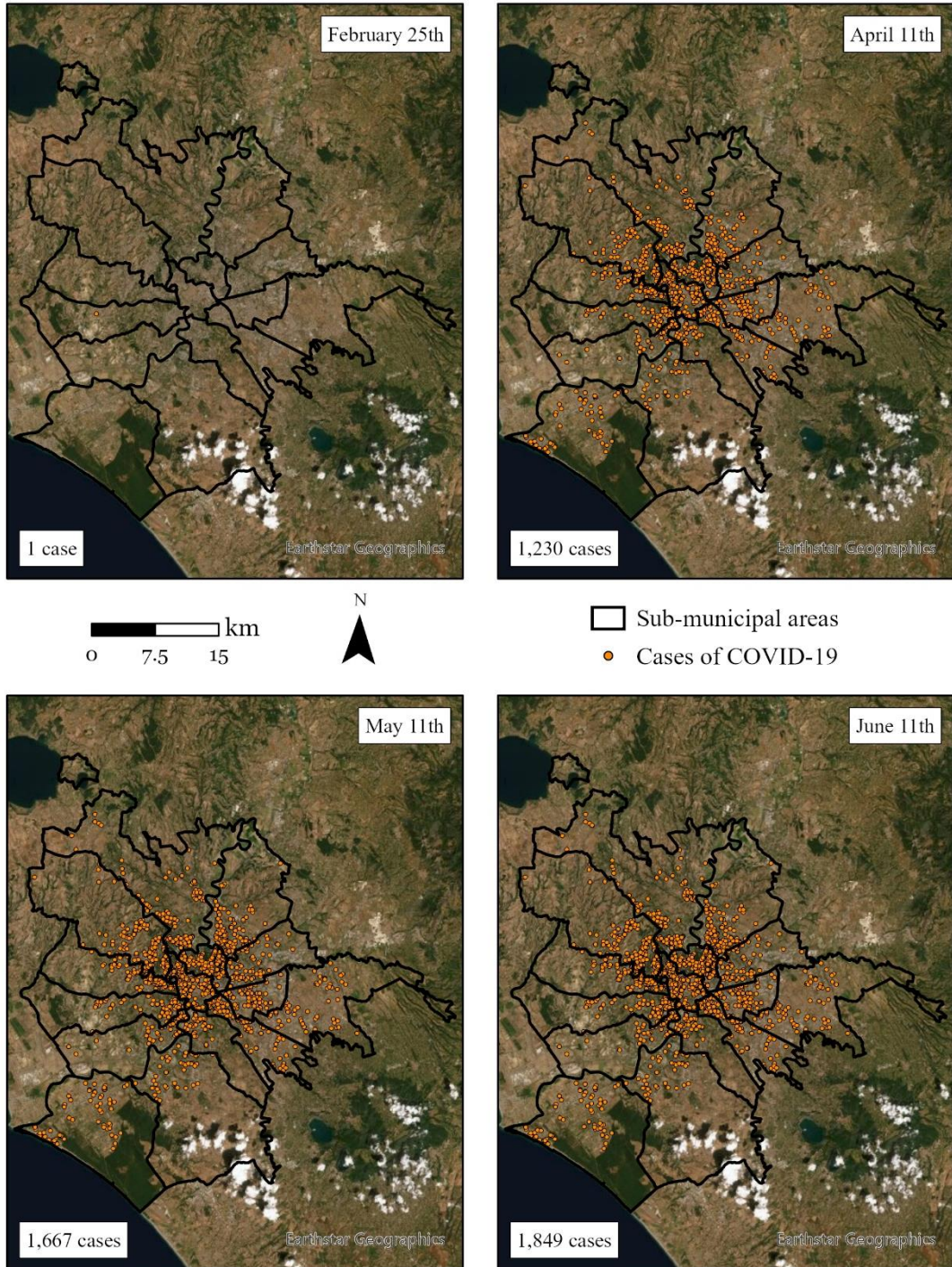
Fig. 3a. Four screenshots extracted by the dynamic space-time diffusion simulator in a GIS environment regarding the number of cases of COVID-19 in Rome, for the period February 25th - June 11th, on the basis of the data provided by the UOC Hygiene and Public Health Service – Local Health Unit Rome 1, over a satellite image and with sub-municipal areas of Rome.
Source: Authors' elaboration.
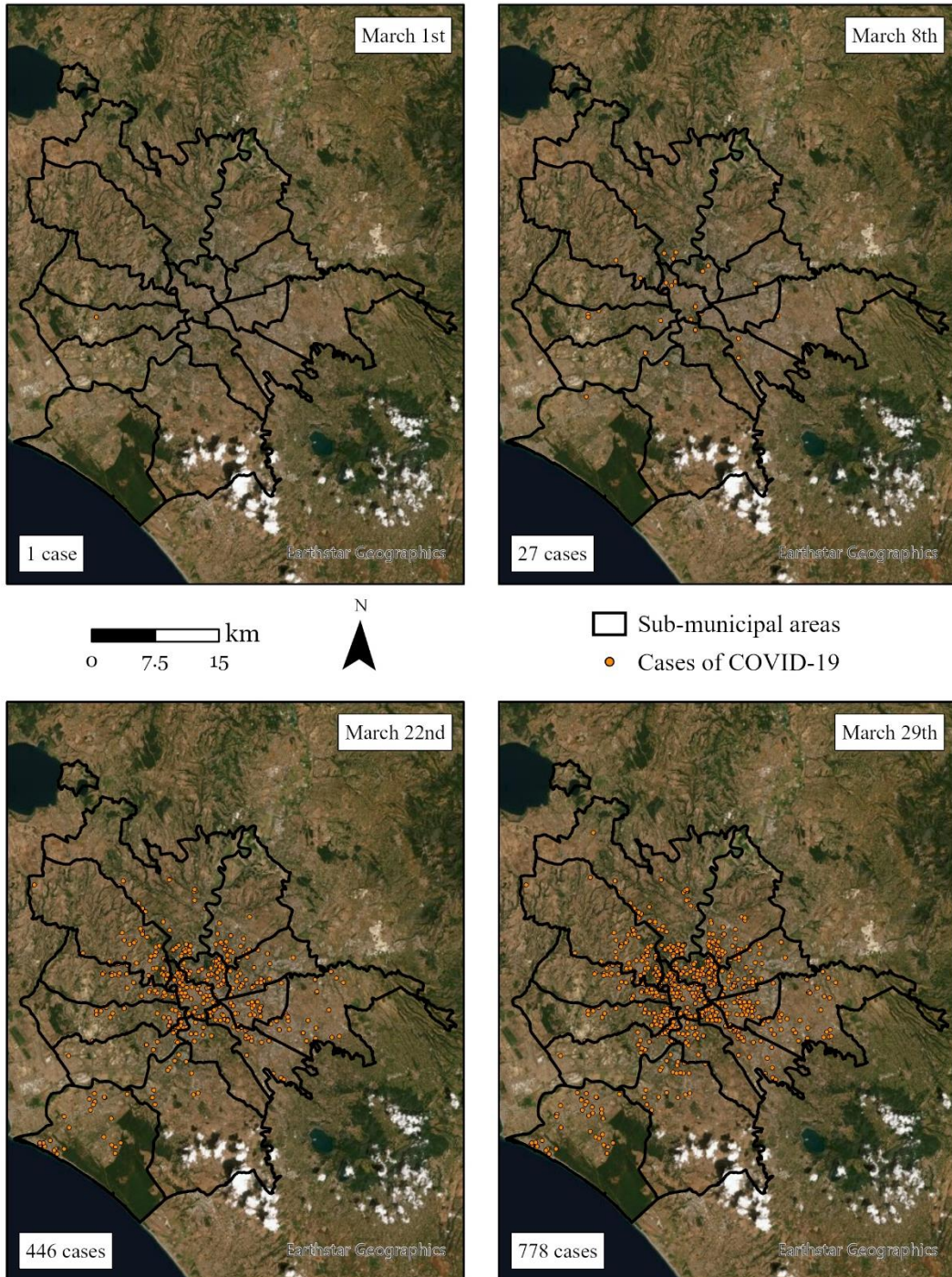
Fig. 3b. Four screenshots extracted by the simulator regarding the number of cases of COVID-19 in Rome, for the period March 1st - March 29th, on the basis of the data provided by the UOC Hygiene and Public Health Service – Local Health Unit Rome 1, over a satellite image and with sub-municipal areas of Rome. Source: Authors' elaboration.

4.2. Discussions and results

4.2.1. The period February 25th - June 11th, and a focus on March

Fig. 3a first of all shows the passage from the first COVID-19 case recorded in Rome on the basis of the data available, in a sub-municipal area in the west sector, to the 1,230 cases recorded on April 11th, that it is to say about one month and a half later. In this period the diffusion of COVID-19 was numerically greatly accelerated and spatially spread out, with a high concentration in the centre but with several clusters, thickening and axes in different sub-municipal areas. **Fig. 3a** moreover shows the subsequent slowing down which led to 1,667 cases on May 11th, while according to the previous trend a notably greater number of cases could have been recorded. Therefore, it is worthy to note the positive effects determined by the lockdown which make it possible to obstruct a widespread diffusion that could have been even more dramatic.

The positive effects of the lockdown and other measures (social distancing, devices like face masks etc.) were particularly remarkable in the successive months, since on June 11th 1,849 cases were recorded, with a contained increase of the cases.

Fig. 3b – which can be considered a geographical lens on the month of March, in order to understand the dynamic in this delicate period – shows the still small number of cases (27) on March 8th and makes it possible to have a detailed picture of their geolocalisation, clearly evidencing the potential added value of having similar applications in real-time to support decision making, to arrange the interventions into a hierarchy, to deploy specific facilities and sanitary services around the territory. **Fig. 3b** also shows that in the successive weeks the increase of the cases was rapid (446 and 778, respectively on March 22nd and 29th) also because the effects of the lockdown and ad hoc measures had a temporal phase shift and in the proximity of the cases already recorded on March 8th a series of new cases were added.

4.2.2. The period June 12th - September 26th

Fig. 4 first of all shows the sharp rise in the COVID-19 diffusion during the summer months. Specifically, in terms of evolutionary dynamic, it is possible to see the geolocalisation of 7 cases on June 12th and then the 172 cases on July 26th, the 544 cases on August 26th and the 1,207 cases on September 26th. As far as concerns the spatial distribution, the cases were mainly condensed into the Great Ring Road (*Grande Raccordo Anulare*), with a particular thickening in the central-north-western sector since August 26th. **Fig. 4** also puts in evidence the fact that, in this period, there was a slow increase in the first month and a half, owing to the last effects of the previous months and measures and a certain psychological fear, while the increases became faster and faster in August and September, also laying the potential bases for a rapid diffusion in the successive months. The concomitance between the easing of the restrictive measures and the progressive psychological recovery, and the connected desire to return to normality, relights a fuse in August and September that had previously been kept under control and able to break out into an accelerated rhythm.

4.2.3. The period February 25th - September 26th, and a focus with bimonthly cadence on a zone of Rome centre

Fig. 5a shows the combination of the data sets, in a cumulative way, through an overlay layer and makes it possible to follow the passage from 1,856 cases on June 12th (1,849 until June 11th and 7 on June 12th), to 2,021 cases on July 26th (1,849 until June 11th and 172), to 2,393 on August 26th (1,849 until June 11th and 544), to 3,056 on September 26th (1,849 until June 11th and 1,207). Therefore, the screenshot concerning June 12th represents the *trait d'union* among the two available data sets, the screenshot regarding July 26th shows a summation of orange and red points which slowly advance, while the screenshots concerning August 26th and September 26th put in evidence previous and new diffusion areas and axes, in a general mixed framework, with a notable overlapping of cases.
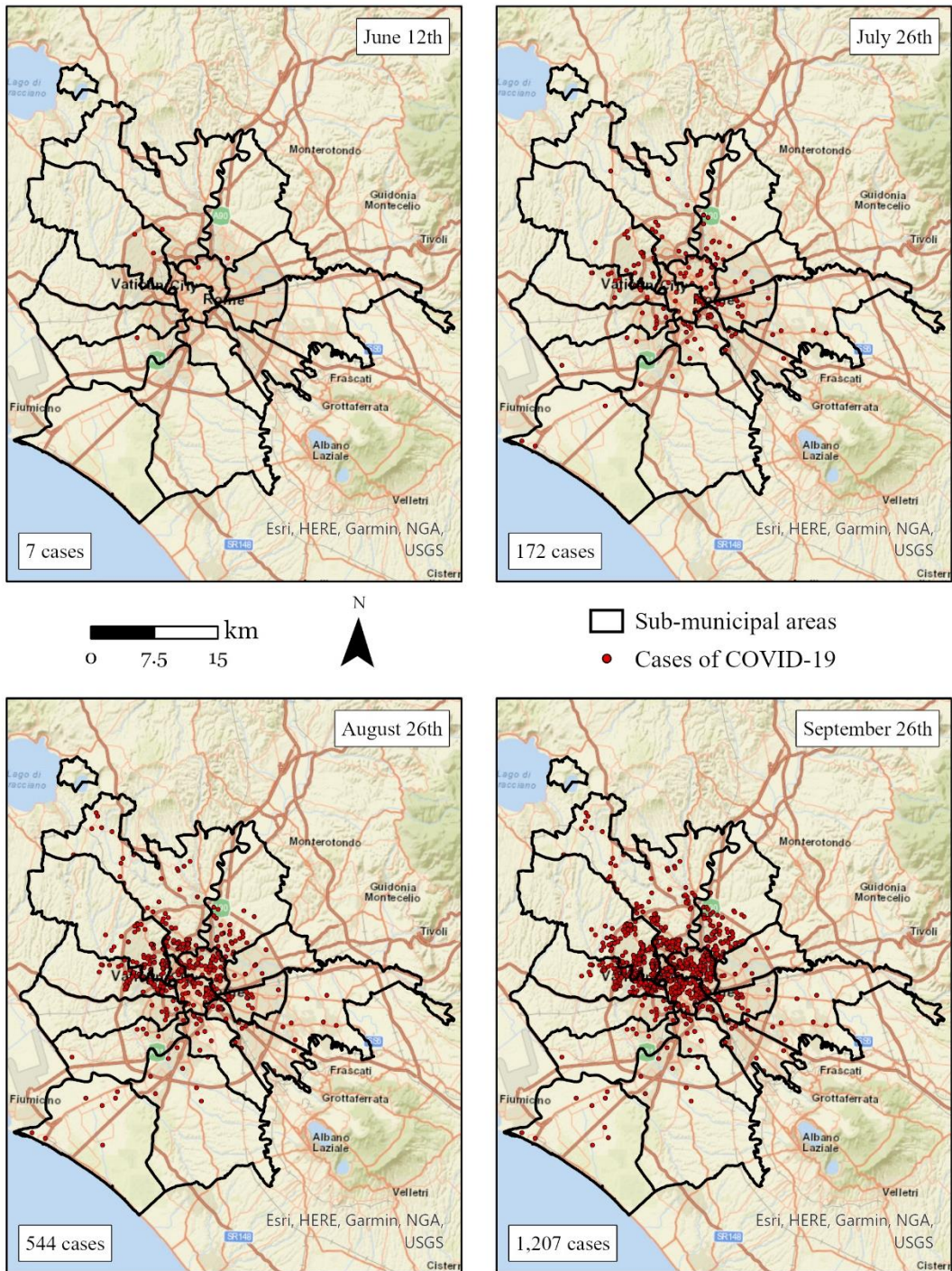
Fig. 4. Four screenshots extracted by the simulator regarding the number of cases of COVID-19 in Rome, for the period June 12th - September 26th, on the basis of the data provided by the UOC Hygiene and Public Health Service – Local Health Unit Rome 1, over a digital street map and with sub-municipal areas of Rome. Source: Authors' elaboration.
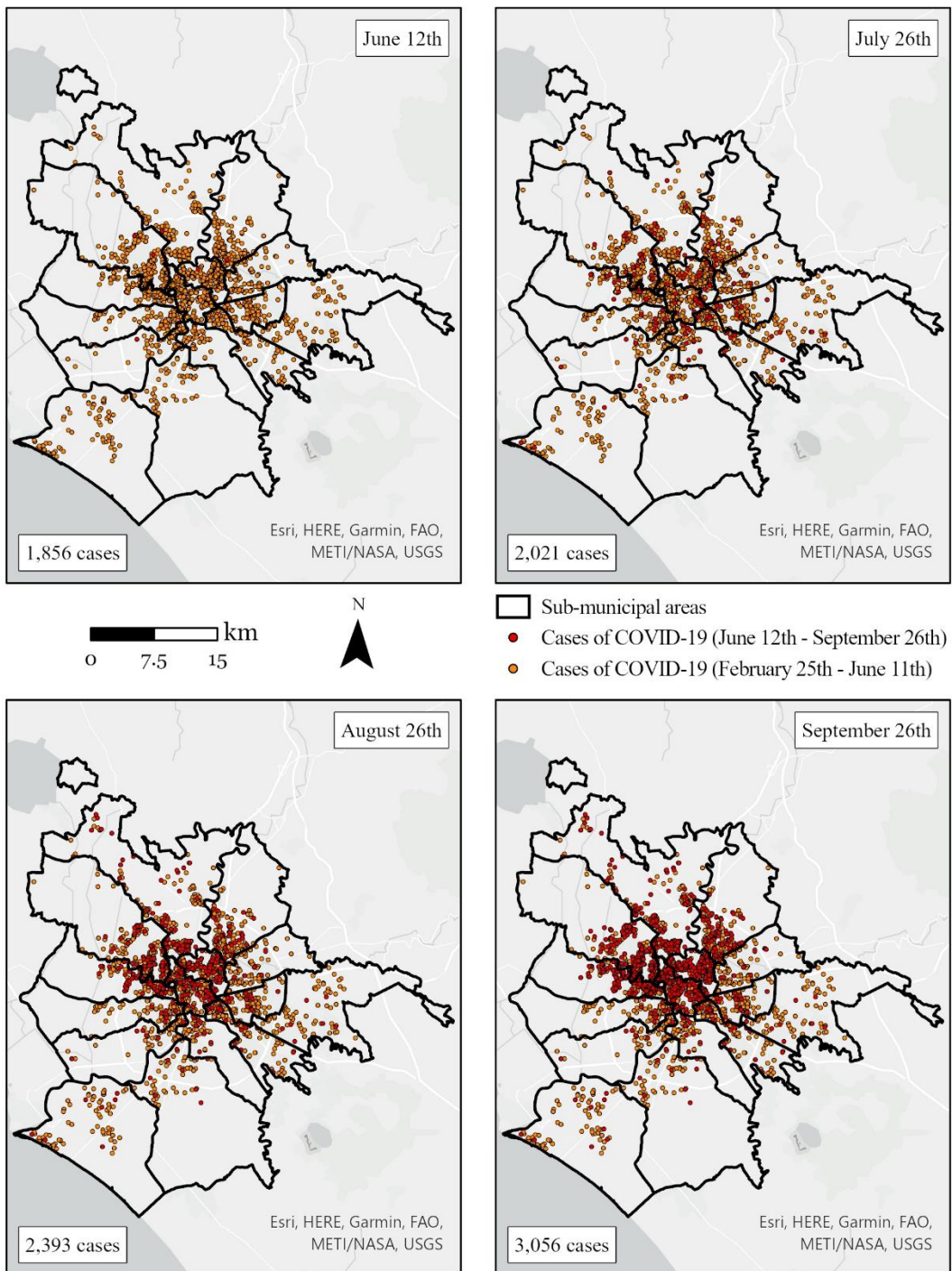
Fig. 5a. Four screenshots extracted by the simulator regarding the total number of cases of COVID-19 in Rome, for the period February 25th - September 26th, on the basis of the data provided by the UOC Hygiene and Public Health Service – Local Health Unit Rome 1, over a Light Gray Canvas as background template and with sub-municipal areas of Rome. The first screenshot, dated June 12th, is due to the sum of the cases recorded from February 25th to June 11th plus the cases recorded on June 12th.
Source: Authors' elaboration.
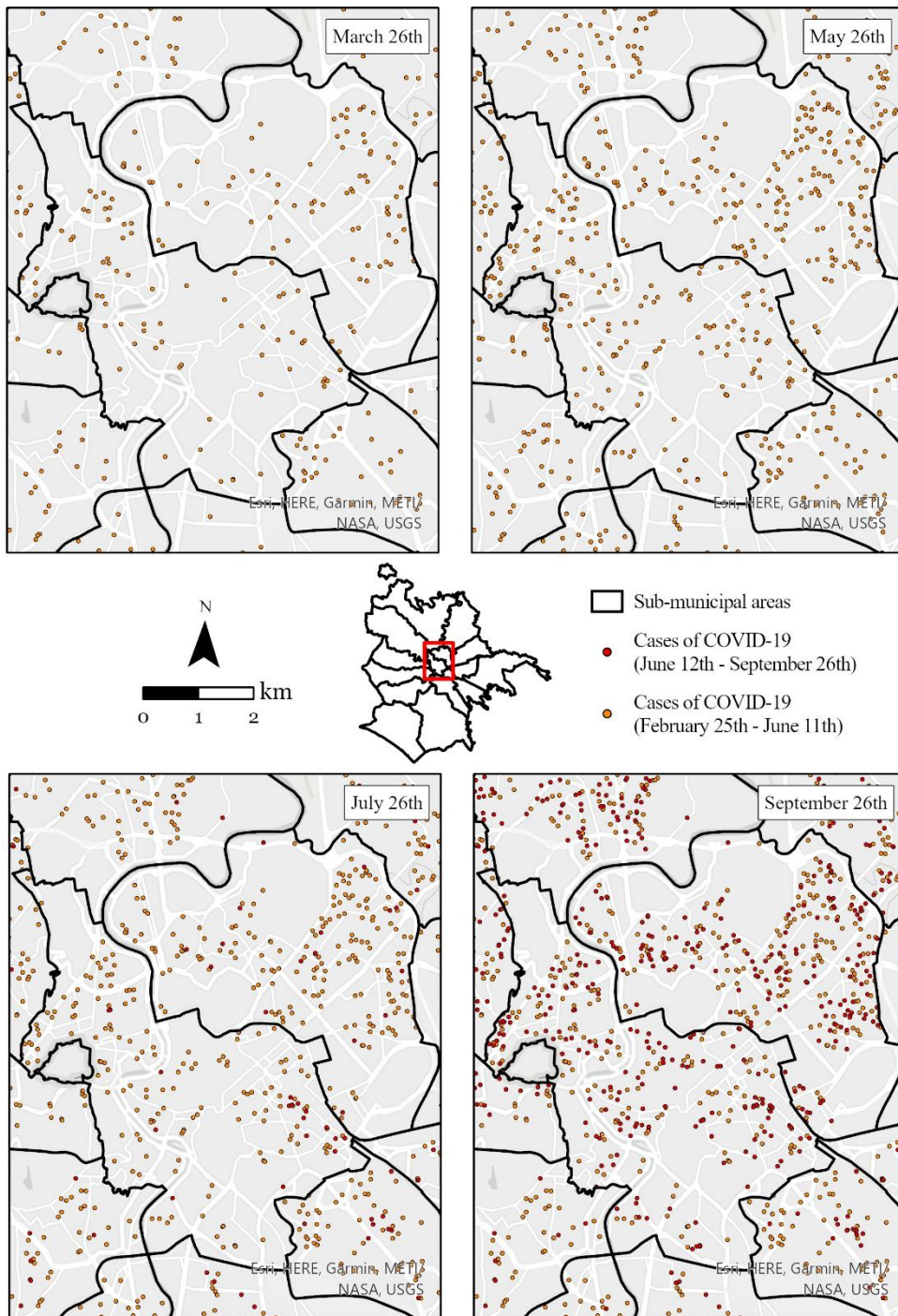
Fig. 5b. Four screenshots extracted by the simulator regarding the total number of cases of COVID-19 in a zone of the Rome centre, for the period March 26th - September 26th, on the basis of the data provided by the UOC Hygiene and Public Health Service – Local Health Unit Rome 1, over a Light Gray Canvas as background template and with sub-municipal areas of Rome.
Source: Authors' elaboration.

In order to provide an exemplifying contribution at detailed geographical scale, with **Fig. 5b** we have focussed the attention on a zone of Rome centre, extracting by the simulator four screenshots with bimonthly cadence. It is possible to appreciate the analytical capacity to make in-depth, in terms of applied and interdisciplinary research, intervention planning, targeted closures, interventions weighed on the dynamics in place and distributive patterns. Practically, it is possible to identify – also changing the background template – the streets and buildings where the number of cases is high and tend to rapidly increase, and at the same time it is possible to distinguish clusters and axes which should be immediately kept under particular observation as potential widespread and recharge basins.

5. CONCLUSIONS

The here presented dynamic simulator, which can be consulted in video mode on the basis of a specific timeline and according to different time intervals (also every 24 or 48 hours), shows the continuous thickening of points and make it possible to identify, on the basis of the data provided by the UOC Hygiene and Public Health Service – Local Health Unit Rome 1, clusters, patterns and trends, underlining the importance of having a similar application in the surveillance and analysis of the disease.

This simulator is also predisposed and configured to represent only the new cases and remove from the general count those recovered and/or the deceased, through a system of switching and turning off. A similar function makes it possible to geovisualise only the new criticalities, progressively focussing the attention on the different thickening areas with the time pass and evidencing key elements concerning the different weeks, months and waves.

Moreover, the simulator is predisposed to obtain aggregate data i.e. for census sections (CS), census areas (CEA) and sub-municipal areas (SCA), also with the addition of graphs to represent the data subdivided by sex and classes of age. Therefore, it is possible to elaborate choropleth maps that become very useful above all in the case of many data which tend to overlap for the number of cases and the proximity of the addresses. Similar choropleth maps, which can derive from geocoding processes and dot maps, return explanatory aggregate digital representations and would be able to illustrate indexes i.e. built as a ratio between the number of cases and number of residents (also according to the age of the population), number of cases and number of beds in intensive care, number of deaths due to COVID-19 and total deaths etc., above all if a harmonic and interactive system of data collection was set up and in relation to demographic and social-healthcare data of official statistics.

Among the various other perspectives that are opened for future research (reducing the geographical scale) and that can draw added value from models and simulators like the ones here presented are also those of correlating data on positives and mortality-lethality with data on environmental aspects inferable by remote sensing and Earth observation, such as temperatures and heat waves, humidity and precipitation, pressure and winds speed, pollution and the presence of fine dust (which can be loaded as superimposable layers).

In fact, disease digital mapping and GIS methods for efficacious exploration, modelling and visualisation can be used not only to detect, identify and show spatial and temporal distribution, clusters and hotspots of COVID-19, but also to explore and analyse relationships of COVID-19 with other factors, revealing a wide set of the most up-to-date applied approaches in the fields of health and medical geography and spatial epidemiology (Fatima et al., 2021, 11-12).

We agree that detailed spatial-temporal mapping and analysis provide a significant picture regarding where the confirmed cases of COVID-19 tend to be concentrated and can also help to evaluate and verify possible correlations. From the quantitative and qualitative points of view it is possible to differentiate in dynamic digital elaborations and video modes the areas with the highest concentration of cases from the zones with low concentration and the territorial contexts that are in the transition range; so this applicative and scientific approach proves to be relevant in supporting social, health and sanitary actions and for working in the perspectives of real-time surveillance and contagion prevention (da Silva et al., 2021, 15). At the same time, it can be useful to increase and

optimise the location of integrative health services and structures in specific places and to improve health care delivery with ad hoc measures (Dumitrache et al., 2020, 1). Therefore, painstakingly studying the spatial-temporal dynamics of COVID-19 is a key action to its mitigation, and GIS elaboration, disease mapping and interdisciplinary data analysis are becoming recurrent topics, also in order to inspire new beneficial researches, models and reflections (Franch-Pardo et al., 2020, 9).

We hope that the dynamic space-time diffusion simulator in a GIS environment here presented to tackle the COVID-19 emergency and the relative foundations of application methodology can provide inputs also in the direction of experimenting innovative and harmonised geotechnological solutions to be ready, with quick and effective reaction, in the case of ill-fated future need.

ACKNOWLEDGEMENTS

R E F E R E N C E S

Aschwanden, C. (2021) Five reasons why COVID herd immunity is probably impossible. *Nature*, 591, 520–522.

Atek, S., Pesaresi, C., Eugeni, M., Gaudenzi, P., De Vito, C., Cardinale, V., Mecella, M., Maraschini, A., Pistillo, P. & Vora, A. (2021) An Earth Observation Cognitive System in Response to Sars-Covid-19 Emergency. *72nd International Astronautical Congress 2021*, Abstract, Paper ID: 64144 oral.

Avand, M., Moradi, H. & Ramazanzadeh lasboyee, M. (2021) Using machine learning models, remote sensing, and GIS to investigate the effects of changing climates and land uses on flood probability. *Journal of Hydrology*, 595, 125663.

Cosgriff, C.V., Ebner, D.K. & Celi, L.A. (2020) Data sharing in the era of COVID-19. *Lancet Digit Health*, 2, 5, e224.

Cristea, C. & Jocea, A.F. (2016) GIS Application for Wind Energy. *Energy Procedia*, 85, 132–140.

Dangermond, J., De Vito, C. & Pesaresi, C. (2020) "Using GIS in the Time of the COVID-19 Crisis, casting a glance at the future. A joint discussion". *J-READING (Journal of Research and Didactics in Geography)*, 1, 9, 195–205.

Dardanelli, G., Marretta, R., Santamaria, A.S., Streva, A., Lo Brutto, M. & Maltese, A. (2017) Analysis of Technical Criticalities for GIS Modelling an Urban Noise Map. *Geographia Technica*, 12, 2, 41–61.

da Silva, C.C. et al. (2021) Covid-19 Dynamic Monitoring and Real-Time Spatio-Temporal Forecasting. *Frontiers in Public Health*, 9, 1–17.

de Kadt, J., Götz, G., Hamann, C., Maree, G. & Parker, A. (2020) Mapping vulnerability to COVID-19 in Gauteng. GCRO Map of the Month, Gauteng City-Region Observatory. Available at https://gcro.ac.za/outputs/map-of-the-month/detail/mapping-vulnerability-to-covid-19/.

Desjardins, M.R., Hohl, A. & Delmelle, E.M. (2020) Rapid surveillance of COVID-19 in the United States using a prospective space-time scan statistic: Detecting and evaluating emerging clusters. *Applied Geography*, 118, 1–7.

Dumitrache, L., Nae, M., Simion, G. & Talos, A.-M. (2020) Modelling Potential Geographical Access of the Population to Public Hospitals and Quality Health Care in Romania. *International Journal of Environmental Research and Public Health*, 17, 1–18.

Fatima, M., O'Keefe, K.J., Wei, W., Arshad, S. & Gruebner, O. (2021) Geospatial Analysis of COVID-19: A Scoping Review. *International Journal of Environmental Research and Public Health*, 18, 1–14.

Franch-Pardo, I., Napoletano, B.M., Rosete-Verges, F. & Billa, L. (2020) Spatial analysis and GIS in the study of COVID-19. A review. *Science of the Total Environment*, 739, 1–10.

Horton, R. (2021) Offline: The lessons of smallpox eradication for COVID-19. *Lancet*, 2021, 3961951.

Kamel Boulos, M.N. & Geraghty, E.M. (2020) Geographical tracking and mapping of coronavirus disease COVID-19/severe acute respiratory syndrome coronavirus 2 (SARS-CoV-2) epidemic and associated events around the world: how 21st century GIS technologies are supporting the global fight against outbreaks and epidemics. *International Journal of Health Geographics*, 19, 8.

Kupferschmidt, K. (2020) Europe is locking down again-but its strategy is unclear. *Science*, 370, 644–645.

Lloyd-Sherlock, P., Sempe, L., McKee, M. & Guntupalli, A. (2021) Problems of Data Availability and Quality for COVID-19 and Older People in Low- and Middle-Income Countries. *Gerontologist*, 61, 2, 141–144.

Looi, M.K. (2020) COVID-19: Is a second wave hitting Europe? *BMJ*, 371, m4113.

McGill COVID19 Vaccine Tracker Team (2021) COVID19 Vaccine Tracker. Available at https://covid19.trackvaccines.org/.

Ministero della Salute (2021). Report Vaccini Anti COVID-19. Available at www.governo.it/it/cscovid19/report-vaccini/.

Nistor, M.-M., Rahardjo, H., Satyanaga, A., Leong, E., Hao, K.Z., Sham, A.W.L. & Wu, H. (2019) GIS-Based Approach to Identify the Suitable Locations for Soil Sampling in Singapore. *Geographia Technica*, 14, 1, 103–117.

Pesaresi, C. (2020) A geographical and crosscutting look at the COVID-19 pandemic in an international framework. Introduction. *J-READING – Journal of Research and Didactics in Geography*, 2, 9, 13–19.

Pesaresi, C., Migliara, G., Pavia, D. & De Vito, C. (2020a) Emergency Department Overcrowding: A Retrospective Spatial Analysis and the Geocoding of Accesses. A Pilot Study in Rome. *ISPRS International Journal of Geo-Information*, 9, 579, 1–26.

Pesaresi, C. & Pavia, D. (2021) Radio Base Stations and Electromagnetic Fields: GIS Applications and Models for Identifying Possible Risk Factors and Areas Exposed. Some Exemplifications in Rome. *ISPRS International Journal of Geo-Information*, 10, 3, 1–21.

Pesaresi, C., Pavia, D. & De Vito, C. (2020b) Three geotechnological proposals to tackle health emergencies and the monitoring of infectious diseases. Inputs from the COVID-19 pandemic for future preparedness. *Bollettino della Associazione Italiana di Cartografia*, 170.

Riffe, T., Acosta, E. & COVerAGE-DB project team (2020) COVerAGE-DB: A database of age-structured COVID-19 cases and deaths. Preprint available at https://www.medrxiv.org/content/10.1101/2020.09.18.20197228v2.full.pdf, 1–13.

Smith, C.D. & Mennis, J. (2020) Incorporating Geographic Information Science and Technology in Response to the COVID-19 Pandemic. *Preventing Chronic Disease*, 17, E58, 1–7.

Tse, E.G., Klug, D.M. & Todd, M.H. (2020) Open science approaches to COVID-19. *F1000Research*, 9, 1043, 1–6.

Valjarević, A., Milić, M., Valjarević, D., Stanojević-Ristić, Z., Petrović, L., Milanović, M., Filipović, D., Ristanović, B., Biljana, B. & Lukić, T. (2020) Modelling and mapping of the COVID-19 trajectory and pandemic paths at global scale: A geographer's perspective. *Open Geosciences*, 12, 1603–1616.

Wolkewitz, M. & Puljak, L. (2020) Methodological challenges of analysing COVID-19 data during the pandemic. *BMC Medical Research Methodology*, 20, 81, 1–4.

Xiong, Y., Wang, Y., Chen, F. & Zhu, M. (2020) Spatial Statistics and Influencing Factors of the COVID-19 Epidemic at Both Prefecture and County Levels in Hubei Province, China. *International Journal of Environmental Research and Public Health*, 17, 1–26.

Xu, M., Cao, C., Zhang, X., Lin, H., Yao, Z., Zhong, S., Huang, Z. & Duerler, R.S. (2021) Fine-Scale Space-Time Cluster Detection of COVID-19 in Mainland China Using Retrospective Analysis. *International Journal of Environmental Research and Public Health*, 30, 18, 3583.

DELINEATION RADAR ZONES OF GLACIERS
IN THE ALA-ARCHA VALLEY OF KYRGYZ REPUBLIC

Emilbek ZHOLDOSHBEKOV[1] ⓘ **, Vaibhav GARG[2]** ⓘ **, Praveen Kumar THAKUR[2]** ⓘ **,**
Murataly DUISHONAKUNOV[1] ⓘ **, Mihai VODA[3]** ⓘ

ABSTRACT:
Glaciers are a critical source of freshwater, especially during the lean season. Globally, the glaciers are losing their mass balance rapidly under the influence of climate change. In view of this, the regular study of these glaciers is very vital. However, field-based studies of most of the glaciers is a daunting task. On the contrary, emerging geospatial technology may play an important role in the studies of glaciers. The equilibrium line altitude (ELA) of the glaciers has been considered an essential indicator of climate change. There are numerous methods to delineate the equilibrium line of a glacier; however, each has its own merits and demerits. In the present study, the synthetic aperture radar (SAR) remote sensing-based approach has been used for identifying the ELA of glaciers in the Ala-Archa River catchment of Kyrgyzstan from 2015 – 2019. Initially, the glacier radar zones were mapped using the Sentinel-1 SAR datasets of each year under consideration. It was found that mainly the middle percolation, lower percolation, and bare-ice zones along with debris cover-ice are present in the glaciers. It was observed that the percolation refreeze zone covers approximately 40%, and the Bare-Ice zone covers 48% of the total area. Considering the boundary of lower percolation and bare-ice zone as ELA, the ELA of each glacier in each year was estimated. The lowest ELA of 3462 m was observed in 2018, whereas the highest (4309 m) was recorded in 2019. It was noticed that the trend of ELA is consistently increased from 3839.25 m in 2015 up to in 3868.29 m 2019. The temporal analysis of glacier radar zone estimation and ELA may help in studying the impact of climate change on glacier retreat and mass balance change. It can be concluded that geospatial techniques can make the glacier change studies possible without field survey. However, to validate the results of the study, field observations are a must.

Key-words: *Glacier, Radar zone, Ala-Archa river valley, SAR imagery, Sentinel-1.*

1. INTRODUCTION

The cryosphere is one of the geographical spheres of the Earth, which is characterized by the presence of ice (Dostovalov and Kudryavtsev, 1967). Glaciers are formed as a result of the accumulation and transformation of solid precipitations. However, both these parameters are largely affected by climate change. Most of the glaciers over the globe are showing negative mass balance, and their Equilibrium Line Altitude (ELA) is shifting upwards, or glaciers are treating continuously (Beniston et al. 2018; Das and Chakraborty 2019). It is predicted that most of the glaciers in the High Mountain Asia region may lose their mass balance of approximately 64 ±5% by the end of the century (Hock et al., 2019).

---

[1]*Department of Physical Geography, Kyrgyz National University, Bishkek, Kyrgyz Republic,*
  dzoldoshbekov@mail.ru, dmuratalyt@mail.ru
[2]*Water Resources Department, Indian Institute of Remote Sensing, Dehradun, Uttarakahnd, India,*
vaibhav@iirs.gov.in, praveen@iirs.gov.in
[3]*Director of International Relations, Dimitrie Cantemir University, Targu Mures, Romania,*
mmvoda@yahoo.com

As glaciers are one of the major freshwater sources, the runoff from them is especially important in summer and early autumn when the water demand is high and the flowis minimal (Bolch2015). Therefore, their mass loss may impact water resources availability in the region. It is to be noted that the ELA has been considered as one of the critical parameters of climate change impact. Further, the glacier area below the ELA may be considered as ablation and the area above it as accumulation. The ratio of accumulation area and the total area is known as the area accumulation ratio (AAR) (Meier, 1962). It is again an important parameter for glacier mass balance studies. The accumulation area ratio has a significant effect on the retreat or advance of the glacier (Brahmbhatt et al., 2014), because both parameters are highly affected by air temperature and precipitation.

On the contrary, these are located in high altitudes or rugged terrain; therefore, their study through physical field surveys or visits is a daunting task. Geospatial technology has emerged as an effective tool in mapping and monitoring these glaciers at regular intervals throughout the year (Garg et al., 2021). Initially, the optical remote sensing data were extensively used for glacier mapping. Glacier mapping helps to generate snow line, consequently equilibrium linealtitude, accumulation area ratio. The equilibrium line is usually considered as the snow line at the end of the glacier melt season. A clear relationship exists between its position and the annual mass balance (Meier at all., 1962). By continuing the same survey for several years, temporal changes of such mentioned elements can be generated. Most glacier dynamics researches and glacier mapping in Kyrgyzstan are based on optical images (Aizen et all., 2007; Shabunin 2018). The optical remote sensing data has constraints with respect to the presence of clouds, due to which glaciers may not be visible during a large period of time in a year.

However, with the advent of synthetic aperture radar (SAR) technology, it is now possible to study the glaciers anytime in a year. Radar surveying has a number of advantages and features compared to optical and infrared sensors (Mouginot et al., 2017; Brancato et al., 2020; Mohajeraniet al., 2021):

- Meteorological independence: mostly the microwave frequencies remains unaffected by cloud cover or aerosols
- Independence from light conditions: Observation process during dark time is possible
- High accuracy in measuring geometric features of the target
- Possibility of making 3D models and mapping
- Ability to obtain physical parameters such as dielectric constant and structure

SAR has now become the most suitable technique in cryosphere monitoring and observation. The technology has been utilized for the determination of dry and wet snow/ice, glacier radar zone mapping, glacier surface velocity, etc. extensively. The main goal of this research was to map different glacier radar zones for better estimation of ELA. Earlier, the optical data of the end of the ablation period was generally used for the purpose; however, during this time, the probability of cloud in the images is high. Therefore, the ELA retrieval after or before this time period may be erroneous. Further, the ELA is usually identified in these images based on visual interpretation. The accuracy of the identified ELA again depends upon the capabilities of the observer. The researchers have also proposed hypsometric or geodetic approaches for the ELA with the use of a digital elevation model (DEM). However, the availability of DEM with high Spatio-temporal resolution and accuracy is further a constraint in such analysis. However, the SAR data may have different backscattering in different seasons, attributing to snow/ice conditions. Exploiting the backscattering mechanism in different seasons, researchers have identified distinct glacier radar zone. It is considered that the boundary of the bare ice zone and the adjacent wet snow or percolation-refreeze zone is generally called an actual transient snow line. Therefore, the present study is performed in virtue of Sentinel-1 SAR datasets. Sentinel-1 is the Copernicus Program satellite which was developed by European Space Agency (ESA). C-band sensors of Sentinel-1A satellites have 10 m resolution and swath up to 400 km along with the temporal resolution of 12 days.The glaciers in Ala-Archa River Basin are considered for the present study. The basin water is the main source to the capital city of Kyrgyzstan, i.e., Bishkek and arable lands of Chui valley.

2. STUDY AREA

The high elevation of the Tien Shan mountains (JengishChokusu Peak 7439 m and 4895 m in Kyrgyz Ala-Too range) allows forming permanent ice, snow, and firn in high altitudes. The Ala-Archa river catchment remains one of the most glacierized zones, as it is surrounded bythe highest and central part of the Kyrgyz Ala-Too mountain range in the northern Kyrgyz Republic. The basin is located between 42°15'00" – 43°15'00" N latitude and 74°15'00" – 75°00'00" E longitude as shown in **Fig. 1**. Glaciers occupy 29.8 km² between the elevation range from 4716 to 3271 m (Zholdoshbekov 2020).The Kyrgyz Ala-Too (Kyrgyz Range) represents the north-western part of the Tien Shan mountain system. Kyrgyz Ala-Too is the second most extensive mountain range after the Kakshaal range in Tien Shan. It extends in a longitudinal direction over 454 km (Atlas of Kyrgyz SSR, 1987).It is separated from other parts of the Tien Shan Mountains from the east side with Boom (Boam) canyon, from the south side with Kochkor, Suusamyr, and Talas intermountain depressions. As Voda et al. (2019) pointed out, the morphometric characteristics of the river basin are very important. It can be seen that the slopes are asymmetrical;on the southern side, it is short and steep, whereas on the northern slope gentle and long. The northern slope is fractured with deep (1000-1500) valleys such as Ala-Archa in the meridional direction. Altitudes range from 630 m on the Ala-Archa river mouth to 4895 m on BatyshAlamudun peak, the highest point of the Kyrgyz Ala-Too range.The lower part of the Ala-Archa river basin contains part of Chui valley. The total area of the catchment is 270 km².

According to data of hydrometeorolgical sevice of Kyrgyz Republic the mean annual discharge of the Ala-Arch ariver is 4.69 m³/sec (Kashka-Suu river mouth). The Ala-Archa river contributes the water from glacier and snowmelt water (Water resources of USSR 1973). Water from the Ala-Archariveris used for irrigation using drainage canals andthe Ala-Archa reservoir. In the mountainous part of the catchment, a national park was established in 1976 with the same name.
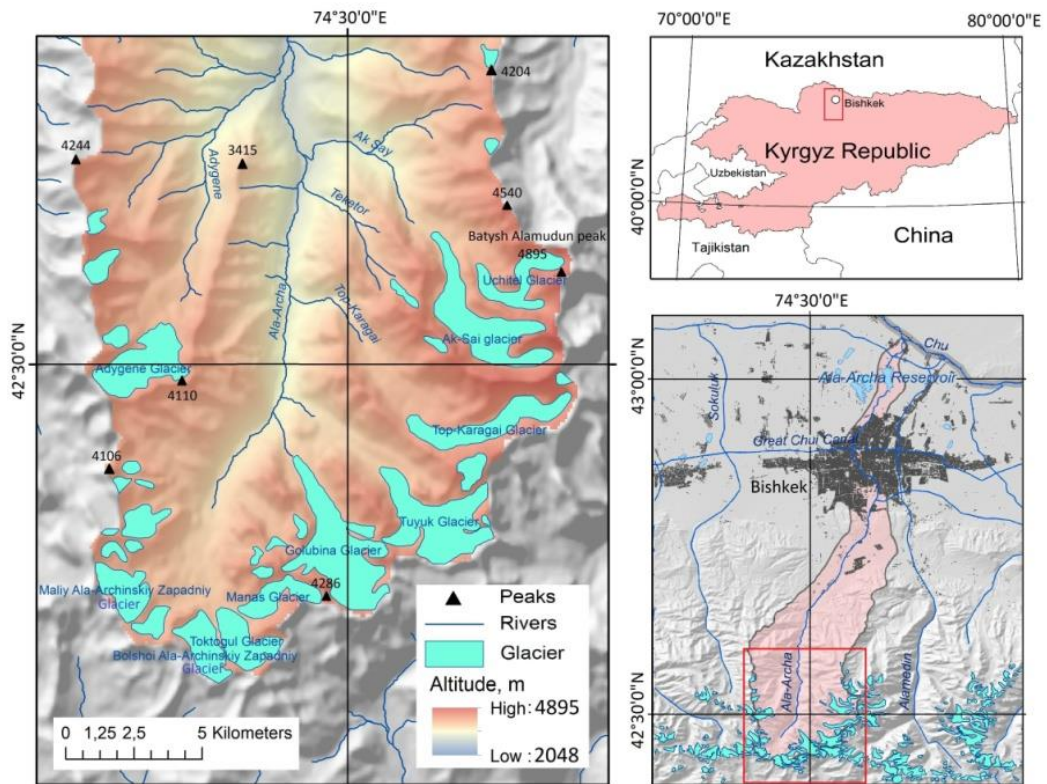

Fig. 1. The location oftheAla-Archariver catchmentand its glaciers inthe Kyrgyz Republic (SRTM DEM utilized for physical map, topography shade generation and RGI for distribution of glaciers).

3. DATA AND METHODS

Variation in glacier's ELA is an important indicator of climate change impact (Thakur et al., 2016; Gupta et al., 2018).Therefore, the identification of ELA with higher accuracy is critical in such studies. Generally, the optical remote sensing data has been used for the delineation of ELA. However, the data suffer from the availability of cloud-free data during and of ablation period. On the other hand, the geodetic methods require a high-resolution DEM dataset for the year of analysis. Considering the limitations of optical remote sensing data and DEMs, in the present study, SAR data-based technique has been adopted, as shown in **Fig. 2**. The temporal Sentinel-1 C-band VV Polarization SAR datasets for the years 2015-2019 were utilized (details are provided in **Table 1**). Cross-polarization (VH or HV) gives information based largely on volume scattering, whereas co-polarized signals (HH or VV) are large contributions from surface scattering (Massom and Lubin, 2006). According to Fu et al. (2020), the cross-polarization is practically comparable to the co-polarization having an absolute value lower than 6 dB.

Our interest was to retrieve surface backscatter;in this study, images with VV polarization were utilized. The data was initially pre-processed for orbit, radiometric and geometric corrections. Co-registration is applied using external DEM, i.e., SRTM 90 m. After taking the subset of the area of interest,the geometric correction was completed. After geometric correction due to side-looking characteristics of SAR image, some distortions could be formed. Layover shadows can be reached 3% among glacier areas in the current research area. Finally, the intensity values were converted into dB.Then, theRGB composite of the SAR data of three different seasons was generated for each year under consideration. In the northern slope of the Kyrgyz Ala-Too range, the peak of dry snow occurs at the end of January and the start of February, wet snow in May, and the peak of glacier melting at the end of August. The different tonal variations in the backscattering of composite images represent different glacier radar zones (Mahagaonkar, 2019). Therefore, the images from spring (wet snow facies may occur), summer (peak of glacier melting), and winter (peak of dry snow accumulation) seasons, when glacier surface remains in different backscatter conditions, were used. The spring image was used in Red, summer in Green, and winter for the Blue channel to generate RGB composite.
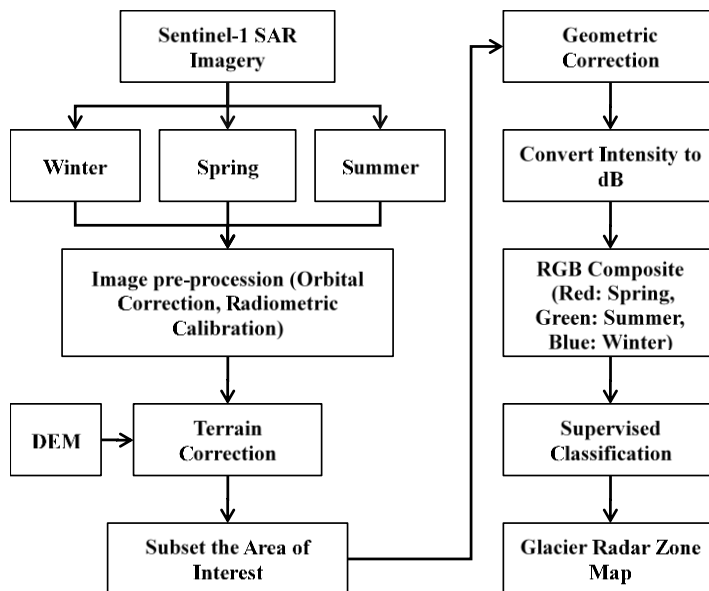
Fig. 2. Methodological flowchart for classification glacier zones by using multi-temporal Sentinel-1 SAR data.

List of C-band Sentinel-1 datasets used for glacier radar zone estimation.

Mission	Product type	Beam mode	Orbit	Orbit type	Polarization	Date
S1A	GRDH	IW	4124	A	VV	11.01.2015
S1A	GRDH	IW	5699	A	VV	29.04.2015
S1A	GRDH	IW	7449	A	VV	27.08.2015
S1A	GRDH	IW	9724	A	VV	30.01.2016
S1A	GRDH	IW	11124	A	VV	05.05.2016
S1A	GRDH	IW	12874	A	VV	02.09.2016
S1A	GRDH	IW	15149	A	VV	05.02.2017
S1A	GRDH	IW	16374	A	VV	30.04.2017
S1A	GRDH	IW	18124	A	VV	28.08.2017
S1A	GRDH	IW	20224	A	VV	19.01.2018
S1A	GRDH	IW	21799	A	VV	07.05.2018
S1A	GRDH	IW	23549	A	VV	04.09.2018
S1A	GRDH	IW	25627	A	VV	25.01.2019
S1A	GRDH	IW	27027	A	VV	01.05.2019
S1A	GRDH	IW	28777	A	VV	29.08.2019

S1A: Sentinel-1 A; GRDH: Ground Range Detected High Resolution; IW: Interferometric Wide (IW) swath;
A: orbit type represents ascending pass; VV: Vertical-Vertical polarization.

The entire analysis till this step was carried out in SNAP software. In the RGB image, the debris-covered area would appear bright due to high scattering in all seasons, bare ice – greenish, low percolation zone as blue/purple, and middle percolation zone with pink/magenta color. A bare ice zone represents the ablation zone of the glacier. An ablation zone is also characterized by the presence of a surface water flow of melted ice. If crevasses are more and denser, the surface flows may decrease. Clean water and pure ice have a low dielectric constant. Therefore, signals in the microwave region will penetrate into pure ice thickness up to 10 meters (Woodhouse, 2006). Due to the high percolation of microwaves, the bare ice zone appears dark in RGB of the SAR images.

Percolation zones: After the co-registration process, we can see in RGB image three high, middle, and low percolation zones. Low percolation takes place in dry snow, which has less liquid content and high porosity. This phenomenon can be observed at high altitudes with an annual temperature is about -25°C. During the snowmelt, due to excessive water content, backscattering may decrease. In RGB image middle percolation zone appears in pink or purple, low percolation area in blue color. In the case of icefalls and dense crevasses, backscatter increases due to specular reflectance due to high surface roughness. Debris-covered ice can be classified as different glacier zone due to different physical properties. Ice surface moraine, which is represented by debris cover, closes direct sun radiation and delays ice melting. Due to high reflectivity by the low dielectric constant and surface roughness, debris covers appear from SAR imagery with light and grey light color. Further details on glacier radar zones may be found at Partington (1998); Rau et al. (2000).

For better extraction of glacier radar zone, the Support Vector Machine (SVM) classification technique was used. This algorithm is suitable for classifying complex and noisy images. It separates the classes with a decision surface that maximizes the margin between the classes (SVM Tutorial, 2020). The literature suggested that the algorithm is most suitable for snow cover classification (Tsai et al., 2019; Alifu et al., 2020). For classification, signature sets were chosen according to backscattering characteristics and represented by the colors of each zone in the RGB image. SVM classification was performed in ENVI software. The following parameters were chosen for the classification: Kernel Type as Radial Basis Function, $\gamma = 0.33$, and the Penalty Parameter as 100. Glaciers of Ala-Archa valley are classified in the following classes based on backscattering phenomena: debris-covered ice; bare ice; low and middle percolation zones. In the classified image, the debris-covered area was represented with yellow color, bare ice–brown, low percolation zone with blue, and middle percolation zone as pink color. It is worth noting that it is hard to distinguish the

shadow region which appears after geometric correction and debris-covered areadue to the high backscattering of both in SAR composite.However, shadowareas can be differentiated by terrain correction using SNAP software. Generally, the line demarcating the bare-ice and lower percolation/wet-ice zone is considered as ELA. In this way, the ELA of each year for each glacier of Ala-Archa valley was identified. The identified ELA was then overlaid on the ALOS PALSAR 12.5 m DEM to determine the elevation in each year. The change in elevation would suggest the impact of climate change.

4. RESULTS

The flow in the Ala-Archa River is very vital for Bishkek, the capital of the Kyrgyz Republic. It mainly depends on the melting of snow or glaciers in the valley. However, most of the glaciers are showing negative balance across the globe under changing climate. The ELA of a glacier is being considered one of the primary indicators of climate change. Thereare a number of techniques to estimate the ELA of a glacier; each has its own advantages and disadvantages. For the present analysis, SAR based technique has been used. Initially, the glacier radar zones of all the glaciers falling in Ala-Archa River valley were mapped using the Sentinel-1 SAR data for 2015-2019.

4.1. Glacier Radar Zone classification

The SAR images of different seasons in each year were stacked to generate an RGB composite, as mentioned in the Method Section. As the liquid water content of a glacier changes due to season, the glacier surface features would reflect different tonal variations. For the example, the SAR images of the different season and RBG composite of the year 2019 is shown in **Fig. 3**. The tonal variation (as discussed in the Method section for each zone) of the backscatter values in the composite was then used for the identification of glacier radar zones.
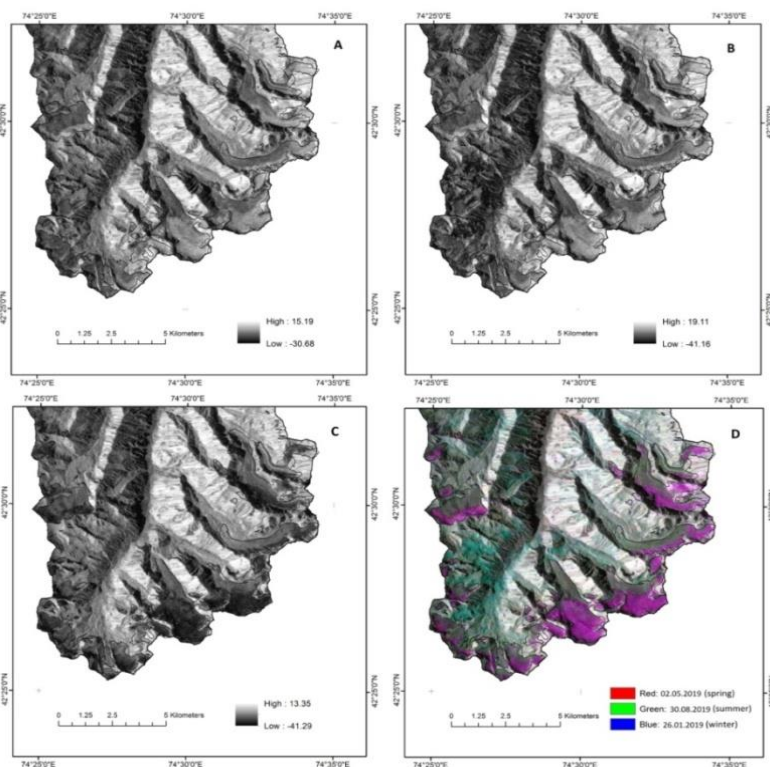

Fig. 3. Backscatter intensity images with VV polarization for A) 26.01.2019, B) 02.05.2019, C) 30.08.2019, and D) RGB composite image created by using multi-temporal backscatter images.

The glaciers of Ala-Archa valley showed three distinct zones bare ice, low and medium percolation, and debris-covered ice. Further, the change in ablation and accumulation zones over time can be verified by temporal variations of glacier radar zones.

To assess the area under each zone, the RGB composites of each year under consideration were classified using the SVM method, as discussed earlier. The results of classified glacier radar zones are provided in **Fig. 4**. The temporal changes in each zone area are provided in **Table 2**. Share of middle percolation zone estimated around 40% from the glacier area. It has the maximum area in Golubina and Tuyuk glaciers, as seenin **Fig. 4**. Ablation zone has the greatest area in Adygine, Top-Karagai, Maliy Ala-Archinskiy Zapadniy, Bolshoi Ala-Archinskiy Zapadniy glaciers.

The highest variability of glacier zones is observed in small glaciers. In some years, small glaciers overlay under almost the same glacier zone, and this statement can be rapidly changed next year. Here the accumulation zone, which comprises low and middle percolation areas, occupies 37.3% in 2015, 43.64% in 2017, 43.54% in 2018, and 44.94 in 2019 from the total area of the glacier. It can be seen that the accumulation zone area has increased by around 8.54% in the observed years. The debris-covered zone was keeping around 10% of the total area during the study period. The bare ice zone represents the ablation zone. It can be seen that the bare-ice zone maintains an area of around 48% throughout except for the year 2019.
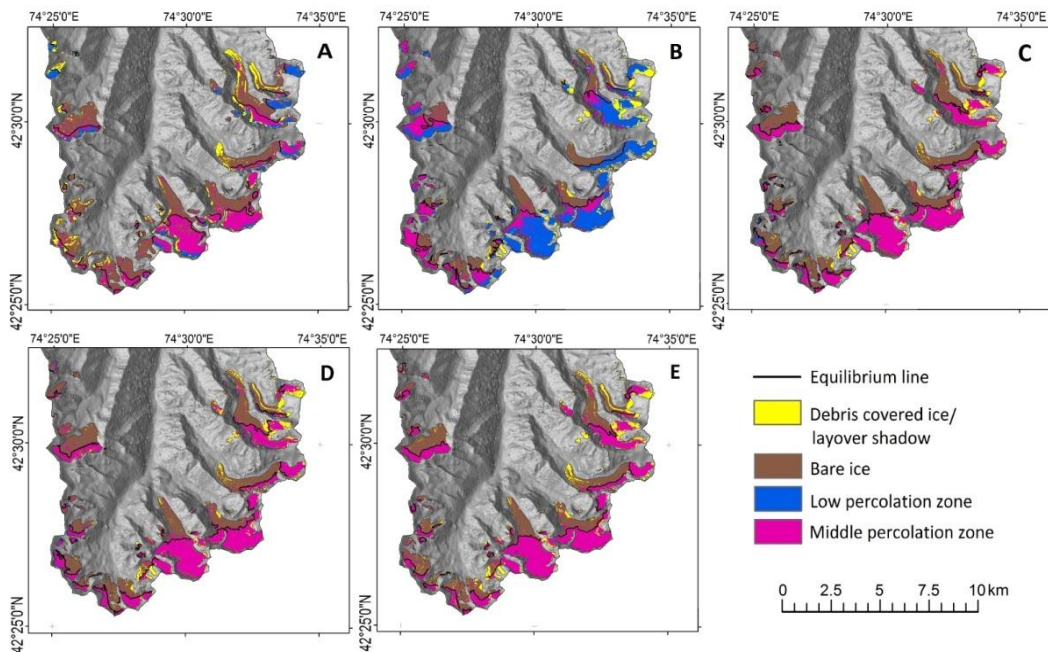
Fig. 4. Classified maps of Ala-Archa valley glacier for A) 2015, B) 2016, C) 2017, D) 2018 and E)2019. Hill shaded map on the background generated by using ALOS PALSAR DEM.

Table 2.

Annual changes of glacier radar zones in Ala-Archa valley (in %).

Glacier faces	2015	2016	2017	2018	2019
Debris covered ice	14.39	10.76	8.47	9.76	12.96
Bare ice	48.29	27.28	48.18	46.70	42.09
Middle percolation	28.37	22.89	41.78	41.97	43.88
Low percolation	8.93	39.05	1.86	1.57	1.06

4.2. ELA Analysis

The boundary between the bare ice zone and low percolation area is generally identified as the equilibrium line. Overlaying the equilibrium line over the DEM,one can generate ELA. For ELA calculation ALOS PALSAR DEM was utilized as mentioned in the previous section. The mean value of ELA was found to be 3853.4 m. According to Aizen et al., (1997) the ELA of the Ala-Archa glaciers was 3848 m. The lowest value of ELA 3462 m was observed in 2018. The highest elevation of the snow line was recorded in 2019 (4309 m). The lowest elevation of ELA was observed in 2019 was 3662 m which was close to the mean ELA (**Table 3**).

The high variation of minimum and maximum values of ELA can be explained due to the location of an ablation zone in a higher elevation (**Fig. 4**). The wind blows snow cover, and ice can be bared in high elevation zones. Also, due to different expositions, ELA gives high-altitude ranges. The trend of ELA for each glacier is shown in **Fig. 5**. Most of the small glaciers are coming in the ablation zone. The linear trend of ELA increased from 3839.25 m in 2015 to 3868.3 m in 2019 (**Fig. 5**). The variation observed in the shift of ELA or change in glacier radar zones is mainly attributing to climatic conditions around the glaciers.

Table 3.

The statistics of ELA of the glaciers in the Ala-ArchaBasin.

Assessment year	ELA (in m)		
	Minimum	Maximum	Mean
2015	3588	4302	3892.09
2016	3499	4095	3762.31
2017	3963	4256	3865.96
2018	3462	4261	3880.34
2019	3662	4309	3869.37
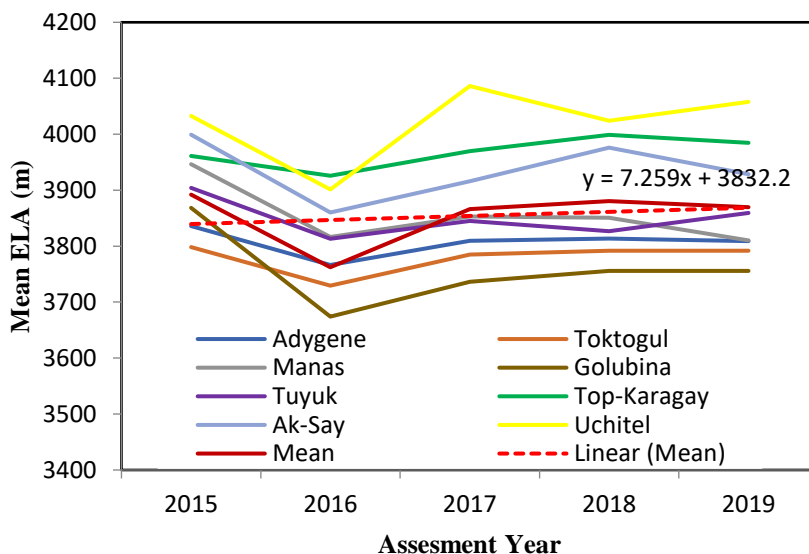
Fig. 5. ELA of large glaciers 2015-2019.

The analysis showed that the area of the Bare-Ice zone is reducing and the Percolation zone is increasing. This means more accumulation has been taken place. It is recommended that the findings must be validated with the field observations. As the position of ELA is driven by climatic factors, further, the meteorological data on precipitation and temperature must be analyzed. To detect the trend in ELA, long-term remote sensing data should be analyzed along with climatic data. With the analysis of 5 years of data, it can't be said that glaciers are generally retreating or advancing.

5. DISCUSSION AND CONCLUSIONS

It is generally agreed that SAR imageries are one of the most convenient tools in glacier radar zone mapping (Fu et al., 2020;Huang et al., 2013; Akbari et al., 2013; Zhou and Zheng, 2017). Cloud-free images make the SAR applications indispensable in glacier studies. The evidence suggests increasing the implementation of SAR data in different glacier studies (radar zone; dray or wet ice; surface velocity; etc.) in the Tian Shan region. Therefore, the methodologies of glacier investigations and their local seasonal specifics can be created. The same kinds of manuals are prominent for the Himalayan and Alpine regions.

The objective of this work was to map radar zones and concomitant parameters estimation of the glaciers in Ala-Archa valley using the Sentinel-1 SAR datasets. The 12-day repeat cycle of the Sentinel-1 product is quite suitable, as an analysis requires season data. Glaciers of Ala-Archa valley are classified into 4 glacier radar zones, namely bare ice, low and middle percolated zones, and debris-covered areas. A high percolation zone is not observed in this study area. Accompanying parameters like trends of ELA, AAR are improving glacier retreat tendency.

The line demarcating the bare ice and lower percolation zones are termed the ELA. A general upward shift in ELA was found; in some large glaciers (Manas, Tuyuk, Ak-Sai), ELA was showing a downward shift as well. It was noticed that the mean ELA has come down by around 23 m from 2015 to 2019.

Research limitations contain several important points:

- Side-looking view geometry increases overlay shadow area, especially in mountainous terrain. In this situation, overlay shadow limitation can be prevented by using imagery with another track.
- Equilibrium line is provided strongly between bare ice and middle, low percolation zones. In some cases, this approach gives ambiguous value. The high amplitude of ELA is caused not only by exposition (solar angle), here also wind speed and direction is important due to exposing the ice by blowing the snowpack. Due to the instability of wind direction and speed in mountainous terrain, it is hard to estimate the occurrence of wind-bared zones.

Those points are suggested to improve the quality of the work:

- The obtained data about disposition and elevation of equilibrium line, which obtained from glacier radar zone mapping, can be utilized in glacier mass balance estimation.
- In order to better understand trends in glacier dynamics, the observation time scale should be extended.
- Same research should be provided to the entire Kyrgyz Ala-Too mountain range.
- Climatic and other products of ground observations should be implemented to validate the findings.
- In-depth analysis of the results and their causes is required.

R E F E R E N C E S

Aizen V., Aizen E., Kuzmichonok V.A. (2007) Glaciers and hydrological changes in the Tien Shan: Simulation and prediction. *Environmental Reearch. Lett*ters, 2 (4) 045019, DOI: 10.1088/1748-9326/2/4/045019.

Aizen V.B., Aizen E.M. (1997) Hydrological cycles on the north and south peripheries of mountain-glacier basins of central Asia *J.Hydrol.Proc*. 11 451-69.

Akbari, V., Doulgeris, A.P.& Eltoft, T. (2013) Monitoring glacier changes using multitemporal multipolarization SAR images. *IEEE Trans. Geosci. Remote Sens.*, 52, 3729–3741.

Alifu, H., Vuillaume, J-F, Johnson, B.A.&Hirabayashi, Y. (2020) Machine-learning classification of debris-covered glaciers using a combination of Sentinel-1/-2 (SAR/optical), Landsat 8 (thermal) and digital elevation data. *Geomorphology*, 369, 2020,107365

Atlas of Kyrgyz, SSR (1987)*Main Administration of Geodesy and Cartography of the USSR*. Atlas (in Russian)

Beniston M, Farinotti D, Stoffel M et al (2018) The European mountain cryosphere: a review of its current state, trends, and future challenges. *The Cryosphere*, 12, 759-794. https://dx.doi.org/10.5194/tc-12-759-2018.

Bolch T. (2015) Glacier area and mass balance changes since 1964 in the Ala Archa Valley, Kyrgyz Ala-Too, northern Tien Shan. *Ice and Snow*, 129(1), 28-39.

Brahmbhatt, R., Nainwal, H.& Kulkarni, A. (2014) Impact of accumulation area ratio (AAR) on glacial change: few examples of Jammu & Kashmir. *Journal of Geomatics*, 8(1), 61-65.

Brancato, V. *et al.*(2020) Grounding line retreat of Denman Glacier, East Antarctica, measured with COSMO-SkyMed radar interferometry data. *Geophys. Res. Lett.* 47, e2019GL086291.

Das, S. & Chakraborty, M. (2019) Mass balance of ChhotaShigri Glacier using dual-polarised C band SAR data. *Remote Sensing Applications: Society and Environment*, 13, 150-157.

Dostovalov B.N.&Kudryavtsev V.A. (1967) *Obsheemerzlotovedenie* [General geocryology]. Moscow: Publishing house of Moscow university.

Fu, W., Li, X., Wang, M.& Liang, L. (2020) Delineation of Radar Glacier Zones in the Antarctic Peninsula Using Polarimetric SAR. *Water*, *12*, 2620. https://doi.org/10.3390/w12092620.

Garg, V., Kudekar, A.R., Thakur, P.K. et al. (2021). Glacier Change Studies under Changing Climate Using Geospatial Tools and Techniques. *J Indian Soc Remote Sens,* https://doi.org/10.1007/s12524-021-01388-5

Gupta, S.K., Negru, R.&Voda, M. (2018). The Indian Himalaya's unique attributes: Hemkund Sahib and The Valley of Flowers. *GeographiaTechnica*, 13 (2), 62-73.

Hock, R., Rasul, G., Adler, C.*et al.* (2019) *High Mountain Areas*. In: Pörtner H-O et al (eds) IPCC Special Report on the Ocean and Cryosphere in a Changing Climate. In press.

Huang, L., Li, Z.& Tian, B. (2013) Monitoring glacier zones and snow/firn line changes in the Qinghai–Tibetan Plateau using C-band SAR imagery. *Remote Sens. Environ*., 137, 17–30.

Mahagaonkar, A.V. (2019)*Glacier Surface Velocity Estimation & Faces Classification using InSAR and Multi-Temporal SAR Techniques in Indian Himalaya*, Enschede, The Netherlands.

Massom, R.&Lubin, D. (2006)*Polar Remote Sensing*: Volume II: Ice Sheets. Springer-Verlag, Berlin.

Meier, M. F. & Post, A. S. (1962) Recent variations in mass net budgets of glaciers in western North America. *International Association of Scientific Hydrology Publication 58 (Symposium at Obergurgl 1962 –2014; Variations of Glaciers)*, 63–77.

Meier, M. F. (1962)Proposed definitions for glacier mass budget terms. *Journal of Glaciol*ogy, 4 (33), 252–263.

Mohajerani, Y., Jeong, S., Scheuchl, B. *et al.*(2021) Automatic delineation of glacier grounding lines in differential interferometric synthetic-aperture radar data using deep learning. *Sci Rep*11, 4992, https://doi.org/10.1038/s41598-021-84309-3.

Mouginot, J., Rignot, E., Scheuchl, B. & Millan, R. (2017) Comprehensive annual ice sheet velocity mapping using Landsat-8, Sentinel-1, and Radarsat-2 data. *Remote Sens.,* 9, 364.

Partington, K. G. (1998) Discrimination of glacier faciès using multi-temporal SAR data. *Journal of Glaciology*, 44(146), 42–53.

Rau, F., Braun, M., Friedrich, M., Weber, F., &Goßmann, H. (2000) Radar glacier zones and their boundries as indicators of glacier mass balance and climatic variability. *EarselEProceedings*, 1, 317–327.

Shabunin A. G. (2018) The Catalogue of Claciers of Kyrgyzstan, *Central Asian Institute for Applied Geosciences (CAIAG).*

SVM Tutorials (2020) Harris Geospatial Solutions, Inc.[Online]. Available from: https://www.l3harrisgeospatial.com/docs/backgroundsvmgeneral.html. [Accessed September 2020].

Thakur, P.K., Aggarwal, S.P., Gunasekaran, A.&Sood, S. (2016) Estimation of Snow Cover Area, Snow Physical Properties and Glacier Classification in Parts of Western Himalayas Using C-Band SAR Data, *Journal of the Indian Society of Remote Sensing*, 45, 525-539. DOI: 10.1007/s12524-016-0609-y.

Tsai, Y-LS., Dietz, A., Oppelt, N.& Kuenzer, C. (2019). Remote Sensing of Snow Cover Using Spaceborne SAR: A Review. *Remote Sensing*, 11(12), 1456. https://doi.org/10.3390/rs11121456

Vieli, A. & Payne, A. J. (2005) Assessing the ability of numerical ice sheet models to simulate grounding line migration, *Journal of Geophysical Research,* 110(F1). doi:10.1029/2004jf000202.

Voda, M., Sarpe, C.A.& Voda, A.I. (2019) Romanian river basins lag time analysis. The SCS-CN versus RNS comparative approach developed for small watersheds. *Water Resources Management*, 32 (14).

Water resources of USSR (1973) Issyk-Kul lake, Chu, Talas and Tarim River Basin. Volume 14 Central Asia, issue 2, *Gidrometeoizdat*, Saint-Petersburg, USSR, 55-58p.

Woodhouse, I.H. (2006) Introduction to Microwave Remote Sensing, *CRC Press, Taylor & Francis Group.*

Zholdoshbekov, E. (2020) Glacier Dynamics studies OF Ala-Archa valley of Kyrgyz Republic using Geospatial Data. Post Graduate Diploma in Remote Sensing & Geographic Information System project thesis of Centre of Space Science and Technology Education in Asia and the Pacific (CSSTEAP) (Affiliated to the United Nations), Dehradun., India, 29.

Zhou, C.X.& Zheng, L. (2017) Mapping radar glacier zones and dry snow line in the Antarctic Peninsula using Sentinel-1 images. *Remote Sens*., 9, 1171.

IDENTIFYING SUITABLE SITES FOR RAINWATER HARVESTING USING RUNOFF MODEL (SCS-CN), REMOTE SENSING AND GIS BASED FUZZY ANALYTICAL HIERARCHY PROCESS (FAHP) IN KENITRA PROVINCE, NW MOROCCO

Mohamed AGHAD[1], Mohamed MANAOUCH[1] , Mohamed SADIKI[2] , Mohcine BATCHI[1] and Jamal AL KARKOURI[1]

ABSTRACT:
The rising need for water coupled with an increasing scarcity in many parts across the world especially in the middle east and north african countries (MENA) requires more sustainable solutions for effective water conservation. In Morocco, water ressource is characterized by significant spatio-temporal variability. So, to ensure the availability of water for domestic and agro-industrial uses, it is advised to develop some alternatives that improve the local water resources management throughout the country. Rainwater harvesting (RWH) has been proven to be a very promising alternative to water shortage problem. However, identifying appropriate sites for RWH remains a complex task in the management of rainwater. The present study aims to identify optimal sites for RWH using GIS based Fuzzy Analytical Hierarchy Process (FAHP) method in the Kenitra province, NW Morocco. For preparing thematic layers, several data sources were used including remote sensing data (RS), digital elevation model (DEM), the soil and precipitation data were used to create the necessary database using ArcGIS software. Next, the model of the soil conservation service-curve number (SCS-CN) was adopted to generate the map of the annual potential runoff. Then, five thematic layers including runoff, slope, soil texture, land use/land cover (LULC) and drainage density were assigned apropriate weights for generating the RWH suitability map. The resultant map of runoff depth revealed that it ranges from 137 to 738 mm. Moreover, the RWH suitability map showed that Kenitra province can be classed into five RWH candidate areas: (i) unsuitable (12.7%), (ii) less suitable (10.9%), (iii) suitable (20.3%), (iv) very suitable (36%) and (v) extremely suitable (19.9%). The extremely suitable areas for RWH are distributed in the central and northeastern parts. Based on the area under curve (AUC) of the receiver operating caracteristics (ROC), the success rate for predicting suitable RWH sites was 51%.

Key-words: RWH Suitability, SCS-CN, FAHP, RS, GIS, Kenitra province.

1. INTRODUCTION

In Morocco, precipitation varies greatly in space and time (Tramblay et al., 2013). Morocco's climate varies from sub-humid in the northwest to arid in the south (Born et al., 2008). Average annual rainfall reaches 800 mm. yr^{-1} in the north, whereas the southern parts receives 100 mm. yr^{-1} (El Moçayd et al., 2020).

The water shortage problems in the south has led the Moroccan government to develop a strategic policy to improve the local management of water resources throughout the country by installation of some great hydraulic infrastructures such as El Wahda dam's in the north. The late sixties, King

---

[1] *Laboratory of Environment, Societies and Territories, Department of Geography, Faculty of Humanities and Social Sciences, Ibn Tofail University, Kenitra, Morocco, aghad.mohamed@uit.ac.ma; mohamed.manouch@uit.ac.ma ; alkarkourij@yahoo.fr*
[2] *Laboratory of Geo-Sciences, Department of Geology, Faculty of Sciences, Ibn Tofail University, Kenitra, Morocco, sadikimed2002@gmail.com*

Hassan II launched a strategic project to increase the irrigated area to reach 1 Million ha by 2000. Nowadays, the situation is worsened due to the population growth and the associated expansion of agricultural activities, imposing a remarkable burden on the limited available and uncertain water supply. Moreover, several studies (Doukkali, 2005) have reported that although these efforts resulted in the significant optimization of water resource management in Morocco, they remain insufficient to ensure water and food security. A new policy is needed to complement these efforts.

In 2020, only the northern watersheds have registered a water excess compared with the demand. Then, it was proposed a water transfer project from the north to south (Water Highway) which aims to supply water to the arid southern regions from the northern watersheds. Other studies have suggested that Moroccan arid and semiarid regions should develop new policy in order to adapt to climate change (Kahil et al., 2015). As reported by man researchers (Greve et al., 2018), different policies could be adopted, including investments in structures for transferring water from one basin to another.

On the other hand, many countries across the world have been used some alternative measures such as Rainwater Harvesting (RWH) to ensure water availability for domestic, agricultural and industrial uses. This strategic alternative has been widely adopted for water shortage problem and has led to decrease groundwater extraction. In arid and semi-arid areas, RWH term has been employed by researchers to describe the various methods aimed at the use of, collection, and storage of rain runoff for increasing the availability of water for drinking and irrigation (Agarwal et al., 2001). Accordingly, RWH has been used to safeguard water by satisfying the increasing water supply–demand gap for both domestic and agricultural uses to enhance the quality of life by improving the social, environmental, and economic development in these areas.

In the last decades, Kenitra province has experienced a series of changes including significant population growth, expansion of agricultural activities, rapid urbanization and strong industrialization which have resulted in an increasing demand for water. This situation creates the need for continued economic development and places pressure on existing water resources. According to this water demand increase in Kenitra province, RWH can be used as a water source for additional irrigation in case of agricultural water supply shortage (e.g. use of small dams for collecting runoff). However, the rainwater harvesting suitability study is a complex and delicate task as identifying potential and effective locations is not always easy. Thus, RWH sites should be sitting scientifically by using efficient techniques.

The use of GIS coupled with fuzzy multi-criteria decision analysis (MCDA) method has been used widely as an efficient approach. Since, the GIS software toolbox includes many spatial analysis tools that facilitate the management of big geo-spatial data. Therefore, the present study aims to suggest optimal RWH sites in Kenitra province using the fuzzy multi-criteria decision making coupled with the geographic information system. This proposed approach combines the FAHP method, SCS-CN model and GIS techniques in order to increase the successful implementation of RWH. The findings of this research will be of interest to water managers and other potential stakeholders to identify areas where RWH can be most effective for increasing sustainable agricultural development and water accessibility in Kenitra province, NW Morocco.

2. MATERIELS AND METHODS

2.1. Study area

Kenitra Province is one of the northwest regions of Morocco bordered by Larache province on the north, Ouezzane province on the northwest, Salé and Khemisset provinces on the south, Atlantic Ocean on the west and the two provinces of Sidi Kacem and Sidi Sliman to the east and northeast, respectively. It consists of 3 urban communes and 20 rural communes. The administrative center is Kenitra city located 40 km northwest of Rabat, the capital of Morocco. Mehdia, Souk Tlet, Souk El Arba, Mograne, Lalla Mimouna, Sidi Allal Tazi, Moulay Bousselham, Sidi Taybi, Ameur Saflia, Sidi Mohamed Ben Mansour, Mnasra, Haddada, Oulad Slama and Arbaoua are other major towns in this province.

Covering a total area of 3,052 km^2 (**Fig.1**), Kenitra province is limited by latitudes 7°10′34 ′'- 8° 42′ 46″N and longitudes 38° 41′ 14 ′'- 40° 43′58″W. The Kenitra province's altitudes range from 6 to 606 m a.s.l. According to the last national census report (HCP, 2014), there were 1,061,435 people in this province with a population density of 224 km^2.

During the period from 2000 to 2019, Kenitra province recorded a minimum average T of 13.1 ° C and a maximum average T of 20.1 ° C. The rainfall in Kenitra province falls between mid-October to mid-April and the annual average is 450 mm (HCP, 2014). The LULC types in the study area are classified into seven major classes such as matorral or scrub, forest, agricultural fields, covered plantations, lagoons, settlements and water bodies with both types of matorral and forest have larger proportions.
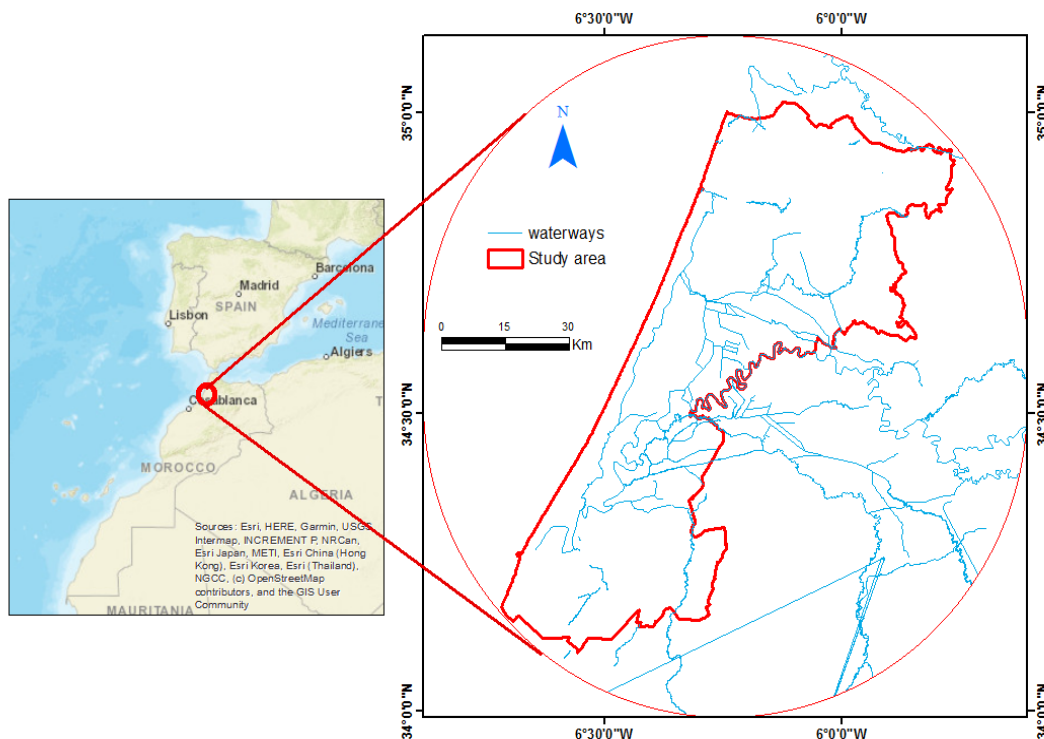
Fig. 1. Location of the Kenitra province on a map of Morocco.

2. 2. Data sources and adopted methodology

For the purpose of this study, a set of data was collected from different sources such as LULC from RS, DEM from SRTM, soil texture from previous studies, precipitation from the Sebou watershed agency (ABHS). Then, this database was processed in ArcGIS 10.5 software. The DEM-SRTM downloaded freely from the United States Geological Survey (USGS) site with a resolution of 30 m and used to delineate the Kenitra province watershed. The LULC map was compiled using Landsat 8 OLI satellite imagery, acquired on February 3, 2021, with a resolution of 30 m.

Rainfall data from the climate research unit of ABHS (ABHS, 2021) extending from 2000 to 2019. The geological map was obtained from the geological service of Morocco (SGM, 1985). The following figure (**Fig. 2**) presents a flow chart of the methodology adopted to produce the potential RWH map.
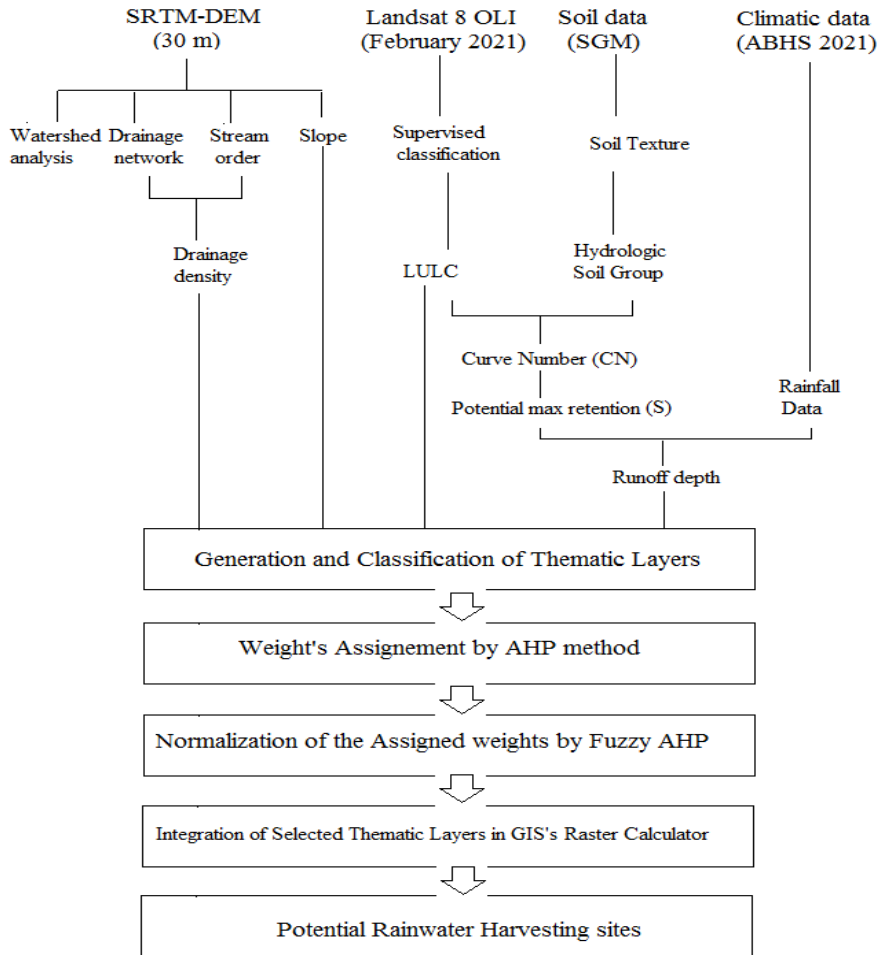
Fig. 2. Flow chart of the methodology used.

2.3. SCS-CN Model

The study area's potential runoff was estimated by the Soil Conservation Service-Curve Number (SCS-CN) model developed by the United States Department of Agriculture (SCS-CN USDA, 1956) which later became Natural Resources Conservation Service (NRCS). This SCS-CN model is a largely used approach for estimating the surface runoff (Ramakrishnan et al., 2009). CN value is the function of Hydrologic Soil Groups (HSGs), LULC and Antecedent Moisture Conditions (AMC). CN values for various Hydrologic Soil-LULC can be obtained for Kenitra province using NRCS (2004) data. To estimate the depth of runoff according to the SCS-CN method (Ramakrishnan et al., 2009), the following formula is used:

$$Q = \begin{cases} \frac{(P-\lambda S)^2}{P+(1-\lambda)S} & (P < S) \\ Q = 0 & (P > \lambda S) \end{cases} \tag{1}$$

$$S = \frac{25400}{CN} - 254 \tag{2}$$

where:

Q	-height of runoff (mm);
P	-annual precipitation (mm);
S	-maximum potential retention after the onset of runoff (mm);
λ	-abstraction of surface runoff (dimensionless);
CN	-value of the curve number which is between 0 and 100, reflecting the % of runoff.

A standard condition for the SCS value considers the parameter λ to be equal to 0.2 (SCS, 1985) and for CN, large values mean most precipitation is transformed into surface runoff and vice versa.

2.4. Thematic criteria layers preparation

Analysis of previous studies shows that six main factors which have been listed by the Food and Agriculture Organization (FAO) are widely used for selecting potential RWH areas including climatic data, hydrologic conditions, topography, agronomy, soils, and socio-economics data (FAO, 2003; Kahinda, 2008). Accordingly, the basic thematic layers in this study were rainfall, soil texture, LULC, slope, and drainage network. The choice of layers was intended to satisfy the rainfall-runoff model's requirements. However, socio-economic factors were not considered due to the lack of data and to make the interpretation of the results easier.

2.5. Fuzzy set theory

In classical set theories, an element is a full member of a set or not a member of a set. From 1965, Zadeh (Zadeh, 1965) has proposed a "Fuzzy set theory" as a simple new method for precise decisions from unclear situations (Balezentiene, 2013). It consists of assigning a membership value between 0 and 1 to each element (Zadeh, 1965). This approach has been widely used to model decision-making processes based on imprecise data such as decision-maker preferences. In geo-spatial sciences, fuzzy logic can be used for making choices to perform a spatial object on a map as a member. "Since a feature object can be used as membership values between 0 and 1 by fuzzy set theory, this represents the degree of membership function (Zadeh, 1965)".

More details on the principle of the fuzzy set is illustrated by the following equation (McBratney and Odeh, 1997):

$$A = \{x, \mu A(x) \text{ for each } x\} \tag{3}$$

where, μA is the MF (membership function of an element x in fuzzy set A) so that:

If x is not a member of A then μA = 0.
If x is a full member of A then μA = 1.
If x belongs in a certain level to A then:

$$0 < \mu A(x) < 1 \tag{4}$$

As displayed in the equation above, linear MF was used for runoff, hydrologic soil group, drainage density and LULC (Feizizadeh and Blaschke, 2013).

$$\mu A(x) = \begin{cases} 0 & x \leq a \\ \frac{x-a}{b-a} & a < x < b \\ 1 & x \geq b \end{cases} \tag{5}$$

where:

x	-the considered parameter;
a	-the minimum value of the parameter x;
b	-the maximum value of the parameter x.

To estimate the effect of the slope on the suitability for RWH, the linear MF was used according to this equation (Feizizadeh and Blaschke, 2013):

$$\mu A(x) = \begin{cases} 0 & x \le a \\ \frac{b-x}{b-a} & a < x < b \\ 1 & x \ge b \end{cases} \tag{6}$$

where:

    x   - the slope's value;

    a   - the maximum value of the slope;

    b   - the minimum value of the slope.

In the present study, five criteria for identifying the suitable sites for harvesting water were considered including runoff, slope, drainage density, soil texture and LULC (**Tab. 1**). In the fuzzy map of each criterion, each pixel's value ranges between the minimum 0 and the maximum 1. The value 0 means that the pixel is not a member of a set "not suitable" and the value 1 means that the pixel is a full member of a set "very suitable".

Table 1.

Fuzzy set memberships and control points used for identifying suitable RWH sites.

Criteria	Fuzzy / Membership Function	Control points (a=min & b=max)
Runoff (mm)	Linear, increasing	**a=257.7 & b=561.4**
Slope (%)	Linear, decreasing	**a=28.3 & b=3.8**
Drainage density (km/km2)	Linear, increasing	**a=0.28 & b=1.85**
Soil Texture	Categorical	**-**
LULC	Categorical	**-**

2.6. Analytic Hierarchy Process (AHP) method

For investigating the weight of the criteria or factors, the Saaty's AHP is the most used among MCDM methods. The fundamental concept of AHP is based on the simple binary comparison matrix to compute the criteria weights. The comparison is very important for determining the degree at which one criterion is more important than another is. The AHP method generally consists of three steps: determining the hierarchy, creating the pairwise comparison matrix, and calculating the weights (Saaty, 2008). After the hierarchy is established, **Tab. 2** is used to determine the level of importance among them for pairwise comparison. Then, the comparison's results are acceptable if the consistency ratio (CR) value is below 10% (Saaty, 2008).

Table 2.

AHP criteria pairwise comparison.

	Runoff depth	Slope	Dd	ST/HSG	LULC	Weight
Runoff depth	1	2	3	4	5	0.41
Slope	0.5	1	2	3	4	0.26
Dd	0.33	0.5	1	2	3	0.16
ST/HSG	0.25	0.33	0.5	1	2	0.09
LULC	0.2	0.25	0.33	0.5	1	0.06
Consistency ratio (CR= 0.02); Random index (RI=1.12) and Consistency index (CI=0.226).						

*The value 0.02 of CR means that the judgments derived from the pairwise matrix of **Tab.2** are consistent.*

3. RESULTS AND DISCUSSIONS

3.1. Rainfall

Precipitation in Kenitra province is highly variable in terms of amount, time and space. Their regime is bimodal (two periods of precipitation occur separated by a dry period). About 90 percent of annual precipitation occurs from mid-October to mid-April (HCP, 2015). The precipitation map was developed using data from meteorological stations and the inverse weighted distance interpolation (IDW) method, which allows to estimate the values of any point in the study area. Average annual rainfall value ranges from 467 to 740 mm. yr^{-1}. Low values occupy the central eastern parts. However, high values are observed in the northwestern borders (**Fig. 3**).
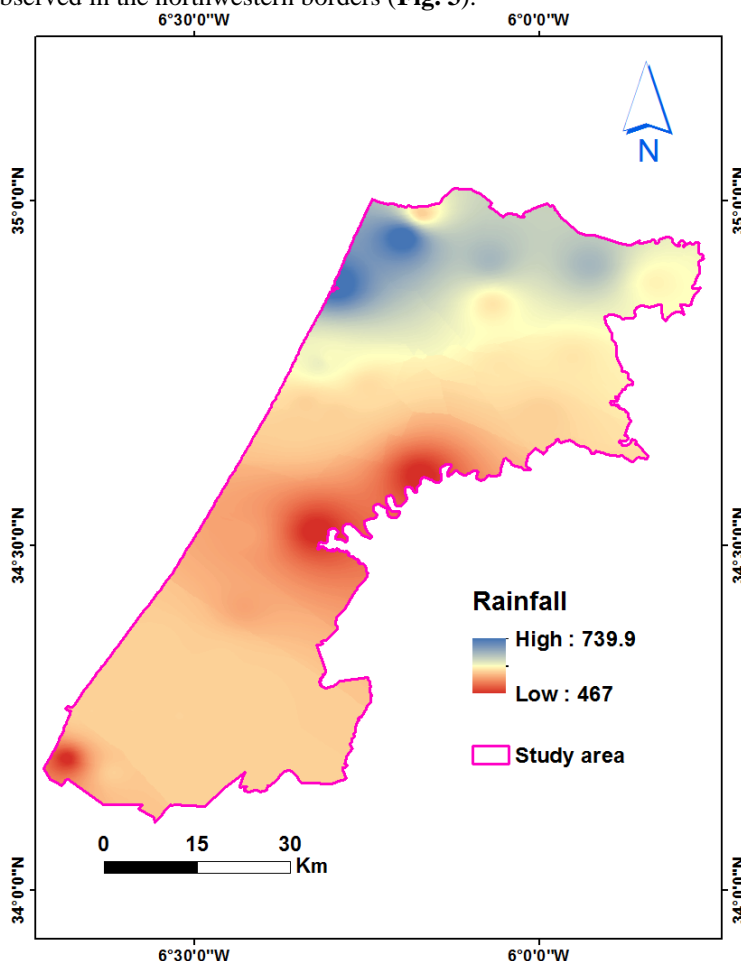
Fig. 3. Annual precipitation (in mm) in Kenitra province using ABHS data.

3.2. LULC

Kenitra province's LULC map was derived from Landsat 8 OLI images taken in February, 2021 with spatial resolution 30m. Then, the supervised classification was used to classify the study area into six categories: Matorral or scrub land, forest, agricultural fields, covered plantations and water bodies (**Fig. 4**). The studied area is largely covered by matorral, agricultural fields and forest covering 56.2%, 25.6% and 16.5%, respectively (**Tab. 3**). The covered plating takes up 1% of the total area. Conversely, water bodies and settlements occupy about 1% are considered unsuitable for harvesting rainwater. Thus, it is apparent that both matorral and forest which take up 72% of the study region are the most favorable areas for collecting runoff rainwater.
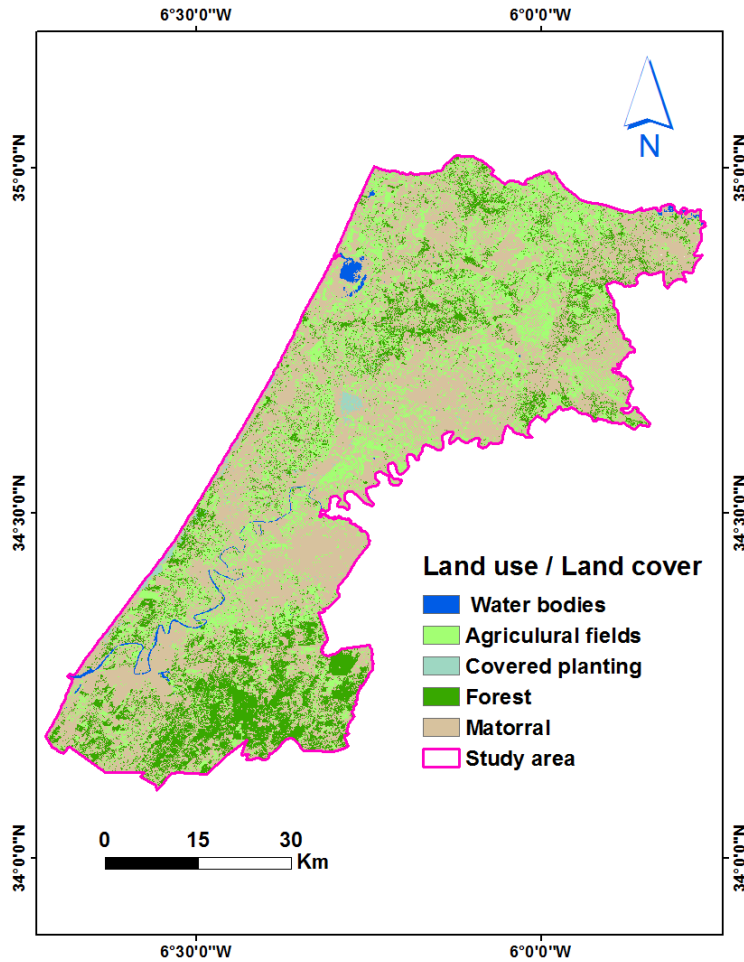
Fig. 4. LULC map of the study area.

Table 3.

LULC suitability class.

Factor	Type	Rate	Classification	Coverage (%)
LULC	Covered plantations	1	Unsuitable	1
	Agricultural fields	2	Less suitable	25.6
	Water	3	Suitable	0.7
	Forest	4	Very suitable	16.5
	Matorral or scrub	5	Extremely suitable	56.2

3.3. Soil Texture

Soil texture of in Kenitra province can be split into four classes based on previous studies (Batchi et al., 2017): fine, fine-medium, medium and coarse. Using the infiltration rates and soil classification data, this area contains the four types of HSG: A, B, C and D (**Fig. 5**). The parts extending to the center, northeast and west of the study area are covered by HSG-D occupying 35.2%. While, HSG-A and HSG-C cover 28.4% and 23.8% of the total area, respectively. Finally, HSG-B is spreading in small patches in the south-east (**Tab. 4**).
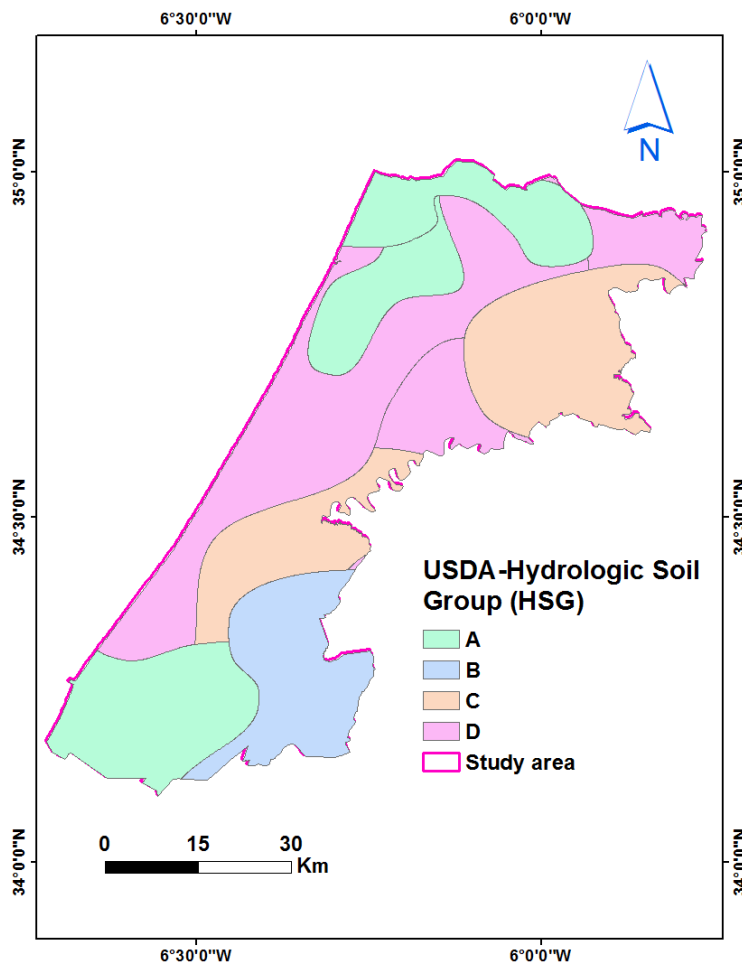
Fig. 5. Soil Texture Suitability Class.

<div align="right">

Table 4.
</div>

Soil texture and HSGs suitability class.

Factor	Texture	Class	Rate	Classification	Coverage (%)
Soil Texture / HSGs	Fine	A	1	Unsuitable	28.4
	Fine-medium	B	2	Less suitable	12.6
	Medium	C	3	Suitable	23.8
	Coarse	D	4	Very suitable	35.2

3.4. Slope

The developed slope map (**Fig. 6**) was classified into five intervals: (I) almost flat (<3%), (II) gentle (from 3 to 8%), (III) moderate (from 8 to16%), (IV) steep (from 16 to 28%) and (V) very steep (> 28%). The almost flat and gentle slope categories, together occupying almost 86%, these areas are considerably suitable for RWH. The moderate slope class is distributed over small plots in the northeast and occupying about 10%. The steep and very steep classes occupy 4.2%, are considered unsuitable areas for the RWH (**Tab. 5**).
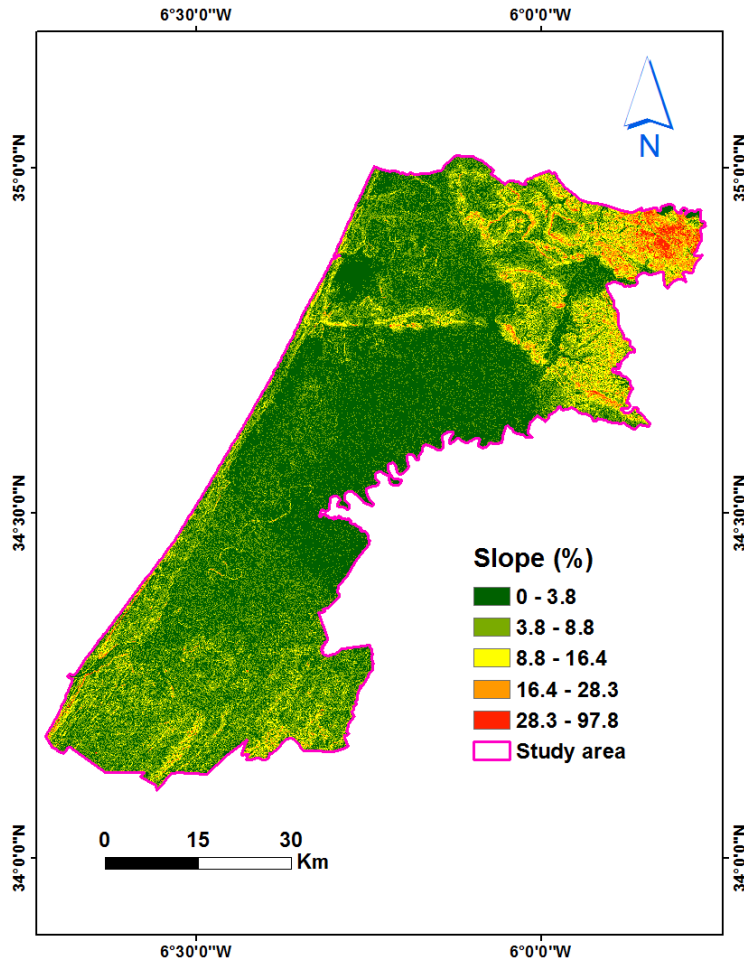
Fig. 6. Slope suitability map.

Table 5.

Slope suitability class.

Factor	Interval	Rate	Classification	Coverage (%)
Slope (%)	>28	1	Unsuitable	0.8
	16-28	2	Less suitable	3.4
	8-16	3	Suitable	10.2
	3-8	4	Very suitable	31.5
	<3	5	Extremely suitable	54.1

3.5. Runoff

The produced map of hydrologic soil group based on Kenitra province's soil texture and the LULC map were selected for intersection. Then, a resultant map with new polygons representing the merged hydrologic soil group and LULC (HSGs-LULC map) was generated using ArcGIS software. After this process and using the standard table given by SCS (SCS, 1985), the appropriate CN value was assigned for each polygon (**Tab.6**) in the new HSGs-LULC map to generate the CN map. The CN values range from 30 (HSG$_A$-Forest) to 100 (Water bodies and covered plantings), implying different runoff ability within the study area (**Tab.6**). Based on the CN map, the maximum potential retention map (S) was calculated by **Eq. (2)**. The runoff potential map was calculated using **Eq. (1)**.

Fig. 7 illustrates the spatial distribution of the runoff values in mm. These values ranging from 137 to 738 mm. yr^{-1} and depend on the climate, topography and environment of the study area.

Then, the prepared runoff depth map was classified into five categories (**Tab. 7**): unsuitable (<257 mm. yr^{-1}), less suitable (257-377), suitable (377-497), very suitable (497-561) and extremely suitable (>561 mm. yr^{-1}). Areas where the runoff depth is high is considered extremely suitable for RWH while those where this depth is low is considered unsuitable. About 46% of the study area is occupied by the "very suitable" class. While the "extremely suitable" class occupies 12.6% and the "suitable" and "less suitable" runoff classes occupy 19.6% and 7.7% of the total area, respectively. inappropriate areas occupy only 13.7%.
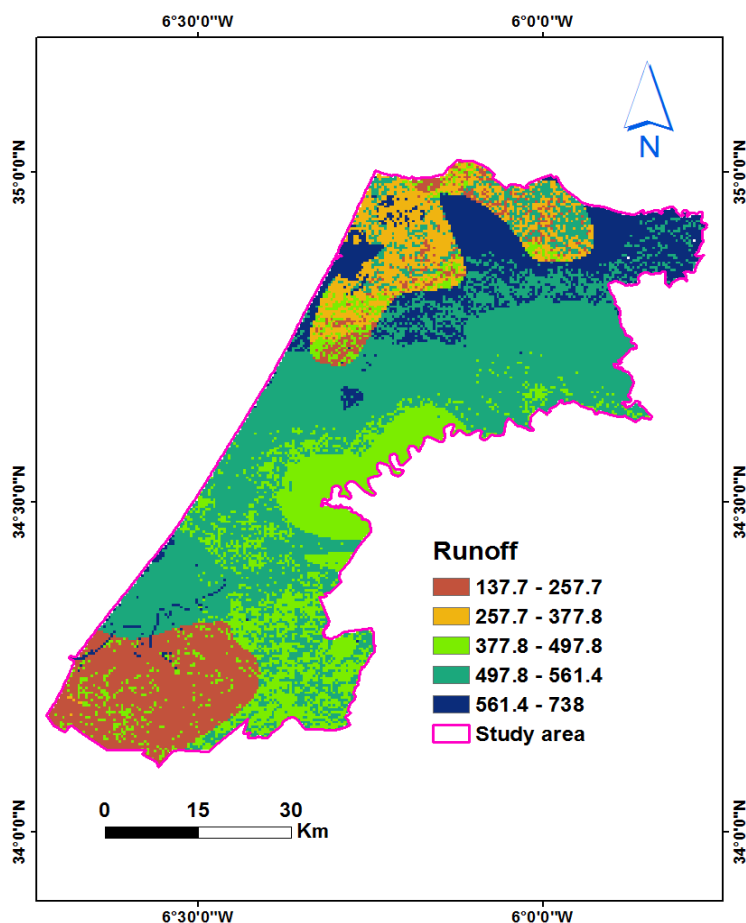
Fig. 7. Runoff depth suitability class.

Table 6.

CN as a function of LULC and HSGs. (USDA-SCS, 1985).

LULC types	CN-II			
	HSG_A	HSG_B	HSG_C	HSG_D
Agricultural field	67	77	83	87
Surface water	100	100	100	100
Forest land	30	67	77	83
Matorral or scrub	35	86	91	94
Covered plantations	100	100	100	100

Runoff depth suitability class.

Factor	Class	Rate	Classification	Coverage (%)
Runoff depth (mm)	I	1	Unsuitable	13.7
	II	2	Less suitable	7.7
	III	3	Suitable	19.6
	IV	4	Very suitable	46.3
	V	5	Extremely suitable	12.6

3.6. Drainage density

The developed drainage density map was grouped into five groups according to their importance to RWH suitability. These groups are: (I) Unsuitable (0-0.28 km. km^{-2}), (II) Less suitable (0.28-0.7), (III) Adapted (0.7-1.17), (IV) very suitable (1.17-1.85), (V) extremely suitable (1.85-3.06 km. km^{-2}) (**Fig. 8**). The spatial distribution of these categories shows that I covers 42%, and II covers 23.4% of the study region. However, III, IV and V cover 19.9% 9.8% and 5% respectively. The extremely appropriate category V is distributed in the central parts (in spots) of the study area (**Tab. 8**).
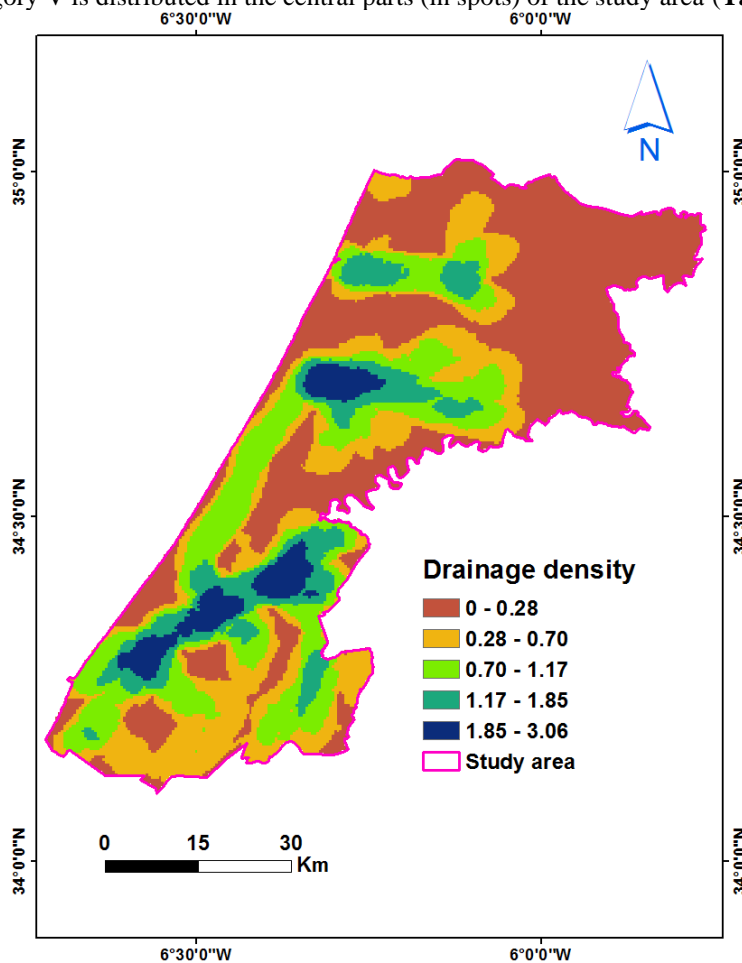
Fig. 8. Drainage density map.

Drainage density suitability class.

Factor	Interval	Rate	Classification	Coverage (%)
Drainage density (km. km-2)	<0.28	1	Unsuitable	42
	0.28-0.7	2	Less suitable	23.4
	0.7-1.17	3	Suitable	19.9
	1.17-1.85	4	Very suitable	9.8
	>1.85	5	Extremely suitable	4.9

3.7. Fuzzy thematic layers

Using "Fuzzy Membership Function" tool of the ArcGIS 10.5 software, all the selected thematic layers used in this study were transformed into fuzzy raster maps with values ranging from 0 to 1. In each fuzzy raster map, pixels with a value of zero means that they are not suitable and those with a value of one means that they are extremely suitable. In these fuzzy raster maps shown in **Fig. 9**, the blue colored areas indicate suitable sites for RWH.

0
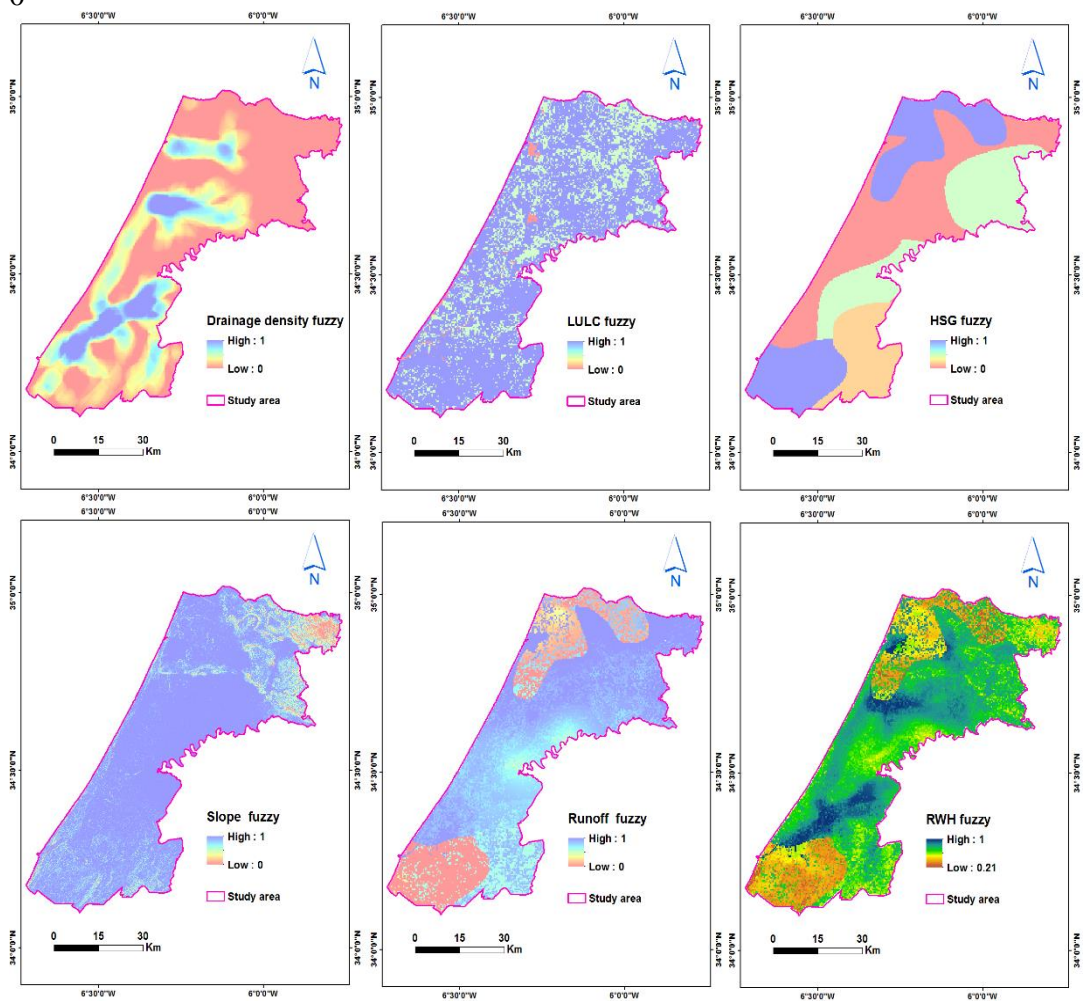
Fig. 9. Fuzzy maps of the parameters used for the RWH suitability study.

3.8. RWH Potential Map

After a consistent weighting (CR <0.1) of the factors which influence the identification of suitable RWH sites, the RWH potential map was developed by integrating the weighted thematic layers of runoff, slope, soil texture, LULC and drainage density (**Fig. 10**).
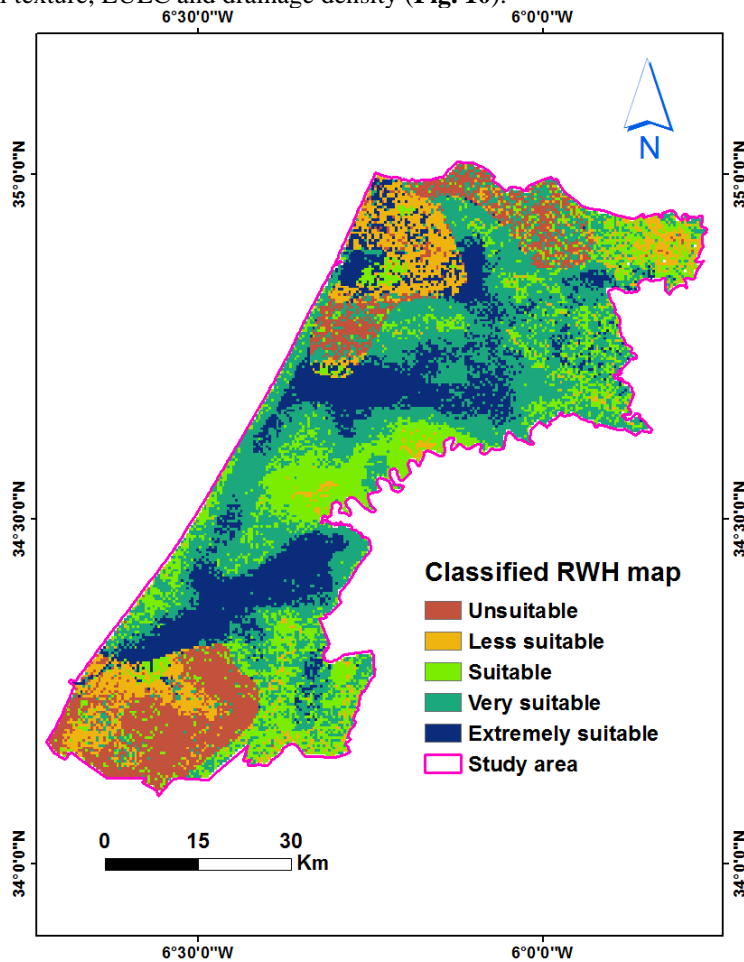
Fig. 10. Classified RWH suitability map.
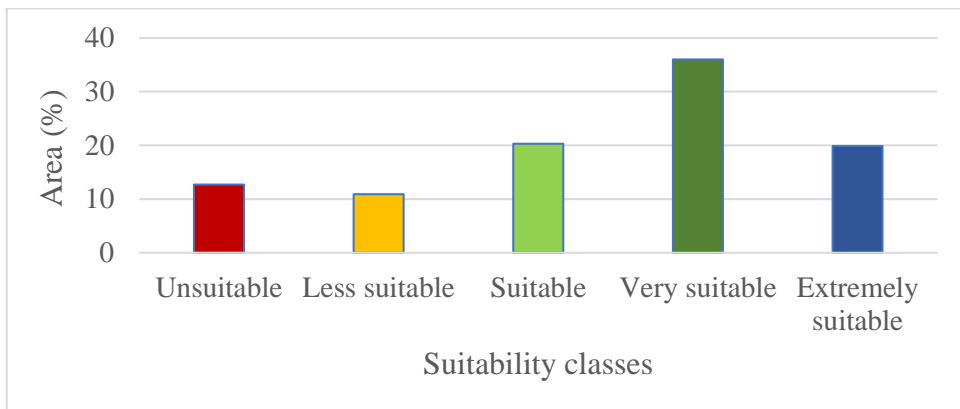
Fig. 11. Distribution of areas covered by the RWH suitability classes.

Then, this map was classified into five main groups: (I) unsuitable, (II) less suitable, (III) suitable, (IV) very suitable and (V) extremely suitable (**Fig. 11**). Group IV is the most dominant, accounting for 35%. Groups III, II and I occupy 20%, 10% and 12% respectively. While group V is distributed in the center and northeast, representing 19% of the study area. Thus, we conclude that a significant part of the study area is optimal for the RWH (**Fig. 12**).

3.9. Validation of the predicted RWH sites with existing ponds or merja

Using an inventory of certain natural ponds and lakes also locally called merjas (In Kenitra province and the Gharb plain in general, the term "merja" designates the lowlands liable to temporarily retain runoff, flood and rainwater) for checking the accuracy of the predicted results by Fuzzy-AHP model. Then, the predicted suitable sites by this model were compared with the existing natural ponds and lakes in the study area and which have been considered as really suitable sites.
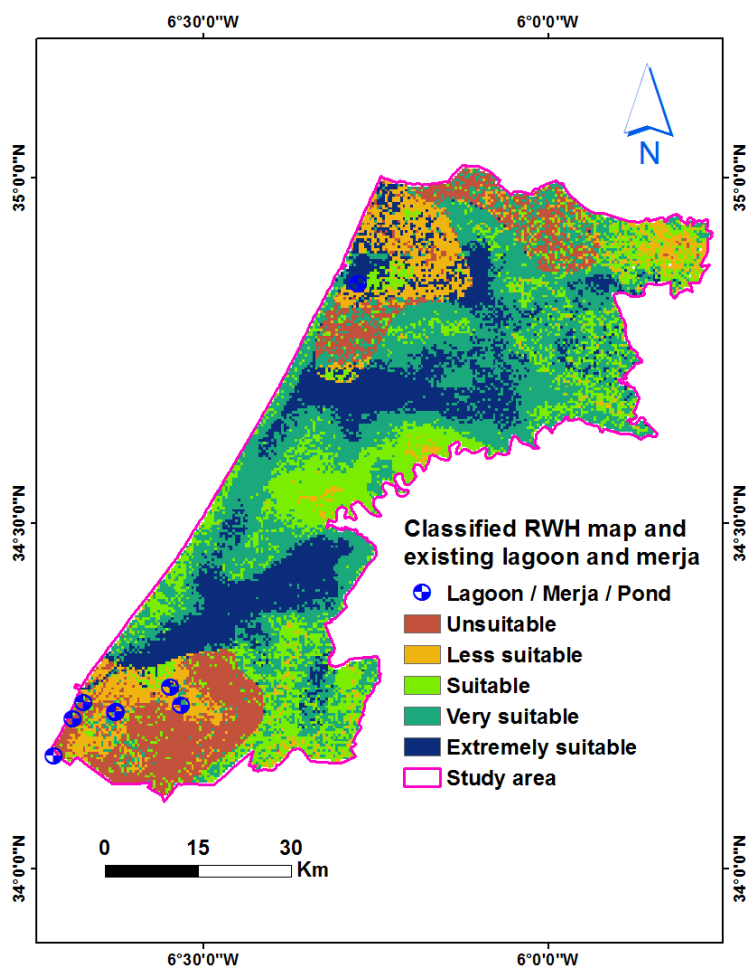
Fig. 12. Classified RWH suitability map and existing natural ponds, lagoons and merjas.

For the validation process, the receiver operating characteristics (ROC) curve was drawn, and the area under curve (AUC) value was calculated by using the ArcSDM software package. The AUC represents the quality of the model to reliably predict the suitability of RWH sites. A good fit model has AUC values that range from 0.5 to 1, while values below 0.5 represent a random fit.

In this work, a success rate curve has been used for validation, as shown in **Fig. 13**. The success rate curve is obtained by plotting the cumulative percentage of existing ponds and merjas against the areal cumulative percentage in decreasing RWH suitability values. The area under the curve can be used to assess the prediction accuracy qualitatively (Lee, 2005). The AUC for the RWH suitability map produced using the FAHP model is 0.51, which means that the overall success rate of the RWH suitability map is 51%. The results obtained from success rate graph indicate that the FAHP model look to be less accurate in terms of the performance of RWH suitability mapping and has acceptable prediction accuracy in the study area.
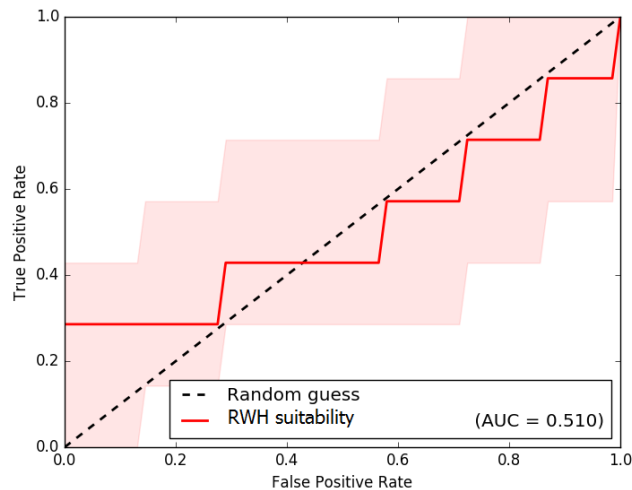
Fig. 13. Success rate curve of the predicted RWH suitability model.

4. CONCLUSIONS

RWH is a strategic alternative source of water in many regions around the world. We selected the Kenitra province in NW Morocco as a representative area experiencing significant demographic growth with rapid expansion of agricultural and industrial activities. We developed and assessed a methodology that integrates a procedure of continuous runoff accounting based on the SCS-CN model with GIS based FAHP method to identify potential sites for harvesting rainwater.

In the present study, the RWH suitability analysis process is due to the ability to integrate into GIS environment a multilayer of relevant parameters such as runoff, slope, soil texture, LULC and drainage density, which give smaller units of suitability as a composite layer. This methodology does not require a lot of time and resources so it is advantageous and profitable for the identification of potential RWH sites.

The runoff depth was estimated by the SCS-CN approach, which was employed using the mean annual rainfall data for the period of 2000–2019 and land use/land cover superimposed by the Kenitra province's soil data. The generated map of runoff showed that the quantity of water runoff is low in the southwest of the study area while it is high in the northeast.

For the RWH potential areas, the results showed that 19.9% of the study area is extremely suitable and 36% is very suitable. On the other hand, 44% remaining distributed in the south-west, center and north-west is moderately adapted or totally useless to the collection of rainwater.

The results of this study are very interesting for water resource managers in the Kenitra province, especially for water supply studies. However, additional fieldwork needs to be carried out in areas considered so suitable for RWH to confirm the results of this study. The techniques used in this work are simple and applicable so they can be used in other parts of the world with water scarcity problems.

REFERENCES

Agence du Basin Hydraulique du Sebou (2021) www.abhsebou.ma Accessed 10 February 2021

Agarwal, A., Narain, S., Khurana I. (2001) Making water everybody's business: practice and policy of water harvesting. Centre for Science and Environment, New Delhi.

Balezentiene, L., Streimikiene, D., Balezentis, T. (2013) Fuzzy decision support methodology for sustainable energy crop selection. Renew. Sustain. Energy Rev., 17, 83–93.

Batchi, M., Al Karkouri, J., Fenjiro, I. & El Maaqili, M. (2017) « Étude comparative de deux modèles (DRASTIC et SI) pour l'évaluation de la sensibilité de la nappe phréatique de Mnasra (Maroc nord-occidental) à la pollution d'origine agricole ». Physio-Géo, 11(1), 43-64. https://doi.org/10.4000/physio-geo.5213

Born, K., Christoph, M., Fink, A., Knippertz, P., Paeth, H., and Speth, P. (2008) Moroccan climate in the present and future: combined view from observational data and regional climate scenarios, Climatic changes and water resources in the Middle East and North Africa, Springer, (pp. 29–45). Berlin: Heidelberg.

Doukkali, M. (2005) Water institutional reforms in Morocco, Water Policy, 7, 71–88.

FAO (2003) Land and Water Digital Media Series, 26. Training Course on RWH (CD-ROM). Planning of Water Harvesting Schemes, Unit 22; Food and Agriculture Organization: Rome, Italy.

Feizizadeh, B., Blaschke, T. (2013) GIS-multicriteria decision analysis for landslide susceptibility mapping: comparing three methods for the Urmia lake basin, Iran. Nat Hazards, 65(3), 2105-2128. https://doi.org/10.1007/s11069-012-0463-3

Haut-Commissariat au Plan (2021) www.hcp.ma   Accessed 20 February 2021

Greve, P., Kahil, T., Mochizuki, J., Schinko, T., Satoh, Y., Burek, P., Fischer, G., Tramberend, S., Burtscher, R., Langan, S., and Wada, Y. (2018) Global assessment of water challenges under uncertainty in water scarcity projections, Nat. Sustainabil., 1, 486–494.

Kahil, M.T., Dinar, A., and Albiac, J. (2015) Modeling water scarcity and droughts for policy adaptation to climate change in arid and semiarid regions, J. Hydrol., 522, 95–109. https://doi.org/10.1016/j.jhydrol.2014.12.042, 2015

Kahinda, J.M., Lillie, E. Taigbenu, A. Taute, M. Boroto, R. (2008) Developing suitability maps for rainwater harvesting in South Africa. Phys. Chem. Earth, Parts A/B/C, 33, 788–799. doi:10.1016/j.pce.2008.06.047.

Lee, S. (2005) Application of logistic regression model and its validation for landslide susceptibility mapping using GIS and remote sensing data. Int J Remote Sens, 26(7), 1477–1491.

McBratney A.B., Odeh, I.O.A. (1997) Application of fuzzy sets in soil science: fuzzy logic, fuzzy measurements and fuzzy decisions. Geoderma, 77, 85-113. https://doi.org/10.1016/S0016-7061(97)00017-7

El Moçayd, N., Kang, S., and Elfatih A.B.E. (2020) Climate change impacts on the "Water Highway" project in Morocco. Hydrol. Earth Syst. Sci., 24, 1467–1483, available online at www.hydrol-earth-syst-sci.net/24/1467/2020/

Ramakrishnan, D., Bandyopadhyay, A., Kusuma, K.N. (2009) SCS-CN and GIS-based approach for identifying potential water harvesting sites in the Kali Watershed, Mahi River Basin, India. J Earth Syst Sci., 118, 355–368.

Saaty, T.L. (2008) Decision making with the analytic hierarchy process. Int. J. Serv. Sci., 1, 83. doi:10.1504/ijssci.2008.017590.

SCS (1956) Hydrology. National Engineering Handbook, Supplement A, Section 4. Soil Conservation Service. US Department of Agriculture, Washington, DC.

SCS (1985) Hydrology. In National Engineering Handbook; United States Department of Agriculture, Soil Conservation Service, US Government Printing Office: Washington, DC, USA.

Service Geologique du Maroc (1985) Notes et Memoires N°260. www.geojamal.com Accessed 20 February 2021

Tramblay, Y., Ruelland, D., Somot, S., Bouaicha, R., and Servat, E. (2013) High-resolution Med-CORDEX regional climate model simulations for hydrological impact studies: a first evaluation of the ALADIN-Climate model in Morocco. Hydrol. Earth Syst. Sci., 17, 3721–3739. https://doi.org/10.5194/hess-17-3721-2013

Zadeh, L.A. (1965) Fuzzy sets. Inf. Control, 8, 338–353. doi:10.1016/s0019-9958(65)90241-x

COMPARISON OF SENTINEL-2 AND MULTITEMPORAL SENTINEL-1 SAR IMAGERY FOR MAPPING AQUACULTURE POND DISTRIBUTION IN THE COASTAL REGION OF BREBES REGENCY, CENTRAL JAVA, INDONESIA

Nurul Afdal HARIS[1] , *Sandiaga Swahyu KUSUMA[1], Sanjiwana ARJASAKUSUMA[1]** , *Pramaditya WICAKSONO[1]*

ABSTRACT:
The identification of land cover and land use is necessary to support the strategic management of coastal areas. The utilization of remote sensing technology such as synthetic aperture radar (SAR) data has been widely used for mapping the distribution of land cover and land use. This application includes the detection of aquaculture ponds in coastal areas due to SAR's sensitivity to surface water content. In addition, multitemporal Sentinel-1 data helps to distinguish between ponds and rice fields that possess a visually similar appearance during the flooding stage. This study aims to explore the accuracy of the gray level of co-occurrence model (GCLM) textures of multitemporal Sentinel-1 data for aquaculture pond mapping in Brebes Regency, Central Java Province, Indonesia. In addition, single-date Sentinel-2 optical imagery was used to compare the results from Sentinel-1 data. The Sentinel-2 data has been identified using supervised classifications, e.g., maximum likelihood (ML), minimum distance (MD), random forest (RF), and K-nearest neighbor (KNN) algorithms, and the most accurate algorithm was selected to classify the Sentinel-1 data using GLCM textures. The results indicated that the Sentinel-1 imagery showed the best results using GLCM metrics from VH polarization with an accuracy value of 92.2% using the ML algorithm, while the best results from Sentinel-2 were also produced using ML, with an 88.4% overall accuracy. These results demonstrate that multitemporal Sentinel-1 data have higher accuracy than Sentinel-2 data when used for pond detection. This shows the potential of the combination of both sensors to increase the accuracy of aquaculture pond mapping.

Key-words: Sentinel-1, Sentinel-2, Aquaculture Ponds, Texture, Supervised Classification

1. INTRODUCTION

Indonesia is an archipelago consisting of approximately 17,504 large and small islands, having the longest coastline in the world with a length of 104,000 km (Lasabuda, 2013). The massive coastal areas of the islands in Indonesia are suitable for the development of brackish water aquaculture. Brackish water aquaculture, as one of the supporting factors for the economy of coastal communities, has triggered the expansion of new ponds, which will continue to occur to fulfill the surrounding community's needs (Joffre et al., 2019; Ottinger et al., 2016; Porporato et al., 2020). It is necessary to monitor the sustainability of the aquaculture ponds and formulate management strategies in coastal areas to support coastal environmental conditions. For sustainable coastal area management, understanding pond distribution is the first step in determining the strategies that need to be implemented. It is essential to understand that direct data collection and monitoring of ponds individually will be a lengthy and expensive process due to the vast area of the ponds (Gusmawati et al., 2016a; Gusmawati et al., 2016b). Therefore, technology is needed to assist in pond monitoring (Duan et al., 2020; Ottinger et al., 2016).

Synthetic aperture radar (SAR) satellite observation is part of the remote sensing active system that can provide observations day and night and at various weather conditions due to its ability to

[1]*Master Program in Remote Sensing, Department of Geographic Information Science, Faculty of Geography, Universitas Gadjah Mada, Yogyakarta, Indonesia, nurul.afdal.haris@mail.ugm.ac.id, sandiaga.kusuma@mail.ugm.ac.id, * corresponding author sanjiwana.arjasakusuma@ugm.ac.id, prama.wicaksono@ugm.ac.id*

penetrate clouds. One of the satellites that use SAR technology is Sentinel-1. The Sentinel-1 satellite provides SAR imagery free of charge and covers the whole world with a high temporal and spatial resolution (Obida et al., 2019). The Sentinel-1 mission employed C-band with dual-polarization capabilities using the combination of vertical transmittance, vertical or horizontal returns (VV and VH, respectively), short revisit times, and fast product delivery for global observation using the constellation of two satellites (Sentinel-1A and Sentinel-1B) orbiting the poles (European Space Agency, 2013). Several studies have been conducted using solely multitemporal radar data or using radar and optical imagery in combination for aquaculture pond mapping, such as the utilization of multitemporal Sentinel-1 radar images and Landsat optical images for mapping aquaculture characteristics (Stiller et al., 2019), aquaculture pond identification based on Google Earth Engine's use of Sentinel-1 and Sentinel-2 images (Xia et al., 2020), aquaculture pond identification using the object-based image analysis (OBIA) and normalized difference water index (NDWI) methods in Taiwan, and using multitemporal Sentinel-1 radar data for pond mapping (Chen et al., 2018; Ottinger et al., 2017). Sentinel-1 data also has a significant ability to distinguish flooded land cover, such as a paddy field in the inundation phase, by utilizing cross-polarization data from Sentinel-1, although misclassification can still occur, especially regarding land cover that possesses similar characteristics with the flooded paddy field (Arjasakusuma et al., 2020). However, the textural information from Sentinel-1 has not been fully explored, especially for mapping applications.

Sentinel-1 data has been widely utilized for aquaculture pond identification, but the assessment of textural information from Sentinel-1, the gray level of co-occurrence metrics (GLCM) textures, has not been studied to identify aquaculture ponds. In this study, the mapping capability using GLCM for aquaculture pond identification as an input dataset was tested and compared with the ability of Sentinel-2 optical imagery for aquaculture pond mapping.
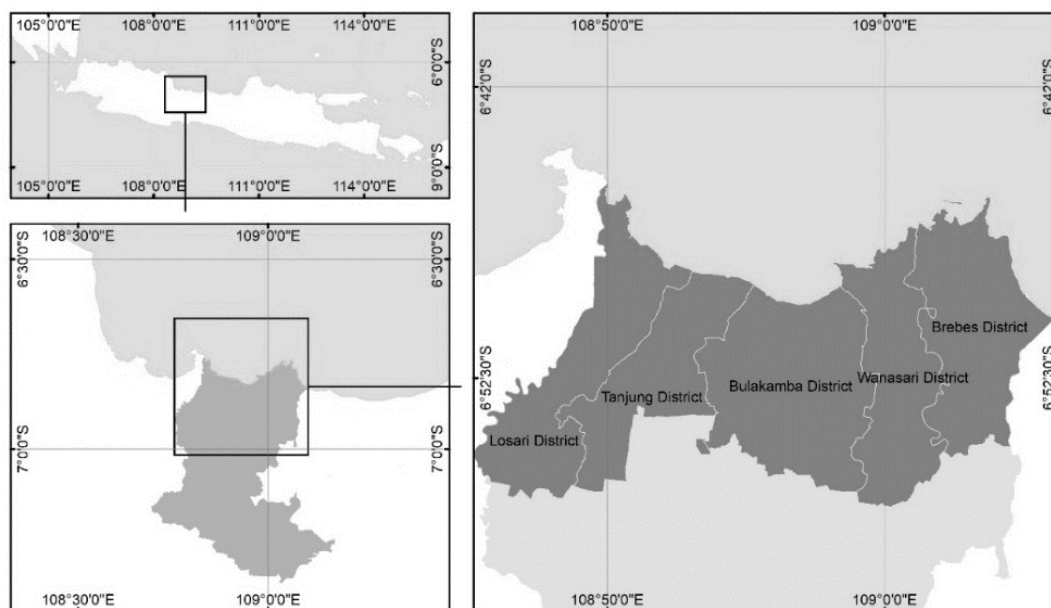
Fig. 1. Study area in the coastal area of Brebes Regency, Central Java Province.

2. STUDY AREA

The study area was located in Brebes Regency, Central Java Province, Indonesia. Brebes Regency is located between 6° 44'- 7° 21' S and 108° 41'- 109° 11' E (**Fig. 1**). The northern part of the study area is adjacent to the Java Sea, the eastern part is adjacent to the Tegal City and Tegal Regency, the southern part is adjacent to the Banyumas Regency, and the western part is adjacent to

the West Java Province. Brebes Regency consists of 17 Districts, five of which (Losari, Tanjung, Bulakamba, Wanasari, and Brebes) are directly adjacent to the sea, and approximately 19.92% to 42.01% of the area is used for aquaculture ponds, with the Brebes district having the largest area of aquaculture ponds (**Table 1**).

Table 1.

Total Area of Ponds in the Coastal Area of Brebes Regency.

District	District Area (Ha)	Ponds Area (Ha)	Percentage (%)
Losari	9179	2602	28.35
Tanjung	7209	2555	35.44
Bulakamba	12036	2215	18.40
Wanasari	7534	1501	19.92
Brebes	9223	3875	42.01

Source: (BPS-Statistics of Brebes Regency, 2020).

3. DATA AND METHODS

3.1. Sentinel-1 Data

This study used 12 Sentinel-1A, dual-polarization (VV and VH) images in interferometric wide-swath mode (IW-SM) and ground range detected high resolution (GRDH) format with a 10-meter spatial resolution in descending orbit with a period from September 2019 to August 2020. More details regarding the Sentinel-1 images used in this analysis are presented in Appendix 1 and Appendix 2.

Preprocessing was completed using the SNAP Sentinel-1 ToolBox application by following the steps suggested by Filipponi (2019). During processing, the Sentinel-1 images were cropped to the extent of the study area. Then, the *Apply Orbit File* was applied by updating the metadata to acquire an accurate satellite position, followed by *Thermal Noise Removal* to reduce the noise effect in inter-sub-swath textures. Another step, namely, *Calibration,* was used to convert the pixel digital number value to a unitless radiometrically calibrated radar backscatter followed by *Speckle Filtering* to remove speckle and improve the visual quality of the SAR images. In this study, a Refined Lee Filter with a 5x5 window size was selected because it could remove noise while maintaining the quality of the pixel points and edges of the image (Rana & Suryanarayana, 2019).

Additional steps such as *Terrain Correction* were applied to the data by using the digital elevation model (DEM) from the Shuttle Radar Topographic Mission (SRTM) with a 30-meter spatial resolution. Also, the orbit files were used to geometrically correct the distortion of the images caused by topography such as layover, foreshortening, and shadow. Lastly, the terrain-corrected data was converted from the previously unitless backscatter to decibel (dB) by using logarithmic transformation. In addition, to identify the variety of land cover, false-color composite or band combination using multitemporal Sentinel-1 data was completed. This step was conducted so that the existing land cover could be identified which was then used to determine the training samples for classification.

3.2. Sentinel-2 Data

Sentinel-2 is an optical imaging program launched as part of the European Space Agency's (ESA's) Copernicus program. Sentinel-2 data were often used to carry out terrestrial observations such as forest monitoring, land cover change detection, and natural disaster management. Sentinel-2 data are included in a multispectral, medium-resolution image with 13 spectral bands. For this study, Sentinel-2 data was acquired in July and has an 11.13% cloud cover, mostly located outside of the study area. More details on the Sentinel-2 data characteristics are presented in Appendix 3.

Atmospheric correction was applied to the data to eliminate atmospheric disturbances. This process was completed using Command Prompt by utilizing the system from Sen2Cor 2.8.0. Band

selection was conducted to choose bands having a 10-meter spatial resolution, which were used as analysis material to match with the spatial resolution of the Sentinel-1 data. Therefore, only Band 2, Band 3, Band 4, and Band 8 were used in the image classification process. False-color composite (RGB: Band 8, Band 4, Band 3) was used to interpret the Sentinel-2 images of the training and validation areas (**Fig. 2**). All of the processing steps for the Sentinel-2 data were conducted using SNAP.

Fig. 2. Visual differences in band composite (a) True-color composite (RGB: 432); (b) False-color composite (RGB: 843).

3.3. Generating GLCM

Textural analysis was performed on the Sentinel-1 data using the GLCM calculation in the SNAP software. GLCM contains integrated information concerning the direction, interval, and extent of changes of the gray level, serving as the basis for analysis of local area features in an image and their arrangement patterns (Hall-Beyer, 2017). Haralick et al. (1973) identified 14 types of texture features as part of the GLCM dataset. In this study, we used 10 types of textures (angular second moment (ASM), correlation, contrast, dissimilarity, energy, entropy, mean, variance, homogeneity, and max). These textures were used as the input dataset for the classification process. The results of the GLCM texture analysis from VH polarization can be seen in **Fig. 3**.
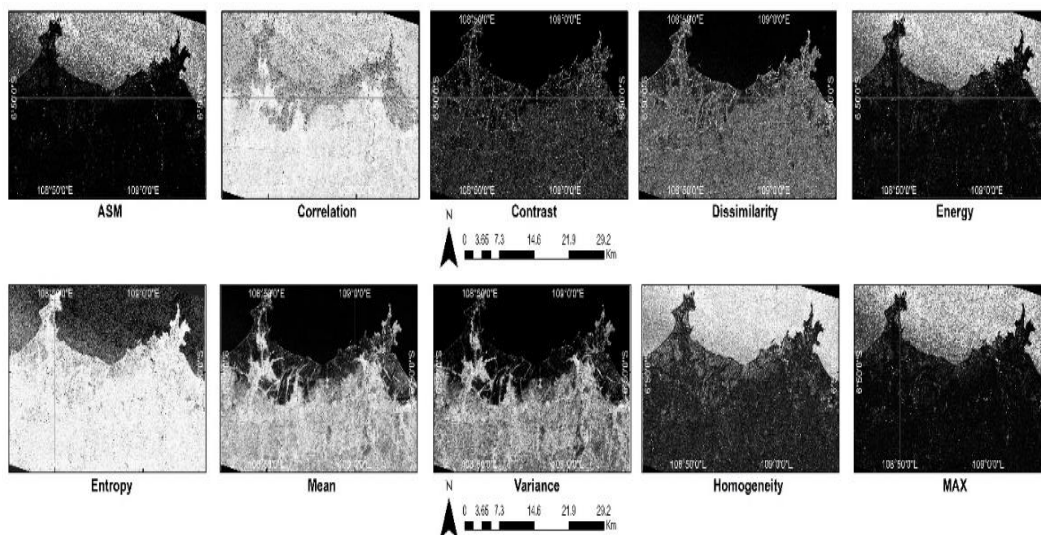
Fig. 3. GLCM texture extraction results from Sentinel-1 VH polarization.

3.4. Supervised Classification and Validation Analysis

Supervised classification was used to differentiate between ponds and paddy fields using the algorithms available in the SNAP software for Sentinel-2 imagery, such as minimum distance (MD) (Rajalakshmi et al., 2013), maximum likelihood (ML) (Marini et al., 2013), K-nearest neighbor (KNN), and random forest (RF) (Kulkarni & Lowe, 2016).
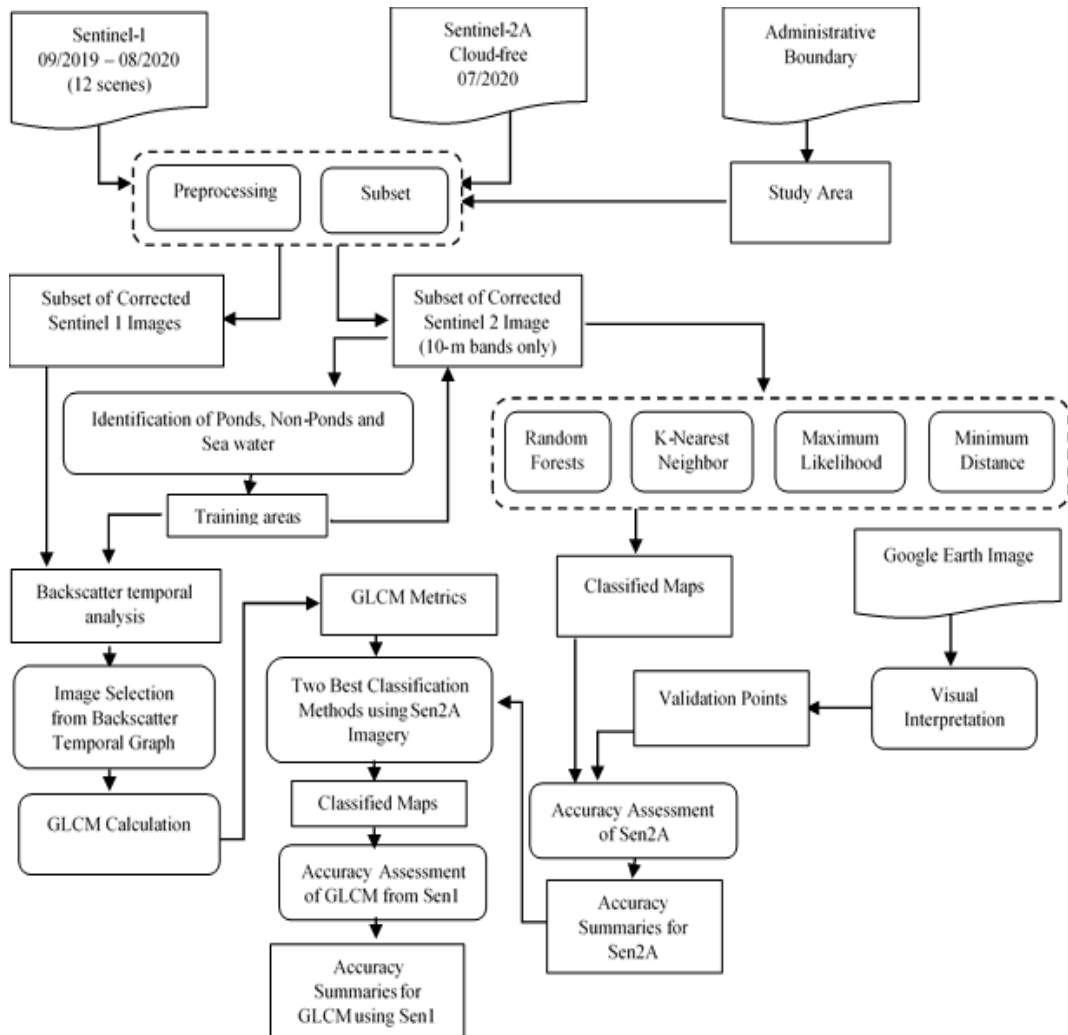
Fig. 4. Workflow of processing that was conducted in this study.

A brief explanation of each method is presented below:
1. The ML classification assumes that the statistical distribution occurs normally in each class of each band and that the calculation of the probability of a certain pixel falls into a certain class. Additionally, the pixels are assigned to a class that has a high probability (Richard, 1999).
2. The MD classification calculates the Euclidean distance from each unknown pixel to the mean vector for each class and uses the mean vector of each end member. Pixels are classified according to the nearest class based on the specified conditions except for the specified standard deviation or threshold. However, some pixels may be unclassified because they do not meet the predetermined criteria (Richards, 1999).

3. The KNN algorithm works by classifying the number (*k*) of neighbors that are located near to the training samples by calculating the Euclidean distance from the training data to the unclassified data (Li & Cheng, 2009).
4. RF is a bootstrap aggregating method that creates a multiple-tree classifier by iteratively resampling the original data. The final class for the classification is determined by majority voting (Breiman, 2001).

Before classification, the training areas were collected by conducting visual interpretation using the image composite from the Sentinel-2 data. Three classes were represented in the classification process, including pond, non-pond, and seawater areas. More details about the data processing flow can be seen in **Fig. 4**.

The classification results obtained from Sentinel-1 and Sentinel-2 imagery were validated by using the information from the high-resolution satellite image (HRSI) available from Google Earth. Approximately 2.520 points were collected and used to test the accuracy of the classification results from the Sentinel-1 and Sentinel-2 imagery analysis. The accuracy tests were carried out using the confusion matrix and kappa coefficient methods by calculating the producer, user, and overall accuracies (PA, UA, and OA, respectively).

4. RESULTS AND DISCUSSIONS

4.1. Classification Results Using Sentinel-2 Optical Bands

The classification of Sentinel-2 images used the same classes as Sentinel-1 radar images (sea, pond, and non-pond) and used the same training data. Image classification was carried out by supervised classification with the RF, ML, MK, and KNN algorithms using the SNAP application. The purpose of using these four algorithms was to determine which algorithm was the most accurate when classifying images using the same sample data applied to Sentinel-1 image classification. The results of the Sentinel-2 image classification using the aforementioned algorithms and the comparison with the composite image using false-color can be seen in **Fig. 5** below.
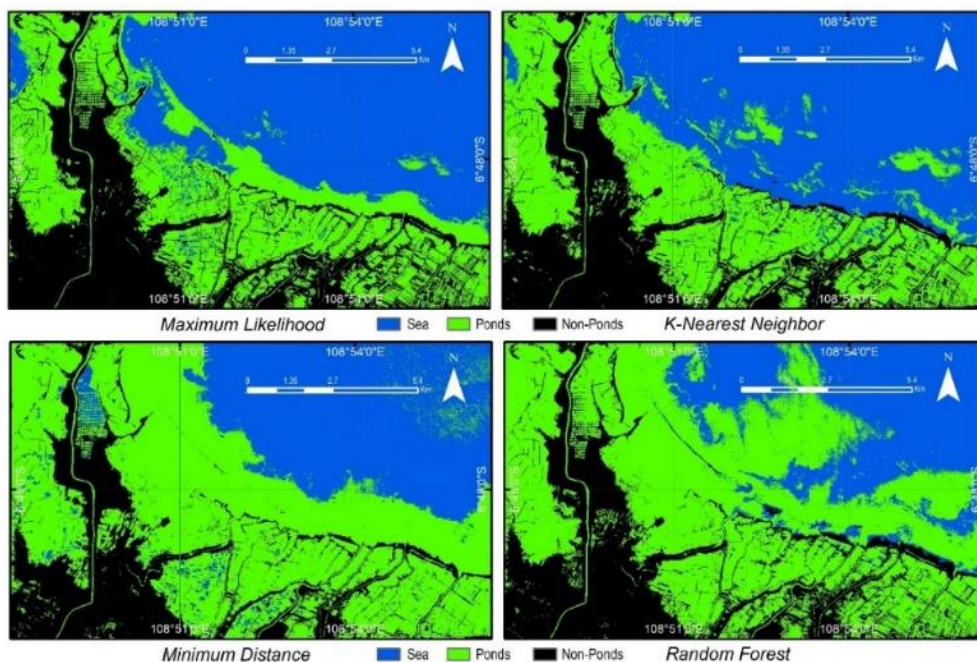
Fig. 5. Result of Sentinel-2 image classification using RF, ML, MK, and KNN algorithms.

A narrow area is required to show more clearly the comparison of the classification results for each algorithm, as well as to identify the pond according to the given sample data based on the interpretation results. The ML and KNN classifications give good results with 0.884 and 0.876. The accuracies of ML and KNN were better when compared to the MD and RF classifications. The results, which are a test of the accuracy of each algorithm using the confusion matrix, are presented in **Table 2** below. From **Table 2**, it can be seen that the classification using the ML algorithm produced a better overall accuracy (88.4%) when compared to the other classifications. The KNN algorithm follows with an overall accuracy of 87.6%. The result that gives the lowest overall accuracy is the classification using the MD algorithm, having an overall accuracy of 75.4%.

Table 2.

Accuracy Test Result of Sentinel-2 Image Classification.

Method	Producer Accuracy (%)	User Accuracy (%)	Overall Accuracy (%)
Minimum Distance	69.004	72.059	75.4
Random Forest	72.671	86.761	81.0
Maximum Likelihood	87.056	89.998	88.4
K-Nearest Neighbor	83.944	89.807	87.6

4.2. Selection of Sentinel-1 Data Images for Producing GLCM Features

The GLCM textures were produced from the Sentinel-1 VH polarization data. VH polarization was used to describe surface conditions because it has a more precise visualization than VV polarization and because VH is more sensitive to changes in moisture on the surface cover (Arjasakusuma et al., 2020). The appearance of each image at a particular time (September 2019–August 2020) can be seen in **Fig. 6** below. In addition, we selected scenes with the most contrast between seawater and paddy fields to derive the GLCM metrics.
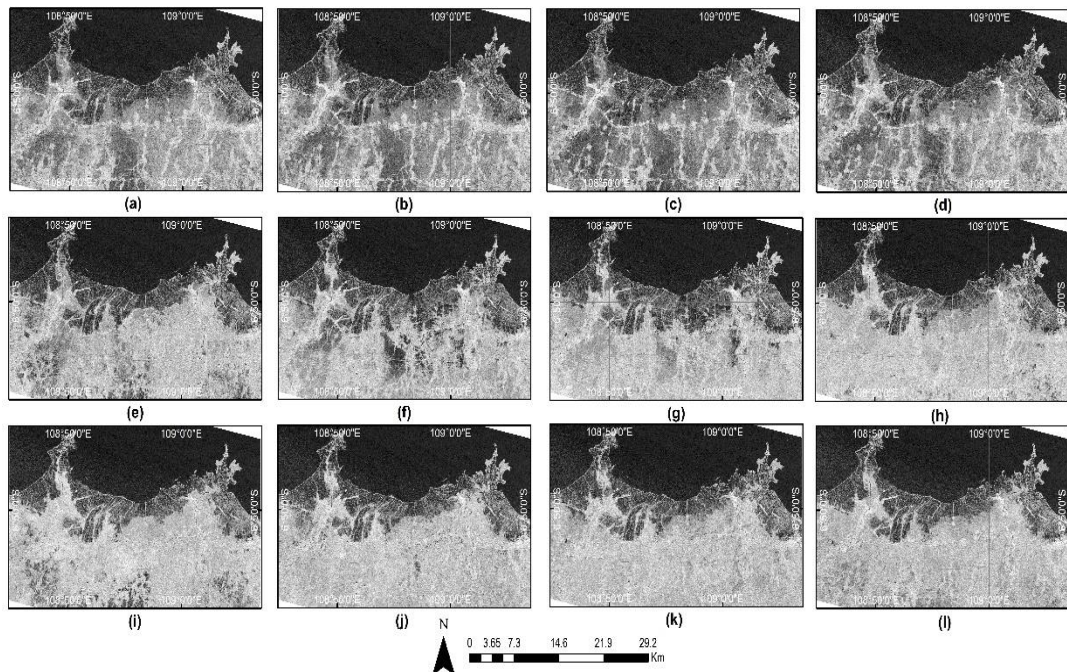
Fig. 6. Sigma_VH Polarization of Sentinel-1 (a) 07 September 2019, (b) 01 October 2019, (c) 06 November 2019, (d) 12 December 2019, (e) 05 January 2020, (f) 10 February 2020, (g) 05 March 2020, (h) 10 April 2020, (i) 04 May 2020, (j) 09 June 2020, (k) 03 July 2020, (l) 08 August 2020.

Based on **Fig. 6**, which shows the Sentinel-1 image at various points in time, it can be seen that there is a different tone of the land area that is somewhat far from the coast. Based on the results of a rough interpretation, it can be assumed that these features are rice fields, which have different appearances at certain times (dark-light-dark). To prove this, further analysis was carried out by stacking or merging bands on Sentinel-1 image data at different times into one unit. After that, an RGB composite with a different time composition was formed by utilizing the same variation, which in this case was the VH polarization.

The results of this RGB composite show objects that change over time. The changes that occur can be recognized by the appearance of a variety of colors. For several objects previously interpreted, further identification and analysis of the intensity of the dB values were conducted, especially for sea, ponds, and paddy fields, which at one time may have similar appearances (inundation phase). The differences between the spectrum of each object sampled over 12 months can be seen in **Fig. 7**. From **Fig. 7**, we selected October 2019, June 2020, and July 2020 as the input data for calculating the GLCM textural features, due to the large differences between ponds and paddy fields during these timeframes.
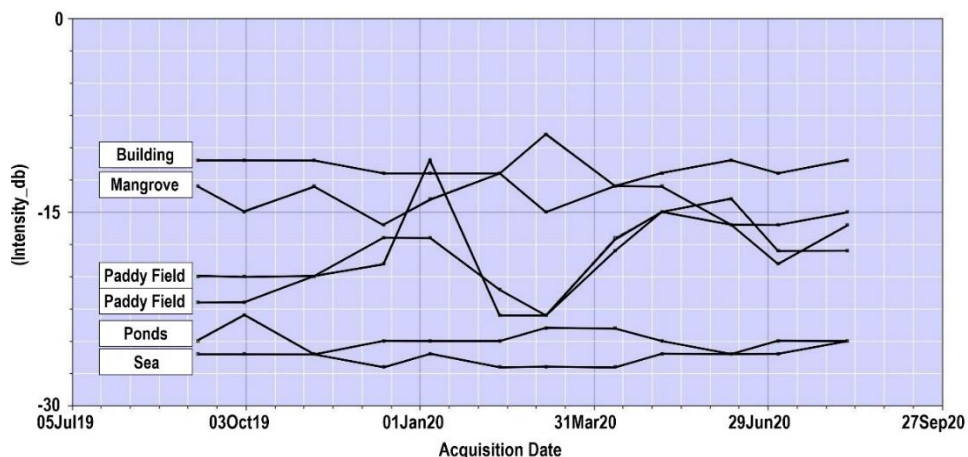
Fig. 7. The VH-backscatter spectrum of objects on Sentinel-1 images
between September 2019 and August 2020.

4.3. Supervised Classification using GLCM from Selected Sentinel-1 Data

Supervised classification was conducted by using the generated GLCM textures from selected images on October 2019, June 2020, and July 2020. There were 10 GLCM textures for each image, which brings the total number of input variables for classification to 30 textures for one polarization. We conducted the comparison of supervised classification with the ML and KNN algorithms using GLCM textures from VH polarization. The ML and KNN algorithms were employed since they performed well during the Sentinel-2 classification. However, we also conducted the supervised ML and KNN classification using VV polarization for comparison purposes. The classification results from both polarizations can be seen in **Fig. 8.**

The accuracy assessment conducted on the results in **Fig. 8**, using the input GLCM textures from multitemporal VH polarization, identified the ML algorithm as the most accurate, having an OA of 92.16%. For the aquaculture ponds class, the PA was 89.30% with a UA of 94.23%. The worst classification result was produced by using textures from VV, which showed a misclassification between seawater and pond. The accuracy using VV polarization lies between 88.11% (KNN) and 89.2% (ML). Complete results of the PA, UA, and OA for the aquaculture class can be found in **Table 3**.
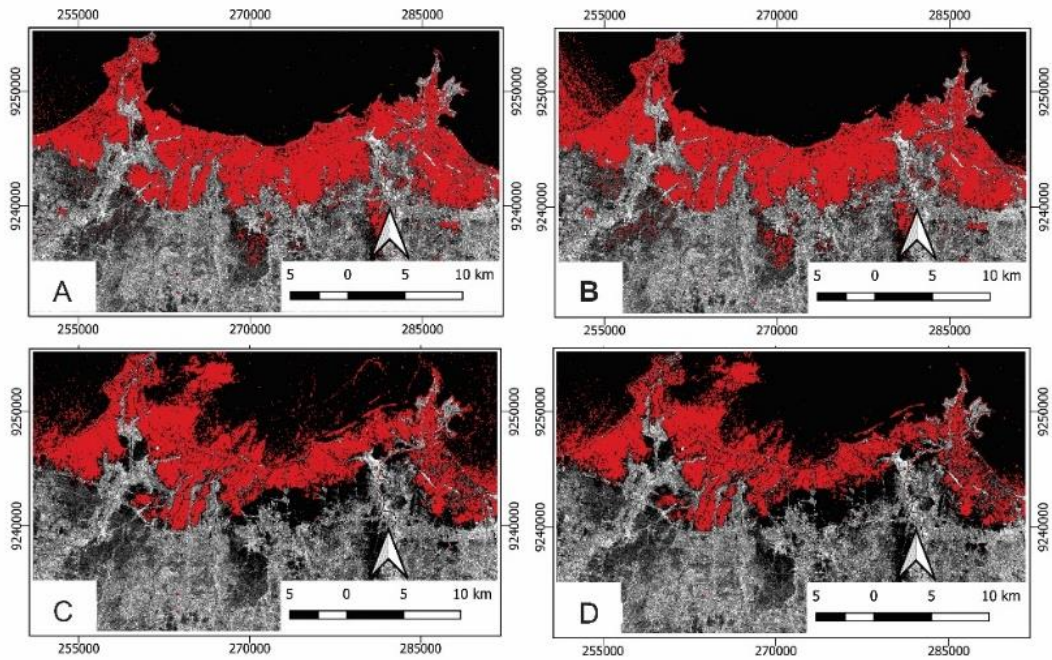
Fig. 8. Results of classification with textures from VH using (a) ML and (b) KNN,
and from VV using (c) ML and (d) KNN.

Table 3.

Accuracy Assessment using GLCM from Sentinel-1 as the Input for Image Classification.

Polarization	Method	Producer Accuracy (%)	User Accuracy (%)	Overall Accuracy (%)
VV	Maximum Likelihood	87.86	89.66	89.20
	K-nearest neighbor	81.91	92.72	88.11
	Maximum Likelihood	89.30	94.23	92.15
VH	K-nearest neighbor	89.71	91.47	90.95

5. CONCLUSIONS

This study has analyzed the potential of textural information using GLCM from multitemporal Sentinel-1 data for classifying aquaculture ponds when compared with the 10-meter bands of optical Sentinel-2 data. Sentinel-1's GCLM textures using VH polarization were better than Sentinel-2's for distinguishing aquaculture ponds, with a 92% OA, 89.30% PA, and 94.23% UA using the ML algorithm. Meanwhile, the highest OA produced by the Sentinel-2 data was 88.4% using the ML algorithm. Misclassification of ponds was frequently generated due to the similarities between ponds and seawater during coastal flooding that often occurred in the study area. In the future, the combination of all GLCM features or the combination from radar backscatter and texture with optical image classification can be tested with various methods to produce the highest accuracy.

Author Contribution: S.A. and P.W. assist in designing research concepts. S.A, S.S.K, N.A.H. prepare up to data processing. S.K. and P.W. provide input in research results.

R E F E R E N C E S

European Space Agency. (2013). Sentinel-1: Instrument Payload. https://sentinel.esa.int/

Arjasakusuma, S., Swahyu Kusuma, S., Rafif, R., Saringatin, S., & Wicaksono, P. (2020). Combination of Landsat 8 OLI and Sentinel-1 SAR Time-Series Data for Mapping Paddy Fields in Parts of West and Central Java Provinces, Indonesia. ISPRS International Journal of Geo-Information, 9(11), 663. https://doi.org/10.3390/ijgi9110663

BPS-Statistics of Brebes Regency. (2020). Kabupaten Brebes dalam Angka (Brebes Regency in Figures) (B.-S. of B. Regency (ed.)). BPS-Statistics of Brebes Regency. https://brebeskab.bps.go.id/publication/2020/04/27/d3f4377eb63e5edd93cb6217/kabupaten-brebes-dalam-angka-2020.html

Breiman, L. (2001). Random forests. Random Forests, 45, 5‑32. https://doi.org/10.1023/A:1010933404324

Chen, W., Lin, Y., & Tseng, K. (2018). Monitoring Temporal Variation of Ecological Ponds in Taiwan by Using Sentinel Images. 20, 11976. https://ui.adsabs.harvard.edu/#abs/2018EGUGA..2011976C/abstract

Duan, Y., Li, X., Zhang, L., Chen, D., Liu, S., & Ji, H. (2020). Mapping national-scale aquaculture ponds based on the Google Earth Engine in the Chinese coastal zone. Aquaculture, 520(November 2019), 734666. https://doi.org/10.1016/j.aquaculture.2019.734666

Gusmawati, Niken F., Zhi, C., Soulard, B., Lemonnier, H., & Selmaoui-Folcher, N. (2016). Aquaculture pond precise mapping in Perancak Estuary, Bali, Indonesia. Journal of Coastal Research, 1(75), 637‑641. https://doi.org/10.2112/SI75-128.1

Gusmawati, Niken Financia, Andayani, A., & Mu'awanah, U. (2016). Pemanfaatan Data Penginderaan Jauh Resolusi Tinggi Untuk Pemetaan Tambak Di Kecamatan Ujung Pangkah, Gresik. Jurnal Kelautan Nasional, 11(1), 35. https://doi.org/10.15578/jkn.v11i1.6065

Hall-Beyer, M. (2017). GLCM Texture: A Tutorial v. 3.0. Arts Research & Publications, 2017‑03, 75. https://prism.ucalgary.ca/handle/1880/51900%0Ahttp://hdl.handle.net/1880/51900

Haralick, R. M., Shanmugam, K., & Dinstein, I. (1973). Textural Features for Image Classification. SEG Technical Program Expanded Abstracts, 3(6), 610‑621. https://doi.org/10.1190/segam2015-5927230.1

Joffre, O. M., Poortvliet, P. M., & Klerkx, L. (2019). To cluster or not to cluster farmers? Influences on network interactions, risk perceptions, and adoption of aquaculture practices. Agricultural Systems, 173(February), 151‑160. https://doi.org/10.1016/j.agsy.2019.02.011

Lasabuda, R. (2013). Regional Development in Coastal and Ocean in Archipelago Perspective of The Republic of Indonesia. Jurnal Ilmiah Platax, I, 92‑101. https://doi.org/10.35800/jip.1.2.2013.1251

Li, Y., & Cheng, B. (2009). Oh 2. 2009 17th International Conference on Geoinformatics, Geoinformatics 2009, 1‑4. https://doi.org/10.1109/GEOINFORMATICS.2009.5293389

Obida, C. B., Blackburn, G. A., Whyatt, J. D., & Semple, K. T. (2019). River network delineation from Sentinel-1 SAR data. International Journal of Applied Earth Observation and Geoinformation, 83(July), 101910. https://doi.org/10.1016/j.jag.2019.101910

Ottinger, M., Clauss, K., & Kuenzer, C. (2016). Aquaculture: Relevance, distribution, impacts and spatial assessments - A review. Ocean and Coastal Management, 119(2016), 244‑266. https://doi.org/10.1016/j.ocecoaman.2015.10.015

Ottinger, M., Clauss, K., & Kuenzer, C. (2017). Large-scale assessment of coastal aquaculture ponds with Sentinel-1 time series data. Remote Sensing, 9(5). https://doi.org/10.3390/rs9050440

Porporato, E. M. D., Pastres, R., & Brigolin, D. (2020). Site Suitability for Finfish Marine Aquaculture in the Central Mediterranean Sea. Frontiers in Marine Science, 6(January), 1‑12. https://doi.org/10.3389/fmars.2019.00772

Rana, V. K., & Suryanarayana, T. M. V. (2019). Evaluation of SAR speckle filter technique for inundation mapping. Remote Sensing Applications: Society and Environment, 16(October), 100271. https://doi.org/10.1016/j.rsase.2019.100271

Stiller, D., Ottinger, M., & Leinenkugel, P. (2019). Spatio-temporal patterns of coastal aquaculture derived from Sentinel-1 time series data and the full Landsat archive. Remote Sensing, 11(14), 1‑18. https://doi.org/10.3390/rs11141707

Xia, Z., Guo, X., & Chen, R. (2020). Automatic extraction of aquaculture ponds based on Google Earth Engine. Ocean and Coastal Management, 198(September), 105348. https://doi.org/10.1016/j.ocecoaman.2020.105348

LANDSLIDE SURFACE DEFORMATION ANALYSIS USING SBAS-INSAR IN THE SOUTHERN PART OF THE SUKABUMI AREA, INDONESIA

Muhamad Khairul ROSYIDY[1], Muhammad DIMYATI[2*], Iqbal Putut Ash SHIDIQ[3] (ID),
*Faris ZULKARNAIN[3], Nurul Sri RAHANINGTYAS[3], Riza Putera SYAMSUDDIN[3]
and Farhan Makarim ZEIN[3]*

ABSTRACT:
Landslide is a natural phenomenon that frequently occurs on the Java Island of Indonesia, causing significant damage and casualties. Due to advances in remote sensing technology, radar imaging can detect and evaluate ground surface deformation. This study examines the ground surface deformation and displacement in each landslide location in terms of spatial and temporal and identifies the different types and characteristics of landslides in the Sukabumi area of West Java, Indonesia. The Small Baseline Subset Interferometric Synthetic Aperture Radar (SBAS-InSAR) methodology was used in this study, and the DinSAR method was applied. We combined the LiCSAR data product with the Python coding-based LiCSBAS processing package to derive a surface displacement value at each landslide location. The results show that the DinSAR approach can detect surface deformation by integrating the LiCSAR product with the Python coding-based LiCSBAS processing software. According to quantitative data, the research area experienced surface deformation with a surface displacement velocity of -36,297 mm/year to 58,837 mm/year. The ground surface displacement at each landslide location ranged from -9.79 mm/year to +33.69 mm/year, with most of the landslides occurring on moderate to steep slopes (16^0-35^0). These results are suitable to use for support regional development planning in reducing losses and casualties.

Key-words: *Displacement, Deformation, Landslide, LICSBAS, SBAS-InSAR*

1. INTRODUCTION

Indonesia is prone to several different sorts of natural disasters. There were over 1,800 disasters between 2005 and 2015, with 78 percent (11,648) hydro-meteorological disasters such as floods, extreme waves, land and forest fires, drought, and extreme weather. Meanwhile, natural disasters such as earthquakes, tsunamis, volcanic eruptions, and landslides accounted for 22% (3,810 disasters) of the disasters (Amri et al., 2018). The number of disasters in Indonesia increased from 1732 in 2015 to 2342 in 2016, 2372 in 2017, and 3721 in 2019. In Indonesia, there were 702 landslides (18.9%) in 2019, resulting from 3,721 disasters (BNPB, 2019). Six hundred fifty-seven natural disasters registered in January-February 2021, with 282 fatalities, 3,421,871 people suffering and dying, and 53,287 housing being damaged (BNPB, 2021).

The surrounding area of the Sukabumi area, West Java, is one of the areas in Indonesia that frequently experiences disasters such as landslides, floods, and extreme weather (Damayanti et al.,

[1]Departement of Geography, Faculty of Mathematics and Natural Sciences, Universitas Indonesia, 16424 Indonesia; khairulnajwa1@gmail.com
[2*]Faculty of Mathematics and Natural Sciences, Universitas Indonesia, 16424 Indonesia, Corresponding author, muh.dimyati.ristekdikti@gmail.com
[3]Faculty of Mathematics and Natural Sciences, Universitas Indonesia, 16424 Indonesia, iqbalputut@sci.ui.ac.id, faris.zulkarnain@sci.ui.ac.id, nurul.sr@ui.ac.id,

2020). According to Alfarabi et al. (2019), the terrain, types of bedrock, and geomorphic processes can cause variations in landslides in the Sukabumi area. Pelabuhanratu and Cisolok areas, as a part of the Sukabumi regency, have moderate to high levels of soil movement and landslide vulnerability (Alfarabi et al., 2019; Sugianti et al., 2016). In 2018, a relatively large landslide buried 30 houses in Cisolok District, Sukabumi Regency (BNPB, 2018). This area has physical characteristics that can increase the potential of landslides (Ristya et al., 2019).

Ground movement is a geological hazard that commonly occurs in hilly areas and can result in casualties, infrastructure damage, and economic losses (Malinowska et al., 2020; North et al., 2017; Nowicki Jessee et al., 2020; Perera et al., 2018). An example of a soil movement phenomenon is landslides. Landslides are a phenomenon of the movement of soil, rocks, and organic matter down the slope due to the influence of gravity (Bobrowsky & Highland, 2013). The hydrological characteristics, geological-geotechnical conditions, slope, land use, and human activities can cause soil movement (Bogaard & Greco, 2018; Cogan & Gratchev, 2019; El Jazouli et al., 2020; Martins et al., 2020; Persichillo et al., 2017). In addition, soil movement can also be caused by human activities, such as water extraction, mining activities, cutting slopes for road construction, and others (Bateson et al., 2015; Cigna & Sowter, 2017; Hearn et al., 2020; Persichillo et al., 2017). In addition, ground movements due to landslides can cause topographic changes (Dehghani & Javadi, 2013; Guo et al., 2020). Therefore, monitoring and mapping ground movements such as landslides are necessary to minimize the risk of landslides and other ground movements (Crosetto et al., 2018; Skrzypczak et al., 2021). The value of surface deformation can be a measurable indicator for detecting landslides (Aslan et al., 2020; Qu et al., 2016; Shirani & Pasandi, 2019). The surface ground deformation can be detected using radar remote sensing, namely Synthetic Aperture Radar (SAR). SAR is also used for other applications such as measuring topographic effects by volcanic activity (Remy et al., 2003), shoreline identification (Zollini et al., 2020) and assessing ground movement by a landslide using interferometric SAR (Wasowski & Bovenga, 2014).

Interferometric SAR (InSAR) and advanced differential InSAR (A-DInSAR) are techniques that can provide centimeter to millimeter-level records of terrain topographic changes and surface deformations (Pawluszek-Filipiak & Borkowski, 2020; Ramirez et al., 2020; Roccheggiani et al., 2019). According to Ramirez et al. (2020), the DinSAR technique utilizes phase information in two or more SAR images taken at different times in the same area to form interferometric pairs. However, DinSAR has a weakness limited to signal de-correlation at the specific land cover, which interferes with interpreting deformations (Cigna & Sowter, 2017). In order to minimize the effect of de-correlation, it is necessary to use interferometric data with a short or small baseline (Pepe & Calò, 2017; Qu et al., 2016). Therefore, this study uses an advanced technique from DinSAR, namely the Small Baseline Subset Interferometric Synthetic Aperture Radar (SBAS-InSAR) approach. According to Bateson et al. (2015), this approach consists of many SAR data acquisitions spread over a small subset of baselines. SBAS-InSAR approach allows for an effortless combination of computationally calculated InSAR data and standard processing techniques based on deformation time sequences (Bateson et al., 2015). This approach relies on using a large number of SAR data acquisitions and applying an effortless combination of a selected and computed set of multi-look DinSAR interferograms so that the result is a time-series map of the mean velocity of deformation and ground motion (Casu et al., 2006; De Luca et al., 2018; Yastika et al., 2019). According to Bateson et al. (2015), SBAS is suitable to detect land surface deformation in rural areas. To carry out this technique, LiCSBAS is used to process SAR data. LiCSBAS is a LiCSAR product data processing package developed by Morishita et al. (2020) to process time-series InSAR and estimate deformation velocity. LiCSAR is a collection of free-access interferogram data of Sentinel-1 imageries from the COMET-LiCS portal (Morishita et al. 2020). Sentinel-1 imagery data can be used for various geotechnical engineering phenomena because it has a C band, a 10-meter resolution, and free-open access with worldwide coverage (Ramirez et al., 2020). Other researchers have not widely used LiCSAR products and LiCSBAS processing packages because they are relatively new and are still under development by Morishita et al.

Several researchers have studied and researched using the SBAS-DinSAR technique and have proven to be better for producing deformation maps than conventional DinSAR techniques. For example, Lanari et al. (2007) used the SBAS-InSAR method for the phenomenon of fault creep using 45 ERS-1/2 images. As a result, they succeeded in calculating the relative soil movement along the fault with better accuracy of 1 mm/year than field deformation measurements. SBAS can also detect ground motion due to human activities such as mining and groundwater extraction. For example, Bateson et al. (2015) utilized 55 ERS-1/2 SAR images for the 1992-1999 period to detect movements in coal mining areas in the UK using the SBAS method.

Regarding landslides, Qu et al. (2016) used the SBAS method to detect soil movement in the landslide area extracted from TerraSAR data for 2014-2015. (Novellino et al. 2017) that as many as 266 landslides with low-velocity movement (shallow landslides) were detected using the SBAS-DinSAR method. According to Novellino et al. (2017), the SBAS- DinSAR method can generate relevant information to detect slow soil movements such as slides, flows, and creep movements that dominate the evolution of slope geomorphology. Cianflone et al. (2018) conducted a mapping of landslides and land surface deformations in 2004-2010 in the Crati valley (southern Italy) using the SBAS-InSAR technique. The results showed the most soil movements detected by mass movements InSAR gravity, such as landslides and a decrease in the quaternary sediment that fills the valley.

The SBAS-InSAR technique, combined with the LICSAR and LICBAS processing packages, is still not widely utilized to assess surface ground deformation, as indicated by the references above. Meanwhile, the dynamics of landslides in Indonesia, particularly in steep and difficult-to-reach areas and densely populated areas, are being explored. Areas with an increased risk of landslides, such as Sukabumi, have missed the attention of previous researchers in this assessment. Access to radar images, on the other hand, is improving. As a result, we intend to research using radar imagery to analyze surface ground deformation in Sukabumi. This study uses the Small Baseline Subset Interferometric Synthetic Aperture Radar (SBAS-InSAR) technique by combining the LICSAR product and the LICSBAS Package. The last is conducting field surveys and documentation as the basis for determining the location of landslides.
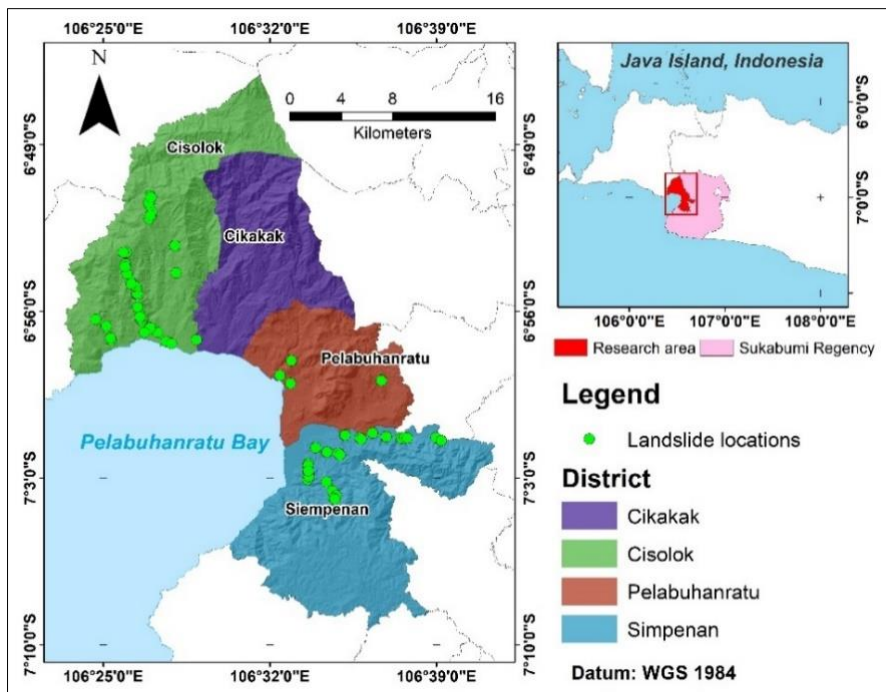

**Fig. 1**. Study area and Landslide location.

2. STUDY AREA

The study area is in the southern part of the Sukabumi area, includes Pelabuhanratu, Simpenan, Cisolok, and Cikakak Districts of Sukabumi area, West Java Province, Indonesia (**Fig. 1**). The study area is geographically located at 6°46'4 " S latitude - 7°9'25 " S latitude and 106°23'22 " E longitude - 106°41'27 " E longitude whole study area has a total area of 55,038 ha. The slopes in the study area range from modest to quite steep. The volcanic material associated with Quaternary volcanic eruptions such as breccias, lava, lahars, and tuff dominates the Sukabumi Regency area. Predominantly, the southern part of Sukabumi consists of an accumulation of alluvium deposits and coastal sediment deposits (Sugianti et al., 2016). Soil types in the study area consist of alluvial sulfic, andosol, cambisol, cambisol eutric, and podsolic haplic (Alfarabi et al., 2019). The study area has a medium to a high level of landslide susceptibility, which is impacted by physical factors of the location (geology, soil type, rainfall, land use, and geomorphology). Those factors increase the possibility for soil movements such as landslides (Alfarabi et al., 2019; Ristya et al., 2019; Sugianti et al., 2016). Based on Indonesian disaster information data obtained from https://dibi.bnpb.go.id/, 90 Landslides disasters occurred in the Sukabumi Regency from 2017 to 2020.

3. DATA AND METHODS

3.1. LiCSAR Dataset

The images utilized in this study are processed data from Sentinel-1A IW SLC images with VV polarization that were processed and downloaded to the COMET-Lics (Center for the Observation and Modeling of Earthquake Volcanoes and Tectonics) online portal named LiCSAR (comet.nerc.ac.uk). Processing sentinel-1 imageries data through the stages of correlation, spectral diversity correction, unwrapping, and multi-look to produce time-series coherence, and unwarp phase data in the form of an interferogram with pixel size or spatial resolution of 100 meters in the LiCSAR product (Morishita et al., 2020). LiCSAR time-series Sentinel-1 data with ascending satellite records from April 9, 2019 to August 13, 2020 was used in this study. **Fig. 2** illustrates the perpendicular baseline network. The basis for selecting the acquisition period is that the imageries have a low temporal baseline, resulting in low noise in the interferogram data. Sentinel-1a single look complex (SLC) imagery wide swath mode (IW) with VV polarization, ascending satellite recording direction, and LiCSAR frame id 047D 09652 111009 were the image data parameters used in this study. There are 107 interferograms in total.
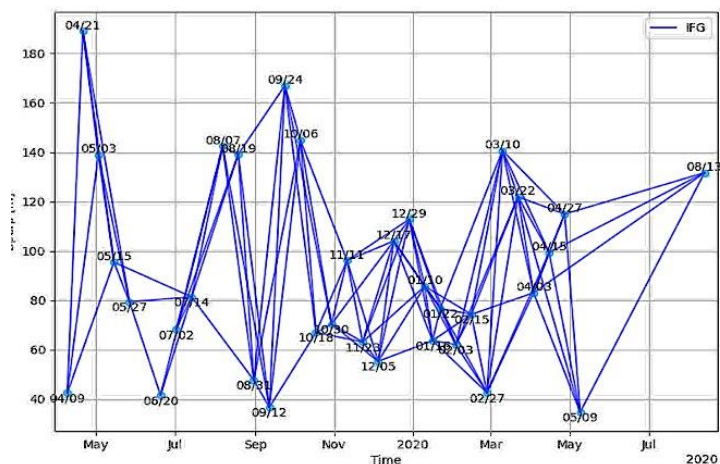
Fig. 2. Temporal baseline network of 107 interferograms constructed from 33 Sentinel-1 Imageries.

3.2. SBAS-InSAR Method using LiCSBAS Processing Package

The Small Baseline Subset (SBAS) approach analyzes LiCSAR data through LiCSBAS on the Linux Ubuntu 20.04 LT operating system. Berardino et al. (2002) developed SBAS, an advanced processing approach for the DinSAR (Differential Interferometric Synthetic Aperture Radar) methodology (Berardino et al., 2002). The goal of this method is to measure multi-temporal ground motion and map the average deformation velocity with an accuracy of up to millimeters by combining unwrapped interferograms by spatially isolating them from the baseline between each orbital acquisition at short intervals (Berardino et al., 2002; De Luca et al., 2018). The essence of this approach is the improvement of the inversion of unwrapped interferograms for time-series deformation (Lanari et al., 2007). In addition, the SBAS processing produces a soil movement map with a precision of mm/year. In this study, the SBAS method processing runs using LicSBAS, which is a LicSAR data processing tool based on Python 3 coding, and Bourne Again Shell (bash), which operates without using software (open source) (Morishita et al., 2020). According to Morishita et al. (2020), LiCSBAS lets users interpret InSAR data in time series and estimate soil movement velocity using LiCSAR products available on the COMET-Lics.

Figure 3 shows a research workflow that illustrates the detailed analysis process. Data preparation from a series of unwrapped images and multi-temporal analysis are the two critical processes of LiCSBAS's InSAR processing. First, data preparation comprises downloading LiCSAR data from the COMET-Lics web page in the form of unwrapped and coherent GeoTIFF files (comet.nerc.ac.uk). The data comes from Sentinel-1 frame ID image 047D 09652 111009, acquired for 1.35 years, from April 9, 2019, to August 13, 2020. The following stages converge GeoTIFF into a single-specification point format and use GACOS to correct atmospheric disturbances on the unwrapped interferogram (Generic Atmospheric Correction Online Service). Masking and clipping the interferogram to remove areas with less than 0.5 coherence and cutting the research area with coordinates ("106°19'48 N / 107°4'58,8 S / 7°27'14,2 W / 6°42'3,6 E") and a square area of interest are the final steps in data preparation.
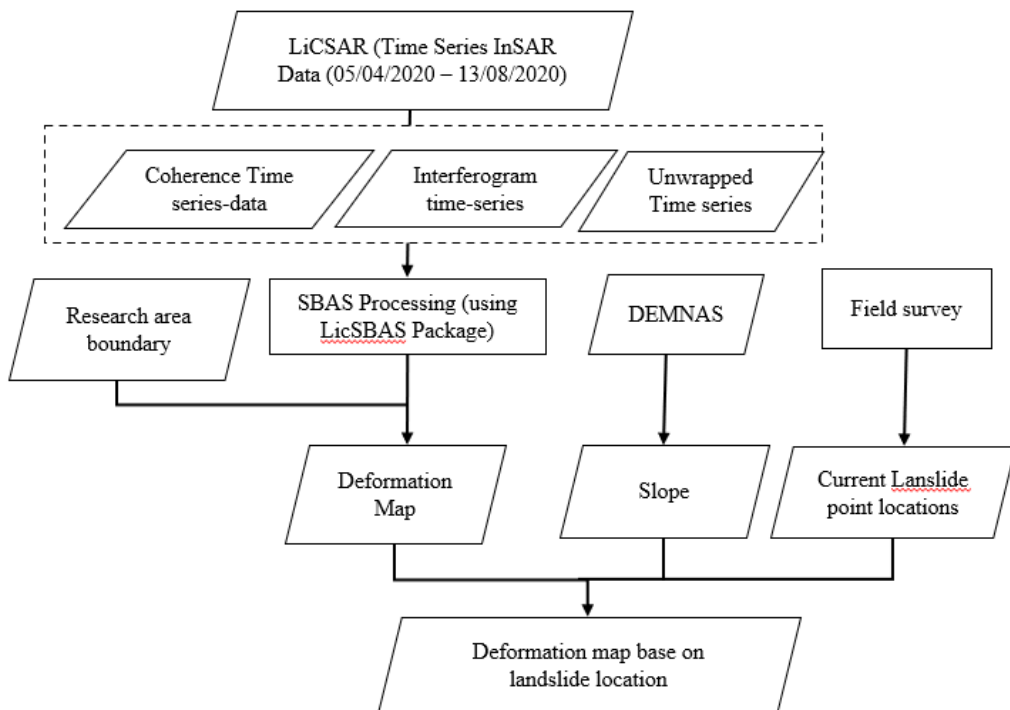
Fig 3. Research Workflow.

The multi-temporal analysis step is divided into multiple stages, beginning with a quality check of the LiCSAR interferogram result by determining the coherence average to eliminate the impacts of de-correlation caused by vegetation or other factors. The next step is to use a closed-loop to repair the network by removing unwrapping errors. The next step is the inversion of the small baseline network, which calculates the pixel surface's vertical and horizontal movement velocity from April 9, 2019, to August 13, 2020. The final steps determine the standard velocity deviation, masking of noisy pixels, and spatial-temporal filtering. The results are Line-of-Sight Displacement or LoS Displacement, which is an indicator of ground surface movement velocity. The LoS value is the result of measuring the movement of the surface at a place on the earth's surface estimated by the SAR antenna, according to Li et al. (2019). The LoS Displacement value is assumed to directly reflect vertical movement or elevation changes (Ng et al., 2012).

The landslide locations of the southern part of the Sukabumi area, which includes Pelabuhanratu, Simpenan, Cisolok, and Cikakak District, are overlaid with the deformation map derived using the SBAS method. The overlay intends to use a spatially descriptive approach to assess the deformation that occurs at landslide locations.

To analyze the landslide point elevation and deformation value, we overlay the 8-meter resolution DEMNAS obtained from the Geospatial Information Agency webpage at http://tides.big.go.id/ over the landslide locations. On November 21-25, 2020, eighty-nine landslide point locations were collected using survey and field documentation.

4. RESULTS AND DISCUSSIONS

4.1. Spatial Distribution of Surface Deformation

The results of InSAR processing using the SBAS method from LiCSAR data suggest that the study area has a relatively coherence value. The coherence value has a minimum of 0.032 and a high of 0.834 in the research area. The coherence value indicates how accurate InSAR processing is (**Fig. 4**). The closer the InSAR processing results are to 1, the more accurate they will be. A high coherence value means that the entering backscatter signal is nearly identical to the reflected backscatter signal, allowing the reflected signal to maintain its amplitude without considerable change. The incoming signal collides with a stationary or immovable object, such as built-up or bare land. Because it is a port area and many built-up areas, the coastline region in the study area has a high coherence value. Environments with poor coherence values, on the other hand, are found in densely vegetated areas such as forests. Because radar wave emission does not fully represent the deformation process in low coherence locations, areas with low coherence are not always deformed. Increased noise levels in the InSAR phase measurement are related to reduced coherence values in the interferogram (Anjasmara et al., 2020).

According to data processing, from April 9, 2019 to August 13, 2020, the rate of change in land elevation ranges from -36,297 mm/year to 58,837 mm/year (**Fig. 5**). Negative rate values imply land surface subsidence, whereas positive rate values indicate land surface increase (uplift). In the research area, negative results for the rate of change in height can be seen in coastal and hilly locations.

Land subsidence ranging from 10 mm/year to 5 mm/year has been seen in the coastal areas of Pelabuhanratu in the south and the North Coastal Area in Simpenan District. Positive displacement values are seen in most coastal locations in the research area, particularly in flat and intensively built-up areas. In the area along the coast, the displacement velocity is typically negative. In the area near the coast, displacement values range from less than -10 mm/year to more than +10 mm/year.
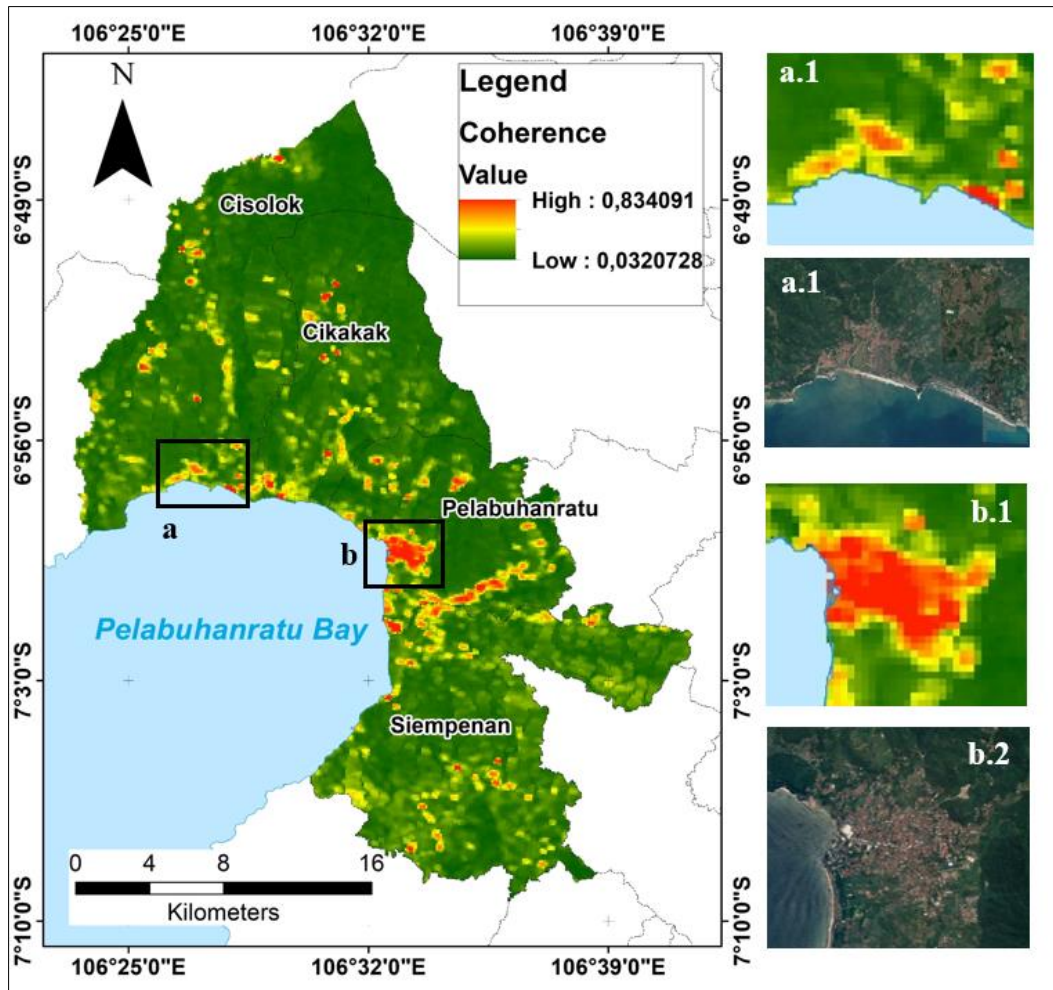
Fig.4. Coherence Map in Research Area. **4.a.1** and **4.a.2** show the built-up land with a high level of coherence in the Coastal area of Cisolok District. **4.b.1** and **4.b.2** shows built-up land with a high level of coherence in the Coastal of Pelabuhanratu District**.**

According to data analysis, the uplift area is larger than the sinking area. The area affected by subsidence was 1,623 hectares (2.9%), while the area affected by uplift was 8,275 hectares (15.0 %). Subsidence is most common in locations where the slopes are gentle to slightly steep. As a result, there are cracks in the buildings and a substantial change in ground level in the surrounding area experiencing subsidence. Fields that experience an uplift are usually development or land accumulation near rivers and valleys. According to the field study, there is development along the coast, particularly in the coastal area of the Pelabuhanratu District.

4.2. Surface Displacement in Each Landslide Locations

The landslide locations were collected as part of a field survey in November 2020, with several of the 89 points being landslide/soil movement locations. The major landslides found in the study area are Translation landslides, rockfalls, and spreads (**Fig. 6**).

(a) **(b)**
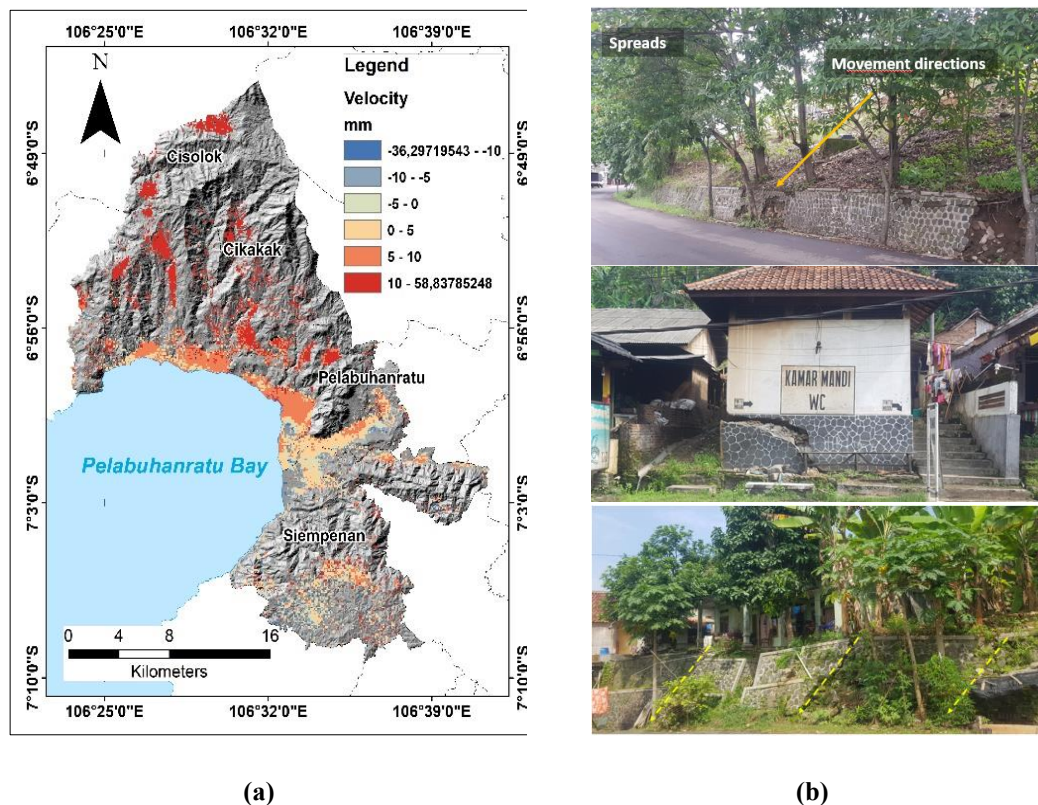
Fig. 5. (5.a) Spatial distribution of Surface Deformation in Pelabuhanratu District,
(5.b) Subsidence in Research Area.

In the research area, translational landslides occur in mountainous areas with steep to steep slopes, causing the soil mass movement to slide down the slope (Bobrowsky & Highland, 2013)**.** In the translational landslides, scrub vegetation dominated the land cover. The translation landslides found in the field survey are primarily shallow, 4 to 8 meters deep. Cisolok and Simpenan districts are prone to translational landslides. Rockfalls were found in the south part of the study area (Simpenan District). In general, rockfalls are found predominantly in cliff locations and along roads (**Fig. 6**). The vegetation is relatively dense and dominated by dense vegetation because the surrounding area is a forest. Spreads are generally slow-moving (Bobrowsky & Highland, 2013). This landslide was recognized by the cracks between the road and houses, resulting in differences in height (**Fig. 5.b**). Soil sediment can occur due to mechanical processes on slopes, pedo-genetic, and bio-geomorphic activity, and it can also be influenced by deformed tree cover in forest environments (Pawlik & Šamonil, 2018).

Landslide locations are analyzed based on the degree of slope, slope characteristics, and their relationship to landslides (**Fig 7**). According to (Berhane et al., 2020), slope angle can be related to landslides because slopes can determine surface and subsurface flow direction and significantly impact soil moisture availability, which affects slope stability. The classification of slopes is based on Zuidam et al. (1985) (Zuidam, 1985). The 89 collected landslide locations with a slope of (16^0-35^0) have the highest frequency of deformation, indicating a relatively steep slope. The highest frequency of subsidence was found at a landslide location on a very steep slope (16^0-35^0), where 22 landslide locations were identified.

Fig. 6. landslides found in the study area.
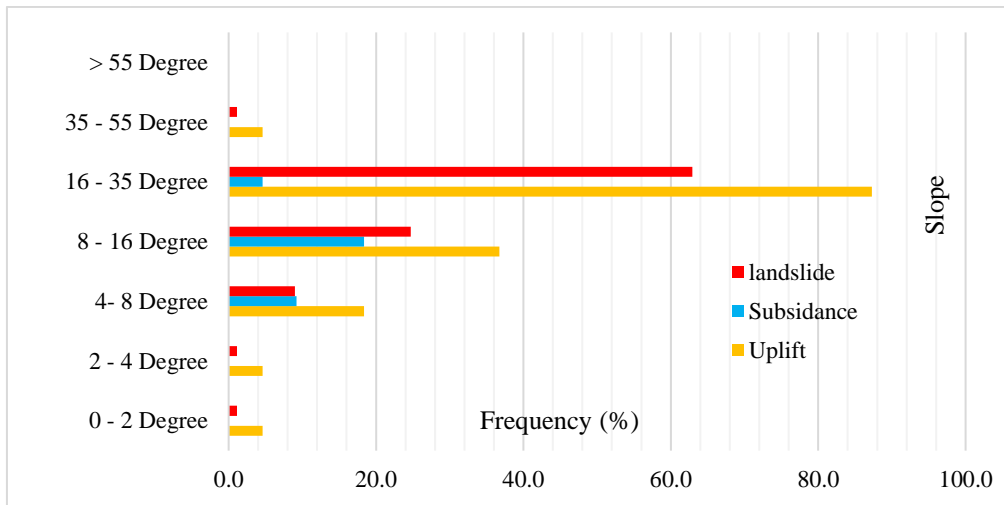
Fig. 7. Landslide frequency in each slope and deformation frequency in each slope based on landslide location.

Thus, there were 22 landslides, with the highest frequency occurring at landslide locations with varied slopes, from moderate to steep slopes (16^0-35^0). Because erosion is frequent and soil movement is gradual, landslides are more likely to occur on slopes of (16^0-35^0) and less than 15 (Çellek, 2020). Furthermore, landslides are rare on slopes with a slope angle greater than 35^0 since the bedrock has been exposed to erosion. This condition is because the slope vulnerability is inversely proportional to the angle value on the slope since it increases the soil shear stress (Çellek, 2020).
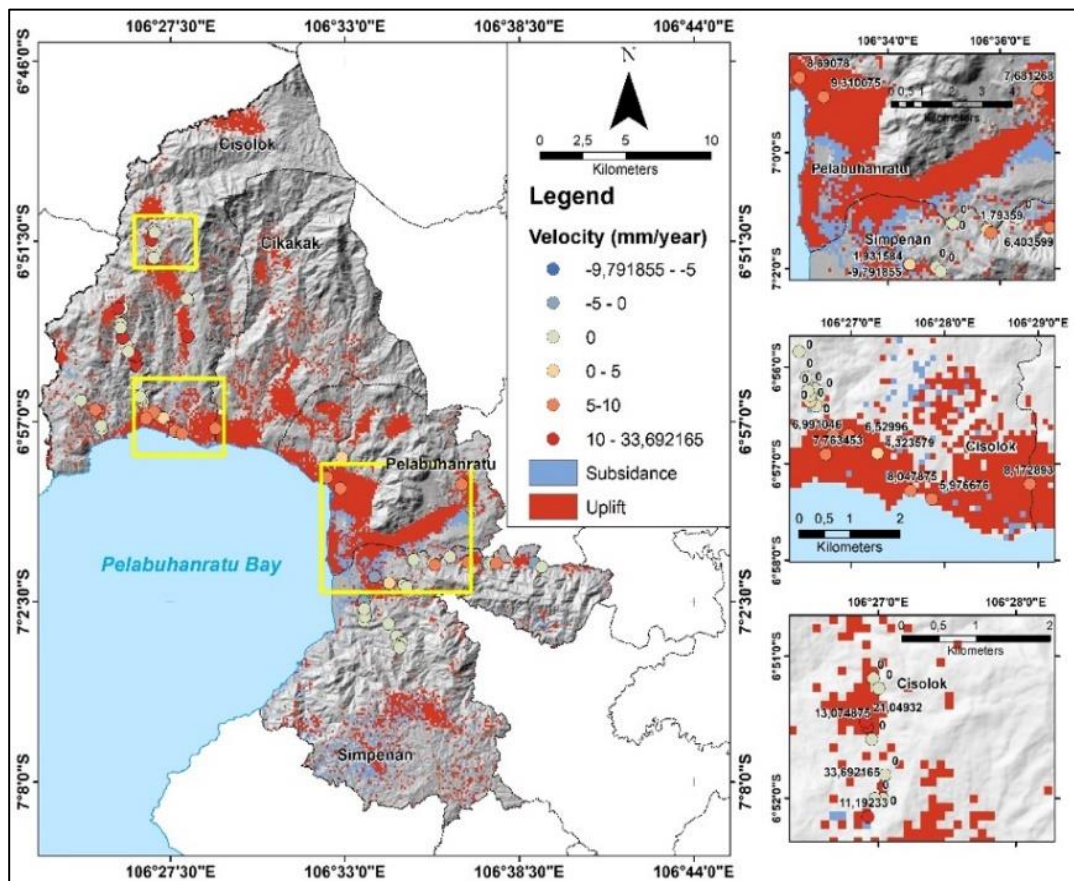
Fig. 8. Deformation value distribution in landslide point locations.

The landslide location is used to extract the displacement value acquired through LiCSBAS processing, resulting in a landslide location distribution map based on the displacement value (**Fig. 8**). Seven landslide locations in the study area experienced subsidence, whereas 33 landslide locations experienced uplift, according to the results of the deformation map overlay and landslide locations in the study area. The remaining are landslide locations that are not detected by satellite signals because vegetation cover interfering with satellite signals or processing errors in InSAR data. Each landslide location's deformation velocity was divided into six categories. The landslide's displacement velocity varies from -9.79 mm/year to +33.69 mm/year at each point. There is one landslide location in the Pelabuhanratu and Simpenan Districts with a displacement velocity of less than 5 mm/year, a minimum velocity of 9.79 mm/year, and a maximum velocity of 4.54 mm/year. There are four landslide locations with displacement velocities ranging from -5 mm/year to 0 mm/year. The most negligible displacement velocity is 4.54 millimeters per year, while the maximum velocity is 0.068 millimeters per year. The Cisolok and Simpenan Districts were the sites to the majority of the landslide locations that experienced negative displacement. The negative value at the landslide location is assumed to be a depletion zone, while the positive value is assumed to be an accumulation zone. Because the distance between a location on the earth's surface and the radar satellite sensor is far from each other, the depletion zone has a negative displacement value. The displacement value is positive because the point on the earth's surface approaches the radar satellite sensor (Aslan et al., 2020).

Positive displacement landslide areas have a minimum velocity of 1.79 mm. Favorable displacement velocity locations with a minimum velocity of 1.79 mm/year and a maximum velocity of 33.69 mm/year are found in 33 locations in the Cisolok, Cikakak, Pelabuhanratu, and Simpenan Districts. In the Cisolok District, the landslide location with the highest positive displacement value is 33.69 mm/year. There are ten landslide locations with displacement values of more than 10 millimeters per year. The displacement velocities of 16 landslide areas range from 5 mm/year to 10 mm/year. Positive displacement values of less than 5 mm/year are found in seven landslide locations. Forty-nine landslide locations had displacement with a value of 0. The SBAS-DinSAR technique does not detect the landslide location since DinSAR's ability is limited to locations with minor de-correlation and errors. Furthermore, development in the Pelabuhanratu coastline area has an impact on the displacement value.

5. DISCUSSIONS

The displacement value was obtained from 107 interferograms resulted from 33 Sentinel-1 images recorded from April 9, 2019 to August 13, 2020. The Sentinel-1 image interferogram obtained from the COMET-Lics web portal was used to process LiCSBAS. The displacement value obtained from the SBAS-DinSAR processing is -36.29 mm/year to 58.83 mm/year. This study shows that most of the displacements with positive values (uplift) are in residential areas, in coastal areas, and several locations in hilly areas, such as in Cisolok, Pelabuhan Ratu, and Cikakak districts. Meanwhile, the negative displacement value (subsidence) is located on the coast of Simpenan District, dominated by hills. With the same method, Anjasmara et al. (2020) produced displacement values in the City of Surabaya in a range of -40 mm/year to +30 mm/year using 28 Sentinel-1 images recorded from 2015-2017 (Anjasmara et al., 2020). Most of the subsidence occurs in industrial and residential areas in the coastal area of Surabaya City. Virk et al. (2019) used the same imagery dataset and 23 descending Sentinel-1 images and the PS-InSAR approach to monitoring ground displacement on landslide locations (Virk et al., 2019).

In addition, Zaenudin et al. (2018) used data from 15 ALOS PALSAR images recorded between 2006 and 2008 to derive a subsidence value of more than 30 mm/year in Bandar Lampung City. The coastline area of Bandar Lampung City has a subsidence value of more than 5 mm/year, according to Zaenudin et al. (2018). Ng et al. (2012) employed another InSAR approach, the PS-InSAR, to map land surface deformation in the Jakarta area and its surrounds using 17 ALOS PALSAR (band L) images acquired between 2007 and 2010. A survey including GPS measurements was used to round out the results of the study. In the northern part of Jakarta, the subsidence value reached 260 mm/year, with the Bekasi metropolitan region having the highest subsidence value of 155 mm/year. Prasetyo et al. (2019) used Sentinel-1 imagery data from 2014 to 2017 to study land subsidence in Semarang City using the PS-InSAR technique. The measured displacement ranges from -4.4 cm/year (-44 mm/year) to -3.4 cm/year (34 mm/year). According to the research, the displacement value produced above is generally higher than 30 mm/year.

Land cover/use is the most common factor influencing the displacement value (Anjasmara et al., 2020). The type of land cover/land use significantly impacts the data's accuracy (Castellazzi & Schmid, 2021; Zaenudin et al., 2018). The land cover/land use type significantly impacts the data's accuracy (Castellazzi & Schmid, 2021; Zaenudin et al., 2018). The information on deformation velocity obtained by the InSAR-SBAS approach gets less accurate as the area becomes more dynamic than usual. The quality of the deformation information generated is not appropriate for measuring deformations with one-millimeter accuracy.

This research provided use of the LiCSAR dataset and the LiCSBAS processing package, which was recently developed by Morishita et al. (2020) and claimed to minimize processing time efficiency and demonstrate promising results in describing deformation in a relatively large area that has not been widely used. The difference between this study and Morishita's research is that this study was conducted in the Sukabumi area. In order to minimize the contribution of noise reduction and the detailing of deformation values, this study uses different characteristics of temporal data.

We also look at the deformation at each landslide location and evaluate it according to the slope. Because of the differences in the characteristics and environment of the research area, this was done. The study demonstrates that at the Sukabumi area, the accuracy of displacement and deformation data is relatively good. Therefore, the result of the study is consistent with Morishita's findings.

The types of land cover in the research area impact the accuracy of this study's displacement and deformation measurements (Zaenudin et al., 2018; Anjasmara et al., 2020; Castellazzi & Schmid, 2021). The vegetation land cover dominates the southern part of the Sukabumi area. The density of vegetation might affect the coherence value and contribute noise to the processing results. As a result, the study's surface deformation is shown in areas with little vegetation, such as villages and bare land. The more dynamic an object is on the earth's surface, the detected deformation and displacement value information get less accurate for measuring deformation with millimeter accuracy (Zaenudin et al., 2018).

6. CONCLUSIONS

The ground surface deformation at each landslide location in the Sukabumi area was studied and mapped using the InSAR method using the SBAS approach. The surface deformation was processed using a python coding-based LiCSAR dataset and the LiCSBAS processing package, recently developed by Morishita et al. (2020). These products and packages might detect ground surface deformation in landslides as radar images become more accessible because they are not widely used to analyze ground surface deformation. Those methods were reported to have an mm/year precision and the ability to reduce processing time and produce good results in describing deformation in a relatively large area that had not ever been studied. Pixels with a dimension of 100 meters x 100 meters reflect the rate of change in ground surface elevation. Morishita's research differs from ours because of the diverse locations and environment and temporal radar data, the evaluation of deformation at each landslide location, and slope evaluation. For the Sukabumi area, we use LiCSAR product data, which is Sentinel-1 image data already in the form of unwrapped interferograms, recorded from April 9, 2019, to August 13, 2020. The processing findings using the SBAS approach demonstrate that the Pelabuhanratu area and its surroundings experienced land surface deformation from April 2019 to August 2020, with rates of change in elevation ranging from -36,297 mm/year to 58,837 mm/year. The area affected by subsidence was 1,623 hectares (2.9 percent), while the area affected by uplift was 8,275 hectares (15.0 percent). The rest was an area where surface deformation was not identified.

At each landslide location documented in the field, we also measured the rate of ground surface deformation. The displacement rate at each landslide location ranges from -9.79 mm/year to +33.69 mm/year, based on data LiCSBAS processing using the SBAS method. Uplift was observed in 37.1 percent of landslide locations (Pelabuhanratu, Simpenan, Cikakak, and Cisolok Districts), while subsidence was detected in 7.9 percent (Simpenan and Cisolok Districts). The positive displacement value at the landslide location is assumed to be the landslide's accumulation point. The landslide locations found in the field are often shallow landslides with a depth of fewer than 10 meters, with a typology of translation landslides, spreads, and rockfalls.

The most significant frequency of landslide locations and their movements (subsidence and uplift) found in the field are on moderately sloping to steep slopes, according to the results of the landslide location analysis of the physicochemical properties of slopes in the study area (16^0-35^0). The detection of surface deformation and displacement at each landslide location in the southern Sukabumi area was successfully demonstrated in this study. The findings are consistent with Morishiuta's study findings.

ACKNOWLEDGEMENTS

REFERENCES

Alfarabi, M. S., Supriatna, Manessa, M. D. M., Rustanto, A., & Ristya, Y. (2019). Geomorphology and Landslide-Prone Area in Cisolok District, Sukabumi Regency. *E3S Web of Conferences*, *125*(201 9), 1–6. https://doi.org/10.1051/e3sconf/201912501005

Amri, M. R., Yulianti, G., Yunus, R., Wiguna, S., W. Adi, A., Ichwana, A. N., & Randongkir, Roling Evans Septian, R. T. (2018). RBI (Risiko Bencana Indonesia). In *BNPB Direktorat Pengurangan Risiko Bencana* (Vol. 9, Issue 3).

Anjasmara, I. M., Yulyta, S. A., & Taufik, M. (2020). Application of time series InSAR (SBAS) method using Sentinel-1A data for land subsidence detection in Surabaya city. *International Journal on Advanced Science, Engineering and Information Technology*, *10*(1), 191–197. https://doi.org/10.18517/ijaseit.10.1.6749

Aslan, G., Foumelis, M., Raucoules, D., De Michele, M., Bernardie, S., & Cakir, Z. (2020). Landslide mapping and monitoring using persistent scatterer interferometry (PSI) technique in the French Alps. *Remote Sensing*, *12*(8). https://doi.org/10.3390/RS12081305

Bateson, L., Cigna, F., Boon, D., & Sowter, A. (2015). The application of the intermittent SBAS (ISBAS) InSAR method to the South Wales Coalfield, UK. *International Journal of Applied Earth Observation and Geoinformation*, *34*(1), 249–257. https://doi.org/10.1016/j.jag.2014.08.018

Berardino, P., Fornaro, G., Lanari, R., & Sansosti, E. (2002). A new algorithm for surface deformation monitoring based on small baseline differential SAR interferograms. *IEEE Transactions on Geoscience and Remote Sensing*, *40*(11), 2375–2383. https://doi.org/10.1109/TGRS.2002.803792

BNPB. (2018). Indonesia Disaster Infographics in December 2018. Retrieved from https://bnpb.go.id/uploads/24/info-bencana-desember-2018.pdf. [July 17, 2021]

BNPB. (2019). Indonesia Disaster Infographics in 2019. Retrieved from https://bnpb.go.id/infografis. [July 17, 2021]

BNPB. (2021). Indonesia Disaster Infographics in 2021. Retrieved from https://bnpb.go.id/infografis. [July 17, 2021]

Bobrowsky, P., & Highland, L. (2013). The Landslide Handbook- A Guide to Understanding Landslides: A landmark publication for landslide education and preparedness. In *Landslides: Global Risk Preparedness*. https://doi.org/10.1007/978-3-642-22087-6_5

Bogaard, T., & Greco, R. (2018). Invited perspectives: Hydrological perspectives on precipitation intensity-duration thresholds for landslide initiation: Proposing hydro-meteorological thresholds. *Natural Hazards and Earth System Sciences*, *18*(1), 31–39. https://doi.org/10.5194/nhess-18-31-2018

Castellazzi, P., & Schmid, W. (2021). Interpreting C-band InSAR ground deformation data for large-scale groundwater management in Australia. *Journal of Hydrology: Regional Studies*, *34*(December 2020), 100774. https://doi.org/10.1016/j.ejrh.2021.100774

Casu, F., Manzo, M., & Lanari, R. (2006). A quantitative assessment of the SBAS algorithm performance for surface deformation retrieval from DInSAR data. *Remote Sensing of Environment*, *102*(3–4), 195–210. https://doi.org/10.1016/j.rse.2006.01.023

Çellek, S. (2020). Effect of the Slope Angle and Its Classification on Landslide. *Natural Hazards and Earth System Sciences*, *May*, 1–23. https://doi.org/10.5194/nhess-2020-87

Cianflone, G., Tolomei, C., Brunori, C. A., Monna, S., & Dominici, R. (2018). Landslides and subsidence assessment in the Crati Valley (Southern Italy) using InSAR data. *Geosciences (Switzerland)*, *8*(2). https://doi.org/10.3390/geosciences8020067

Cigna, F., & Sowter, A. (2017). The relationship between intermittent coherence and precision of ISBAS InSAR ground motion velocities: ERS-1/2 case studies in the UK. *Remote Sensing of Environment*, *202*, 177–198. https://doi.org/10.1016/j.rse.2017.05.016

Cogan, J., & Gratchev, I. (2019). A study on the effect of rainfall and slope characteristics on landslide initiation using flume tests. *Landslides*, *16*(12), 2369–2379. https://doi.org/10.1007/s10346-019-01261-0

Crosetto, M., Copons, R., Cuevas-González, M., Devanthéry, N., & Monserrat, O. (2018). Monitoring soil creeps landslides in an urban area using persistent scatterer interferometry (El Papiol, Catalonia, Spain). *Landslides*, *15*(7), 1317–1329. https://doi.org/10.1007/s10346-018-0965-5

Damayanti, A., Angin, F., Adib, A., & Irfan, M. (2020). Geomorphological Characteristic of Landslide Hazard Zones in Sukarame Village, Cisolok Subdistrict, Sukabumi Regency. *IOP Conference Series: Earth and Environmental Science*, *412*(1). https://doi.org/10.1088/1755-1315/412/1/012009

De Luca, C., Bonano, M., Casu, F., Manunta, M., Manzo, M., Onorato, G., Zinno, I., & Lanari, R. (2018). The parallel SBAS-DINSAR processing chain for the generation of national scale sentinel-1 deformation time-series. *Procedia Computer Science*, *138*, 326–331. https://doi.org/10.1016/j.procs.2018.10.046

Dehghani, M., & Javadi, H. R. (2013). Remote sensing of ground deformation. *SPIE Newsroom*, *November*, 2–5. https://doi.org/10.1117/2.1201303.004772

El Jazouli, A., Barakat, A., & Khellouk, R. (2020). Geotechnical studies for Landslide susceptibility in the high basin of the Oum Er Rbia river (Morocco). *Geology, Ecology, and Landscapes*, *00*(00), 1–8. https://doi.org/10.1080/24749508.2020.1743527

Guo, J., Yi, S., Yin, Y., Cui, Y., Qin, M., Li, T., & Wang, C. (2020). The effect of topography on landslide kinematics: a case study of the Jichang town landslide in Guizhou, China. *Landslides*, *17*(4), 959–973. https://doi.org/10.1007/s10346-019-01339-9

Hearn, G., Howell, J., & Hunt, T. (2020). Performance of slope stabilization trials on the road network of Laos. *Quarterly Journal of Engineering Geology and Hydrogeology*, *54*(1), 2021. https://doi.org/10.1144/qjegh2020-064

Lanari, R., Casu, F., Manzo, M., & Lundgren, P. (2007). Application of the SBAS-DInSAR technique to fault creep A case study of the Hayward fault, California. *Remote Sensing of Environment*, *109*(1), 20–28. https://doi.org/10.1016/j.rse.2006.12.003

Li, L., Yao, X., Yao, J., Zhou, Z., Feng, X., & Liu, X. (2019). Analysis of deformation characteristics for a reservoir landslide before and after impoundment by multiple D-InSAR observations at Jinshajiang River, China. *Natural Hazards*, *98*(2), 719–733. https://doi.org/10.1007/s11069-019-03726-w

Malinowska, A. A., Witkowski, W. T., Guzy, A., & Hejmanowski, R. (2020). Satellite-based monitoring and modeling of ground movements caused by water rebound. *Remote Sensing*, *12*(11). https://doi.org/10.3390/rs12111786

Martins, B. H., Suzuki, M., Yastika, P. E., & Shimizu, N. (2020). Ground surface deformation detection in complex landslide area—bobonaro, Timor-Leste—using SBAS DinSAR, UAV photogrammetry, and field observations. *Geosciences (Switzerland)*, *10*(6), 1–26. https://doi.org/10.3390/geosciences10060245

Morishita, Y., Lazecky, M., Wright, T. J., Weiss, J. R., Elliott, J. R., & Hooper, A. (2020). LiCSBAS: An open-source InSAR time series analysis package integrated with the LiCSAR automated sentinel-1 InSAR processor. *Remote Sensing*, *12*(3), 5–8. https://doi.org/10.3390/rs12030424

Ng, A. H. M., Ge, L., Li, X., Abidin, H. Z., Andreas, H., & Zhang, K. (2012). Mapping land subsidence in Jakarta, Indonesia using persistent scatterer interferometry (PSI) technique with ALOS PALSAR. *International Journal of Applied Earth Observation and Geoinformation*, *18*(1), 232–242. https://doi.org/10.1016/j.jag.2012.01.018

North, M., Farewell, T., Hallett, S., & Bertelle, A. (2017). Monitoring the response of roads and railways to seasonal soil movement with persistent scatterers interferometry over six UK sites. *Remote Sensing*, *9*(9). https://doi.org/10.3390/rs9090922

Novellino, A., Cigna, F., Sowter, A., Ramondini, M., & Calcaterra, D. (2017). Exploitation of the Intermittent SBAS (ISBAS) algorithm with COSMO-SkyMed data for landslide inventory mapping in north-western Sicily, Italy. *Geomorphology*, *280*, 153–166. https://doi.org/10.1016/j.geomorph.2016.12.009

Nowicki Jessee, M. A., Hamburger, M. W., Ferrara, M. R., McLean, A., & FitzGerald, C. (2020). A global dataset and model of earthquake-induced landslide fatalities. *Landslides*, *17*(6), 1363–1376. https://doi.org/10.1007/s10346-020-01356-z

Pawlik, Ł., & Šamonil, P. (2018). Soil creep The driving factors, evidence, and significance for bio-geomorphic and pedogenic domains and systems – A critical literature review. *Earth-Science Reviews*, *178*(January), 257–278. https://doi.org/10.1016/j.earscirev.2018.01.008

Pawluszek-Filipiak, K., & Borkowski, A. (2020). Integration of DInSAR and SBAS techniques to determine mining-related deformations using Sentinel-1 data: The case study of rydultowy mine in Poland. *Remote Sensing*, *12*(2). https://doi.org/10.3390/rs12020242

Pepe, A., & Calò, F. (2017). A review of interferometric synthetic aperture RADAR (InSAR) multi-track approaches for retrieving Earth's Surface displacements. *Applied Sciences (Switzerland)*, *7*(12). https://doi.org/10.3390/app7121264

Perera, E. N. C., Jayawardana, D. T., Jayasinghe, P., Bandara, R. M. S., & Alahakoon, N. (2018). Direct impacts of landslides on socio-economic systems: a case study from Aranayake, Sri Lanka. *Geoenvironmental Disasters*, *5*(1). https://doi.org/10.1186/s40677-018-0104-6

Persichillo, M. G., Bordoni, M., & Meisina, C. (2017). The role of land-use changes in the distribution of shallow landslides. *Science of the Total Environment*, *574*, 924–937. https://doi.org/10.1016/j.scitotenv.2016.09.125

Prasetyo, Y., Firdaus, H. S., & Diyanah. (2019). Land Subsidence of Semarang City Using Permanent Scatterer Interferometric Synthetic Aperture Radar (Ps-Insar) Method in Sentinel 1a between 2014-2017. *IOP Conference Series: Earth and Environmental Science*, *313*(1). https://doi.org/10.1088/1755-1315/313/1/012044

Qu, T., Lu, P., Liu, C., & Wan, H. (2016). Application of time series InSAR technique for deformation monitoring of large-scale landslides in mountainous areas of western China. *International Archives of the Photogrammetry, Remote Sensing and Spatial Information Sciences - ISPRS Archives*, *2016-Janua*(July), 89–91. https://doi.org/10.5194/isprsarchives-XLI-B1-89-2016

Ramirez, R., Lee, S. R., & Kwon, T. H. (2020). Long-term remote monitoring of ground deformation using sentinel-1 interferometric synthetic aperture radar (InSAR): Applications and insights into geotechnical engineering practices. *Applied Sciences (Switzerland)*, *10*(21), 1–20. https://doi.org/10.3390/app10217447

Remy, D., Bonvalot, S., Briole, P., & Murakami, M. (2003). Accurate measurements of tropospheric effects in volcanic areas from SAR interferometry data: Application to Sakurajima volcano (Japan). *Earth and Planetary Science Letters*, *213*(3–4), 299–310. https://doi.org/10.1016/S0012-821X(03)00331-5

Ristya, Y., Supriatna, & Sobirin. (2019). Spatial pattern of potential landslide area by SMORPH, INDEX STORIE, and SINMAP method in Pelabuhanratu and surrounding area, Indonesia. *IOP Conference Series: Earth and Environmental Science*, *338*(1). https://doi.org/10.1088/1755-1315/338/1/012033

Roccheggiani, M., Piacentini, D., Tirincanti, E., Perissin, D., & Menichetti, M. (2019). Detection and monitoring of tunneling induced ground movements using Sentinel-1 SAR interferometry. *Remote Sensing*, *11*(6). https://doi.org/10.3390/rs11060639

Shirani, K., & Pasandi, M. (2019). Detecting and monitoring of landslides using persistent scattering synthetic aperture radar interferometry. *Environmental Earth Sciences*, *78*(1), 1–24. https://doi.org/10.1007/s12665-018-8042-x

Skrzypczak, I., Kokoszka, W., Zientek, D., Tang, Y., & Kogut, J. (2021). Landslide hazard assessment map as an element supporting spatial planning: The flysch Carpathians region study. *Remote Sensing*, *13*(2), 1–20. https://doi.org/10.3390/rs13020317

Sugianti, K., Sukristiyanti, S., & Tohari, A. (2016). Model Kerentanan Gerakan Tanah Wilayah Kabupaten Sukabumi Secara Spasial Dan Temporal. *Jurnal RISET Geologi Dan Pertambangan*, *26*(2), 117. https://doi.org/10.14203/risetgeotam2016.v26.270

Virk, A. S., Singh, A., & Mittal, S. K. (2019). Monitoring and analysis of displacement using InSAR techniques for Gulaba landslide site. *Journal of Engineering Science and Technology*, *14*(3), 1558–1571.

Wasowski, J., & Bovenga, F. (2014). Investigating landslides and unstable slopes with satellite Multi-Temporal Interferometry: Current issues and future perspectives. *Engineering Geology*, *174*, 103–138. https://doi.org/10.1016/j.enggeo.2014.03.003

Yastika, P. E., Shimizu, N., & Abidin, H. Z. (2019). Monitoring long-term land subsidence from 2003 to 2017 in the coastal area of Semarang, Indonesia by SBAS DInSAR analyses using Envisat-ASAR, ALOS-PALSAR, and Sentinel-1A SAR data. *Advances in Space Research*, *63*(5), 1719–1736. https://doi.org/10.1016/j.asr.2018.11.008

Zaenudin, A., Darmawan, I. G. B., Armijon, Minardi, S., & Haerudin, N. (2018). Land subsidence analysis in Bandar Lampung City based on InSAR. *Journal of Physics: Conference Series*, *1080*(1). https://doi.org/10.1088/1742-6596/1080/1/012043

Zollini, S., Alicandro, M., Cuevas-González, M., Baiocchi, V., Dominici, D., & Buscema, P. M. (2020). Shoreline extraction based on an active connection matrix (ACM) image enhancement strategy. *Journal of Marine Science and Engineering*, *8*(1). https://doi.org/10.3390/jmse8010009

Zuidam, R. A. van. (1985). Aerial photo interpretation in terrain analysis and geomorphologic mapping. In *Aerial photo interpretation in terrain analysis and geomorphologic mapping*. Smits.

THE CONTRIBUTION OF OPEN-SOURCE GIS SOFTWARE AND OPEN SPATIAL DATA FOR THE RE-EVALUATION OF LANDSLIDE RISK AND HAZARD IN VIEW OF CLIMATE CHANGE

Valerio BAIOCCHI[1] , Felicia VATORE[1], Mara LOMBARDI[2] ,
Felicia MONTI[1], Roberta ONORI[3]

ABSTRACT :
Recent events, including the floods in central Europe in May 2021, have highlighted how climate change is giving rise to scenarios that were neither foreseen nor predictable. One problem this poses is the need to rethink the logic of various environmental constraints that are often based on return times of 20-50 years or 100-200. A single event does not change the statistical expectations for the recurrence of the event itself, but the recurrence of several extraordinary events in a few years is a clear indication of a changing trend. The prevention of the effects of such events is based on the definition of the areas at greater or lesser risk specifically based on the return times of the exceptional events, so it is foreseeable that a series of territorial plans, mostly carried out a few decades ago, will have to be updated or re-executed from scratch. These reworkings will be able to take advantage of the open-source software and open spatial data that have become available in the meantime, facilitating the entire process, and making it more open and shareable. In this paper we tested on a real case (the May 1999 pyroclastic flows in Campania, southern Italy) the actual possibility of implementing a model for forecasting such events using only open-source software and open data.

It has been demonstrated that the entire process can be carried out using only open-source resources and it has been verified that the predictions of the hazard and risk model obtained with only input data prior to the event, give an output prediction that is significantly coincident with the events that actually occurred as documented by the authorities.

Key-words: climate change, Campania, landslide risk, landslide hazard, pyroclastic flows, Sarno, GIS

1. INTRODUCTION

The climate changes in progress cause undeniably new weather and precipitation situations for which we are not prepared as the recent events in Central Europe demonstrate (**Fig.1**). In particular, events characterized by high rainfall concentrated in short time intervals can trigger various events with high hazard and risk in time intervals even very short among which one of the most damaging is the liquefaction of soils (**Fig.1** again). It is easy to understand that the most efficient and effective strategy is prevention trying to evaluate a priori the major risks due to meteorological scenarios, not predictable until a few years ago. In fact, the study of hazard and risk from landslides has been dealt with geomatic methods for several years and many countries (including most European countries) have equipped themselves with digital maps that grade the various risks involved (Vallelongo, 2020; Papathoma-Köhle et al., 2011). It is clear, however, that the new scenarios require the redesign and remapping of a whole series of risks including, for example, that of the potential movement of loose materials (Chen et al., 2011; Canovas et al., 2016; Bernardini et al. 2021). One of the current advantages over a few years ago, when many of these mappings were performed, is the greater availability of open software and data that can significantly facilitate these operations. In fact, in the last years, open software and data have been used for geomatic applications to various fields such as

[1]*Sapienza University of Rome, Department of Civil, Constructional and Environmental Engineeering (DICEA), Italy, valerio.baiocchi@uniroma1.it, felicia.vatore@uniroma1.it, felicia.monti@uniroma1.it*

[2]*Sapienza University of Rome, Department Chemical Engineering Materials Environment (DICMA), Italy, mara.lombardi@uniroma1.it*

[3]*European Union Satellite centre (SatCen), Madrid, Spain, roberta.onori@satcen.europa.eu*

speleology (Troisi et al., 2017), archaeology (Alessandri et al., 2019; Costantino et al., 2010; Dominici et al., 2013), agriculture (Aguilar et al. 2016), cultural heritage (Bitelli et al., 2019; Brigante et al., 2014), geodesy and positioning (Dardanelli et al., 2020), structural monitoring (Radicioni et al., 2017; Nerilli et al., 2020) or for emergency management (Baiocchi et al. 2014) but also for spatial and/or geographical studies (Lupia et al., 2017; Baiocchi et al. 2017; Maglione et al. 2014; Costantino et al., 2011).

About the availability of open-source software, it is undeniable that in recent years even complex functions once available in high-level commercial software are now available in environments such as QGIS and toolboxes within it such as GRASS or SAGA. At the same time, initiatives such as the European INSPIRE (European commission, 2021) have stimulated and encouraged the dissemination of spatial data by facilitating the retrieval of updated and consistent databases by the various agencies. These two factors together provide new possibilities and potential for the reworking of the perimeter of the areas at risk using complex algorithms in an efficient and effective way by all stakeholders (Waiyasusri et al., 2021; Eslaminezhad et al., 2021).

In the following a model for the prediction of the liquefaction of pyroclastic materials in the area that was affected by similar phenomena in 1998 in Campania is shown and it's verified using open data and software.

Fig. 1. Effects of climate change in central Europe (summer 2021).

2. STUDY AREA

The landslides referred to are those that occurred in Campania in 1998 because of high meteoric events that were particularly concentrated in terms of temporal duration.

The May 1998 landslides affected a large area, mainly in the municipalities of Bracigliano, Episcopio, Quindici, Sarno, and Siano (**Fig. 2**).

This part of the Campanian Apennines is characterized by Mesozoic carbonate sequences, consisting of limestones, dolomitic limestones, and platform dolomites, in layers and banks, with variously oriented layering and inclination. The state of tectonization is variable from area to area; equally variable are the thicknesses of the most superficial portion of fractured, degraded and altered rock (Brancaccio et al., 1995; Lizárraga et al. 2017). The aforementioned carbonate sequences are covered by a layer of loose pyroclastic deposits with gradually decreasing thicknesses from the *Piana*

Campana towards the interior of the chain. The covers are represented by loose materials of volcanic origin, consisting of a generally irregular alternation of pumice, lapilli, slag and ash. The pyroclastic materials are referable, almost exclusively, to the apparatus of Somma-Vesuvius and, in particular to the eruption of Plinian type of 79 A.D. and to the following volcanic activity until the last phase of 1944. The deposits of 79 A.D. are, however, by far preponderant (Santacroce, 1987; Sigurdson et al., 1985; Calcaterra et al., 2003). Because of their particular characteristics, the loose pyroclastites have intensely suffered the effects of exogenous dynamics with consequent modifications of the original situations that have led to reworking and washouts that have modified the granulometric composition, physical properties, resistance characters, hydrogeological aspects, giacitural conditions and topographic position. Consequently, one can distinguish pyroclastites in situ and others fluctuated by tractive transport and in mass (Rolandi et al. 1993, Lirer et al., 1973).

The materials of pyroclastic origin covering the carbonate massifs present, in general, variable technical characteristics as a consequence of the volcanic phenomena of formation and, above all, of the subsequent reworking processes that have substantially modified the original depositional, granulometric and hydrogeological characteristics. The permeability of pyroclastic materials varies from very high values in the pumiceous levels, up to values around 10-5 cm/sec in the reworked pyroclastites. In carbonate rocks the permeability coefficient presents considerable variations not only in the horizontal sense but also along the same vertical (Celico et al., 1986).

The area affected by the landslides of May 1998 is (**Fig. 2**) made up of the slopes of Monte Torrenone which, from some maps as the one of the National Geological Service, is covered with pyroclastites (yellow color) only at the base and in its summit, near the base are, moreover, cartographed of the debris of stratum (white with blue dots); the remaining zones green areas are limestone and dolostone.
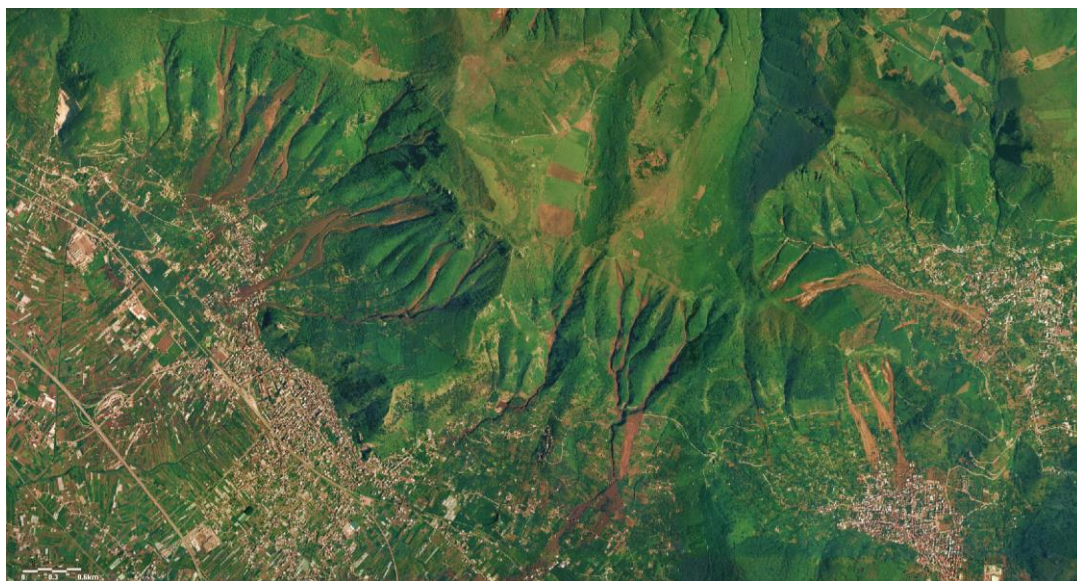
Fig. 2. May 1998 Campania landslides (image acquired in 1999).

The causes of the triggering of these landslides have been debated in the scientific field, for this study has been considered one of the most accredited theories. From the hydrogeological point of view these rocky masses can be divided into three parts that, from top to bottom, include: the loose pyroclastic cover; a layer of a few tens of meters of very fractured and degraded carbonate rock; the underlying less fractured carbonate rock. In dry period, the scarce rainwater, generally well distributed in time, are easily absorbed and retained by the pyroclastic layer as it has a very high porosity. During

the flood period, a band of saturated fractures can be created in the transition zone between the fractured carbonates and the less fractured carbonates below. Since in this case the base of the fractured limestone must be considered as an impermeable formation, an aquifer circulation is created with a sub-parallel trend to the lines of maximum slope gradient. In case of very intense precipitations concentrated in a short period of time, this saturated layer can rise up to the level of the pyroclasts, thus determining conditions of confined or semi-confined water table and under pressure of the pyroclastic layer.

3. DATA AND METHODS

3.1 Materials needed for model development

As stated in the introduction, a focus of this contribution is to verify whether the availability of open data allows the updating of the layers of risk and landslide hazard that will be necessary as a function of the effects of climate change now evident. The situation, at least in Europe, has changed a lot in recent years, in fact only a few years ago the realization of such a model required the not always easy research and obtaining data, often in paper form, from the bodies responsible for environmental protection. This constraint, actually only logistical/bureaucratic, however, heavily influenced the actual feasibility of a series of plans. In Italy, probably thanks to the stimulus provided by the INSPIRE directive of the European Commission, a whole series of spatial data whose accessibility was previously limited and partial have become directly and freely available. Many territorial bodies have released web pages generally called geoportals from which data can always be consulted through web viewers but also within GIS using protocols such as WMS and WFS as, for example, for cadastral coverages (Agenzia delle Entrate, 2021). In some cases, the data are even downloadable such as some of those made available by the Ministry of Environment on the most consulted geoportal at national level: the "National Geoportal" (Ministry of Environment, 2021). Other data at a larger scale, such as base maps at 1:5000 scale, are available on the geoportals of local authorities such as the provincial administration of Salerno (Campania Region, 2021).

Below are the open data that you can freely use for the realization of the model of hazard and risk for movements:

From the National Geoportal of the Ministry of Environment (www.pcn.minambiente.it/mattm/):
    - "Catalogo delle frane, poligoni" (Catalogue of landslide, polygons) (scale 1:5000), year 2009
    - "Carta geologica" (Geological map), scale 1:500000, year 2009
    - "Carta geolitologica" (Geolithological map), scale 1:500000, year 2009
    - "Tavole dei grigliati Lidar 1*1" (Lidar Grids) resolution 1 metre, year 2008

From ISPRA (Istituto superiore per la protezione e la ricerca ambientale, Superior Institute for Environmental Protection and Research) Geoportal (ISPRA, 2021), (http://sgi.isprambiente.it/)
    - Carta Geologica (Geological Map), scale 1:100000, year 1971

From Campania Region Geoportal (https://sit2.regione.campania.it/servizio/carta-tecnica-regionale):
    - Carta tecnica regionale (Regional technical map), scale 1:5000, year 1998
    - Carta tecnica regionale (Regional technical map), scale 1:5000, year 2004- 2005

3.2 Possible model implementation in open-source GIS

The most immediate model for landslide hazard is to relate a slope map with a geolithological map: by assigning a certain hazard score to the various slope classes and to the various lithologies, it is possible to obtain a derived map obtained simply by adding the values corresponding to a given area in the two maps. Areas with steep slopes and lithologies subject to movements will obtain the

maximum hazard values, flat areas with lithologies not subject will obtain the minimum values. The software that allows this kind of elaborations normally work on raster files because the discretized format of these files allows an easier calculation. It must be underlined that these cartographies constitute only a cognitive instrument for the individuation of zones to high dangerousness, to this first phase must always follow an accurate geological survey of detail.

Anyway, to implement any model of landslide hazard it is necessary to have a digital elevation model of the area we want to study; from the DEM it is in fact possible to derive themes that are essential for any study of movements. Using GIS raster functions, it is quite easy to derive precise information on the inclination and direction of slopes, preferential drainage lines and on these to estimate distances. These are some of the functions were very useful in implementing the described model.

The algorithms present in the toolboxes that we could define of "Map Algebra" allow to use several more complex functions such as the calculation of a grid of preferential drainage directions from the DTM or the possibility to measure distances on the same grid once defined, this allows to implement and test a simple model of hazard a bit more complex already described in the literature (Baiocchi, 1998). The model can be considered as a development of other models: starting from a hazard map (obtained perhaps with the simple procedure just described) that already indicates the "dangerous" areas. Are considered "dangerous" also all the areas that are located in correspondence of drainage lines, downstream of a hazard area within a certain distance measured in the drainage network. This model derives from the observation that the material moved in the landslides of loose materials, in many cases acquires a fluid consistency or practically liquid, for this reason the material is channelled in the preferential lines of drainage scavenging everything that meets on its way for a few hundred meters (in some cases for kilometres). For this reason, the model considers risky not only the zones in which the movement of material could happen, but also the zones, often distant, in which the material, so moved, could arrive. What was more interesting to experiment, were the possibilities of the algorithms to identify and follow the preferential drainage lines comparing them with those along which the landslides developed.

The application of data to the model starts from the elaboration of the slope map that can be obtained for example with the "classic" command contained in QGIS under the path "Raster > Analysis > Slope".

The layer thus obtained must be resampled into dangerous zones and non-dangerous zones according to the degree of acclivity; deciding which is the inclination that separates dangerous zones from non-dangerous zones is a particularly delicate choice. For local studies in geotechnics this angle is chosen based on the angle of internal friction of the material, but in the case of the drafting of a study of this extension the materials involved may be very variable and present variable states of aggregation, for this reason introducing a single angle for the entire mapped area is in any case an approximation. The inclination value to be inserted is, together with the distance to be calculated along the drainage lines, one of the two variables of the model that must be experimentally tested to calibrate the model itself. However, good agreement was observed with the areas that could be estimated at risk from an initial morphological examination of the cartography, using an inclination value of 25 degrees.

4. RESULTS AND DISCUSSIONS

4.1. Derivation of maps of preferential drainage directions

A further refinement of the cartography can derive from the intersection with the geological cartography, but in this case, since the most "dangerous" formations (the volcanites) are located in the valley floors, areas that will be considered dangerous by the program as preferential drainage lines, in this first test have not been included. Further considerations of the necessary geolithological data are discussed in more detail later. The main purpose of this first step is to evaluate mainly the possibilities of identifying drainage lines.

To obtain the grid of the drainage lines and study the diffusion along the drainage can be used various algorithms including, for example, the one contained in the plugin "FlowPathDown_BB" (Valentinotti, 2013). The plugin starting from the areas considered dangerous or trigger areas follows the drainage lines for a certain distance, this distance is the second parameter that must be chosen to calibrate the model. The distance that the handled loose materials can travel inside the drainage lines varies mainly according to the consistency of the material (which in case, for example, of mudflows is practically liquid). Also, in this case various values have been tried and it has been finally decided to start with a value of 100 meters that is surely insufficient for the events then regularly happened in the area but it allows to quickly carry out evaluations; in fact, the elaboration times of such an algorithm can also be long.

It is necessary to remember that, for how the model has been thought, in this phase of test, what must be verified is above all the correspondence with the real event in the low part of the landslide, where the moved material is channeled in the preferential drainage lines. The most interesting result was obtained on the landslide east of Episcopio: here it was possible to compare the results obtained from the model with the perimeter available on the "Geoportale Nazionale" (**Fig. 3a**).

4.2. Estimation of the importance of the input DEM resolution

We wanted to verify in particular if these models could also be used with DEM of lower resolution such as those available freely as ASTER and SRTM but also very interesting is the possibility of using the model Tinitaly (Tarquini et al., 2012) produced by the National Institute of Geophysics and Volcanology (INGV) with a resolution of 10 meters. To this end, an intentional degradation of the resolution of the original DEM has been made to evaluate the effects at various resolutions, but unfortunately converting from the original resolution of 1 meter to that of 5 meters, the results are yet unsatisfactory significantly degrading the final result compared to the polygons of comparison reported on the "Geoportale nazionale" web site (**Fig. 3b**).

4.3. Characteristics of available geolitological maps in input

Considering these first results we wanted to verify if it was possible to further refine the model by inserting information on geolithology according to the simple criterion exposed previously or consider unstable areas with high slopes and that present a lithology that can easily be subject to landslides. Actually, this test must be considered almost as a provocative in the sense that, as already anticipated, the available geological and geolithological maps cannot be of valid help in this specific case because the material shifted by this type of event is actually a layer of some meters of thickness of pyroclastic soil that conventionally is not reported on the same geological maps. For this reason, since the date of the events under study (1998), research and surveys have been carried out to map the thickness of these soils in the area, but their validation is still a debated issue in the literature (Del Soldato et al., 2016) and therefore an official model of these thicknesses has not been released and therefore could not be tested.

It is already evident that the introduction of these data in the model will not improve the model performance because the lower part considered at risk will remain unchanged, while the upper part (where the movement started and from where most of the moved materials detached) will be not at risk (**Fig. 3c**). The lack of representation of the pyroclastic covers of the upper part of the slopes is not to be considered an error of the surveyor, in fact at very small scales like these, what we want to map are the large tectonic structures, a cover of a few meters of pyroclasts is not relevant for these purposes. The inclusion of geolithology data will therefore be useful only if data are available at an appropriate scale and surveyed for such a use: some experiments in this sense (survey of only quaternary cover at large scale) in Sacramento County (California, USA) have, already in the past, obtained satisfactory results (Howell et al., 1999; Brabb, 1985).
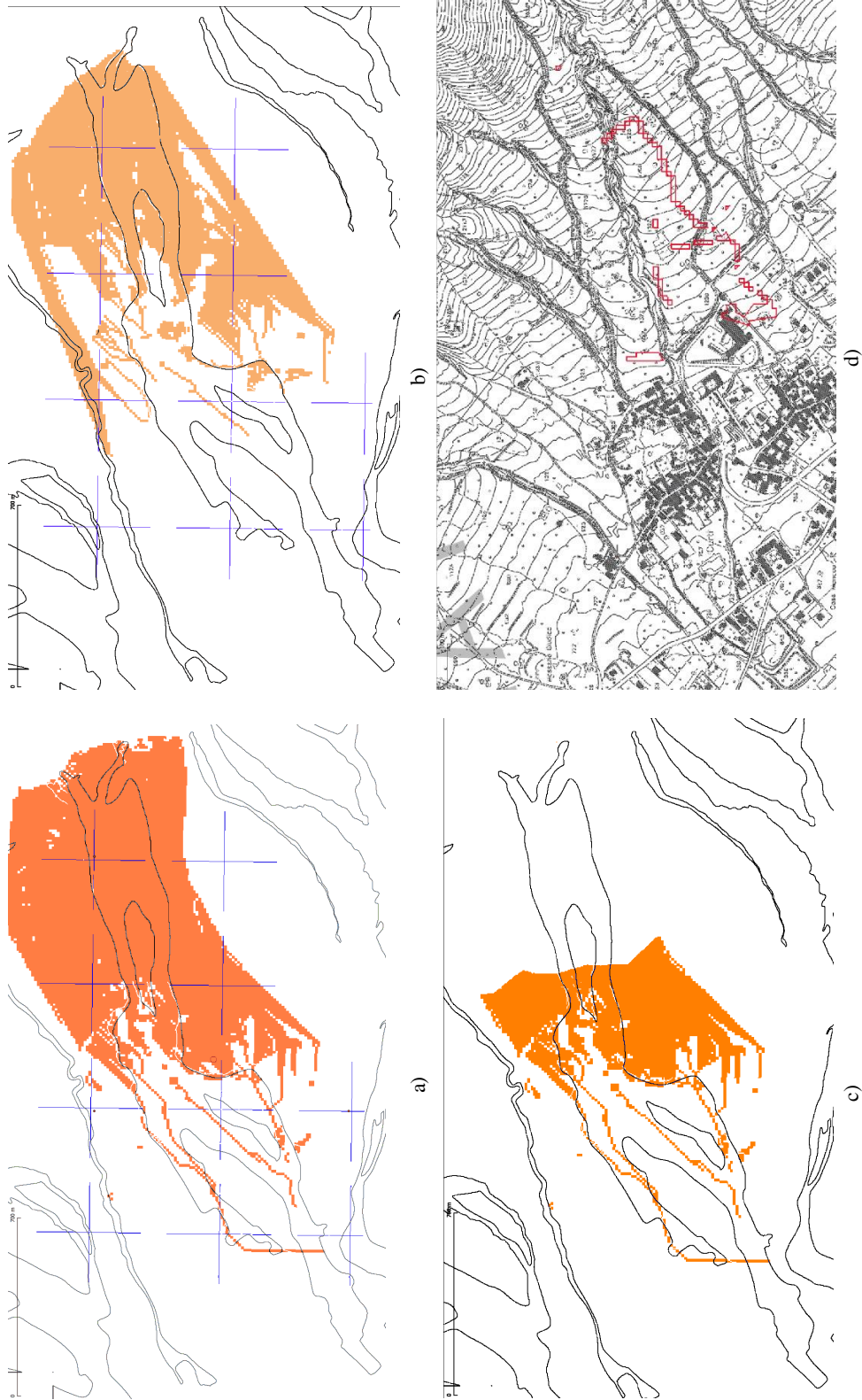
Fig. 3. Results of the model implemented: a) the first test with full resolution DEM, b) the same model with degraded DEM, c) the original model with the geological map data and d) the population risk map.

4.3. Layers for population risk assessment

The overlapping of hazard layers thus created with vector layers of the built-up area and transport infrastructures (areas in which it is more likely that the population is concentrated during the 24 hours) allows to identify the areas at greater risk for the population itself. The building and infrastructure layer were extracted from 1:5000 base maps from Campania Region. In this case we have added a buffer of ten meters around the areas evaluated "dangerous" from the model because the building or the infrastructure involved also in part from the event must obviously consider all to risk.

The result of this evaluation of risk has effectively identified all and only the areas that have then been really interested from the event as then happened (**Fig. 3d**).

5. CONCLUSIONS

This paper demonstrates how even complex studies on land vulnerability can be effectively carried out by implementing advanced models using open-source software and open data. This possibility is even more interesting given the need to rethink and redesign several environmental constraints due to the evident climate changes as the recent events in Central Europe have shown. This is made possible by the recent availability of open-source software which now has functions that are absolutely comparable with those of commercial software and, in some cases, even more sophisticated. It can be said that this availability of software has developed completely over the last two decades. Moreover, the even more recent availability of open data, stimulated in Europe by the INSPIRE directive, has been very important, in a certain sense revolutionizing the policy of dissemination of spatial data by public administrations, which until a few years ago kept all spatial information as confidential material, with few exceptions, and now publish it all, with few exceptions. This "revolution" has taken place completely in the last two to three years and, in fact, many of the data mentioned in this contribution have only just become available. The specific web diffusion protocols for spatial data, such as WMS and WFS, have also contributed greatly. These allow us all to work on the same layer update and to load locally only the part of the data that is of interest, as for example in the case of the landslide catalogue used in this study, which covered the entire national territory but of which only a few polygons were of interest here. This new possibility of working with open data and open software is a great advantage for the scientific community, which has more and more possibilities to elaborate and develop new models by testing them on real data. It is also a great advantage for public administrations, which can immediately adopt the suggestions of the research world, and it can be a great help for developing countries, where the costs of commercial software often limit the possibilities of complex spatial studies. Unfortunately, there is often not yet such a wide dissemination of data in these countries, and this is a gap that more developed countries should help overcome.

R E F E R E N C E S

Agenzia delle Entrate (2021) Accesso alle cartografie catastali mediante WMS. Last access on August 2021, https://www.agenziaentrate.gov.it/portale/it/web/guest/schede/fabbricatiterreni/consultazione-cartografia-catastale/servizio-consultazione-cartografia

Aguilar, M. A., Aguilar, F. J., García Lorca, A., Guirado, E., Betlej, M., Cichon, P., Nemmaoui, A., Vallario, A., and Parente, C. (2016) Assessment of multiresolution segmentation for extracting greenhouses from worldview-2 imagery, *Int. Arch. Photogramm. Remote Sens. Spatial Inf. Sci.*, XLI-B7, 145‑152, https://doi.org/10.5194/isprs-archives-XLI-B7-145-2016

Alessandri, L., Baiocchi, V., Del Pizzo, S., Rolfo, M. F., Troisi, S. (2019) Photogrammetric survey with fisheye lens for the characterization of the La Sassa cave, *Int. Arch. Photogramm. Remote Sens. Spatial Inf. Sci.*, XLII-2/W9, 25‑32, https://doi.org/10.5194/isprs-archives-XLII-2-W9-25-2019.

Baiocchi, V., Barbarella, M. (1999) Applicazione di algoritmi automatici per lo studio dei movimenti di materiali sciolti (Application of automatic algorithms for the study of movements of loose materials), in Proceedings of third ASITA national conference, pp. 187‑194, Naples, Italy, 9-12 November 1999.

Baiocchi, V., Dominici, D., Milone, M.V., Mormile, M. (2014) Development of a software to optimize and plan the acquisitions from UAV and a first application in a post-seismic environment, *European Journal of Remote Sensing*, 47:1, 477-496, DOI: 10.5721/EuJRS20144727

Baiocchi, V., Zottele, F., Dominici, D. (2017) Remote Sensing of Urban Microclimate Change in L’Aquila City (Italy) after Post-Earthquake Depopulation in an Open Source GIS Environment. *Sensors* 17, 404. https://doi.org/10.3390/s17020404

Bernardini, G., Finizio, F., Postacchini, M., Quagliarini, E., (2021) Assessing the flood risk to evacuees in outdoor built environments and relative risk reduction strategies, *International Journal of Disaster Risk Reduction*, Volume 64, 2021, 102493, https://doi.org/10.1016/j.ijdrr.2021.102493.

Bitelli, G., Balletti, C., Brumana, R., Barazzetti, L., D'Urso, M. G., Rinaudo, F., Tucci, G. (2019) The GAMHER research project for metric documentation of cultural heritage: current developments, *The International Archives of the Photogrammetry, Remote Sensing and Spatial Information Sciences*, GEORES 2019 ‑ 2nd International Conference of Geomatics and Restoration, Volume XLII-2/W11 8‑10 May 2019, Milan, Italy, pp. 239-246

Brabb, E.E. (1985) Innovative approaches to landslide hazard and risk mapping, USGS Publications Warehouse. Last access on August 2021, http://pubs.er.usgs.gov/publication/70197529

Brancaccio, L., Cinque, A., Romano, P, Rosskopf, C., Russo, F., Santangelo N. (1995) L'evoluzione delle pianure costiere della Campania: geomorfologia e neotettonica. *Memorie Società Geologica Italiana* 53: 313‑336.

Brigante, R., Radicioni, F. (2014) Georeferencing of historical maps: GIS technology for urban analysis. *Geographia Technica*, 9, (1), 10-19.

Calcaterra, D., Parise, M., Palma, B. (2003) Combining historical and geological data for the assessment of the landslide hazard: a case study from Campania, Italy, *Nat. Hazards Earth Syst. Sci*., 3, 3‑16, https://doi.org/10.5194/nhess-3-3-2003, 2003.

Cánovas, J.B., Stoffel, M., Corona, C., Schraml, K., Gobiet, A., Tani, S., Sinabell, F., Fuchs, S., Kaitna, R. (2016) Debris-flow risk analysis in a managed torrent based on a stochastic life-cycle performance. *Sci. Total Environ.* 2016, 557, 142‑153.

Celico P., Guadagno F. M., Vallario A. (1986) Proposta di un modello interpretativo nei terreni piroclastici, Geologia applicata e idrogeologia V. 21.

Chen, C. Y., Yu, F.C. (2011) Morphometric analysis of debris flows and their source areas using GIS. *Geomorphology,* 129, 387‑397.

Costantino D., Angelini M.G. (2010) Realization of a Cartographic GIS for the Filing and Management of the Archaelogical Excavations in the Nelson's Island. *Lecture Notes in Computer Science*, vol 6436. Springer, Berlin, Heidelberg. https://doi.org/10.1007/978-3-642-16873-4_42

Costantino, D., Angelini, M. G. (2011) Features and ground automatic extraction from airborne LIDAR data. *International Archives of the Photogrammetry, Remote Sensing and Spatial Information Sciences - ISPRS Archives*, vol. 38(5W12), pp. 19‑24

Dardanelli, G. Lo Brutto, M., Pipitone, C.(2020) GMSS CORS network of the university of Palermo: design and first analysis of data. *Geographia Technica*, Vol. 15, Issue 1, 2020, pp 43 to 69. https://doi.org/10.21163/GT_2020.151.05

Del Soldato, M., Segoni, S., De Vita, P., Pazzi, V., Tofani, V., & Moretti, S. (2016) Thickness model of pyroclastic soils along mountain slopes of Campania (southern Italy). Paper presented at the Landslides and Engineered Slopes. Experience, Theory and Practice, 2 797-804. DOI:10.1201/b21520-93

Dominici, D., E. Rosciano, E., Alicandro, M., Elaiopoulos, M., Trigliozzi, S., Massimi, V. (2013) Cultural heritage documentation using geomatic techniques: Case study: San Basilio's monastery, L'Aquila, *Digital Heritage International Congress*, pp. 211-214, DOI: 10.1109/DigitalHeritage.2013.6743735.

Eslaminezhad, S. A., Omarzadeh, D., Eftekhari, M., Akbari, M. (2021) Development of a data-driven model to predict landslide sensitive areas. *Geographia Technica*, Vol 16, Issue 1, 2021, pp. 97-112, DOI: 10.21163/GT_2021.161.09

European Commission (2021) The INSPIRE directive. Last access on August 2021, https://cordis.europa.eu/article/id/22376-commission-proposes-measures-to-inspire-better-geographical-information

Howell, D. G., Brabb, E. E., Ramsey, D. W. (1999) How Useful Is Landslide Hazard Information? Lessons Learned in the San Francisco Bay Region, *International Geology Review*, 41:4, 368-381, DOI: 10.1080/00206819909465147

ISPRA (2021) Carta geologica d'Italia on line, Last access on August 2021, http://sgi.isprambiente.it/geologia100k/

Lirer L., Pescatore T., Booth B., Walker G.P.L (1973) Two Plininan Pumice-falls deposits from Somma-Vesuvius. Italy. *Geol Soc. Am Bull*., 84, 759-772.

Lizárraga J.J., Frattini P.,. Crosta G.B., Buscarnera, G. (2017) Regional-scale modelling of shallow landslides with different initiation mechanisms: Sliding versus liquefaction. *Engineering Geology*, Volume 228, 2017, Pages 346-356, ISSN 0013-7952, https://doi.org/10.1016/j.enggeo.2017.08.023.

Lupia, F., Baiocchi, V., Lelo, K., Pulighe, G. (2017) Exploring Rooftop Rainwater Harvesting Potential for Food Production in Urban Areas. *Agriculture*, 7, 46. https://doi.org/10.3390/agriculture7060046

Maglione, P., Parente, C., Santamaria, R., Vallario, A. (2014) Modelli tematici 3D della copertura del suolo a partire da DTM e immagini telerilevate ad alta risoluzione WorldView-2 | [3D thematic models of land cover from DTM and high-resolution remote sensing images WorldView-2]. *Rendiconti Online Società Geologica Italiana*, DOI: https://doi.org/10.3301/ROL.2014.08

Ministero dell'Ambiente (2021) Geoportale nazionale. Last access on August 2021, http://www.pcn.minambiente.it/mattm/

Nerilli, F., Imperatore, S., Zucconi, M. (2020) Preface of the "Symposium on New Trends in Numerical Computation for Solids and Structural Mechanics", AIP Conference Proceedings 2293, 240001 (2020), DOI: https://doi.org/10.1063/5.0026941

Papathoma-Köhle, M., Kappes, M., Keiler, M., Glade, T. (2011). Physical vulnerability assessment for alpine hazards: state of the art and future needs. *Nat Hazards* 58, 645‑680. https://doi.org/10.1007/s11069-010-9632-4

Radicioni, F., Matracchi, P., Brigante, R., Brozzi, A., Cecconi, M., Stoppini, A., Tosi, G. (2017) The Tempio della Consolazione in Todi: integrated geomatic techniques for a monument description including structural damage evolution in time, *Int. Arch. Photogramm. Remote Sens. Spatial Inf. Sci.*, XLII-5/W1, 433‑440, https://doi.org/10.5194/isprs-archives-XLII-5-W1-433-2017.

Regione Campania (2021) Geoportale della Regione Campania. Last access on August 2021, https://sit2.regione.campania.it/servizio/carta-tecnica-regionale

Rolandi, G., Maraffi, S., Petrosino, P., Lirer, L. (1993) The Ottaviano eruption of Somma-Vesuvio (8000 y B.P.): a magmatic alternating fall and flow-forming eruption, *J. Volcanol. Geotherm*. Res., 58, 43‑65.

Santacroce R. (1987) Somma-Vesuvius. Quaderni de la Ricerca Scientifica, n. 114, Roma.

Sigurdsson, H., Carey, S., Cornell, W., Pescatore, T. (1985) The eruption of Vesuvius in A.D. 79, *National Geographic Re*s., 1, 3, 332‑387.

Tarquini S., Vinci S., Favalli M., Doumaz F., Fornaciai A., Nannipieri L. (2012) Release of a 10-m-resolution DEM for the Italian territory: Comparison with global-coverage DEMs and anaglyph-mode exploration via the web, *Computers & Geosciences*, 38, 168-170. DOI:10.1016/j.cageo.2011.04.018

Troisi, S., Baiocchi, V., Del Pizzo, S., Giannone, F. (2017) A prompt methodology to georeference complex hypogea environments, *Int. Arch. Photogramm. Remote Sens. Spatial Inf. Sci*., XLII-2/W3, 639‑644, https://doi.org/10.5194/isprs-archives-XLII-2-W3-639-2017.

Valentinotti, R. (2013) FlowPathDown_BB plugin. Last access on August 2021, https://plugins.qgis.org/plugins/FlowPathDown_BB/

Vallelongo, F. (2020) Analisi delle distanze di arresto di debris flow in area alpina attraverso l'utilizzo di open data. (Analysis of debris flow stopping distances in the Alpine area using open data.) *Phd thesis*, University of Padua. Last access on August 2021, http://tesi.cab.unipd.it/65303/1/Vallongo%2C_Francesca.pdf

Waiyasusri, K., Kulpanich, N., Worachairungreung, M., Sae-Ngow, P.,Chaysmithikul, P. (2021) Flood prone risk area analysis during 2005‑2019 in Lam Se Bok watershed, Ubon Ratchathani province, Thailand. *Geographia Technica*, Vol. 16, Issue 1, 2021, pp 141 to 153, DOI: 10.21163/GT_2021.161.12

CORRECTING THE TOPOGRAPHIC EFFECT ON SPOT-6/7 MULTISPECTRAL IMAGERIES: A COMPARISON OF DIFFERENT DIGITAL ELEVATION MODELS

Zylshal ZYLSHAL[1]* , *Athar Abdurrahman BAYANUDDIN[1]* , *Ferman Setia NUGROHO[1]* ,
Sutan Takdir Ali MUNAWAR[1]

ABSTRACT :
The topographic effect on satellite imagery has long been acknowledged and several methods have been proposed to address it. These methods mostly employ a digital elevation model to identify topographic conditions. The availability of various digital elevation models (DEMs) with different spatial resolutions prompts a thorough investigation to select suitable data for use when correcting the topographic effect on high-resolution satellite imagery. The release of Digital Elevation Model Nasional (DEMNAS) with its 8-meter spatial resolution provides a similar spatial resolution with SPOT-6/7 multispectral data (6 meters). This study presents our results for topographic correction performed using three different DEMs on orthorectified SPOT-6/7 multispectral data. These DEMs are Shuttle Radar Topography Mission (SRTM) and ALOS World 3D 30 meters (AW3D30), as well as DEMNAS. All three DEMs were resampled to match SPOT-6/7 spatial resolution (6 meters). Atmospheric correction using the MODTRAN-4 algorithm was conducted on the SPOT-6/7 multispectral images. Our study was conducted on two test sites located in the mountainous region over South Sulawesi Province, Indonesia. The Minnaert correction was chosen as the correction algorithm with the *k* constant calculated for each band over forest land cover. To evaluate the performance of each DEM, visual evaluation and statistical assessment were employed. Pixel values before and after topographic correction were compared over sunlit as well as shaded forest. Coefficient of variation (CV) was used as the statistical assessment tool. Our results show that AW3D30 is able to reduce the topographic effect on SPOT-6/7 multispectral images. The correlation (*r*) between image surface reflectance value and local illumination were reduced from 0.78 to - 0.06 for the best performer on the NIR infrared band. CV was also reduced from 24.46 to 19.02 for the same NIR band. AW3D30 performed the best without the apparent under- and over-correction produced by the two other DEMs. Tweaks and modifications are found to be necessary to resolve the under-correction encountered when using SRTM and the over-correction associated with using DEMNAS on SPOT-6/7 multispectral imagery.

Key-words: *AW3D30, DEMNAS, SRTM, Minnaert correction, SPOT-6, SPOT-7*

1. INTRODUCTION

Recent advances in Earth observation (EO) satellite technology have seen improved spatial resolution in produced imagery. While high-spatial-resolution satellite images can offer greater detail, they are still affected by the environment. The topographic variation of mountainous regions often causes different spectral radiance to the satellite imagery. The combination of terrain's slope and aspect with solar zenith and azimuth angles often causes radiometric distortion (Holben & Justice, 1980). A sun-facing slope appears brighter than a slope facing away from the sun and for homogenous land cover such as forest this can cause a distinctly different reflectance value, potentially leading to misclassification of land cover.

While topographic correction has mainly been investigated for medium-spatial-resolution images, such as those produced by Landsat (Justice, Wharton & Holben, 1981; Kawata, Ueno & Kusaka, 1988; Leprieur, Durand & Peyron, 1988; Civco, 1989; Gu & Gillespie, 1998; Riaño *et al.*,

[1]Indonesian National Institute of Aeronautics and Space (LAPAN), Remote Sensing Technology and Data Center, 17310, Jakarta, Indonesia, *zylshal@lapan.go.id, athar.abdurrahmanb@lapan.go.id, fermansetia@gmail.com, sta.munawar@lapan.go.id

2003; Gao & Zhang, 2009b; Li, Im & Beier, 2013; Vanonckelen *et al.*, 2014; Vázquez-Jiménez *et al.*, 2017), SPOT 5 (Richter, Kellenberger & Kaufmann, 2009), and Sentinel-2 (Chen *et al.*, 2020), high-spatial-resolution imagery also suffers from topographically-induced illumination variation (Law & Nichol, 2004). Thus, topographic correction of high-spatial-resolution satellite images remains essential. Simple band rationing can reduce the spectral discrepancies caused by varying slope aspect (Chavez Jr., 1996). However, this approach comes with consequent reduced radiometric resolution of the data itself. Another method is to use digital elevation model (DEM) data. By using DEMs, the terrain's slope, aspect, inclination to the sun and the satellite's sensor can be modeled.

Several studies have been conducted to find out how different DEMs affect topographic correction results. These studies can generally be categorized into two groups: those using medium-resolution EO satellite data, such as Landsat MSS (Justice, Wharton & Holben, 1981), Landsat-7 ETM+ (Gao & Zhang, 2009b), Landsat-8 OLI (Wu, Jin & Fan, 2016; Pimple *et al.*, 2017; Umarhadi & Danoedoro, 2019), SPOT-4 (Shepherd & Dymond, 2003), and LAPAN-A3 (Zylshal, 2019); and those using high-resolution EO satellite data, such as Quickbird (Wu *et al.*, 2008) and IKONOS (Nichol & Hang, 2013). Correction of topographic effects on medium-resolution data has been extensively studied using globally available DEM data, such as Shuttle Radar Topographic Mission (SRTM), ALOS World 3D DEM (AW3D30), and ASTER GDEM. These DEMs perform well when combined with EO satellite imagery of relatively comparable spatial resolution.

Several studies suggest using comparable spatial resolution of DEM and satellite imagery to achieve the best topographic correction (Kawata, Ueno & Kusaka, 1988; Goyal, Seyfried & O'Neill, 1998; Hantson & Chuvieco, 2011; Pimple *et al.*, 2017). On the other hand, the use of DEM spatial resolution that is relatively coarser than the EO imagery has also have been proven to be able to produce topographically corrected images (Riaño *et al.*, 2003; Richter, Kellenberger & Kaufmann, 2009; Goslee, 2012; Nichol & Hang, 2013). Another problem is the availability of this type of high-resolution DEM data. Typical high-spatial-resolution DEM data such as Light Detection and Ranging (LiDAR) and Airborne Interferometric Synthetic Aperture Radar (IfSAR) is still not fully available for many rural areas in developing countries (Nkwunonwo, Whitworth & Baily, 2020). Fortunately, for the Indonesian region a nationwide high-resolution DEM known as DEM Nasional (DEMNAS) was released for general use in 2018 (BIG, 2018). Two initial studies have been conducted into how well DEMNAS performs in terms of topographic correction (Umarhadi & Danoedoro, 2019; Zylshal, 2019). Results of these studies indicate that topographic correction performed using DEMNAS as the elevation data can subdue topographic effects on EO satellite imagery. Both of these studies, however, tested DEMNAS on medium-spatial-resolution imagery (Landsat and LAPAN-A3). How well it performs on high-spatial-resolution data such as SPOT-6/7 is still unknown. The 8-meter spatial resolution of DEMNAS (BIG, 2018; Julzarika & Durdjani, 2019) is the closest DEM data to the 6-meter multispectral imagery provided by SPOT-6/7.

The SPOT-6 and SPOT-7 constellation is composed of twin satellites operating as a true constellation on the same orbit and phased 180° from each other (referred to throughout this paper as SPOT-6/7). Its large swath combined with its high spatial resolution have proven it to be useful as a monitoring tool that can provide cloud-free imagery over a wide area (Nonin *et al.*, 2013). Its ability to monitor forest areas (Li *et al.*, 2015) and to estimate the above-ground biomass of such forest (Motlagh *et al.*, 2018; Hlatshwayo *et al.*, 2019; Nguyen & Kappas, 2020) gives SPOT-6/7 an important role in efforts to ensure global food security and combat land degradation. With its plan to be in service until 2024 (Nonin *et al.*, 2013), and considering its usefulness, a reference for the most suitable approach and DEM source for topographic correction of SPOT-6/7 imagery is essential. Information about the use of topographic correction on SPOT-6/7 imagery is, however, still limited. A previous study utilizing SCS+C combined with SRTM data showed that topographic correction can improve classification accuracy for SPOT-6/7 images (Rani *et al.*, 2017). However, that research solely used classification accuracy as the evaluator, whereas classification accuracy is actually determined by many factors, including classification algorithm, sample size, and class covariance (Fan *et al.*, 2018; Zylshal, 2020). It is our view that further investigation into SPOT-6/7 topographic correction is still needed.

To understand how well the topographic correction is performed, two well-known, globally available DEMs, namely the 3 arc second SRTM as well as the ALOS World 3D 30 meter (AW3D30) were also investigated. The use of DEMNAS and AW3D30 for specific topographic correction of SPOT-6/7 imagery has never been published before. By using these DEMs with varying spatial resolutions, the objective of this research is to investigate what is the best DEM for topographic correction of SPOT-6/7 imagery. Using the Minnaert correction algorithm on two different test sites, we attempt to investigate how well these DEMs perform on SPOT-6/7 imagery. Our study will be the first to use DEMNAS and AW3D30 as DEM data applied to SPOT-6/7 imagery. The results of this study will advance our understanding of how to appropriately select the DEM to reduce topographic effects on SPOT-6/7 data over mountainous regions.
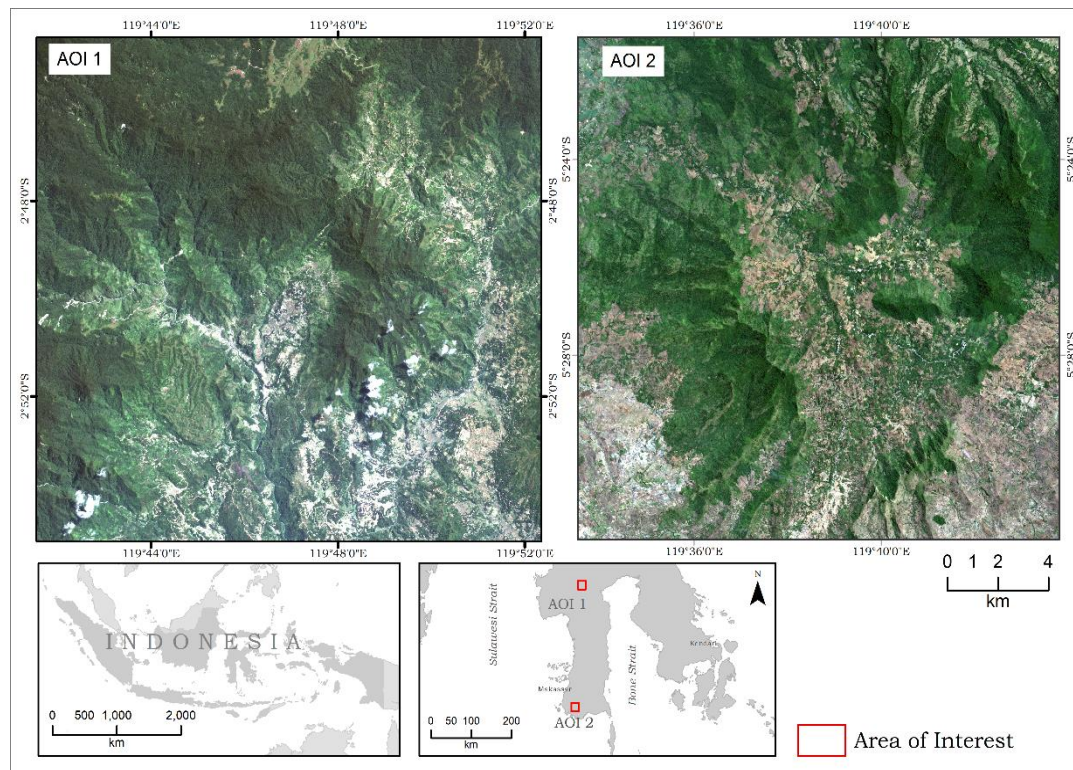
Fig. 1. The test site for topographic correction over the Sulawesi region shown in red–green–blue (RGB) composite images from SPOT-6/7. The left-hand image, AOI1, is over the North Toraja region while the image on the right, AOI2, is over the Gowa region.

2. STUDY AREA

We chose two test sites, both located in the South Sulawesi region of Indonesia. Each test site is 23×23 km wide (**Fig. 1**). Test site 1 (AOI 1) is located in the northern part of the South Sulawesi region. The terrain is oriented in all directions and is dominated by hilly and mountainous relief, with slopes ranging from 0 to 87 degrees. Based on the global land-cover map produced by Copernicus, land cover is mainly forest, herbaceous vegetation, and cropland. AOI 1 is comprised of two landform types. Karst formations cover a small portion of the southeastern part, with volcanic landforms dominating the rest of the site. Test site 2 (AOI 2) is located in the southern part of the South Sulawesi region on an ancient volcanic landform comprising the Baturappe-Cindakko volcanic formation (Tpbv). The terrain is oriented in all directions and dominated by hilly and mountainous relief. The relief undulates with slopes ranging from 0 to 69 degrees (**Fig. 2**). Based on the global land-cover map produced by Copernicus, the dominant land cover at this site is closed forest and cropland.

Climatic conditions at the two sites differ slightly, with AOI 2 being generally drier than AOI 2. As shown in **Fig. 1**, there is an obvious difference in green vegetation coverage between the two sites, even though both data sets are taken during the same season. More detailed information on the imagery used is discussed later in this paper.
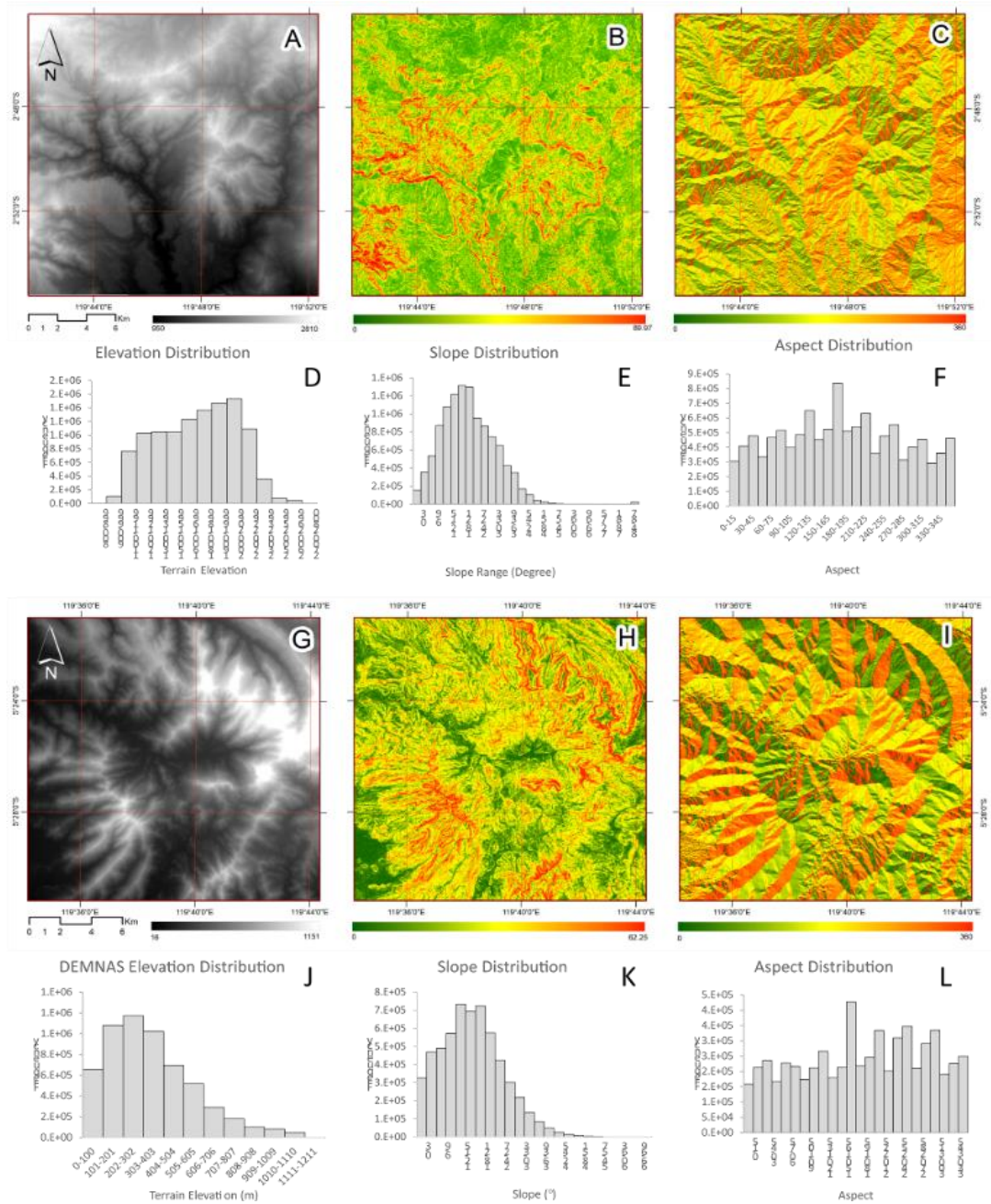
Fig. 2. Terrain conditions in the study area derived from DEMNAS data: (A) elevation map for AOI 1; (B) slope map for AOI 1; (C) aspect map for AOI 1; (D), (E), and (F) distributions for elevation, slope, and aspect, respectively; (G) elevation map for AOI 2; (H) slope map for AOI 2; (I) aspect map for AOI 2; (J), (K), and (L) show distributions of elevation, slope, and aspect, respectively.

3. DATA AND METHODS

3.1. Digital elevation model (DEM)

Fig. 2 shows the DEMs used in this study. SRTM was launched in 2000, and with its global coverage and free-of-charge distribution system, has become one of the most-used sources of DEM data for topographic correction (Vincini & Frazzi, 2003; Trisakti, Kartasasmita & Kartika, 2009; Gao & Zhang, 2009b, 2009a; Balthazar, Vanacker & Lambin, 2012; Vanonckelen, Lhermitte & Van Rompaey, 2013; Li, Im & Beier, 2013; Gao *et al.*, 2016; Park *et al.*, 2017; Pimple *et al.*, 2017; Takaku & Tadono, 2017; Fan *et al.*, 2018; Phiri *et al.*, 2018; Umarhadi & Danoedoro, 2019; Zylshal, 2019). In this study, the 3-arc-second version of SRTM (Version 4) was used. We downloaded the data from the CIAT-CSI SRTM website (http://srtm.csi.cgiar.org/) (Jarvis *et al.*, 2008).

ALOS World 3D-30m (AW3D30) is a Japan Aerospace Exploration Agency (JAXA) project to provide DEM data. The project uses the ALOS PRISM panchromatic stereo sensor, which operated from 2006 to 2011. AW3D30 is a digital surface model (DSM) with a spatial resolution of 30 meters and was first released in March 2017 (Civco, 1989; Japan Aerospace Exploration Agency, 1997; Takaku *et al.*, 2016; Takaku & Tadono, 2017). We used the latest version (Version 3.1) released in April 2020. The data set was downloaded from JAXA's Earth Observation Research Center (EORC) (https://www.eorc.jaxa.jp/ALOS/en/aw3d30/data/index.htm) (Japan Aerospace Exploration Agency, 2020).

DEMNAS was developed and released by the Indonesian Geospatial Information Agency (BIG). It was built from several data sources, including IfSAR data (5 m resolution), TERRASAR-X (5 m resolution), and ALOS-PALSAR (11.25 m resolution), by adding/assimilating mass point data to stereo-plotting results. The spatial resolution of DEMNAS is 0.27 arc seconds, using EGM2008 vertical datum (BIG, 2018). The data was downloaded from the Indonesian Geospatial Agency website (https://tanahair.indonesia.go.id/demnas) (BIG, 2018). DEMNAS is produced by adding/assimilating mass point data into the DSM (IfSAR, TERASAR-X, or ALOS-PALSAR) using GMT surface with a tension of 0.32. Details of the assimilation process can be found in Hell and Jakobsson (2011). The official information on the DEMNAS website states that the data itself is considered as a digital terrain model (DTM). However, studies conducted by Julzarika and Harintaka (2019) argue that DEMNAS should be treated as a DSM rather than a DTM. In this study, we agree with this latter interpretation and treat DEMNAS as a DSM. The fact that SRTM and AW3D30 are also DSMs makes the comparison appropriate. **Table 1** summarizes the DEM data used in this study.

Table 1.

The DEMs used in this study.

No	DEM	Horizontal resolution	Vertical resolution	Vertical datum	Source
1	SRTM	30 m	16 m	EGM96	USGS
2	AW3D30	30 m	4.4 m	EGM96	JAXA
3	DEMNAS	8 m	5 m	EGM08	BIG

3.2. SPOT-6/7

The SPOT-6/7 data used in this study is multispectral bands with 6-meter spatial resolution. Multispectral data was chosen based on the similarity of its resolution to that of DEMNAS (8 m). Furthermore, Standard Ortho (Astrium Services, 2013) products with less than 1 pixel (< 6 m) horizontal accuracy (CE90) were used instead of raw Level 1 (RSensor) data. The complete list of SPOT-6/7 data used is shown in **Table 2**. The data were cropped based on the AOI. The information needed as the input parameters for topographic correction were collected from SPOT-6/7 metadata, as shown in **Table 2**.

Table 2.

SPOT-6/7 data specifications used in this study.

AOI	Scene ID	Acquisition date	Acquisition time (GMT)	Viewing angle	Sun's azimuth	Sun's elevation
#1	SPOT6_201909140204066	Sept 14, 2019	02:04:06	21.16	76.26	60.96
#2	SPOT7_201710130156070	Oct 13, 2017	01:56:07	25.59	95.20	62.20

3.3. Methods

3.3.1. Atmospheric correction

Several topographic correction methods require the satellite imagery to be atmospherically corrected (surface reflectance) (Richter, 1997; Riaño *et al.*, 2003; Vanonckelen *et al.*, 2014; Pimple *et al.*, 2017; Vázquez-Jiménez *et al.*, 2017; Phiri *et al.*, 2018). However, the use of top-of-atmosphere (TOA) reflectance is also not uncommon (Richter, Kellenberger & Kaufmann, 2009). In this study, the SPOT-6/7 imagery was corrected to surface reflectance value using the MODTRAN-4 algorithm (Adler-Golden *et al.*, 1999; Matthew *et al.*, 2000). Studies conducted by Fibriawati (2016) and Rotta *et al.* (2016) point out that MODTRAN-4 performs well for SPOT-6/7 imagery.

Each item of SPOT-6/7 data was converted to TOA reflectance by calculating the incoming solar irradiance. For SPOT-6/7 the TOA radiance is calculated as follows (Astrium Services, 2013):

$$\rho_b(p) = \frac{\mu \cdot L_b(p)}{E_0(b).\cos(\theta_S)} \tag{1}$$

$L_b(p)$ is the TOA radiance and is calculated as follows:

$$L_b(p) = \frac{DC(p)}{GAIN(b)} + BIAS(b) \tag{2}$$

where b is the respective band, *DC(p)* is the pixel value (digital number), and *Lb(p)* is the TOA radiance (in W· 〖sr〗 ^(-1)·m^(-2)· 〖μm〗 ^(-1)). GAIN and BIAS is the absolute radiometric calibration coefficient of SPOT-6/7.

The data is then converted to surface reflectance (SR) value using the MODTRAN-4 algorithm within the FLAASH® module in ENVI®. The program runs with an intuitive graphical user interface (GUI). The user needs to specify several input parameters to model the atmospheric conditions at the time of satellite image acquisition (ENVI, 2009). The input parameters used in this study are shown in **Table 3.**

Table 3.

Input parameters in FLAASH®.

FLAASH parameters	AOI 1	AOI 2
Sensor type	SPOT-6	SPOT-7
Sensor altitude	701.61 km	702.05 km
Ground elevation	0.8 km	0.3 km
Flight date (YYMMDD)	20190914	20171013
Flight time (HH:MM:SS) (GMT)	020406	015607
Atmospheric model	Tropical	Tropical
Aerosol model	Rural	Rural
Initial visibility	100 km	100 km
Zenith angle	29.12	27.89
Azimuth angle	209.1	178.7
Aerosol retrieval	2-band (K-T)	2-band (K-T)
KT upper channel	B3 (825 nm)	B3 (825 nm)
KT lower channel	B0 (485 nm)	B0 (485 nm)

3.3.2. DEM processing

The SRTM data for AOI 2 contains several holes/gaps and so a gap-filling algorithm based on "GDAL fill no data" was applied (GDAL/OGR contributors, 2020). Each DEM was resampled into the same spatial resolution as SPOT-6/7 imagery (6 m). The purpose of resampling was to reduce the errors caused by overshooting the grid value beyond the edge of the pixels (Nichol & Hang, 2013). The resampling procedures were performed using a bilinear algorithm, chosen to reduce aliasing during the upscaling stage. The bilinear algorithm produces a smoothing effect on the resampled DEM (Parker, Kenyon & Troxel, 1983). The use of a smoothed DEM in topographic correction can increase its effectiveness (Riaño *et al.*, 2003; Richter, Kellenberger & Kaufmann, 2009; Goslee, 2012; Nichol & Hang, 2013). Slope and aspect were then derived for the DEMs to be used for further analysis.

Since each set of DEM data is originally delivered with different vertical datum, it then needs to be converted to a unified format. In this study, Earth Gravitational Model (EGM) 2008 (Kenyon & Factor, 2007) was used for all three DEMs.

3.3.3. Topographic correction

The first step in topographic correction using the Minnaert correction method is to calculate the local illumination of the test site. In this study, local illumination modeling was generated for each DEM and calculated as follows (Equation 3):

$$cos\ i = cos\ \theta_s\ cos\ \theta_n(x,y) + sin\ \theta_s\ sin\ \theta_n\ cos\{\phi_n(x,y) - \phi_s\}$$ (3)

where $cos\ i$ is the local solar illumination angle, θ_n is the solar zenith angle, θ_s is the terrain's slope, ϕ_n is the solar azimuth, and ϕ_s is the topographic azimuth. Meanwhile, x and y indicate the pixel's coordinates. The solar zenith and azimuth information were all taken from SPOT-6/7 metadata. The slope and topographic azimuth were derived from the DEM. The $cos\ i$ values range from -1 to 1 (Riaño *et al.*, 2003).

The Minnaert correction algorithm was chosen for this study. This method, proposed by Minnaert (1941), was originally developed to study the lunar surface; however, its performance in topographic correction makes it one of the most-cited non-Lambertian methods (Hantson & Chuvieco, 2011). Several studies have found that Minnaert correction is able to outperform other Lambertian-based topographic corrections (Colby, 1991; Law & Nichol, 2004; Gao *et al.*, 2016). The algorithm is based on a non-Lambertian assumption and introduces the Minnaert constant (k) to the cosine method in the form of a bidirectional reflectance distribution function. The Minnaert correction can be written as follows (Riaño *et al.*, 2003):

$$\rho_H = \rho_T * \left(\frac{cos\ \theta_n}{cos\ i}\right)^k$$ (4)

where ρ_H denotes the reflectance of a horizontal surface, and ρ_T denotes the reflectance of an inclined surface. The k value for each band is calculated by linearization of Equation 4 into:

$$ln(\rho_T) = ln(\rho_H) + k\ ln\left(\frac{cos\ i}{cos\ \theta_n}\right)$$ (5)

Letting $ln\left(\frac{cos\ i}{cos\ \theta_n}\right)$ be *x*, $ln(\rho_T)$ be *y*, and $ln(\rho_H)$ be *m*, we end up with the linear function as follows:

$$y = kx + m$$ (6)

The k values can then be calculated using a linear regression function. The Minnaert constant depends on the land-cover type as well as the wavelength used (Gao *et al.*, 2016). The next step was to calculate the k constant for each image band on the same land-cover feature. Thus, a prior forest classification was employed on SPOT-6/7 imagery. Based on the landuse/land-cover sample points taken from the field survey conducted in 2020 at AOI 1 and in 2018 at AOI 2, a simple random forest (RF) classifier was employed on SPOT-6/7 imagery. The solar zenith and azimuth information is taken from SPOT-6/7 image metadata along with the derived slope and aspect data from the DEM. The next step was to calculate the k constant for each image band. Band-specific k value needs to be extracted from the same land-cover type; for this study we chose forest, as it covers a large portion of both AOIs.

After the forest class was acquired, 2000 sample points were randomly generated for each AOI. These sample points were then used to calculate the Minnaert constant (k) for each SPOT-6/7 band and DEM used. The k value is based on the bidirectional reflectance distribution function and ranges from 0 to 1. The k value depends on the land-cover type as well as the image band. It is computed using a regression-fitting linear equation (Gao *et al.*, 2016). The k values are then fed into the Minnaert correction algorithm as shown in Equation 4.

3.3.4. Performance assessments

The pre-corrected and post-corrected images were compared to assess each DEM's performance. The topographically corrected images were evaluated both visually and statistically. Visual

assessment was employed to see whether there was any over- or under-correction. Meanwhile, for the statistical analysis, sample points were generated specifically for the sunlit and shaded slopes within the forested region. We opted to specifically investigate sunlit pixels and their direct opposite aspect pixels to understand better how topographic correction affects these pixels within SPOT-6/7 imagery. In this study, the sunlit samples were taken from all the pixels within the $\pm 20°$ range of each DEM's aspect from the sun's azimuth for the respective acquisition dates. The shaded region was taken from the exact opposite of the corresponding sunlit slope at $180° \pm 20°$ range from the sun's azimuth. All these samples were forest pixels. We generated 200 random kernels for each AOI with a kernel size of 9 x 9. The sunlit and shaded pixels were all given 100 kernels each (**Table 4**).

Table 4.

Number of sample points used for quantitative assessments.

AOI	# Samples		Total
	Sunlit	Shade	
1	7647	7726	15,373
2	7766	7673	15,439

The pixel value of the pre-corrected and post-corrected images, as well as the local illumination value at the exact location, were extracted. Two methods of statistical evaluation were employed. First, the Pearson correlation *(r)* between the local illumination and the pixel value was calculated (Holben & Justice, 1980; Justice, Wharton & Holben, 1981) and plotted using a scatterplot of density of forest land cover. The best performer should be able to reduce the pixel value's dependency on the topographic condition after correction. Second, the coefficient of variation (CV) was calculated. The CV is widely adopted to identify intra-class homogeneity (Gao & Zhang, 2009a). The difference between CV (CV$_{diff}$) before and after correction was also calculated (Vanonckelen *et al.*, 2014; Pimple *et al.*, 2017; Zylshal, 2020). A successful topographic correction should also be able to reduce the CV. Finally, a matrix table comparing the three DEM sources was prepared and the best performers were ranked. The ranking was based on which DEM was able to reduce topographic dependency as well as CV without inducing over-/under-correction of visual appearance.

4. RESULTS AND DISCUSSIONS

4.1. Results

Table 5 shows the local Minnaert constant (*k*) used in this study for each band and DEM. The *k* values in AOI 2 are generally higher than AOI 1. The *k* values in AOI 1 range from 0.193 to 0.6254. The *k* value of the NIR band in AOI 1 is the highest value for each DEM, while the lowest *k* value appears in the blue band. These values were then fed into Equation 4 for each combination of bands and DEM for both AOIs.

Table 5.

Results of Minnaert constant (*k*) calculation.

SPOT-6/7 band	AOI 1			AOI 2		
	SRTM	AW3D	DEMNAS	SRTM	AW3D	DEMNAS
B	0.4100	0.4108	0.1930	0.7801	0.8008	0.6505
G	0.4424	0.4712	0.3484	0.8327	0.7629	0.8103
R	0.4651	0.4961	0.3809	0.8323	0.7402	0.7943
NIR	0.5848	0.6254	0.5003	0.7256	0.6993	0.6913

4.1.1. Visual evaluation

**Fig. 3** shows the effect of the Minnaert correction algorithm applied to both AOIs, presented in RGB color composite of red-NIR-blue. **Figs. 3A** and **3C** show the uncorrected SPOT-6/7 images for AOI 1 and AOI 2, respectively. **Figs. 3B** and **3D** show the corrected SPOT-6/7 images using AW3D30 over the corresponding AOIs. Both DEMNAS and SRTM yield very similar results when viewed at the overall zoom level of the AOIs.
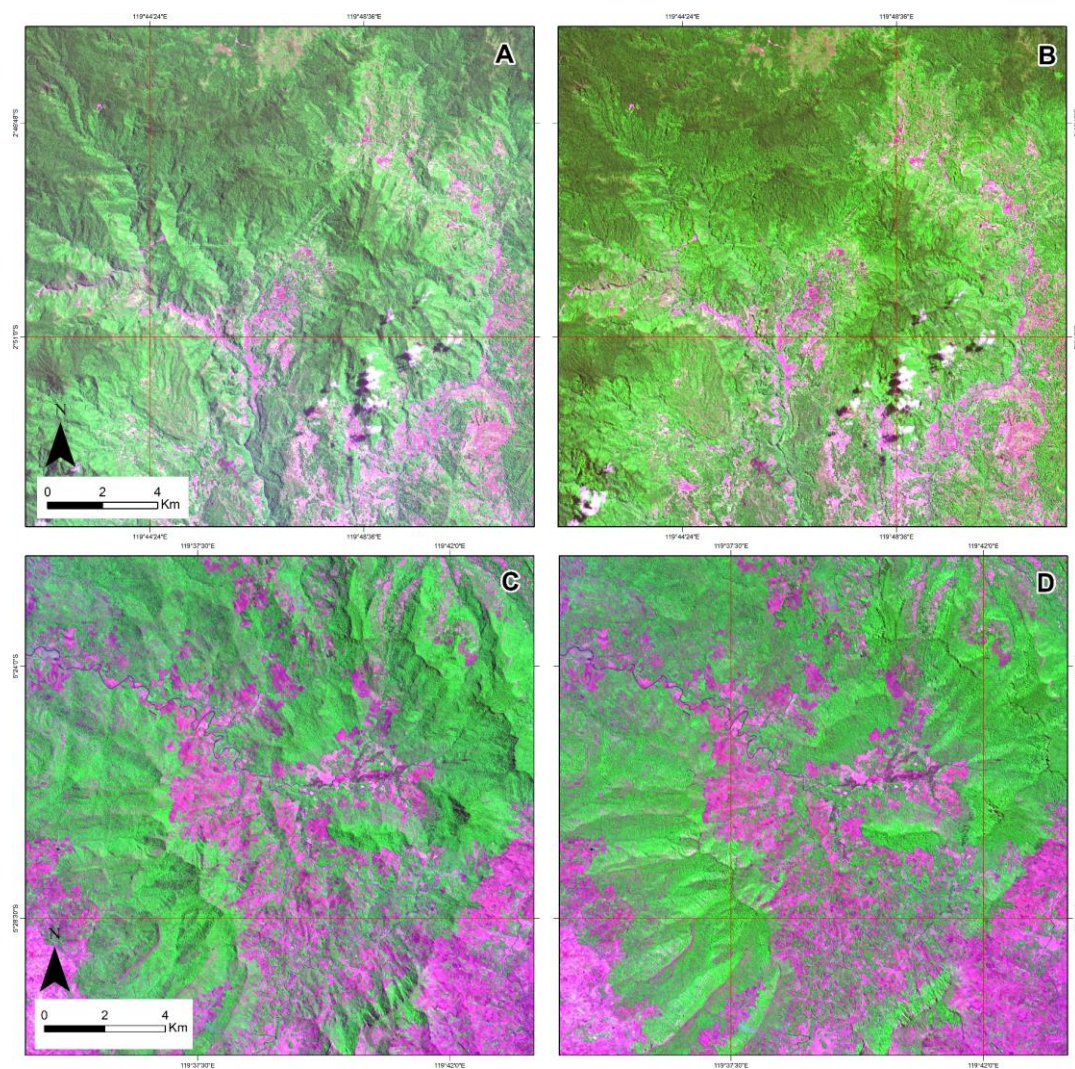
Fig. 3. Visual comparison of topographic correction over the entire AOI using AW3D30 (RGB composite of Red-NIR-Blue); (A) and (C).

The different visual performances, only visible over some areas and with added zoom level, are as shown in **Fig. 4.** The more obvious visual comparisons of all three DEMs, as well as corresponding topographic correction results, are shown in **Fig. 4**. Compared to the pre-corrected images (**Figs. 4A** and **4I**), the use of Minnaert correction on SPOT-6/7 data is visually successful for both AOIs. The different facing slopes on the same forest land cover appear to be in the same contrast and brightness (**Figs. 4B**, **4C**, **4D**, **4F**, **4G**, and **4H**). A closer inspection (yellow circle) shows that under-correction occurs on SRTM for both AOIs, as shown in **Figs. 4B**, **4F, 4J,** and **4N**. AW3D30 and DEMNAS produce a very similar result on AOI 1, as shown in **Figs. 4C** and **4D**. However, AW3D30 has a slight advantage in performance, as shown in the yellow circle in **Fig. 4G** compared to the slightly under-corrected DEMNAS version (**Fig. 4H**). For AOI 2, AW3D30 and DEMNAS perform better visually (**Fig. 4J.** and **Fig. 4K**, respectively**)** than SRTM (**Fig. 4J**). While similar overall, DEMNAS shows over-correction in several areas, mostly located on hill ridges, as indicated by the yellow circle in **Fig. 4P**. AW3D30 also suffered slight over-correction over the same region (**Fig. 4O**), albeit not as high as that of DEMNAS. Visually, AW3D30 performed the best, with DEMNAS a close second, and SRTM performing the least successfully.
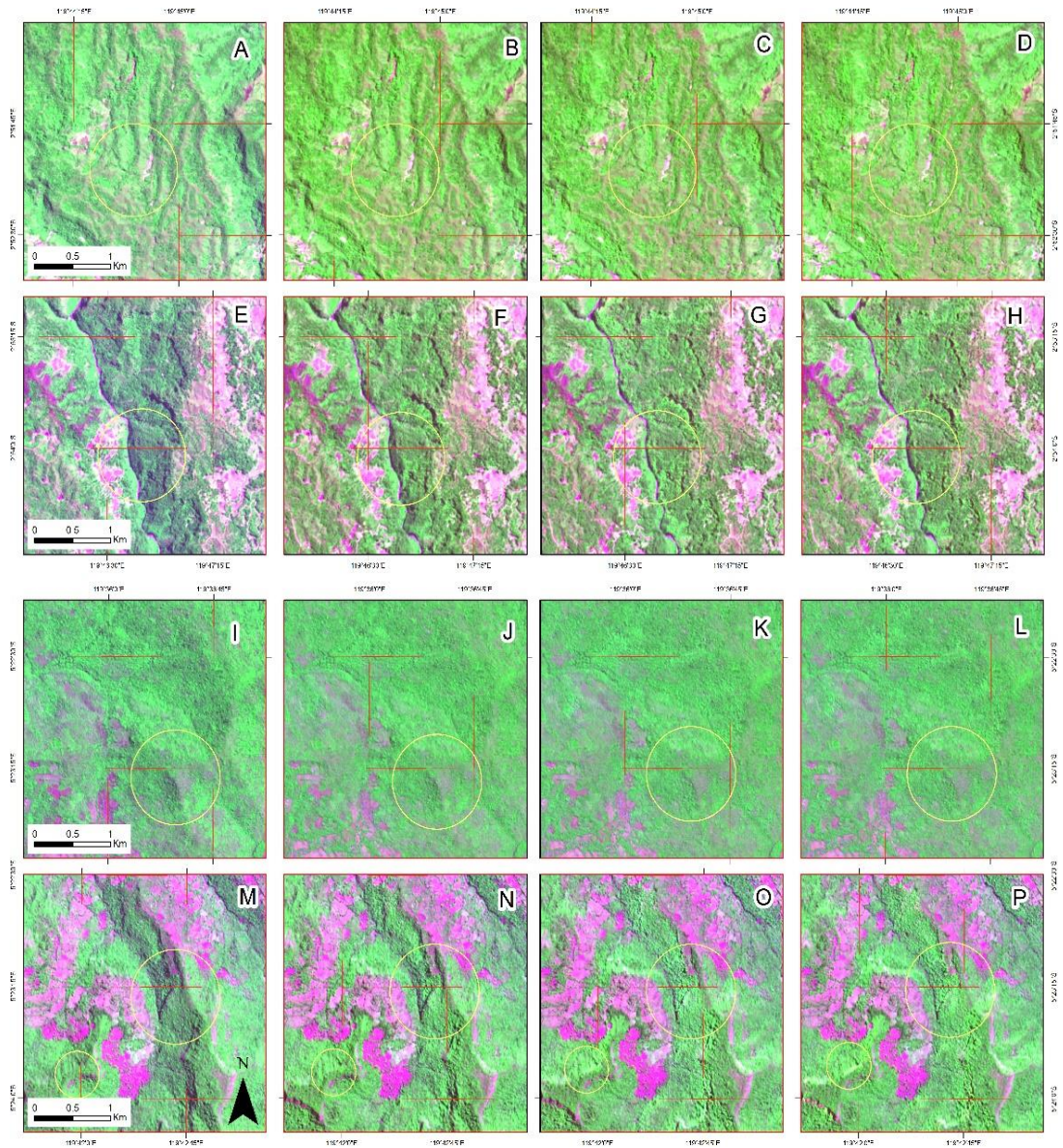
Fig. 4. Visual comparison of topographic correction shown in "natural-color" RGB composite of Red–NIR–Blue over several subset regions of the test sites: pre-corrected surface reflectance SPOT-6/7 on AOI 1 (A and E); topographically corrected AOI 1 using SRTM (B and F), AW3D30 (C and G), and DEMNAS (D and H). Pre-corrected surface reflectance of SPOT-6/7 on AOI 2 (I and M). Topographically corrected AOI2 using SRTM (J and N), AW3D30 (K and O), and DEMNAS (L and P). The yellow circle emphasizes the different performance of each data set.

4.1.1. Quantitative evaluation

Fig. 5 confirms the effect of performing topographic correction on the SPOT-6/7 data. The trend line's gradient has been reduced after the topographic correction. The flat trend line means that the terrain's influence on the image's reflectance value has been reduced. The sun-facing slopes and the slopes facing away from the sun have similar reflectance values. The complete list of how the trend-line gradients (*m*) and *r* change for all data sets in each AOI are shown in **Table 6**.
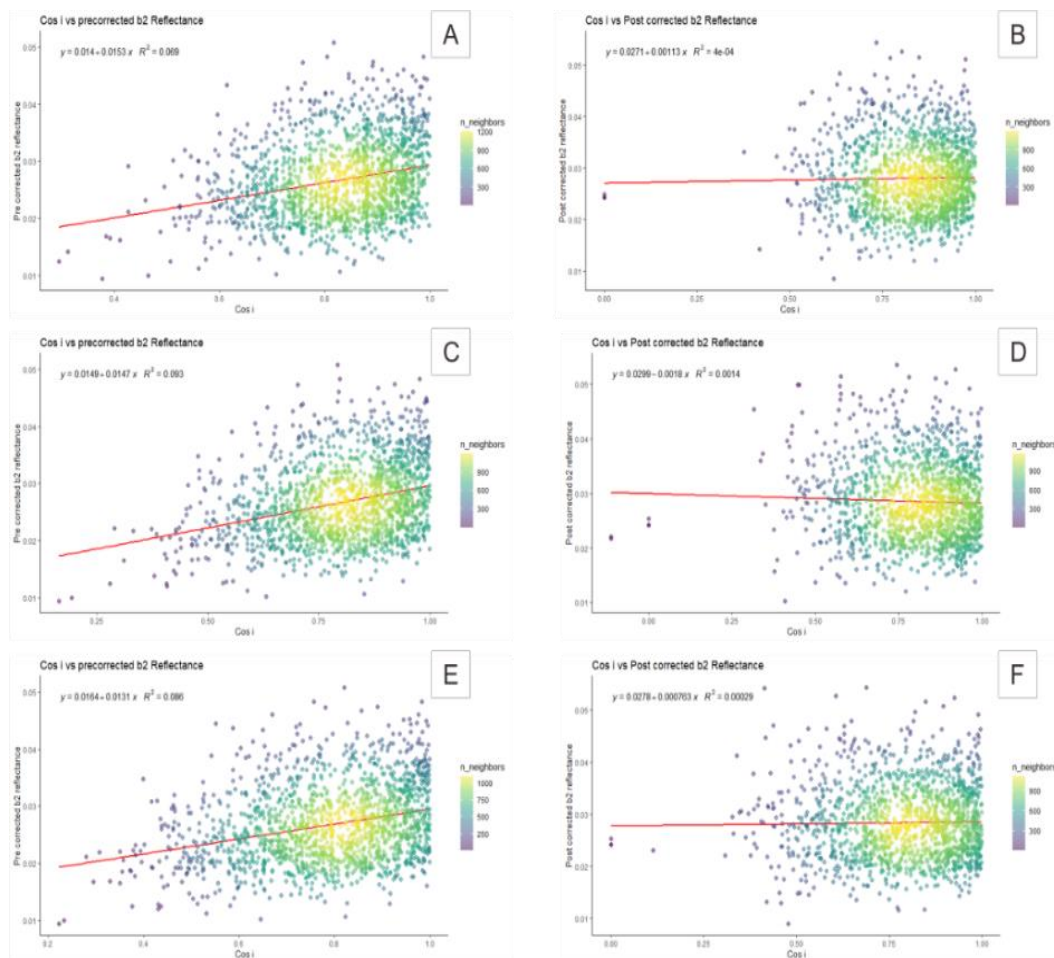
Fig. 5. Scatterplot density between *cos i* and surface reflectance for AOI 1 before and after topographic correction applied to SPOT-6/7 green band: (A) Pre-corrected using SRTM; (B) post-corrected using SRTM; (C) pre-corrected using AW3D30; (D) post-corrected using AW3D30; (E) pre-corrected using DEMNAS; (F) post-corrected using DEMNAS.

Table 6.
Trend-line gradient (*m*) and Pearson correlation (*r*) values before and after correction.

AOI	Band	*m* SRTM		*m* AW3D30		*m* DEMNAS		*r* SRTM		*r* AW3D30		*r* DEMNAS	
		Pre	Post	Pre	Post	Pre	Post	Pre	Post	Pre	Post	Pre	Post
1	B	0.0016	0.0012	0.0016	0.0008	0.0018	0.0013	0.4520	0.2990	0.3820	0.1650	0.4050	0.2610
	G	0.0014	0.0010	0.0017	0.0008	0.0017	0.0012	0.6200	0.4170	0.6160	0.2830	0.6150	0.3870
	R	0.0020	0.0014	0.0025	0.0011	0.0026	0.0016	0.6590	0.4020	0.6710	0.2530	0.6670	0.3690
	NIR	0.0002	0.0001	0.0002	0.0000	0.0002	0.0001	0.6570	0.2950	0.6930	0.1060	0.6850	0.2560
2	B	0.0017	0.0007	0.0021	-0.0003	0.0022	0.0002	0.4602	0.1862	0.4930	-0.0788	0.5027	0.0415
	G	0.0011	0.0007	0.0014	-0.0003	0.0014	-0.0004	0.6388	0.3036	0.6734	-0.1111	0.6803	-0.1836
	R	0.0009	0.0004	0.0011	-0.0002	0.0011	-0.0003	0.4721	0.1867	0.4922	-0.0788	0.4951	-0.1308
	NIR	0.0002	0.0001	0.0002	0.0000	0.0002	0.0000	0.7770	-0.0600	0.7852	-0.0600	0.7852	-0.0589

The SR of pre-corrected images shows a statistically significant correlation to local illumination at 95% confidence level. The Pearson correlation varied with each DEM and SPOT-6/7 band. Prior to correction, the r value varied from 0.0002 to 0.66 for SRTM, 0.38 to 0.78 for AW3D30, and 0.41 to 0.79 for DEMNAS. After correction, all DEMs were able to reduce m as well as r. AW3D30 produced the highest reduction of the correlation on five bands: blue on both AOIs, and green, red, and NIR on AOI 1. DEMNAS performed second best with the three highest CV reductions on green, red, and NIR, all in AOI 2. It is worth noting that in AOI 2, both AW3D30 and DEMNAS produced negative r values, specifically for green and red bands. The negative r value is the quantitative representation of the over-correction shown in **Figs**. **4O** and **4P**.

The under-correction produced by SRTM is confirmed by the total reduction of r in **Table 6**. Apart from the blue band for AOI 1, SRTM consistently produced the least reduction in r for all bands for both AOIs. All DEMs are able to produce higher CV reduction on the NIR band for both AOIs. This is easily explained by the fact that the sample points used were taken on a highly vegetated area (forest land cover) where the spectral value in NIR is typically higher than the visible bands. With these results, we then moved on to calculate the intra-class spectral homogeneity using CV.

Table 7 shows the CV for each band before and after topographic correction, as well as the difference between them. The best performer is that which produces the greatest reduction in CV (Riaño *et al.*, 2003; Richter, Kellenberger & Kaufmann, 2009). AW3D30 produces the greatest CV reduction on the NIR band with a total of 14.23 for both AOIs. As with the correlation value, the value of CV also varied with wavelength (band). SRTM produced the highest CV reduction on four occasions: blue on AOI 1 and AOI 2, and green and red on AOI 2. AW3D30 performed the second-best CV reduction, with three bands having the most reduced CV (green, red, and NIR on AOI 1). DEMNAS came out last with the least number of bands having reduced CV.

Table 7.

CV for each band before and after topographic correction. Bold CV value marks the best performer.

AOI	Band	Original CV	CV			CV$_{diff}$		
			AW3D30	**DEMNAS**	**SRTM**	**AW3D30**	**DEMNAS**	**SRTM**
1	B	194.7179	122.7256	121.662	121.3415	71.99	73.06	**73.38**
	G	37.01004	31.92108	32.50429	32.61597	**5.09**	4.51	4.39
	R	31.31638	25.69942	26.22724	26.68509	**5.62**	5.09	4.63
	NIR	30.2518	21.3648	21.72446	22.96099	**8.89**	8.53	7.29
2	B	41.25368	40.48688	39.43436	38.60342	0.77	1.82	**2.65**
	G	30.25273	23.63064	24.34279	23.41615	6.62	5.91	**6.84**
	R	40.66021	38.52378	39.65421	36.84552	2.14	1.01	**3.81**
	NIR	24.46119	19.11675	19.0159	19.67073	5.34	**5.45**	4.79

5. DISCUSSION

Based on visual appearance, the reduction of *cos i* correlation with surface reflectance, and CV reduction, it is clear that AW3D30 is best suited to being used as the DEM for topographic correction on SPOT-6/7 data (**Table 8**), provided that the Minnaert algorithm is used. This study is the first proof of the suitability of AW3D30 as a DEM source for correcting topographic effects on SPOT-6/7 imagery. Our results are in agreement with results obtained by other authors when comparing different DEM data for topographic correction (Hantson & Chuvieco, 2011; Pimple *et al.*, 2017). The coarser spatial resolution of AW3D30 compared to SPOT-6/7 did not make it inferior to other DEMs with higher spatial resolution (DEMNAS).

Comparison matrix of all DEMs ranked based on the performance assessment used.

DEM	Rankings of performance assessments		
	Visual evaluation	Number of bands with the most reduced *r*	Number of bands with the most reduced CV
AW3D30	1	1	2
DEMNAS	2	2	3
SRTM	3	3	1

Our results also confirm other authors' findings that there is no single source of data or algorithm that is superior in every case (Richter, Kellenberger & Kaufmann, 2009; Ghasemi, Mohammadzadeh & Sahebi, 2011). A similar study conducted in the same area by Zylshal (2019) shows that AW3D30 is superior to DEMNAS, albeit for different EO satellite images. Our study confirms the consensus that the best method varies with different combinations of satellite imagery, study area size (Richter, Kellenberger & Kaufmann, 2009), existing land cover (Gao & Zhang, 2009a), and correction algorithm (Pimple *et al.*, 2017).

Considering the above, our findings are also constrained by the use of the Minnaert algorithm. While it has been shown to have performed well in our study as well as in several other studies (Colby, 1991; Law & Nichol, 2004; Gao *et al.*, 2016), the fact that our test sites are located in a forested mountainous region opens up the possibility of using a different algorithm. Several methods for Minnaert modification have been proposed, including pixel-based Minnaert (PMB) based on slope stratification (Lu *et al.*, 2008), modified Minnaert with IL stratification (Ekstrand, 1996), and SCS + Minnaert (Reeder, 2002). While these approaches may have the potential to perform better than the traditional Minnaert algorithm, algorithm comparison is outside this paper's scope. Another limitation is the fact that the DEMNAS data used in our study is only available for the Indonesian region. Hence, the exact reproducibility of our study in another regions of the world is limited. Crucially, AW3D30 is available worldwide for free, strengthening our confidence in the reproducibility of our results. It is worth noting that our study employed AW3D30 version 3.1 and in several regions, due to cloud and snow cover, AW3D30 still has voids (Takaku & Tadono, 2017). Version 3.2 has since been released with additional tiles to fill these voids. Therefore, we recommend using the newest AW3D30 data available for such regions.

Our study also found that the total area of corrected imagery was also reduced, as reported by Hantson and Chuvieco (2011). The main cause was the fact that local illumination was calculated using a kernel window of 3×3 of the surrounding pixels, causing the edges of the produced images to be practically reduced by 1 pixel. While the best way to mitigate area reduction is by using a DEM with one-third of the pixel size of the image, as suggested by Hantson and Chuvieco (2011), such DEM is unfortunately still not available for our study area. Our recommendation, instead, is to use a slightly wider initial test site than the original AOI and to crop the corrected image at a later stage. While our solution might work with a definitive AOI boundary such as a rectangle, watershed, or administrative boundary, problems might occur when the correction is conducted on a scene-by-scene basis. While AW3D30 has proven to be the best performer, DEMNAS and SRTM also produce adequate results. Since both of these data sources have shown better performance using other algorithms, SRTM's under-correction issue found in this study could be mitigated by using algorithms other than the Minnaert. Alternatively, the over-correction produced by DEMNAS could be mitigated by performing a smoothing filter prior to calculating the *cos i*, as recommended by Riaño *et al.* (2003) and Goslee (2012). The newly released TanDEM-X 90m DEM (TDX90), as well as Copernicus 90 and 30 m DEM, will also be interesting to investigate, given their comparable horizontal and vertical accuracy to AW3D30 (Wessel, 2016). A previous study found that the SCS model is better for use in forest regions (Gu & Gillespie, 1998), while others have argued that the pixel-based Minnaert algorithm is more suitable (Ghasemi, Mohammadzadeh & Sahebi, 2011). It is, however, worth noting that these previous studies were all conducted using coarser satellite data and DEM sources. It would be interesting to investigate whether the use of other algorithms would still produce the same results as ours.

6. CONCLUSIONS

Topographic correction using the Minnaert algorithm was successfully performed on SPOT-6/7 multispectral data. The performance of three different DEMs (DEMNAS, AW3D30, and SRTM) was also successfully assessed and compared. Topographic correction was performed on two different test sites. Based on our performance assessment, both visual and statistical, AW3D30 outperformed the other DEMs. Visual assessment showed that AW3D30 was able to reduce the radiometric difference between sun-facing slopes and slopes facing away from the sun with no over- or under-correction visible. In statistical evaluation, AW3D30 was able to produce the highest reduction of a pixel value's dependency to its corresponding topography in the SPOT-6/7 images tested.

We can conclude that AW3D30 is the best option for correction of topographic distortion on SPOT-6/7 imagery for the Indonesian region. Tweaks and modifications, however, are necessary to resolve the under-correction present when using SRTM or the over-correction when using DEMNAS on SPOT-6/7 imagery. Considering the similar spatial resolution, it is highly advisable to further investigate the performance of DEMNAS using other algorithms.

R E F E R E N C E S

Adler-Golden, S. M. *et al.* (1999) 'Atmospheric correction for short-wave spectral imagery based on MODTRAN4', in *Proceedings of SPIE - The International Society for Optical Engineering*. Denver, USA: Society of Photo-Optical Instrumentation Engineers,Bellingham, WA, United States, pp. 61–69. Available at: https://www.scopus.com/record/display.uri?eid=2-s2.0-0033348265&origin=inward.

Astrium Services (2013) 'SPOT 6 & SPOT 7 imagery user guide', *Astrium Services*, (July), p. 120.

Balthazar, V., Vanacker, V. and Lambin, E. F. (2012) *Evaluation and parameterization of ATCOR3 topographic correction method for forest cover mapping in mountain areas*, *International Journal of Applied Earth Observation and Geoinformation*. Elsevier B.V. doi: 10.1016/j.jag.2012.03.010.

BIG (2018) *DEMNAS - Seamles Digital Elevation Model (DEM) dan Batimetri Nasional*. Available at: https://tanahair.indonesia.go.id/demnas.

Chavez Jr., P. S. (1996) 'Image-Based Atmospheric Corrections - Revisited and Improved', *Photogrammetric Engineering & Remote Sensing*, 62(10), pp. 1025–1036. Available at: https://pdfs.semanticscholar.org/45f1/2625ce130261c7d360d50e09c635355ca919.pdf.

Chen, R. *et al.* (2020) 'Evaluation and normalization of topographic effects on vegetation indices', *Remote Sensing*, 12(14). doi: 10.3390/rs12142290.

Civco, D. L. (1989) 'Topographic Normalization of Landsat Thematic Mapper Digital Imagery', *Photogrammetric Engineering and Remote Sensing*, 55(9), pp. 1303–1309. Available at: https://www.asprs.org/wp-content/uploads/pers/1989journal/sep/1989_sep_1303-1309.pdf.

Colby, J. D. (1991) 'Topographic normalization in rugged terrain', *Photogrammetric Engineering & Remote Sensing*, 57(5), pp. 531–537.

Ekstrand, S. (1996) 'Landsat TM-based forest damage assessment: Correction for topographic effects', *Photogrammetric Engineering and Remote Sensing*, 62(2), pp. 151–161.

ENVI (2009) 'ENVI Atmospheric Correction Module: QUAC and FLAASH user's guide', *Module Version*, p. 44. Available at:
http://scholar.google.com/scholar?hl=en&btnG=Search&q=intitle:ENVI+Atmospheric+Correction +Module:+QUAC+and+FLAASH+user's+guide#0.

Fan, W. *et al.* (2018) 'Topographic correction of forest image data based on the canopy reflectance model for sloping terrains in multiple forward mode', *Remote Sensing*, 10(5). doi: 10.3390/rs10050717.

Fibriawati, L. (2016) 'Koreksi Atmosfer Citra SPOT-6 Menggunakan Metode MODTRAN4', in *Seminar Nasional Penginderaan Jauh 2016*. Depok, Jawa Barat: LAPAN, pp. 98–104. Available at: http://repository.lapan.go.id/index.php?p=show_detail&id=5362.

Gao, M. *et al.* (2016) 'An improved topographic correction model based on Minnaert', *GIScience and Remote Sensing*, 53(2), pp. 247–264. doi: 10.1080/15481603.2015.1118976.

Gao, Y. and Zhang, W. (2009a) 'A simple empirical topographic correction method for ETM + imagery', *International Journal of Remote Sensing*, 30(9), pp. 2259–2275. doi: 10.1080/01431160802549336.

Gao, Y. and Zhang, W. (2009b) 'LULC classification and topographic correction of Landsat-7 ETM+ Imagery in the Yangjia river Watershed: The influence of DEM resolution', *Sensors*, 9(3), pp. 1980–1995. doi: 10.3390/s90301980.

GDAL/OGR contributors (2020) 'GDAL/OGR Geospatial Data Abstraction software Library'. Available at: https://gdal.org.

Ghasemi, N., Mohammadzadeh, A. and Sahebi, M. R. (2011) 'Assessment of different topographic correction methods in ALOS AVNIR-2 data over a forest area', *International Journal of Digital Earth*, 6(5), pp. 504–520. doi: 10.1080/17538947.2011.625049.

Goslee, S. C. (2012) 'Topographic corrections of satellite data for regional monitoring', *Photogrammetric Engineering and Remote Sensing*, 78(9), pp. 973–981. doi: 10.14358/PERS.78.9.973.

Goyal, S. K., Seyfried, M. S. and O'Neill, P. E. (1998) 'Effect of digital elevation model resolution on topographic correction of airborne SAR', *International Journal of Remote Sensing*, 19(16), pp. 3075–3096. doi: 10.1080/014311698214190.

Gu, D. and Gillespie, A. (1998) 'Topographic normalization of Landsat TM images of forest based on subpixel Sun-canopy-sensor geometry', *Remote Sensing of Environment*, 64(2), pp. 166–175. doi: 10.1016/S0034-4257(97)00177-6.

Hantson, S. and Chuvieco, E. (2011) 'Evaluation of different topographic correction methods for landsat imagery', *International Journal of Applied Earth Observation and Geoinformation*, 13(5), pp. 691–700. doi: 10.1016/j.jag.2011.05.001.

Hell, B. and Jakobsson, M. (2011) 'Gridding heterogeneous bathymetric data sets with stacked continuous curvature splines in tension', *Marine Geophysical Research*, 32(4), pp. 493–501. doi: 10.1007/s11001-011-9141-1.

Hlatshwayo, S. T. *et al.* (2019) 'Mapping forest aboveground biomass in the reforested Buffelsdraai landfill site using texture combinations computed from SPOT-6 pan-sharpened imagery', *International Journal of Applied Earth Observation and Geoinformation*, 74(July 2018), pp. 65–77. doi: 10.1016/j.jag.2018.09.005.

Holben, B. N. and Justice, C. O. (1980) 'The Topographic Effect on Spectral Response from Nadir-Pointing Sensors', *Photogrammetric Engineering & Remote Sensing*, 46, pp. 1191–1200. Available at: https://www.asprs.org/wp-content/uploads/pers/1980journal/sep/1980_sep_1191-1200.pdf.

Japan Aerosapce Exploration Agency, E. O. R. C. (1997) 'ALOS Global Digital Surface Model "ALOS World 3D - 30m (AW3D30)" - Product Description', *Japan Aerospace Exploration Agency*. Available at: https://www.eorc.jaxa.jp/ALOS/en/aw3d30/.

Japan Aerospace Exploration Agency (2020) *ALOS Global Digital Surface Model 'ALOS World 3D - 30m (AW3D30)'*. Available at: https://www.eorc.jaxa.jp/ALOS/en/aw3d30/.

Jarvis, A. *et al.* (2008) *Hole-filled seamless SRTM data V4, International Centre for Tropical Agriculture (CIAT)*. Available at: http://srtm.csi.cgiar.org. (Accessed: 10 July 2020).

Julzarika, A. and Durdjani (2019) 'DEM classifications: opportunities and potential of its applications', *J. Degrade. Min. Land Manage*, 6(4), pp. 1897–1905. doi: 10.15243/jdmlm.2019.064.1897.

Julzarika, A. and Harintaka (2019) 'Indonesian DEMNAS: DSM or DTM?', in *AGERS 2019 - 2nd IEEE Asia-Pacific Conference on Geoscience, Electronics and Remote Sensing Technology*. Jakarta, Indonesia, Indonesia: IEEE, pp. 31–36. doi: 10.1109/AGERS48446.2019.9034351.

Justice, C. O., Wharton, S. W. and Holben, B. N. (1981) 'Application of digital terrain data to quantify and reduce the topographic effect on landsat data', *International Journal of Remote Sensing*, 2(3), pp. 213–230. doi: 10.1080/01431168108948358.

Kawata, Y., Ueno, S. and Kusaka, T. (1988) 'Radiometric correction for atmospheric and topographic effects on landsat mss images', *International Journal of Remote Sensing*, 9(4), pp. 1–2. doi: 10.1080/01431168808954889.

Kenyon, S. and Factor, J. (2007) 'Towards The Next Earth Gravitational Model', in *The 77th Annual Meeting of Society of Exploration Geophysicist*. San Antonio, Texas, USA, p. 2. Available at: https://earth-info.nga.mil/GandG/wgs84/gravitymod/new_egm/EGM08_papers/EGM-2007-final.pdf.

Law, K. H. and Nichol, J. (2004) 'Topographic correction for differential illumination effects on ikonos satellite imagery', *XXth ISPRS Congress*, XXXV Part, pp. 641–646. Available at: http://www.cartesia.org/geodoc/isprs2004/comm3/papers/347.pdf.

Leprieur, C. E., Durand, J. M. and Peyron, J. L. (1988) 'Influence of topography on forest reflectance using Landsat Thematic Mapper and digital terrain data', *Photogrammetric Engineering and Remote Sensing*, 54(4), pp. 491–496.

Li, M., Im, J. and Beier, C. (2013) 'Machine learning approaches for forest classification and change analysis using multi-temporal Landsat TM images over Huntington Wildlife Forest', *GIScience and Remote Sensing*, 50(4), pp. 361–384. doi: 10.1080/15481603.2013.819161.

Li, W. *et al.* (2015) 'Geostatistical modeling using LiDAR-derived prior knowledge with SPOT-6 data to estimate temperate forest canopy cover and above-ground biomass via stratified random sampling', *International Journal of Applied Earth Observation and Geoinformation*, 41, pp. 88–98. doi: 10.1016/j.jag.2015.04.020.

Lu, D. *et al.* (2008) 'Pixel-based Minnaert correction method for reducing topographic effects on a landsat 7 ETM+ image', *Photogrammetric Engineering and Remote Sensing*, 74(11), pp. 1343–1350. doi: 10.14358/pers.74.11.1343.

Matthew, M. W. *et al.* (2000) 'Status of atmospheric correction using a MODTRAN4-based algorithm', *Algorithms for Multispectral, Hyperspectral, and Ultraspectral Imagery VI*, 4049, p. 199. doi: 10.1117/12.410341.

Minnaert, M. (1941) 'The reciprocity principle in lunar photometry', *The Astrophysical Journal*, 93(2), pp. 403–410. doi: 10.1086/144279.

Motlagh, M. G. *et al.* (2018) 'Estimating and mapping forest biomass using regression models and Spot-6 images (case study: Hyrcanian forests of north of Iran)', *Environmental Monitoring and Assessment*, 190(6). doi: 10.1007/s10661-018-6725-0.

Nguyen, T. D. and Kappas, M. (2020) 'Estimating the aboveground biomass of an evergreen broadleaf forest in Xuan Lien Nature Reserve, Thanh Hoa, Vietnam, using SPOT-6 data and the random forest algorithm', *International Journal of Forestry Research*, 2020. doi: 10.1155/2020/4216160.

Nichol, J. and Hang, L. K. (2013) 'The Influence of DEM Accuracy on Topographic Correction of Ikonos Satellite Images', *Photogrammetric Engineering & Remote Sensing*, 74(1), pp. 47–53. doi: 10.14358/pers.74.1.47.

Nkwunonwo, U. C., Whitworth, M. and Baily, B. (2020) 'A review of the current status of flood modelling for urban flood risk management in the developing countries', *Scientific African*, 7, p. e00269. doi: 10.1016/j.sciaf.2020.e00269.

Nonin, P. *et al.* (2013) *3D Capabilities of Spot 6*. Available at: http://www.intelligence-airbusds.com/files/pmedia/public/r28533_9_icc2013_3d_capabilities_of_spot_6.pdf.

Park, S. H. *et al.* (2017) 'A quantitative method to evaluate the performance of topographic correction models used to improve land cover identification', *Advances in Space Research*, 60(7), pp. 1488–1503. doi: 10.1016/j.asr.2017.06.054.

Parker, J. a, Kenyon, R. V and Troxel, D. E. (1983) 'Comparison of interpolation methods for image resampling', *IEEE Transactions on Medical Imaging*, 2(1), pp. 31–39. doi: 10.1109/42.7784.

Phiri, D. *et al.* (2018) 'Effects of pre-processing methods on Landsat OLI-8 land cover classification using OBIA and random forests classifier', *International Journal of Applied Earth Observation and Geoinformation*, 73(April), pp. 170–178. doi: 10.1016/j.jag.2018.06.014.

Pimple, U. *et al.* (2017) 'Topographic correction of Landsat TM-5 and Landsat OLI-8 imagery to improve the performance of forest classification in the mountainous terrain of Northeast Thailand', *Sustainability (Switzerland)*, 9(2), pp. 1–26. doi: 10.3390/su9020258.

Rani, M. S. *et al.* (2017) 'The Effect of Topographic Correction on SPOT6 Land Cover Classification in Water Catchment Areas in Bandung Basin, Indonesia', *GISRUK 2017 Proceedings*. Manchester: Geographical Information Science Research UK. Available at: http://eprints.whiterose.ac.uk/115753/.

Reeder, D. H. (2002) *Topographic correction of satellite images: Theory and application*. Dartmouth College.

Riaño, D. *et al.* (2003) 'Assessment of different topographic corrections in landsat-TM data for mapping vegetation types (2003)', *IEEE Transactions on Geoscience and Remote Sensing*, 41(5 PART 1), pp. 1056–1061. doi: 10.1109/TGRS.2003.811693.

Richter, R. (1997) 'Correction of atmospheric and topographic effects for high spatial resolution satellite imagery', *International Journal of Remote Sensing*, 18(5), pp. 1099–1111. doi: 10.1080/014311697218593.

Richter, R., Kellenberger, T. and Kaufmann, H. (2009) 'Comparison of topographic correction methods', *Remote Sensing*, 1(3), pp. 184–196. doi: 10.3390/rs1030184.

Rotta, L. H. S. *et al.* (2016) 'Atmospheric correction assessment of SPOT-6 image and its influence on models to estimate water column transparency in tropical reservoir', *Remote Sensing Applications: Society and Environment*, 4, pp. 158–166. doi: 10.1016/j.rsase.2016.09.001.

Shepherd, J. D. and Dymond, J. R. (2003) 'Correcting satellite imagery for the variance of reflectance and illumination with topography', *International Journal of Remote Sensing*, 24(17), pp. 3503–3514. doi: 10.1080/01431160210154029.

Takaku, J. *et al.* (2016) 'Validation of "Aw3D" Global Dsm Generated From Alos Prism', *ISPRS Annals of Photogrammetry, Remote Sensing and Spatial Information Sciences*, III–4(July), pp. 25–31. doi: 10.5194/isprsannals-III-4-25-2016.

Takaku, J. and Tadono, T. (2017) 'Quality updates of "AW3D" global DSM generated from ALOS PRISM', *2017 IEEE International Geoscience and Remote Sensing Symposium (IGARSS)*, pp. 5666–5669. doi: 10.1109/IGARSS.2017.8128293.

Trisakti, B., Kartasasmita, M. and Kartika, T. (2009) 'Kajian Koreksi Terrain Pada Citra Landsat Thematic Mapper (Tm)', *Jurnal Penginderaan Jauh*, 6, pp. 1–10.

Umarhadi, D. A. and Danoedoro, P. (2019) 'Correcting topographic effect on Landsat-8 images: an evaluation of using different DEMs in Indonesia', (November 2019), p. 41. doi: 10.1117/12.2549109.

Vanonckelen, S. *et al.* (2014) 'Performance of atmospheric and topographic correction methods on Landsat imagery in mountain areas', *International Journal of Remote Sensing*, 35(13), pp. 4952–4972. doi: 10.1080/01431161.2014.933280.

Vanonckelen, S., Lhermitte, S. and Van Rompaey, A. (2013) 'The effect of atmospheric and topographic correction methods on land cover classification accuracy', *International Journal of Applied Earth Observation and Geoinformation*, 24(1), pp. 9–21. doi: 10.1016/j.jag.2013.02.003.

Vázquez-Jiménez, R. *et al.* (2017) 'Topographic Correction to Landsat Imagery through Slope Classification by Applying the SCS + C Method in Mountainous Forest Areas', *ISPRS International Journal of Geo-Information*, 6(9), p. 287. doi: 10.3390/ijgi6090287.

Vincini, M. and Frazzi, E. (2003) 'Multitemporal Evaluation of Topographic Normalization Methods on Decidous Forest TM Data', *IEEE Transactions on Geoscience and Remote Sensing*, 41(11), pp. 2586–2590.

Wessel, B. (2016) *TanDEM-X Ground Segment DEM Products Specification Document*, *Public Document TD-GS-PS-0021*. Available at: https://tandemx-science.dlr.de/ (Accessed: 1 October 2020).

Wu, J. *et al.* (2008) 'A comparison of illumination geometry-based methods for topographic correction of QuickBird images of an undulant area', *ISPRS Journal of Photogrammetry and Remote Sensing*, 63(2), pp. 223–236. doi: 10.1016/j.isprsjprs.2007.08.004.

Wu, Q., Jin, Y. and Fan, H. (2016) 'Evaluating and comparing performances of topographic correction methods based on multi-source DEMs and Landsat-8 OLI data', *International Journal of Remote Sensing*, 37(19), pp. 4712–4730. doi: 10.1080/01431161.2016.1222101.

Zylshal, Z. (2019) 'Performance evaluation of different DEMs for topographic correction on LAPAN-A3: preliminary results', in *Sixth Geoinformation Science Symposium*. SPIE, pp. 159–167. doi: 10.1117/12.2543437.

Zylshal, Z. (2020) 'Topographic Correction of LAPAN-A3/LAPAN-IPB Multispectral Image : a Comparison of Five Different Algorithms', *Quaestiones Geographicae*, 39(3), pp. 33–45. doi: https://doi.org/10.2478/quageo-2020-0021.

ASSESSING THE ACCURACY OF SHALLOW WATER DEPTH ESTIMATION BY USING MULTISPECTRAL SATELLITE IMAGES

Ratna Sari DEWI[1]* , Aldino RIZALDY[1], Prayudha HARTANTO[1] , and Suprajaka SUPRAJAKA[1]

ABSTRACT:
Timely and accurate bathymetry information is needed to support an effective policy on utilization and management of coastal natural resources. Satellite derived bathymetry (SDB) has been widely considered as an advanced and low-cost method for shallow water depth estimation. This is due to the availability of multi-temporal and multi-resolution satellite data. This study focuses on evaluating the accuracy of satellite derived bathymetry derived from multispectral images recorded by various sensors with various spatial resolution. The study area is located in a small island nearby Morotai Island, Indonesia. Four SDB models were compared. The implementation of the SDB model was carried out by combining echo-sounding measurements and the reflectance of blue, green, red, and near infrared bands of three satellite images (World View 2, Sentinel 2A and Landsat 8). Our findings reveal that all three satellite images performed well in assessing SDB at various spatial and spectral resolution, however, the use of high-resolution imagery did not always improve accuracy, for example when using SVM (Support Vector Machine). When using RF (Random Forest), Sentinel 2A produced the best accuracy and when using GAM (Generalized Additive Model), the most feasible result was generated only by using WorldView 2 image. In all cases, RF performed well and provided the most accurate SDB prediction.

Key-words: *Bathymetry, Depth, Satellite-derived bathymetry, Multispectral images, Morotai.*

1. INTRODUCTION

Indonesia as one of the countries with the longest coastline in the world requires an efficient coastal management. In order to support effective policy on utilization and management of coastal natural resources, timely and accurate information such as bathymetry information is needed (Pacheco *et al.*, 2015). Accurate satellite derived bathymetry is considered of fundamental aspect towards monitoring sea floor and deriving nautical charts to support marine navigation. Furthermore, an accurate bathymetry information is necessary to develop shoreline and terrain model, basis data for hydrodynamic modelling, water sediment monitoring, water quality, reconnaissance survey and coral reef monitoring (Hartmann, Wettle and Heege, 2017; Chybicki, 2018).

Remote sensing technology has been widely used to provide shallow water depth information (Brando *et al.*, 2009), because of availability of multi-temporal and multi-resolution satellite data. In addition, remote sensing technique is more efficient in terms of time and budget due to its capability to cover large areas (Cahalane *et al.*, 2019; Kumari and Ramesh, 2020; Zhang *et al.*, 2021). Various methods have been adopted for acquiring shallow water depth information. Conventional methods for i.e., ship-borne echo sounding measurements has restriction in a very shallow area due to safety reason (Pattanaik, Sahu and Bhutiyani, 2015). Meanwhile, LIDAR as an optical remote sensing technique can produce highly accurate measurements. However, LIDAR measurement over an area is also very expensive (Kanno *et al.*, 2013; Kumari and Ramesh, 2020). To overcome those limitation, satellite derived bathymetry (SDB) has been used to estimate the nearshore bathymetry (Philpot, 1989; Stumpf, Holderied and Sinclair, 2003; Kanno *et al.*, 2013; Chénier, Faucher and Ahola, 2018).

---

[1] *Geospatial Information Agency of Indonesia (Badan Informasi Geospasial), *Corresponding Author*
ratna.sari@big.go.id; aldino.rizaldy@big.go.id; prayudha.hartanto@big.go.id; suprajaka@big.go.id

Multiple algorithms have been proposed to develop the SDB models by using single band (Gholamalifard *et al.*, 2013) and multispectral bands (Vinayaraj, Raghavan and Masumoto, 2016; Chénier, Faucher and Ahola, 2018; Sagawa *et al.*, 2019). The SDB algorithms fall into two broad categories: analytical and empirical method. The analytical method works based on the ability of light to penetrate water which requires inputs of various parameters of atmosphere, water column and bottom material (Green *et al.*, 2000). Obtaining the atmosphere and water properties is difficult and requires large samples from field measurement (Gao, 2009). Therefore, the empirical model has become an alternative method since it requires fewer parameters such as training data from echo sounding measurement. The empirical method was implemented based on the relationship between the reflectance of water recorded by sensor and the water depth at sampled locations (Gao, 2009; Hartmann, Wettle and Heege, 2017; Vinayaraj, 2017).

This research focuses on assessing the performance of four SDB algorithms in extracting shallow water depth information by using three different sensors. The methods namely GAM (Generalized Additive Model), MLR (Multiple Linear Regression), SVM (Support Vector Machine) and RF (Random Forest) were tested in small islands located in the southwest of Morotai Island, Indonesia. Three sensors namely: WorldView 2, Sentinel 2A and Landsat 8 OLI/TIRS were used, and several studies have reported the use of each sensors (Chénier, Faucher and Ahola, 2018; Traganos *et al.*, 2018; Sagawa *et al.*, 2019). In this study, comparisons between four SDB techniques as well as accuracy assessments using available bathymetric data were done in order to identify approaches that have the best performance given the environmental conditions of the study site at the time of image acquisition. We used multiple spatial and spectral resolutions to investigate their influences on the accuracy of bathymetry models. Thus, the objectives of this study can be summarized as follows:
   a. To determine the best SDB model for each satellite product through four SDB algorithms.
   b. To compare GAM, MLR, SVM and RF for their SDB prediction accuracies together with the significance of each model's parameter found from objective (a).

2. METHODOLOGY

2.1. Study area

The SDB models were implemented over shallow water area of small islands located in the southwest of Morotai Island, North Moluccas Province, Indonesia (**Fig. 1**). The central point of the study area is at geographical coordinates 2° 7' 30" N and 128° 13' 23" E. The small islands are part of the administrative area of Galo-galo Village. Waters in Galo-galo Village is generally clear with visibility around 10 m (Ismail, 2007). The bottom is composed of sand, seagrass and life coral (Wijaya *et al.*, 2012; S. Halim, 2017).

2.2. Remote sensing dataset

Images used in this study are listed in **Tab. 1**, consisting of WorldView 2, Sentinel 2A and Landsat 8 OLI/TIRS with 2, 10 and 30 m spatial resolution. The WorldView 2 image was obtained from Indonesia Geospatial Information Agency (BIG) in Ortho Ready Standard (OR2A) product. The product is radiometrically corrected and sensor corrected (DigitalGlobe, 2013). Meanwhile, the Sentinel 2A image was in the Level-2A product and obtained from the Copernicus Open Access (ESA et al., 2018). The available product has undergone a standard radiometric and geometric corrections (ESA, 2015). The third image used is Landsat 8 OLI/TIRS which was obtained freely from USGS Earth Explorer (USGS, 2019). For this image, the surface reflectance format was used and a standard radiometric and geometric corrections has been implemented by the provider (USGS, 2015). In addition, for extracting shallow water depth information, four spectral bands were used as in **Tab. 1**. All bands were in visible and near infrared bands.

Fig. 1. Study area in small islands located at the southwest of Morotai Island, North Moluccas Province, Indonesia. Red rectangle shows the study area location. The National Marine Environmental Map is used as the background.

Input images for the SDB model in this study.

Images	Acquisition Date	Resolution (m)	Product format
WorldView 2	March 31st, 2013	2	Ortho Ready Standard
Sentinel 2A	May 21st, 2019	10	Level-2A
Landsat 8 OLI/TIRS	February 20th, 2019	30	Surface Reflectance

2.3. Bathymetry data

For Morotai Island and surroundings, the best data available from the Indonesia Geospatial Information Agency's survey database were multibeam and single beam echosounder surveys completed in August 2018. All datasets were corrected for zero tidal influences by BIG. In this case, the depth measured by echosounder was corrected by adding or subtracting a tidal height which was derived from hourly tide predictions (Bramante, Raju and Sin, 2013; Siermann *et al.*, 2014). These tide prediction data were obtained from the nearest tide gauge station, namely: Jailolo Tide Gauge Station in Halmahera Island, North Moluccas Province. Therefore, for this study, no additional tidal correction is needed as the SDB relationships are based on tide-corrected data. The depth information from the Single Beam Echo Sounder (SBES) ranges from 3 m up to 30 m. **Tab. 2** summarizes the number of measurement points available within 3 m depth ranges.

Table 2.

Number of measurement points within 2 m depth ranges for hydrographic data.

Overall	0–3 m	3–6 m	6–9 m	9–12 m	12–15 m	15–30 m
62,150	N/A	35,007	7,421	4,353	2,490	12,879

In this research, two scenarios were set for the selection of training data to be included in the SDB model. In the first scenario, we selected randomly 20% of training data from the SBES measurements points, and the remaining 80% for the accuracy assessment of the SDB model. Meanwhile, in the second scenario, 80% of training data from the SBES points were selected as training data, and 20% for the accuracy assessment of the SDB model.

2.4. Image pre-processing

2.4.1. Geometric correction

Before the implementation of the SDB algorithm, geo-referencing was implemented to all images. Geo-registration of images (Sentinel-2A and Landsat 8 OLI/TIRS) was conducted using geometrically corrected reference image, namely a WorldView-2 image at 2 m spatial resolution. The spectral band information for each image is available in **Tab. 3**. For each image, we created dataset consists of four bands in blue, green, red, and near infrared bands (visible plus near infrared/NIR bands).

Table 3.

The spectral band information of images used in this research.

| Satellite	Bands	Wavelength (µm)	Satellite	Bands	Wavelength (µm)
WorldView-2	Blue	0.45–0.51	Sentinel 2	Blue	0.49
	Green	0.51–0.58		Green	0.56
	Red	0.58–0.62		Red	0.66
	Near-IR1	0.63–0.69		SWIR	0.66
Landsat 8 OLI/TIRS	Blue	0.45–0.51			
	Green	0.53–0.59			
	Red	0.64–0.67			
	NIR	0.85–0.88			

2.4.2. Image correction

Fig. 2 provides an illustration of spectral reflectance (L_s) in shallow water observed by a sensor consisting of: atmospheric scattering (λ_a), reflection of sea surface (L_r), in-water scattering (L_w), and bottom reflection (L_b) (Kanno, Koibuchi and Isobe, 2011; Vinayaraj, Raghavan and Masumoto, 2016). The recorded spectral reflectance (L_s) is estimated by a function of wavelength as:

$$L_s = L_a + L_r + L_w + L_b \tag{1}$$

In this study, image correction was performed based on the averaged deep water area (Lyzenga, 1981; Spitzer and Dirks, 1987; Gholamalifard *et al.*, 2013) for removal of scattering in the atmosphere and external reflection from water surface. The methods assumed that in deep water, there is no bottom reflectance element in the spectral radiance observed by the sensor. Number of pixels were sampled from deep water and their average radiance value (DN) was then subtracted from all pixels in every band respectively (Green *et al.*, 2000):

$$L = L_i - L_{si} \tag{2}$$

where L_i is the measured reflectance in shallow water for band i and L_{si} is the average reflectance for deep water in band i.
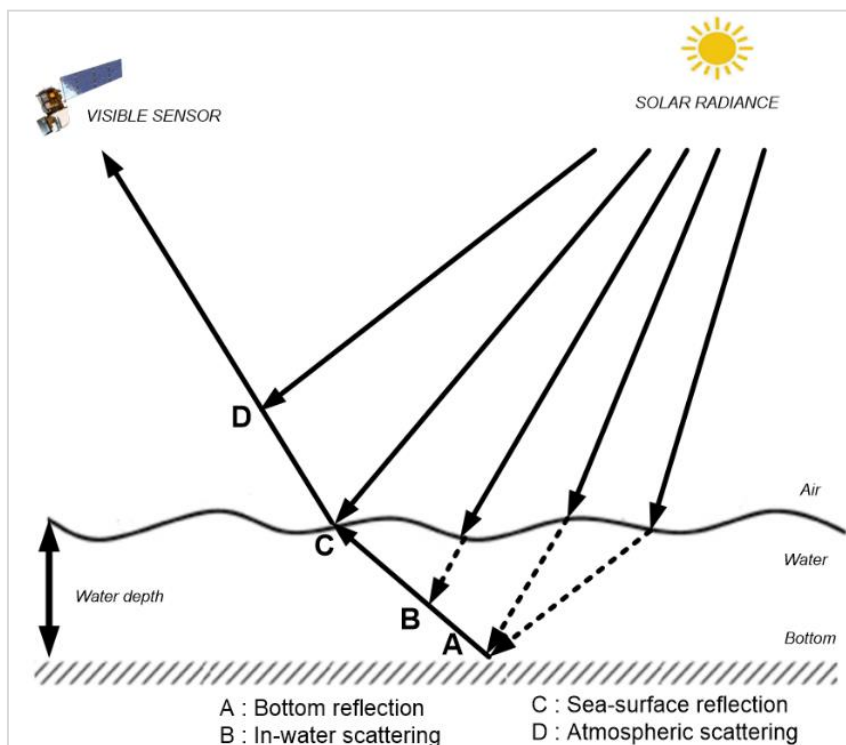
Fig. 2. The visualization of spectral reflectance components recorded by sensor in water area (modified from Kanno, 2011).

2.4.3. Linearize relationship between depth and pixel reflectance

In relatively clear water, light intensity will decline exponentially with the increasing depth. In this step, the value of light intensity (reflectance) were transformed using natural logarithms (ln). The relationship between light intensity and depth becomes linear, and therefore the transformed reflectance values decrease linearly with the increasing depth as written as follows (Green *et al.*, 2000; Gholamalifard *et al.*, 2013):

$$X_i = ln\ (L_i - L_{si}) \tag{3}$$

where X_i is the transformed reflectance values of a pixel in band i, L_{si} is the average reflectance for deep water in band i.

2.5. Modeling of Bathymetry

2.5.1. Semi-parametric regression using spatial coordinates (GAM)

The GAM method is a combination of Lyzenga's method (Lyzenga, 1978) and spatial interpolation method. Kanno (2011) developed the method using semi-parametric regression which models the error term in Lyzenga's method based on its spatial dependency. The formula can be written as (Kanno, Koibuchi and Isobe, 2011):

$$h_z = \mathrm{X}\delta + t(\varphi) + \varepsilon' \tag{4}$$

where X and δ are the Lyzenga's estimators derived from SBES measurements and visible band of images. Meanwhile, $t(\varphi)$ is a smooth nonparametric function of the two-dimensional coordinate vector φ and ε' is a random variable with a zero mean. When solving the equation, a penalized thin-plate regression spline was used. It is included in the 'mgcv' package, specifically the Generalized Additive Model (GAM) smoothing function. This package is available in the R programming language. In addition, we used the smooth term function 's' that was improved using Generalized Cross Validation (GCV) and regression 'splines' with fixed degrees of freedom in this experiment. The definition of this degree of freedom, expressed as k, is a crucial step in adopting the SDB model. According to Wood (2017), the value of k should be neither too large nor too small. We used different k numbers in this experiment, such as 100, 200, 400, 600, 800, and 1000. The RMSE value produced by the model was used to evaluate the results. For further detailed descriptions of this algorithm are available in Wood (2017).

2.5.2. Multiple Linear Regressions (MLR)

Linear regression models the relationship between dependent and independent variables. If there is only one independent variable it is called simple linear regression, while in the case of more than one independent variable it is called multiple linear regression (MLR). The relationships are modeled by linear functions and the parameter are estimated from the data. Due to its simplicity, MLR has been extensively used for predicting bathymetry data in the shallow water area from multi spectral bands of satellite imagery (Clark, Fay and Walker, 1987; Hamilton et al., 1993).

This method assumes that the bottom reflectance and water composition are constant within all part of the image (Van Hengel, 1991). Therefore, this method might work since the bottom reflectance affects multi spectral bands of the imagery. In the case of predicting bathymetry data from multi spectral bands, the dependent variable is the bathymetry depth (W_z) while the independent variables

are the transformed radiance from multi spectral bands (X_n). In order to estimate the parameters of MLR, echo sounding surveys were conducted in the area as the dependent variable W_z. Then the estimated parameters are used to predict the bathymetry depth from the transformed radiance (independent variables). This method is formally described as follow (Van Hengel and Spitzer, 1991):

$$W_z = \beta_0 + \beta_1 X_1 + \beta_2 X_2 + \cdots + \beta_n X_n + \varepsilon \tag{5}$$

where W_z is bathymetry depth, β_0 is the intercept, $\beta_1, \beta_2, \ldots, \beta_n$ are the slopes, n is the number of spectral bands, and ε is the error term. MLR works by estimating β such that ε is minimized.

2.5.3. Support Vector Machine (SVM)

SVM, as one of machine learning algorithm, can do both classification and regressions. In this study, the SVM-based regression was used to model the relation between training data i.e., depth measurement data and the transformed reflectance from satellite images. The accuracy of the SVM-based regression is usually determined by the appropriate selection of kernel and its parameters (Gao, 2015; Misra *et al.*, 2018). From literature, Gao (2009) suggested that the radial basis function (RBF) has a good performance in predicting depth in the Great Lakes. Therefore, in this research, we also applied RBF kernel when performing SVM.

In this study, we determined various values of the smoothing parameter γ, as the parameter of RBF kernel, it controls the shape of the "peaks" and defines the inverse of the influence radius of sample selected as support vectors. In this case low value of γ representing 'far' influence while high values meaning 'close' influence. The SVM model has been implemented in R software by using the package "e1071". For this experiment, we set various λ values (equal to 0.01, 0.1, 1, 10, and 100) and a standard $cost$ parameter of SVM.

2.5.4. Random Forest (RF)

RF, like SVM, is one of machine learning algorithm that can do both classification and regressions (Breiman, 2001). In this research, the RF regression model was used to model the relationship between the water depth data from echo sounding measurement (response variable) and transformed reflectance data from images (predictor variable) (McLaren, McIntyre and Prospere, 2019; Sagawa et al., 2019). The RF model works by creating a random sample from our training data with a similar distribution for all trees and estimating depth based on these tree correlations.

For this study, we used "random Forest" package in R environment. We set a various value for $ntree$ parameter for i.e., 100, 300, 500, 700 and 1000 that represent number of trees to grow for the decision tree estimates. Meanwhile, we keep default values for the other hyperparameters, such as $mtry$ (number of variables randomly sampled as candidates at each split), $sampsize$ (size of sample to draw), $nodesize$ (minimum size of terminal nodes), $maxnodes$ (maximum number of terminal nodes trees in the forest can have).

2.6. Accuracy Assessment of the SDB models

The SDB models were evaluated by estimating the Root Mean Square Error (RMSE) shown in Equation 6. For the accuracy assessment purposes, we used SBES points as testing data based on different scenarios that have been set.

$$RMSE = \sum \sqrt{\frac{(Z_i - Z_i')^2}{N}} \qquad (6)$$

where Z_i is the actual depth value from in-situ measurement data, Z_i' is the expected value of SDB, and N is the number of elements in the data.

3. RESULTS AND DISCUSSIONS

3.1. Generalized adaptive model

Obviously, applying various k values only slightly changed the RMSE values (see **Fig. 3** and **Tab. 4**) both by using 20% and 80% of training data from the SBES measurement points. When using 20% training data, the RMSE values ranged from 2.60 – 2.65 m with R^2 ranged from 0.88 – 0.89 for Landsat 8 OLI/TIRS, 2.44 – 2.46 m with R^2 ranged from 0.893 – 0.894 for Sentinel 2A, and 1.11 – 1.80 m with R^2 ranged from 0.94 – 0.98 for WorldView 2. Meanwhile when increasing the number of training data into 80%, the RMSE values were from 2.60 – 2.65 m with R^2 ranged from 0.878 – 0.884 for Landsat 8 OLI/TIRS, 2.44 – 2.45 m with R^2 ranged from 0.889 – 0.89 for Sentinel 2A, and 1.05 – 1.76 m with R^2 ranged from 0.94 – 0.98 for WorldView 2. In general, the increasing training data ratios only produced little differences in accuracies of the SDB model. Moreover, by using Landsat OLI/TIRS, the increasing training data caused the decreasing of accuracy of the model showing by the decreasing of the R^2 value.

From both results in **Fig. 3**, we can also see that setting higher k did not always provide a better accuracy. Moreover, higher k required a longer processing time to execute the models. The highest accuracy values when using Landsat 8 OLI/TIRS and Sentinel 2A were obtained when setting $k = 200$ while when using WorldView 2, $k = 1000$ provided the best accuracy.

The visualization of those models is available in **Fig. 4**. The SDB models resulted from Landsat 8 and Sentinel 2A were clearly over smoothing comparing to the model resulted from WorldView 2. The experiments revealed that we cannot rely solely on the RMSE values of the predicted result, but it is critical to check the SDB models visually. The experiment concluded that the SDB model by using GAM may be more suitable to be applied for higher resolution image such as WorldView 2 which has 2 m spatial resolution which was supported by the lowest RMSE value obtained (1.054 m).
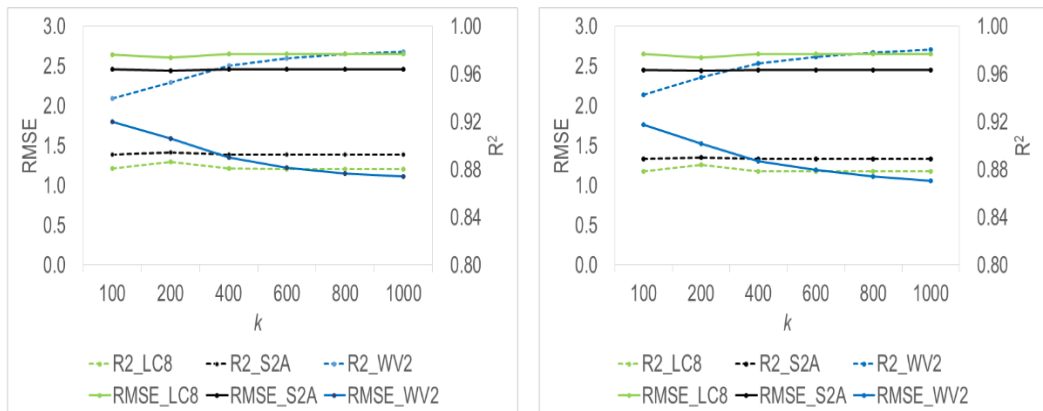

Fig. 3. The RMSE and R^2 values when applying GAM with training data ratio 20% (left) and 80% (right). Dashed-lines show the coefficient correlation values R^2 while solid lines represent RMSE values. Four bands were used by comparing three images from three sensors, namely WV2=Worldview-2, S2A=Sentinel 2A, and LC8=Landsat 8 OLI/TIRS.

Table 4.

The results of accuracy assessment of the SDB model using GAM.

| Datasets	R^2 and RMSE (m)	k					
		100	200	400	600	800	1000
a) Training ratio: 20%							
LC8	R^2	0.88	0.89	0.88	0.88	0.88	0.88
	RMSE	2.64	2.60	2.65	2.65	2.65	2.65
S2A	R^2	0.89	0.89	0.89	0.89	0.89	0.89
	RMSE	2.46	2.44	2.46	2.46	2.46	2.46
WV2	R^2	0.94	0.95	0.97	0.97	0.98	0.98
	RMSE	1.80	1.59	1.34	1.22	1.15	1.11
b) Training ratio: 80%							
LC8	R^2	0.88	0.88	0.88	0.88	0.88	0.88
	RMSE	2.65	2.60	2.65	2.65	2.65	2.65
S2A	R^2	0.89	0.89	0.89	0.89	0.89	0.89
	RMSE	2.45	2.44	2.45	2.45	2.45	2.45
WV2	R^2	0.94	0.96	0.97	0.97	0.98	0.98
	RMSE	1.76	1.52	1.30	1.19	1.11	1.05
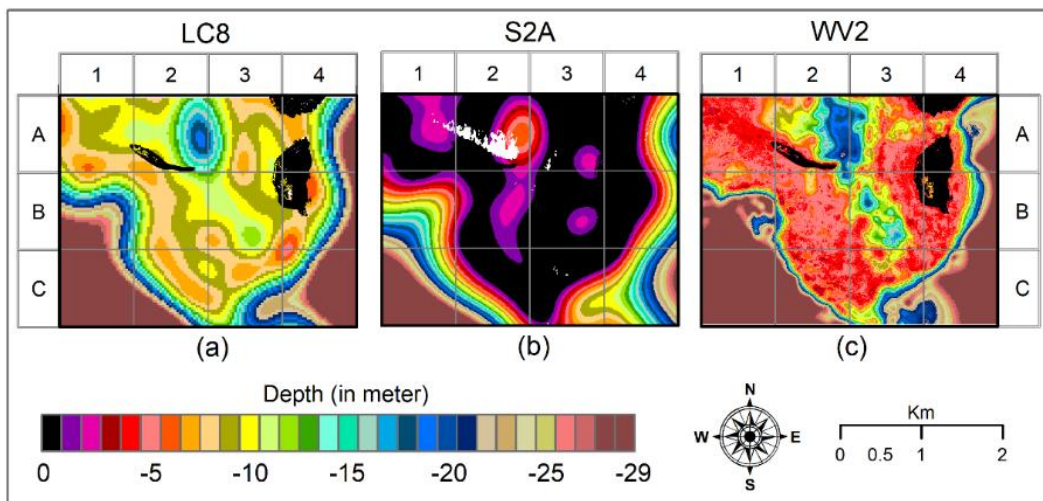
Fig. 4. The visualization of SDB model when applying GAM for: (a) Landsat 8 OLI/TIRS ($k = 200$); (b) Sentinel 2A ($k = 200$); and (c) WorldView 2 ($k = 1000$) images. WorldView 2 presents the best visualization of the results with higher k produced less noisy results. Black pixels represent land area while white pixels indicated no data. For image notations, see the caption of **Fig. 3**.

3.2. Support Vector Machine results interpretation

Setting two training ratios when applying SVM greatly influenced the SDB models as can be seen in **Fig. 5** and **Tab. 5**. When using 20% training data, the RMSE values ranged from 1.59 – 2.96 m with R^2 ranged from 0.86 – 0.96 for Landsat 8 OLI/TIRS, 1.56 – 4.47 m with R^2 ranged from 0.63

– 0.96 for Sentinel 2A, and 1.56 – 5.47 m with R^2 ranged from 0.52 – 0.96 for WorldView 2. Meanwhile when increasing the number of training data into 80%, the RMSE values were from 1.15 – 2.88 m with R^2 ranged from 0.86 – 0.98 for Landsat 8 OLI/TIRS, 1.09 – 2.31 m with R^2 ranged from 0.91 – 0.98 for Sentinel 2A, and 1.470 – 3.80 m with R^2 ranged from 0.77 – 0.96 for WorldView 2. Setting higher proportion of training data resulted in better accuracies of the SDB model. The increasing training data ratios produced large differences in accuracies of the SDB model implying that the SVM was highly dependent on the amount of training data. It is critical to have a large amount of training data. The accuracies of the SDB model obtained in this study, especially when using Sentinel 2A, was worse than the accuracies obtained by the previous study by Mateo-Perez et al., (2020) that was able to achieve RMSE values of 0.3-0.4 m. Meanwhile, Misra et al., (2018) by using Landsat image obtained RMSE values of 2.88 m which was quite similar with our results.
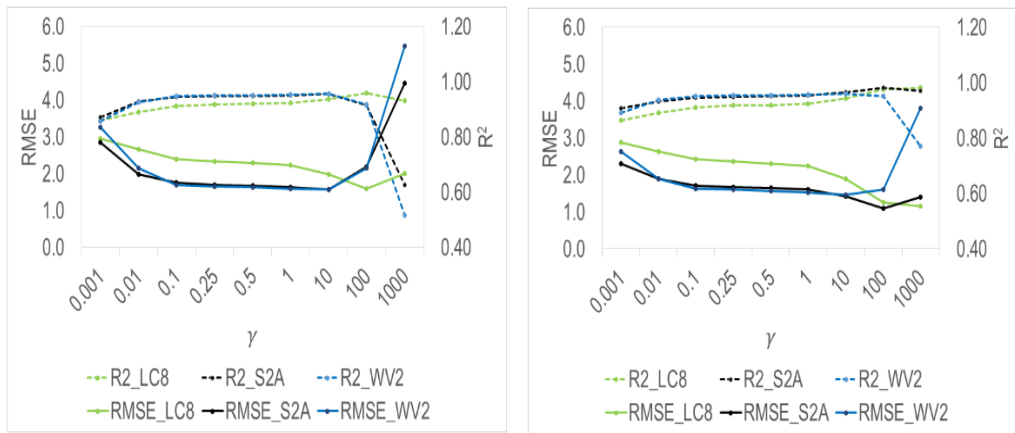

Fig. 5. The RMSE and R^2 values when applying SVM with training data ratio 20% (left) and 80% (right). For image notations, see the caption of **Fig. 3**.

Table 5.

The results of accuracy assessment of the SDB model using SVM

Datasets	R^2 and RMSE (m)	λ								
		0.001	0.01	0.1	0.25	0.5	1	10	100	1000
a) Training ratio: 20%										
LC8	R^2	0.86	0.89	0.91	0.92	0.92	0.92	0.94	0.96	0.93
	RMSE	2.96	2.66	2.40	2.32	2.28	2.23	1.98	1.59	2.01
S2A	R^2	0.87	0.93	0.94	0.95	0.95	0.95	0.96	0.91	0.63
	RMSE	2.85	1.99	1.75	1.70	1.67	1.64	1.56	2.18	4.47
WV2	R^2	0.86	0.92	0.95	0.95	0.95	0.95	0.96	0.92	0.52
	RMSE	3.25	2.14	1.70	1.66	1.64	1.60	1.56	2.15	5.47
b) Training ratio: 80%										
LC8	R^2	0.86	0.89	0.91	0.92	0.92	0.92	0.94	0.98	0.98
	RMSE	2.88	2.63	2.44	2.36	2.31	2.25	1.89	1.26	1.15
S2A	R^2	0.91	0.93	0.95	0.95	0.95	0.95	0.96	0.98	0.97
	RMSE	2.31	1.90	1.71	1.66	1.64	1.61	1.42	1.09	1.41
WV2	R^2	0.89	0.94	0.95	0.95	0.95	0.96	0.96	0.95	0.77
	RMSE	2.63	1.89	1.64	1.61	1.57	1.53	1.47	1.61	3.80

Applying various γ values contributed to changing in the RMSE of the SDB models (see **Fig. 5**) both by using 20% and 80% of training data from the SBES measurement points. From both results in **Fig. 5**, in general, by using Landsat 8 OLI/TIRS, Sentinel 2A and WorldView 2, a lower RMSE value was obtained by increasing γ. When setting 20% training data, the best models were achieved with values of γ equal to 100 and 10 for Landsat OLI/TIRS, and both Sentinel 2A and WorldView, respectively. Meanwhile, by setting training data into 80%, the best SDB models were resulted from γ values equal to 1000, 100 and 10 for Landsat OLI/TIRS, Sentinel 2A and WorldView, respectively. The visualization of those models is available in **Fig. 6**. The SDB model from Landsat 8 OLI/TIRS was clearly noisy while SDB models from Sentinel 2A and WorldView 2 depict a much more representative depth distribution, especially in shallow water area.
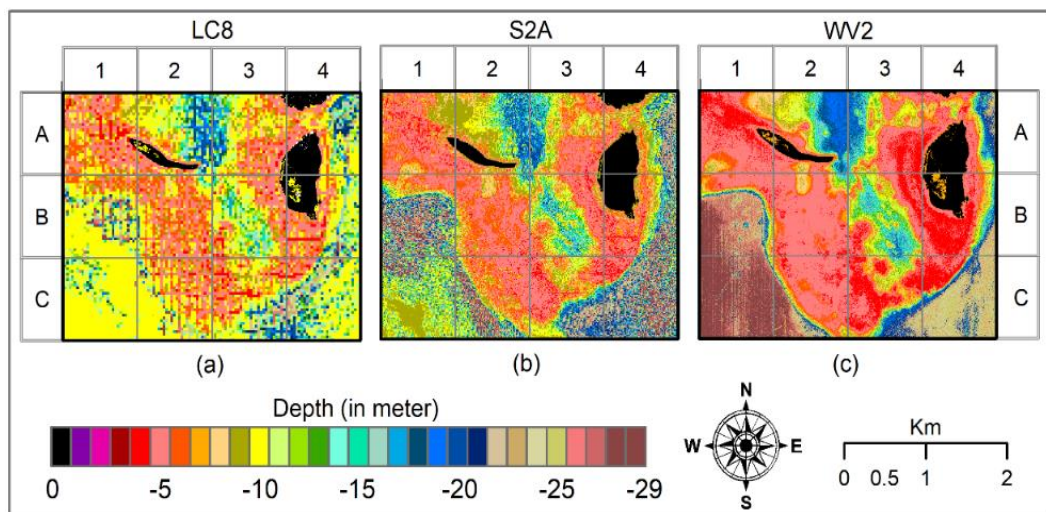
Fig. 6. The visualization of the best SDB model when applying SVM for: (a) Landsat 8 OLI/TIRS ($\gamma = 1000$); (b) Sentinel 2A ($\gamma = 100$); and (c) WorldView 2 ($\gamma = 10$) images. Black pixels represent land area while white pixels indicated no data. For image notations, see the caption of **Fig. 3**.

### 3.3. Multi Linear Regression results interpretation

Applying MLR with various training ratios had little influence on the SDB results. Moreover, increasing training data from 20% to 80% reduced the quality of the SDB model showed by the increase of the RMSE values, except when using WorldView 2. By using WorldView, there was a little decrease of the RMSE from 2.626 to 2.608 m (see **Tab. 6**).

WorldView-2 with 80% training data produced the best accuracy with R^2 equal to 0.871 and RMSE value equal to 2.608. SDB model using Landsat 8 OLI/TIRS outperformed WorldView 2 with RMSE equal to 2.431 and 2.442 m with R^2 equal to 0.888 and 0.886 for 20% and 80% training data, respectively. For this case, a higher image resolution did not result in a better SDB model in terms of RMSE values. When we compared the results obtained from this study with other previous studies, for example when using WorldView 2 datasets, Jawak and Luis (2015) could obtained higher accuracy with RMSE value of 0.21 m. However, in their study, 8 bands of WorldView 2 were included for the implementation of SDB model. In this case, the number and type of bands that were used may have influenced the model accuracy (Manessa *et al.*, 2016).

The validation results obtained by comparing predicted and observed value of depths.
Asterisk notifies the lowest RMSE value.

Datasets	Training Ratio	R^2	RMSE (m)
LC8	20%	0.888	2.431*
	80%	0.886	2.442
S2A	20%	0.858	2.893
	80%	0.853	2.934
WV2	20%	0.869	2.626
	80%	0.871	2.608

Fig. 7 presents the comparisons of the SDB models resulted from MLR applied using three different images showing that MLR were able to represent depth distribution consistently. The variation of training data and the spatial resolution of images did not produce large influences on the predicted SDB results as when using GAM method.
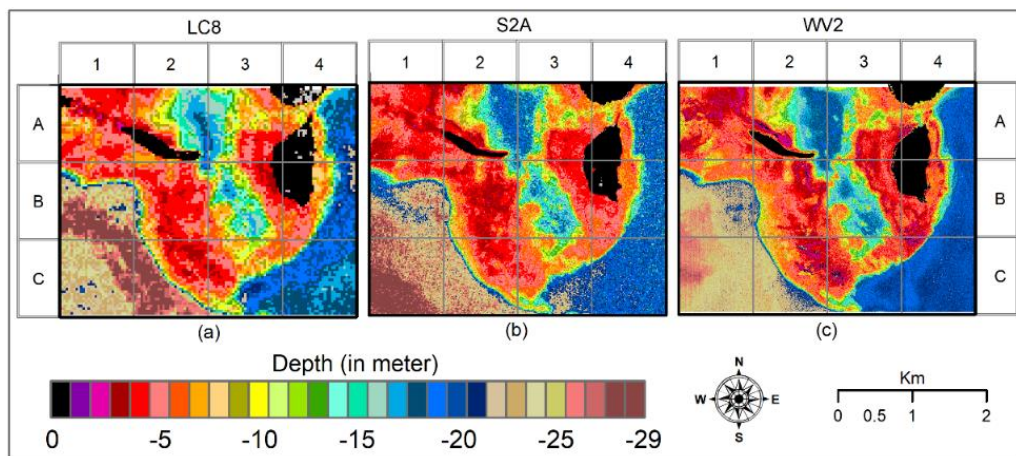
Fig. 7. The visualization of SDB model when applying MLR with 80% of training data for: (a) Landsat 8 OLI/TIRS; (b) Sentinel 2A; and (c) WorldView 2 images. Black pixels represent land area while white pixels indicated no data. For image notations, see the caption of **Fig. 3**.

3.4. Random Forest results interpretation

As SVM, setting two training ratios when applying RF also largely influenced the SDB models as can be seen in **Fig. 8** and **Tab. 7**. When using 20% training data, the RMSE values ranged from 1.097 – 1.099 m with R^2 equal to 0.981 for Landsat 8 OLI/TIRS, 1.265 – 1.272 m with R^2 equal to 0.973 for Sentinel 2A, and 1.442 – 1.456 m with R^2 equal to 0.960 for WorldView 2. Meanwhile when increasing the number of training data into 80%, the RMSE values were 0.934 m with R^2 equal to 0.987 for Landsat 8 OLI/TIRS, 0.667 – 0.670 m with R^2 equal to 0.993 for Sentinel 2A, and 1.204 – 1.210 m with R^2 equal to 0.972 for WorldView 2. Setting higher proportion of training data resulted in better accuracies of the SDB model. The increasing training data ratios produced large differences in accuracies of the SDB model especially for Landsat OLI/TIRS and Sentinel 2A. It was implying that the RF was highly dependent on the amount of training data like SVM and having large amount of training data was important as has been suggested by Sagawa et al., (Sagawa *et al.*, 2019).

    Fig. 8 shows little variation of RMSE values when applying RF by varying the *ntree* values both by using variation in training set ratio. It was implying that variation of *ntree* has little influence on the prediction results. Moreover, applying larger *ntree* values corresponded to the longer time needed for the SDB model.

    The visualization of RF models is available in **Fig. 9**. The SDB model from Landsat 8 OLI/TIRS was a little bit noisy while SDB models from Sentinel 2A and WorldView 2 depict a much more representative depth distribution, especially in shallow water area. Similarly, with MLR method, a higher image resolution did not result in a better SDB model in terms of RMSE values.

Table 7.

The results of accuracy assessment of the SDB model using RF.

| Datasets	R^2 and RMSE (m)	*ntree*				
		100	300	500	700	1000
a) Training ratio: 20%						
LC8	R^2	0.98	0.98	0.98	0.98	0.98
	RMSE	1.10	1.10	1.10	1.10	1.10
S2A	R^2	0.97	0.97	0.97	0.97	0.97
	RMSE	1.27	1.27	1.27	1.27	1.27
WV2	R^2	0.96	0.96	0.96	0.96	0.96
	RMSE	1.46	1.44	1.44	1.44	1.44
b) Training ratio: 80%						
LC8	R^2	0.99	0.99	0.99	0.99	0.99
	RMSE	0.93	0.93	0.93	0.93	0.93
S2A	R^2	0.99	0.99	0.99	0.99	0.99
	RMSE	0.67	0.67	0.67	0.67	0.67
WV2	R^2	0.97	0.97	0.97	0.97	0.97
	RMSE	1.21	1.21	1.21	1.20	1.20

(a)   (b)
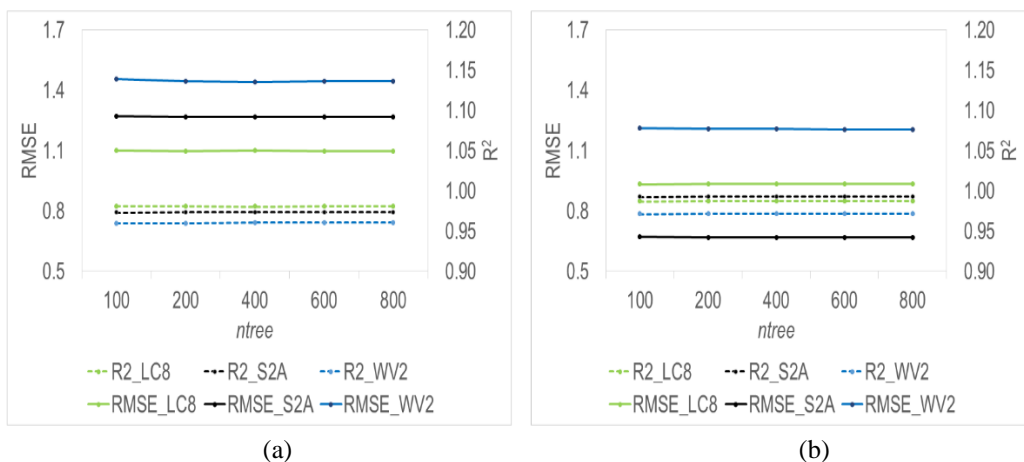
Fig. 8. The RMSE and R^2 values when applying RF with training data ratio 20% (a) and 80% (b). For image notations, see the caption of **Fig. 3**.
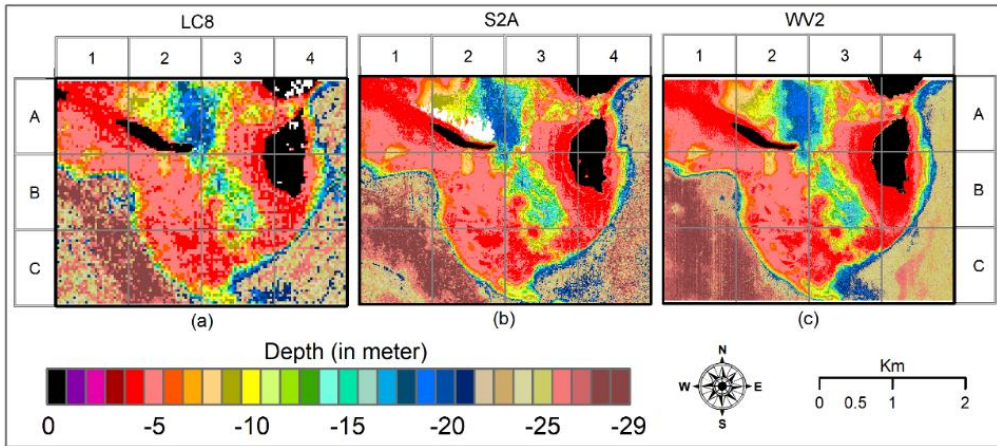
Fig. 9. The visualization of SDB model when applying RF with 80% of training data and $ntree = 500$ for: (a) Landsat 8 OLI/TIRS; (b) Sentinel 2A; and (c) WorldView 2 images. Black pixels represent land area while white pixels indicated no data. For image notations, see the caption of **Fig. 3**.

3.5. Comparison of the Models

A comparison of bathymetric profiles of the four SDB models with combination of multibeam and single-beam measurement data by using three different images is provided in **Fig. 10 - 12**. By using Worldview 2 images (see **Fig. 10**), SDB model from RF had the best fit with the measurement data which was supported by higher accuracies of RF model approximately 1 m (see **Fig. 8b**). In shallow water area of less than 5 m, all the SDB models were also in a good agreement with the measurement data. However, in deeper area from 5-10 m, MLR significantly overestimate the water depth (see **Fig. 8c** and **Fig. 9c** for e. g. gridlines B3, C1 and C2). This was supported by low accuracies given by MLR approximately 2.6 m (see **Tab. 5**). This result was in line with the previous study conducted by Manessa et al., (2016) that RF performed better compared to the MLR.
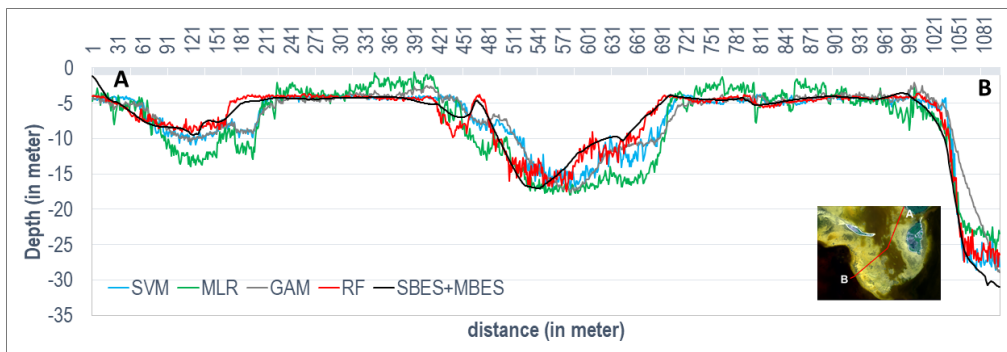

Fig. 10. Transect showing a comparison between the four SDB models and measurement data developed by using WorldView 2. The transects starts from point A to point B.

Fig. 11 presents bathymetry profile of four SDB models by using Sentinel 2A showing that all SDB models except GAM were in a good agreement in shallow water area less than 5 m. GAM model provided a flattened curve shifting away from the other models. **Fig. 4b** shows that large portion of shallow water was predicted as land area (see black pixels). From the profile in **Fig. 11**, RF model obviously had the best fit with the measurement data supported by higher accuracies of RF model approximately 0.67 m (see **Fig. 8b**). Meanwhile, SVM and MLR made errors by producing deeper depth prediction between 5-15 m.
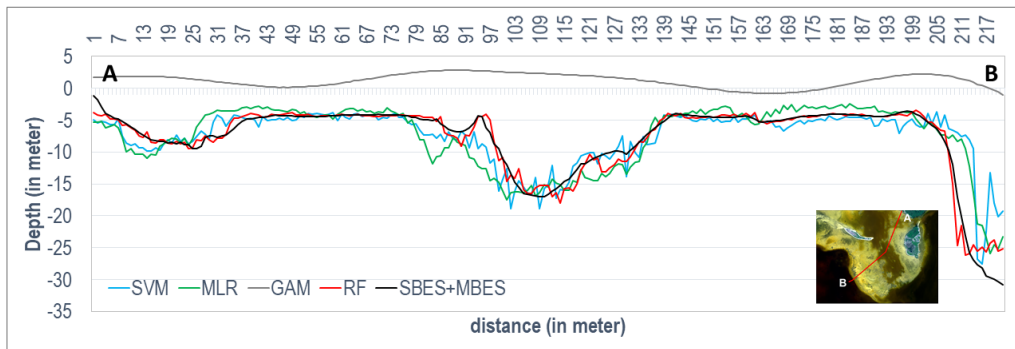
Fig. 11. Transect showing a comparison between the four SDB models and measurement data developed by using Sentinel 2A. The transects starts from point A to point B.

Bathymetric profiles when using Landsat OLI/TIRS image are available in **Fig. 12**. SDB model from RF and MLR fit quite well with the measurement data. It was supported by higher accuracies of RF model approximately 1 m (see **Fig. 8**) and 2.4 m for MLR (see **Tab. 4**). Meanwhile, the bathymetry profiles of SDB model from SVM fluctuated irregularly. GAM model provided a flattened curve shifting away from the other models.
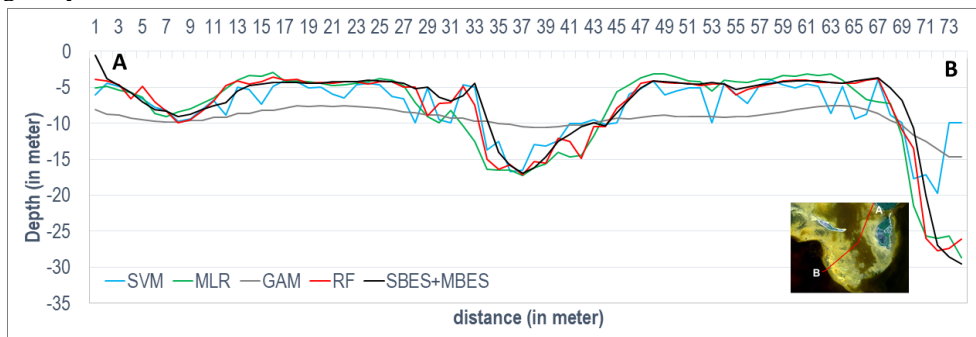
Fig. 12. Transect showing SDB models derived from Sentinel 2A when applying GAM (green), SVM (yellow), MLR (blue) compared to 2018 survey.
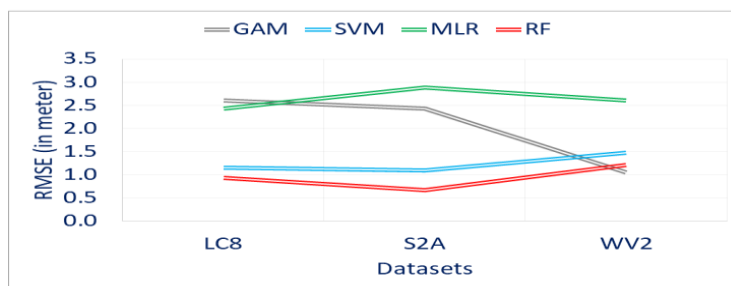
Fig. 13. Accuracy comparisons of the SDB models used by using Landsat OLI/TIRS, Sentinel 2A and WorldView 2.

Fig. 13 shows the performance of each SDB model by using three different images. RF shows consistencies of the best performance. Meanwhile GAM method provided the best accuracy only when using WorldView 2. MLR method provided the largest RMSE errors implying of the most inaccurate model.

4. CONCLUSIONS

In this paper, we compared four methods for satellite derived bathymetry by using three different image resolutions. We also checked the influence of training and testing ratio to the models. In general, by increasing the number of training data, the SDB models obtained higher accuracies. However, when using MLR algorithm with Sentinel 2A and Landsat 8 OLI/TIRS images, increasing the number of training data led to a slight decrease of the accuracies.

Among the four algorithms, SVM and RF were highly influenced by the number of training data used. As also has been mentioned by Sagawa et al., (Sagawa *et al.*, 2019) that a large amount of training data is important for the implementation of machine learning-based SDB algorithm. Not only the amount of the training data but also their coverage is critical. SVM and RF perform poorly when extrapolating beyond the range of the training data set. So it is important to have a slightly wider depth area (Geyman and Maloof, 2019; Sagawa *et al.*, 2019) for the training dataset.

All three satellite imageries provided meaningful results to assess SDB accuracy at various spatial and spectral resolution. However, in this research, the use of high-resolution imagery did not always improve accuracy, for example when using SVM. The accuracy of SVM model by using Landsat 8 OLI/TIRS image was better than the accuracy of SVM model when using Sentinel 2A and World View 2. In addition, when using RF, Sentinel 2A produced the best accuracy. However, when using GAM model, the most feasible result was generated only by using World View 2 image. In all cases, RF performed well and provided the most accurate SDB prediction.

ACKNOWLEDGEMENTS

R E F E R E N C E S

Bramante, J. F., Raju, D. K. and Sin, T. M. (2013) 'Multispectral derivation of bathymetry in Singapore᾽s shallow, turbid waters᾽, *International Journal of Remote Sensing*, 34(6), pp. 2070‒2088. doi: 10.1080/01431161.2012.734934.

Brando, V. E. *et al.* (2009) 'A physics based retrieval and quality assessment of bathymetry from suboptimal hyperspectral data᾽, *Remote Sensing of Environment*, 113(4), pp. 755‒770. doi: 10.1016/j.rse.2008.12.003.

Breiman, L. (2001) 'Random Forests᾽, *Machine Learning*, 45(1), pp. 5‒32. doi: 10.1023/A:1010933404324.

Cahalane, C. *et al.* (2019) 'A comparison of Landsat 8, RapidEye and Pleiades products for improving empirical predictions of satellite-derived bathymetry᾽, *Remote Sensing of Environment*, 233(111414), p. 15. doi: 10.1016/j.rse.2019.111414.

Chénier, R., Faucher, M.-A. and Ahola, R. (2018) 'Satellite-Derived Bathymetry for Improving Canadian Hydrographic Service Charts᾽, *ISPRS International Journal of Geo-Information*, 7(8), p. 306. doi: 10.3390/ijgi7080306.

Chybicki, A. (2018) 'Three-Dimensional Geographically Weighted Inverse Regression (3GWR) Model for Satellite Derived Bathymetry Using Sentinel-2 Observations᾽, *Marine Geodesy*, 41(1), pp. 1‒23. doi: 10.1080/01490419.2017.1373173.

Clark, R. K., Fay, T. H. and Walker, C. L. (1987) 'Bathymetry calculations with Landsat 4 TM imagery under a generalized ratio assumption᾽, *Applied Optics*, 26(19), pp. 4036_1-4038. doi: 10.1364/AO.26.4036_1.

DigitalGlobe (2013) *Base Product Series FAQ*.

ESA (2015) 'SENTINEL-2 User Handbook', *Sentinel-2 User Handbook*.

ESA *et al.* (2018) 'Sentinel-2 Products Specification Document', *Thales Alenia Space*.

Gao, J. (2009) 'Bathymetric mapping by means of remote sensing: methods, accuracy and limitations', *Progress in Physical Geography: Earth and Environment*, 33(1), pp. 103‑116. doi: 10.1177/0309133309105657.

Gao, S. (2015) *Shallow Water Depth Inversion Based on Data Mining Models*. Louisiana State University and Agricultural and Mechanical College. Available at: https://digitalcommons.lsu.edu/gradschool_theses/220.

Geyman, E. C. and Maloof, A. C. (2019) 'A Simple Method for Extracting Water Depth From Multispectral Satellite Imagery in Regions of Variable Bottom Type', *Earth and Space Science*. doi: 10.1029/2018EA000539.

Gholamalifard, M. *et al.* (2013) 'Bathymetric modeling from satellite imagery via Single Band Algorithm (SBA) and Principal Components Analysis (PCA) in Southern Caspian Sea', *International Journal of Environmental Research*, 7(4), pp. 877‑886.

Green, E. P. *et al.* (2000) *Remote Sensing Handbook for Tropical Coastal Management*, *Coastal Management Sourcebooks 3*.

Hamilton, M. K. *et al.* (1993) 'Estimating chlorophyll content and bathymetry of Lake Tahoe using AVIRIS data', *Remote Sensing of Environment*, 44(2‑3), pp. 217‑230.

Hartmann, K., Wettle, M. and Heege, T. (2017) 'The Increasing Importance of Satellite-derived Bathymetry', *GIM International*. Available at: https://www.gim-international.com/content/article/the-increasing-importance-of-satellite-derived-bathymetry#:~:text=Bathymetric data in the shallow,zone management or hydrodynamic modelling.

Van Hengel, W. and Spitzer, D. (1991) 'Multi-temporal water depth mapping by means of Landsat TM', *International Journal of Remote Sensing*, 12(4), pp. 703‑712.

Ismail, M. R. (2007) *Small Islands in North Halmahera Regency (Overview of the Management of Skipjack Fishery Resources)*, *Thesis*. Sekolah Pascasarjana IPB (Bogor Agricultural University). Available at: https://adoc.pub/kajian-pengembangan-wilayah-pulau-pulau-kecil-di-kabupaten-h.html.

Jawak, S. D. and Luis, A. J. (2015) 'Spectral information analysis for the semiautomatic derivation of shallow lake bathymetry using high-resolution multispectral imagery : A case study of Antarctic coastal oasis', *Aquatic Procedia*, 4(Icwrcoe), pp. 1331‑1338. doi: 10.1016/j.aqpro.2015.02.173.

Kanno, A. *et al.* (2013) 'Generalized Lyzenga's Predictor of Shallow Water Depth for Multispectral Satellite Imagery', *Marine Geodesy*, 36(4), pp. 365‑376. doi: 10.1080/01490419.2013.839974.

Kanno, A., Koibuchi, Y. and Isobe, M. (2011) 'Shallow Water Bathymetry from Multispectral Satellite Images: Extensions of Lyzenga's Method for Improving Accuracy', *Coastal Engineering Journal*, 53(4), pp. 431‑450. doi: 10.1142/S0578563411002410.

Kumari, P. and Ramesh, H. (2020) 'Remote sensing image based nearshore bathymetry extraction of Mangaluru coast for planning coastal reservoir', in Sitharam, T. G. et al. (eds) *Sustainable Water Resource Development Using Coastal Reservoirs*. Oxford: Butterworth-Heinemann, pp. 247‑265. doi: https://doi.org/10.1016/B978-0-12-818002-0.00013-7.

Lyzenga, D. R. (1978) 'Passive remote sensing techniques for mapping water depth and bottom features', *Applied Optics*, 17(3), pp. 379‑383. doi: 10.1364/AO.17.000379.

Lyzenga, D. R. (1981) 'Remote sensing of bottom reflectance and water attenuation parameters in shallow water using aircraft and Landsat data (Bahamas).', *International Journal of Remote Sensing*, 2(1), pp. 71‑82.

Manessa, M. D. M. *et al.* (2016) 'Satellite-Derived Bathymetry using Random Forest Algorithm and Worldview-2 Imagery', *Geoplanning: Journal of Geomatics and Planning; Vol 3, No 2 (2016): (October 2016)DO - 10.14710/geoplanning.3.2.117-126*. Available at:

https://ejournal.undip.ac.id/index.php/geoplanning/article/view/12047.

Mateo-Pérez, V. *et al.* (2020) 'Port bathymetry mapping using support vector machine technique and sentinel-2 satellite imagery', *Remote Sensing*. doi: 10.3390/rs12132069.

McLaren, K., McIntyre, K. and Prospere, K. (2019) 'Using the random forest algorithm to integrate hydroacoustic data with satellite images to improve the mapping of shallow nearshore benthic features in a marine protected area in Jamaica', *https://doi.org/10.1080/15481603.2019.1613803*, 56(7), pp. 1065‑1092. doi: 10.1080/15481603.2019.1613803.

Misra, A. *et al.* (2018) 'Shallow water bathymetry mapping using Support Vector Machine (SVM) technique and multispectral imagery', *International Journal of Remote Sensing*, 39(13), pp. 4431‑4450. doi: 10.1080/01431161.2017.1421796.

Pacheco, A. *et al.* (2015) 'Retrieval of nearshore bathymetry from Landsat 8 images: A tool for coastal monitoring in shallow waters', *Remote Sensing of Environment*, 159, pp. 102‑116. doi: 10.1016/j.rse.2014.12.004.

Pattanaik, A., Sahu, K. and Bhutiyani, M. R. (2015) 'Estimation of Shallow Water Bathymetry Using IRS-Multispectral Imagery of Odisha Coast, India', *Aquatic Procedia*, 4, pp. 173‑181. doi: https://doi.org/10.1016/j.aqpro.2015.02.024.

Philpot, W. D. (1989) 'Bathymetric mapping with passive multispectral imagery', *Applied Optics*, 28(8), pp. 1569‑1578. doi: 10.1364/AO.28.001569.

S. Halim, H. (2017) 'Gazing Coastal Ecotourism in Morotai Islands, Indonesia', *Environmental Management and Sustainable Development*. doi: 10.5296/emsd.v6i2.11393.

Sagawa, T. *et al.* (2019) 'Satellite derived bathymetry using machine learning and multi-temporal satellite images', *Remote Sensing*. doi: 10.3390/rs11101155.

Siermann, J. *et al.* (2014) 'Satellite derived Bathymetry and Digital Elevation Models (DEM)', *International Petroleum Technology Conference*. doi: 10.2523/IPTC-17346-MS.

Spitzer, D. and Dirks, R. W. J. (1987) 'Bottom influence on the reflectance of the sea.', *International Journal of Remote Sensing*, 8(3), pp. 279‑290.

Stumpf, R. P., Holderied, K. and Sinclair, M. (2003) 'Determination of water depth with high-resolution satellite imagery over variable bottom types', *Limnology and Oceanography*, 48(1part2), pp. 547‑556. doi: 10.4319/lo.2003.48.1_part_2.0547.

Traganos, D. *et al.* (2018) 'Estimating satellite-derived bathymetry (SDB) with the Google Earth Engine and sentinel-2', *Remote Sensing*. doi: 10.3390/rs10060859.

USGS (2015) 'Landsat 8 (L8) Data Users Handbook', *Earth Resources Observation and Science (EROS) Center*.

USGS (2019) 'EarthExplorer - Home', *U.S. Geological Survey*.

Vinayaraj, P. (2017) 'Development of Algorithms for Near-shore Satellite Derived Bathymetry Using Multispectral Remote Sensing Images', p. 1.

Vinayaraj, P., Raghavan, V. and Masumoto, S. (2016) 'Satellite-Derived Bathymetry using Adaptive Geographically Weighted Regression Model', *Marine Geodesy*, 39(6), pp. 458‑478. doi: 10.1080/01490419.2016.1245227.

Wijaya, S. W. *et al.* (2012) *Pulau Morotai: Sumberdaya Strategis di Kawasan Timur Indonesia*.

Wood, S. N. (2017) *Generalized additive models: An introduction with R, second edition*, *Generalized Additive Models: An Introduction with R, Second Edition*. doi: 10.1201/9781315370279.

Zhang, K. *et al.* (2021) 'Improving Statistical Uncertainty Estimate of Satellite-Derived Bathymetry by Accounting for Depth-Dependent Uncertainty', *IEEE Transactions on Geoscience and Remote Sensing*, pp. 1‑9. doi: 10.1109/TGRS.2021.3069868.

COMPARISON OF DIFFERENT PAN-SHARPENING METHODS APPLIED TO IKONOS IMAGERY

*Emanuele ALCARAS[1]** , *Vincenzo DELLA CORTE[2] , *Giampaolo FERRAIOLI[3] ,
*Elena MARTELLATO[3] , *Pasquale PALUMBO[3] , *Claudio PARENTE[3] ,
*Alessandra ROTUNDI[3]

ABSTRACT :
On board the IKONOS satellite there are sensors operating in the panchromatic and multispectral range: the geometric resolution of the acquired images is higher in the first case (1 m) than in the second one (4 m); on the contrary, panchromatic images have lower spectral resolution than the latter. Pan-sharpening methods allow to reduce the pixel dimensions of the multispectral images to comply with the panchromatic resolution. In this way, it is possible to obtain enhanced detailed data in both geometric and spectral resolution. This work aims to compare the results obtained from the application of eight different pan-sharpening methods, which are totally carried out by using the raster calculator in QGIS: Multiplicative, Simple Mean, Brovey Transformation, Brovey Transformation Fast, Intensity Hue Saturation (IHS), IHS Fast, Gram-Schmidt, and Gram-Schmidt Fast. Each resulting dataset is compared with the original one to evaluate the performance of each method by the following quality indices: Correlation Coefficient (CC), Universal Image Quality Index (UIQI), Relative Average Spectral Error (RASE), Erreur Relative Global Adimensionnelle de Synthèse (ERGAS), Spatial Correlation Coefficient (SCC) and Spatial ERGAS (SERGAS); however, this is a difficult task because the quality of the fused image depends on the considered datasets. Finally, a comparison the various between methods is carried out.

Key-words: *Data fusion, Pan-sharpening, IKONOS, GIS-Application, VHR.*

1. INTRODUCTION

In the last twenty years satellite images with high geometric resolution have found great diffusion in remote sensing applications, such as in data fusion applications (Zhang, 2010). Particularly, data fusion is defined as the combination of data of different kind or source in order to obtain new information (Boulkaboul & Djenouri, 2020), which is referred to as "image fusion" when derived from images. Image fusion is defined as the combination of two or more images, through the use of algorithms, to form a new one synthetizing the characteristics of the inputs (Belgiu & Stein, 2019). If the aim of the image fusion is to inoculate geometric resolution of the panchromatic data (PAN) in each multispectral image (MS_i) preserving its spectral resolution, then it is referred as pan-sharpening (Tomas et al., 2008; Pal et al., 2019).

Usually, image fusion techniques can be classified in three levels: pixel level, feature level and decision level (Abdikan et al., 2014). Among them the most interesting for remote sensing are the pixel level techniques, since they permit the lowest alteration of the input dataset and thus most pan-sharpening methods fall back in this category (Wald & Ranchin, 1997; Zhang, 2004).

---

*Corresponding Author

[1]International PhD Programme "Environment, Resources and Sustainable Development", Department of Science and Technology, Parthenope University of Naples, Centro Direzionale, Isola C4, (80143) Naples, Italy, emanuele.alcaras@uniparthenope.it

[2]IAPS—INAF, Via del Fosso del Cavaliere 100, 00133 Rome, Italy, vincenzo.dellacorte@inaf.it

[3]DIST - Department of Science and Technology, Parthenope University of Naples, Centro Direzionale, Isola C4, (80143) Naples, Italy, giampaolo.ferraioli@uniparthenope.it, elena.martellato@collaboratore.uniparthenope.it, pasquale.palumbo@uniparthenope.it, claudio.parente@uniparthenope.it, rotundi@uniparthenope.it

Pixel level techniques can be either divided in three further categories: colour-related methods, statistics methods and numerical methods (Pohl & van Genderen, 1998). Intensity Hue Saturation (IHS) and IHS Fast (IHSF) methods belong to the first class, Gram-Schmidt (GS) and Gram-Schmidt Fast (GSF) belong to the second class, and Simple-Mean (SM), Multiplicative (MLT), Brovey Transformation (BT), Brovey Transofrmation Fast (BTF), which include arithmetic operations such as sum or multiplication between images, belong to the third class (Ehlers et al., 2010).

The results need to be analysed and compared to evaluate the performance of each technique; in order to achieve this scope several studies have been conducted so far (Du et al., 2007; Yuhendra & Kuze, 2011; Choi et al., 2019). Since no reference multispectral image with the same resolution of the fused image exist, it is difficult to define the accuracy of the pan-sharpening application (Parente & Pepe, 2017). Therefore, several methods and indices have been suggested and still under evaluation for the technique performance review (Meng et al., 2019). Among the most diffused indices for assessing pan-sharpening efficiency some can be categorized as spectral index, such as the Correlation Coefficient (CC), Universal Image Quality Index (UIQI), Relative Average Spectral Error (RASE), Erreur Relative Globale Adimensionalle de Synthèse (ERGAS), and some as spatial index, such as the Spatial Correlation Coefficient (SCC) and the spatial ERGAS (SERGAS). The first group remarks the spectral difference introduced by the pan-sharpening between the fused image and the initial MS image (Shahdoosti & Ghassemian, 2014). The second group remarks the conservation level of the spatial details assured by the pan-sharpening in terms of similarity between the object contours in the fused image and the corresponding one in the panchromatic image (Alcaras et al, 2021). Pan-sharpening techniques can be applied in many fields such as cultural heritage preservation (Baiocchi et al., 2017), shadow detection (Meneghini & Parente, 2015), vegetation mapping (Ibarrola-Ulzurrun et al., 2017), urban development (Hu et al., 2015), coastline evolution (Maglione et al., 2015), etc.

In this study, IKONOS imagery are considered and briefly introduced in the first section; next, eight methods, used to apply pan-sharpening to the original dataset, are explained; consequentially, evaluation indices are applied to the pan-sharpened images and discussed; finally, conclusions are provided in order to remark the importance of the work. All the operations have been carried out in QGIS.

2. DATASET

In this work image fusion techniques are performed on IKONOS imagery.

IKONOS was a commercial high-resolution imaging satellite of DigitalGlobe, launched on September 24, 1999, and retired in 2015. It was equipped with two sensors, which acquired images in panchromatic band with a resolution of 0.8 m (nadir), with a nominal Ground Sampling Distance (GSD)of 1 m, and in multispectral bands with a radiometric resolution of 11 bit and a spatial resolution of 3.2 m (nadir), nominal GSD of 4 m (Amato et al., 2004; DigitalGlobe, 2019).

Table 1 synthetizes the characteristics of IKONOS images (ESA, IKONOS Product Guide, 2006).

Table 1.

Band range of IKONOS satellite imagery.

IKONOS		
Bands	**Wavelength Range (µm)**	**Geometric Resolution (m)**
Panchromatic	0.526 - 0.929	1
Band 1 - Blue	0.445 - 0.516	4
Band 2 - Green	0.506 - 0.595	4
Band 3 - Red	0.632 - 0.698	4
Band 4 - Near Infrared	0.757 - 0.853	4

For this study, an IKONONS scene acquired on 18/01/2005 at 04:23 GMT is selected. The scene concerns a coastal area in the north of Indonesia as shown in **Fig. 1**.
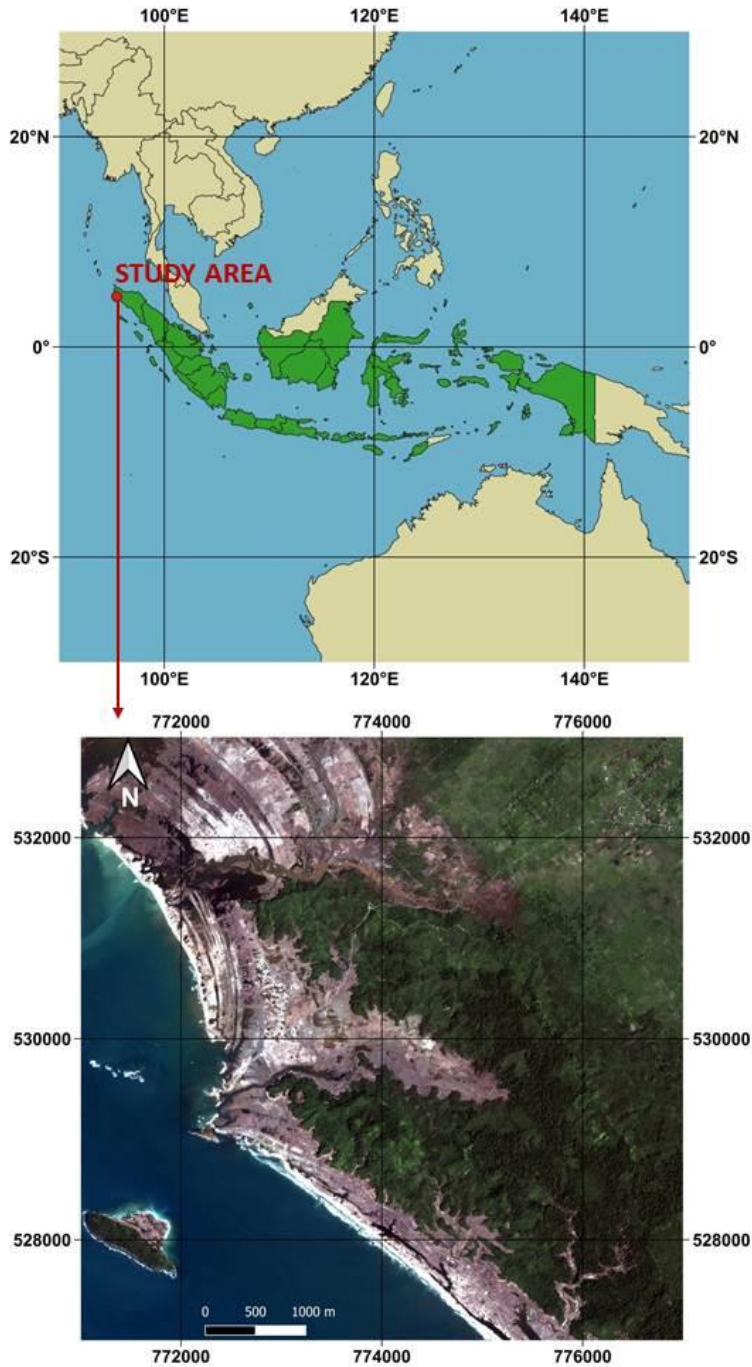
Fig. 1. The location of the study area relatively to Indonesia (*upper*) and RGB true colour composition, obtained with bands 3,2,1, of the considered IKONOS scene (*lower*).

The study area has an extension of 36 km^2 (6 km x 6 km). Particularly, this area extends within the following UTM/WGS84 plane coordinates – 46 zone in the north hemisphere: $E_1 = 771,000$ m, $E_2 = 777,000$ m, $N_1 = 527,000$ m, $N_2 = 533,000$ m.

3. METHODOLOGY

For our performance analysis eight pan-sharpening methods are applied to the IKONOS dataset to achieve the image fusion. The outputs of pan-sharpening application are therefore evaluated by means of spectral indicators (CC, UIQI, RASE, ERGAS) and spatial indicators (SCC, SERGAS). The operations are totally carried out by using the raster calculator tool in QGIS, version 3.16.1 (QGIS, Working with Raster Data, 2020).

3.1. Pan-sharpening Methods

The pan-sharpening methods here considered have been widely used in the image-fusion field and they are described in the following subsections.

3.1.1. Multiplicative (MLT)

The i-th pan-sharpened image (MS_i') is obtained from the following formula:

$$MS_i' = \frac{PAN}{\mu_{PAN}} MS_i \tag{1}$$

where μ_{PAN} is the mean reflectance value of the panchromatic image (PAN) (Crippen, 1987).

3.1.2. Simple Mean (SM)

This method applies a simple arithmetic mean between the i-th multispectral image and the panchromatic image (ESRI, Fundamentals of panchromatic sharpening, 2020). The i-th pan-sharpened image is given by:

$$MS_i' = \frac{PAN + MS_i}{2} \tag{2}$$

3.1.3. Intensity Hue Saturation (IHS)

This pan-sharpening method is based on a RGB colour model to Intensity – Hue – Saturation (IHS) model transformation. The IHS method was introduced by Carper et al. (Carper et al., 1990), and furtherly extended by Tu et al. (Tu et al., 2001) by including the near-infrared (NIR) band into the intensity component. In particular, given *N* multispectral bands, Intensity (I) can be computed as a synthetic band, given by the following formula:

$$I = \frac{\sum_{i=1}^{N} MS_i}{N} \tag{3}$$

3.1.4. IHS Fast (IHSF)

A variation of IHS method can be achieved if specific weights are introduced for each MS_i (Tu et al., 2004):

$$I = \frac{\sum_{i=1}^{N} w_i MS_i}{\sum_{i=1}^{N} w_i} \tag{4}$$

where w_i are the weights.

For IKONOS images the weights are typically 0.08 for Blue, 0.25 for Green, 0.33 for Red and 0.33 for NIR (Aiazzi et al., 2007), and they can be also estimated from the spectral response in **Fig. 2**.
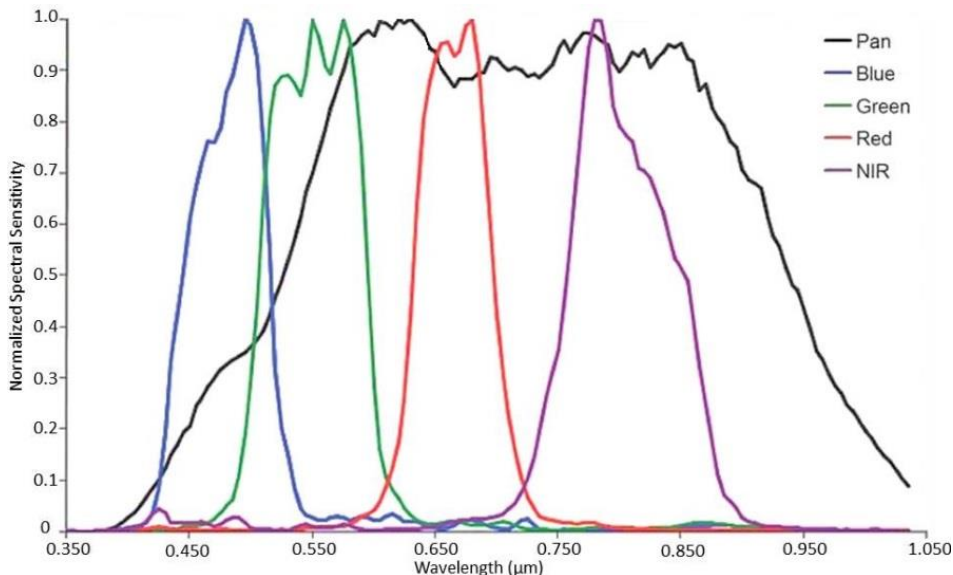
Fig. 2. Spectral response of the IKONOS MS and PAN sensors.

3.1.5. Brovey Transformation (BT)

The Brovey pan-sharpened image can be computed as described by Pohl and van Genderen (Pohl & van Genderen 1998):

$$MS_i' = \frac{PAN}{\frac{1}{N}\sum_{i=1}^{N} MS_i} MS_i \tag{5}$$

3.1.6. Brovey Transformation Fast (BTF)

As for the IHSF method, the same weights can be introduced in for BT:

$$MS_i^i = \frac{PAN}{\sum_{i=1}^{N} w_i\, MS_i} MS_i \sum_{i=1}^{N} w_i \tag{6}$$

3.1.7. Gram-Schmidt (GS)

In the Gram-Schmidt method the pan-sharpened image can be achieved through the subsequent steps:
- Creation of a lower resolution panchromatic image, which is called Simulated panchromatic (S) as the linear combination of the N MS_i bands;
- Application of the Gram-Schmidt orthogonalization starting from S, which is employed as the first band of the transformation;
- Once all the bands are de-correlated, S can be substituted by the high-resolution panchromatic image and the inverse Gram-Schmidt transformation is applied to obtain the pan-sharpened images (Laben & Brower, 2000).

Ultimately, the pan-sharpened image is given by:

$$MS_i' = MS_i + g_i(PAN - S) \tag{7}$$

where, g_i is called gain and is given by:

$$g_i = \frac{cov(MS_i, S)}{var(S)} \tag{8}$$

where $cov(MS_i, S)$ is the covariance between the initial i-th multispectral image and the low resolution panchromatic image; $var(S)$ is S variance.

3.1.8. Gram-Schmidt Fast (GSF)

As in formulas (4) and (6), weights can also be introduced in this method (Maurer, 2013), and S will be obtained as follow:

$$S = \sum_{i=1}^{N} w_i MS_i \tag{9}$$

3.2. Pan-sharpening evaluation

The performance of each method is now evaluated by comparing the original image with the corresponding pan-sharpened image. However, this evaluation is a difficult task: even if the performance of some methods is limited, the quality of the pan-sharpening method cannot be established in an absolute way because it also depends on the considered datasets (Snehmani et al., 2017). As a consequence, different methods are initially applied, and the final image is then the most performant among the resulting pan-sharpened images.

The evaluation task can be carried out in terms of visual, spectral and spatial quality analysis. A visual inspection of the resulting images allows to assess the capability of the method to preserve the colour and to improve the spatial resolution of the represented object (Wang & Bovik, 2002). Spectral analysis, based on appositive indices, is required to establish the spectral similarity between MS and the corresponding MS'. Spatial analysis, also based on appositive indices, is useful to derive the similarities between the shape of the objects included in the MS' and the corresponding one in the PAN (Alcaras et al., 2021).

A brief description of each quality index and spatial index used in this application is reported below.

- *Correlation Coefficient (CC)*

Correlation between two bands is measured, particularly the original image (x) and corresponding pan-sharpened image (y) are compared. CC is given by the following formula (Meng et al., 2016):

$$CC = \frac{\sigma_{xy}}{\sigma_x \sigma_y} \tag{10}$$

where, σ_{xy} is the covariance between x and y images, σ_x and σ_y are the standard deviation of x and y images, respectovely. The closer to 1 is CC the more correlated are x and y (Vijayaraj et al., 2004).

- *Universal Image Quality Index (UIQI)*

It is a product of three components, given by the following formula:

$$UIQI = \frac{\sigma_{xy}}{\sigma_x \sigma_y} \cdot \frac{2\mu_x \mu_y}{\mu_x^2 + \mu_y^2} \cdot \frac{2\sigma_x \sigma_y}{\sigma_x^2 + \sigma_y^2} \tag{11}$$

where μ_x and μ_y are the mean values of x and y images, respectively (Wang & Bovik, 2002). The first component is CC; the second component takes into account the shift of the mean values between x and y; the third component evaluates the similarity of the contrast between the x and y. The closer to 1 is UIQI the more correlated are x and y (Nikolakopoulos & Oikonomidis, 2015).

- *Relative Average Spectral Error (RASE)*

This index includes all the N bands in the formula:

$$RASE = \frac{100}{M} \sqrt{\frac{1}{N} \sum_{i=1}^{N} (RMSE_i)^2} \tag{12}$$

where, M is the mean value of Digital Numbers of the N input images; $RMSE_i$ is the root mean square error between the original i-th image and the corresponding i-th fused image (Ranchin & Wald, 2000). The littler the index the better the quality of the image fusion is.

- *Erreur Relative Globale Adimensionalle de Synthèse (ERGAS)*

It quantifies the spectral quality of the fused images with the following formula:

$$ERGAS = 100 \frac{h}{l} \sqrt{\frac{1}{N} \sum_{i=1}^{N} \left(\frac{RMSE_i}{\mu_i}\right)^2} \tag{13}$$

where, h is PAN spatial resolution; l is MS_i spatial resolution; μ_i is the mean radiance value of the i-th band (Wald, 2000). The littler the index the better the quality of the image fusion.

- *Spatial Correlation Coefficient (SCC)*

Similarly, to CC, SCC measures the correlation between two bands, which are the panchromatic (p) and the fused images (y), obtaining better results when the values are close to one (Li et al., 2002):

$$SCC = \frac{\sigma_{py}}{\sigma_p \sigma_y} \tag{14}$$

where, σ_{py} is the covariance between p and y images, σ_p and σ_y are the standard deviation of p and y images, respectively.

- *Spatial ERGAS (SERGAS)*

To quantify the spatial quality of the fused images, ERGAS can be modified by substituting the RMSE with the spatial RMSE (SRMSE):

$$SERGAS = 100 \frac{h}{l} \sqrt{\frac{1}{N} \sum_{i=1}^{N} \left(\frac{SRMSE_i}{\mu_i}\right)^2} \tag{15}$$

where $SRMSE_i$ is the root mean square error between PAN image and the corresponding i-th fused image (Lillo-Saavedra et al., 2005).

4. RESULTS AND DISCUSSIONS

To show the results of image fusion operations computed by QGIS Raster Calculator, a detail of the study area is selected (**Fig. 3**). The fused images and original bands are compared and shown in the detailed scene RGB compositions in **Fig. 4**.

Fig. 3. The red square, in the left image, represents the chosen detail area, reported in the right image.
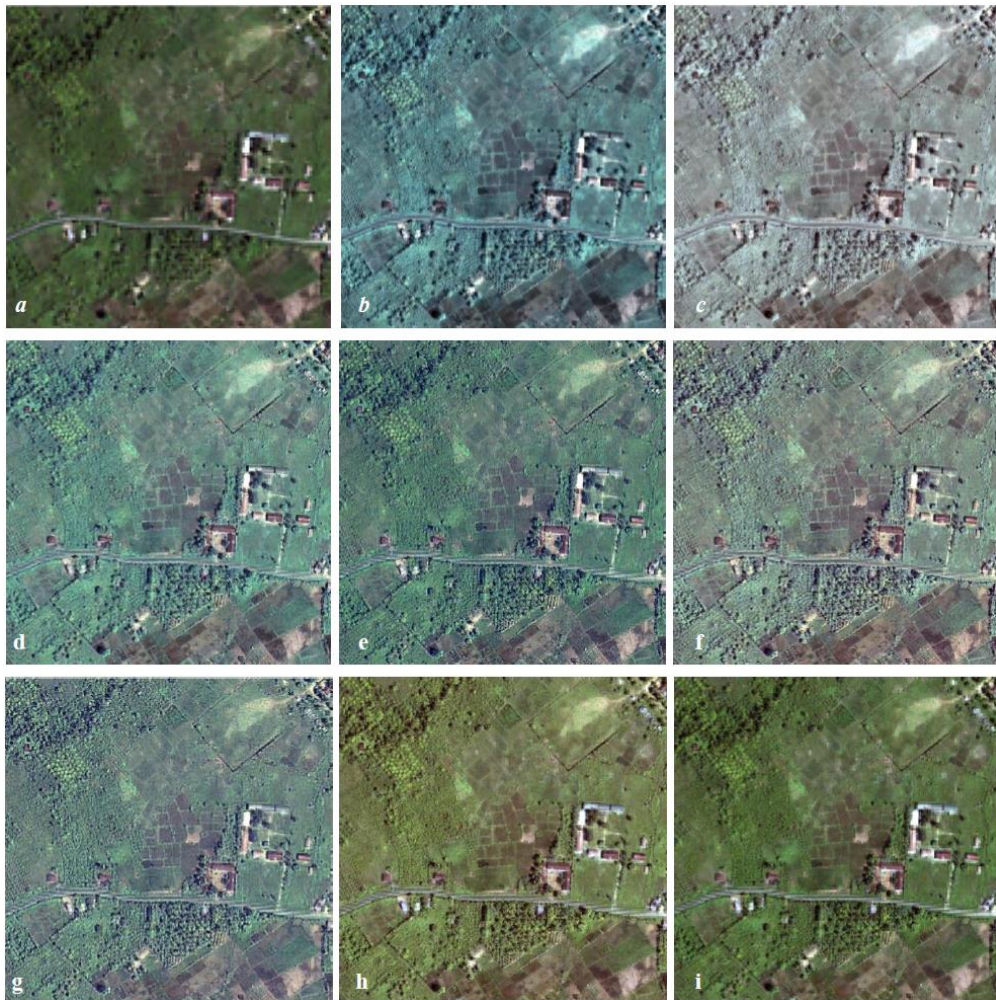
Fig. 4. RGB composition of the original images (a) and RGB compositions of the images derived by the following methods: (b) MLT, (c) SM, (d) BT, (e) BTF, (f) IHS, (g) IHSF, (h) GS and (i) GSF.

In most cases, the colours given by the RGB compositions look natural or simile natural, except for Multiplicative and Simple Mean methods.

The results of the quality evaluation process of the pan-sharpening techniques are reported below, including the values of the adopted indices in the following order: CC (**Tab 2**), UIQI (**Tab. 3**), RASE (**Tab. 4**), ERGAS (**Tab. 5**), SCC (**Tab. 6**) and SERGAS (**Tab. 7**). Particularly, for CC, UIQI and SCC, mean values for each method are provided in the last row.

Table 2.

CC values for pan-sharpened images.

CC								
Bands	**MLT**	**SM**	**BT**	**BTF**	**IHS**	**IHSF**	**GS**	**GSF**
Blue	0.649	0.517	0.512	0.657	0.487	0.597	0.945	0.980
Green	0.829	0.756	0.759	0.824	0.751	0.796	0.768	0.958
Red	0.897	0.829	0.930	0.945	0.844	0.873	0.894	0.955
NIR	0.949	0.989	0.964	0.962	0.990	0.988	0.951	0.944
Mean	0.831	0.773	0.791	0.847	0.768	0.813	0.889	**0.959**

Table 3.

UIQI values for pan-sharpened images.

UIQI								
Bands	**MLT**	**SM**	**BT**	**BTF**	**IHS**	**IHSF**	**GS**	**GSF**
Blue	0.345	0.483	0.484	0.648	0.466	0.583	0.944	0.980
Green	0.517	0.751	0.743	0.821	0.740	0.794	0.753	0.958
Red	0.708	0.809	0.928	0.942	0.835	0.870	0.890	0.954
NIR	0.819	0.920	0.949	0.960	0.981	0.986	0.902	0.934
Mean	0.597	0.741	0.776	0.843	0.755	0.808	0.872	**0.956**

Table 4.

RASE values for pan-sharpened images.

RASE							
MLT	**SM**	**BT**	**BTF**	**IHS**	**IHSF**	**GS**	**GSF**
52.781	27.737	24.825	20.531	21.939	**18.880**	28.450	20.756

Table 5.

ERGAS values for pan-sharpened images.

ERGAS							
MLT	**SM**	**BT**	**BTF**	**IHS**	**IHSF**	**GS**	**GSF**
14.644	7.144	5.633	4.571	5.968	5.072	5.787	**4.005**

Table 6.

SCC values for pan-sharpened images.

SCC								
Bands	MLT	SM	BT	BTF	IHS	IHSF	GS	GSF
Blue	0.842	0.943	0.867	0.634	0.814	0.530	0.447	0.282
Green	0.804	0.919	0.873	0.730	0.852	0.681	0.635	0.571
Red	0.697	0.900	0.734	0.658	0.832	0.705	0.789	0.640
NIR	0.922	0.932	0.901	0.912	0.895	0.897	0.908	0.908
Mean	0.816	**0.924**	0.844	0.733	0.848	0.703	0.695	0.600

Table 7.

SERGAS values for pan-sharpened images.

SERGAS							
MLT	SM	BT	BTF	IHS	IHSF	GS	GSF
18.286	**7.144**	12.966	13.220	12.186	13.232	13.878	13.844

Tables from 2 to 5 report values of indices assessing the spectral quality of the pan-sharpened images.

Considering results by CC (**Tab. 2**), GSF is the most performing method, while IHS presents the lowest value. Considering results by UIQI (**Tab. 3**), GSF is still the most performing method, MLT is the worst performing. Considering results by RASE (**Tab. 4**), this is the only case in which GSF is not the most performing method since it is overridden by IHSF (most performing) and BTF; MLT is still the worst performing method. Considering results by ERGAS (**Tab. 5**), GSF is again the most performing method, while MLT is once more the worst performing one.

By considering the only spectral indicators, we can observe that GSF is the best method among the eight considered ones, BTF also gives a good response (it always falls in the top three methods), while MLT and SM are the worst methods in most cases.

It is also clear that the "fast" methods, so the ones using the weights, are better performant than the respective not weighted ones, in accordance with what found also by other authors (Fasbender et al., 2008; Amro et al., 2011; Maglione et al., 2016).

Tables 6 and 7 report values of indices assessing the spatial quality of the pan-sharpened images.

Considering results by SCC (**Tab. 6**), SM shows higher values, being the only method with a mean value of SCC above 0.900, while GS and GSF performances are quite low. Considering results by SERGAS (**Tab. 7**), SM is once again the most performing method by far while MLT provides inaccurate results. From the comparison of the values obtained in **Tables 6 and 7**, we found that SM is the most performing method if the only spatial quality is considered, followed by IHS and BT. The "fast" methods performances are always lower than the corresponding non-weighted methods.

The experiment results confirm that the choice of the best method is a challenging and non-univoque task, and it depends on the needs of the user. For consequence, as reported in Alcaras et al., (2021), a multi-criteria analysis can be carried out to choose the most suitable method depending on the situation.

5. CONCLUSIONS

Starting from an IKONOS imagery dataset, in this paper eight different pan-sharpening methods are evaluated. Since the IKONOS imagery dataset provides five images (four multispectral images and one panchromatic image), by applying eight pan-sharpening methods, a total of thirty-two new images are obtained. The investigated algorithms are: SM, MLT, IHS, IHSF, BT, BTF, GS and GSF.

Once the outputs are available, each method is tested by comparing the fused images with the initial dataset. In order to evaluate each method 6 different indices are used: CC, UIQI, RASE, ERGAS, SCC and SERGAS. In this way a comparison between different algorithms is possible.

Two methods, which are SM and especially MLT, produce high radiometric distortions on the output. For the other six methods a distinction could be made between the no-weighted and weighted methods: the latter always provide better results in terms of spectral fidelity, and among the three weighted methods, GSF results the most performing one, followed by BTF.

On the other hand, by assessing spatial quality of the fusion products, the performances of the methods behave reversely: SM is the best method and the fast methods do not provide good results.

Evaluating the quality of pan-sharpening products can be a challenging matter, so it is important to use all visual, spectral and spatial quality analyses, to find the better product that meets the user needs.

REFERENCES

Abdikan, S., Balik Sanli, F., Sunar, F., & Ehlers, M. (2014). A comparative data-fusion analysis of multi-sensor satellite images. *International Journal of Digital Earth*, *7*(8), 671-687. https://doi.org/10.1080/17538947.2012.748846

Aiazzi, B., Baronti, S., & Selva, M. (2007). Improving component substitution pansharpening through multivariate regression of MS $+$ $ Pan data. *IEEE Transactions on Geoscience and Remote Sensing*, *45*(10), 3230-3239. https://doi.org/10.1109/TGRS.2007.901007

Alcaras, E., Parente, C., & Vallario, A. (2021). Automation of Pan-Sharpening Methods for Pléiades Images Using GIS Basic Functions. *Remote Sensing*, 13(8), 1550. https://doi.org/10.3390/rs13081550

Amato, R., Dardanelli, G., Emmolo, D., Franco, V., Brutto, M. L., Midulla, P., ... & Villa, B. (2004). Digital orthophotos at a scale of 1: 5000 from high resolution satellite images. *ISPRS Journal of Photogrammetry & Remote Sensing*, 35, 593-598.

Amro, I., Mateos, J., Vega, M., Molina, R., & Katsaggelos, A. K. (2011). A survey of classical methods and new trends in pansharpening of multispectral images. *EURASIP Journal on Advances in Signal Processing*, *2011*(1), 1-22. https://doi.org/10.1186/1687-6180-2011-79

Baiocchi, V., Bianchi, A., Maddaluno, C., & Vidale, M. (2017). Pansharpening techniques to detect mass monument damaging in Iraq. *International Archives of the Photogrammetry, Remote Sensing & Spatial Information Sciences*, 42.

Belgiu, M., & Stein, A. (2019). Spatiotemporal image fusion in remote sensing. *Remote sensing*, *11*(7), 818. https://doi.org/10.3390/rs11070818

Boulkaboul, S., & Djenouri, D. (2020). DFIOT: data fusion for Internet of Things. *Journal of Network and Systems Management*, 1-25. https://doi.org/10.1007/s10922-020-09519-y

Carper, W., Lillesand, T., & Kiefer, R. (1990). The use of intensity-hue-saturation transformations for merging SPOT panchromatic and multispectral image data. *Photogrammetric Engineering and remote sensing*, *56*(4), 459-467.

Choi, J., Park, H., Seo, D., & Han, Y. (2019). Performance Analysis of Pansharpening Algorithms Based on Guided Filtering Applied to KOMPSAT-3/3A Satellite Imagery in Coastal Areas. *Journal of Coastal Research*, *91*(SI), 431-435. https://doi.org/10.2112/SI91-087.1

Crippen, R. E. (1989). A simple spatial filtering routine for the cosmetic removal of scan-line noise from Landsat TM P-tape imagery. *Photogrammetric Engineering and Remote Sensing*, *55*(3), 327-331.

DigitalGlobe, 2019. IKONOS Data Sheet https://dg-cms-uploads-production.s3.amazonaws.com/uploads/document/file/96/DG_IKONOS_DS.pdf (Accessed on: May 02, 2020)

Du, Q., Younan, N. H., King, R., & Shah, V. P. (2007). On the performance evaluation of pan-sharpening techniques. *IEEE Geoscience and Remote Sensing Letters*, *4*(4), 518-522. https://doi.org/10.1109/LGRS.2007.896328

Ehlers, M., Klonus, S., Johan Åstrand, P., & Rosso, P. (2010). Multi-sensor image fusion for pansharpening in remote sensing. *International Journal of Image and Data Fusion*, *1*(1), 25-45. https://doi.org/10.1080/19479830903561985

ESA, IKONOS Product Guide, 2006 https://earth.esa.int/eogateway/documents/20142/37627/IKONOS-Imagery-Product-Guide.pdf (Accessed on: March 18, 2021)

ESRI, Fundamentals of panchromatic sharpening, ArcGIS 10.3-Help, Redlands, CA, USA, 2020. https://desktop.arcgis.com/en/arcmap/10.3/manage-data/raster-and-images/fundamentals-of-panchromatic-sharpening.htm (Accessed on: May 05, 2020)

Fasbender, D., Radoux, J., & Bogaert, P. (2008). Bayesian data fusion for adaptable image pansharpening. *IEEE Transactions on Geoscience and Remote Sensing*, *46*(6), 1847-1857. https://doi.org/10.1109/TGRS.2008.917131

Hu, Y., Jia, G., Pohl, C., Feng, Q., He, Y., Gao, H., ... & Feng, J. (2015). Improved monitoring of urbanization processes in China for regional climate impact assessment. *Environmental Earth Sciences*, *73*(12), 8387-8404. https://doi.org/10.1007/s12665-014-4000-4

Ibarrola-Ulzurrun, E., Gonzalo-Martín, C., & Marcello, J. (2017). Influence of pansharpening in obtaining accurate vegetation maps. Canadian Journal of Remote Sensing, 43(6), 528-544. https://doi.org/10.1080/07038992.2017.1371583

Laben, C. A., & Brower, B. V. (2000). *U.S. Patent No. 6,011,875*. Washington, DC: U.S. Patent and Trademark Office.

Li, S., Kwok, J.T., & Wang, Y. (2002). Using the discrete wavelet frame transform to merge Landsat TM and SPOT panchromatic images. Inf. Fusion, (3), 17‑23.

Lillo-Saavedra, M., Gonzalo, C., Arquero, A., & Martinez, E. (2005). Fusion of multispectral and panchromatic satellite sensor imagery based on tailored filtering in the Fourier domain. International Journal of Remote Sensing, 26(6), 1263-1268. https://doi.org/10.1080/01431160412331330239

Maglione, P., Parente, C., & Vallario, A. (2015). High resolution satellite images to reconstruct recent evolution of domitian coastline. American Journal of Applied Sciences, 12(7), 506. https://doi.org/10.3844/ajassp.2015.506.515

Maglione, P., Parente, C., & Vallario, A. (2016). Pan-sharpening WorldView-2: IHS. *Brovey and Zhang methods in comparison*, *8*(2), 673-679.

Maurer, T. (2013). How to pan-sharpen images using the gram-schmidt pan-sharpen method–A recipe. *International archives of the photogrammetry, remote sensing and spatial information sciences*, *1*, W1. https://doi.org/10.5194/isprsarchives-XL-1-W1-239-2013

Meneghini, C., & Parente, C. (2015). Application for shadow removal from GeoEye-1 RGB composition. *International Journal of Applied Engineering Research*, *10*(6), 15833-15842.

Meng, X., Li, J., Shen, H., Zhang, L., & Zhang, H. (2016). Pansharpening with a guided filter based on three-layer decomposition. *Sensors*, *16*(7), 1068. https://doi.org/10.3390/s16071068

Meng, X., Shen, H., Li, H., Zhang, L., & Fu, R. (2019). Review of the pansharpening methods for remote sensing images based on the idea of meta-analysis: Practical discussion and challenges. *Information Fusion*, *46*, 102-113. https://doi.org/10.1016/j.inffus.2018.05.006

Nikolakopoulos, K., & Oikonomidis, D. (2015). Quality assessment of ten fusion techniques applied on Worldview-2. *European Journal of Remote Sensing*, *48*(1), 141-167. https://doi.org/10.5721/EuJRS20154809

Pal, M. K., Rasmussen, T. M., & Abdolmaleki, M. (2019, September). Multiple Multi-Spectral Remote Sensing Data Fusion and Integration for Geological Mapping. In *2019 10th Workshop on Hyperspectral Imaging and Signal Processing: Evolution in Remote Sensing (WHISPERS)* (pp. 1-5). IEEE. https://doi.org/10.1109/WHISPERS.2019.8921142

Parente, C., & Pepe, M. (2017). Influence of the weights in IHS and Brovey methods for pan-sharpening WorldView-3 satellite images. *International Journal of Engineering & Technology*, *6*(3), 71-77. https://doi.org/10.14419/ijet.v6i3.7702

Pohl, C., & Van Genderen, J. L. (1998). Review article multisensor image fusion in remote sensing: concepts, methods and applications. *International journal of remote sensing*, *19*(5), 823-854. https://doi.org/10.1080/014311698215748

QGIS 2.8 Documentation, QGSI User Guide, Working with Raster Data, 2020. https://docs.qgis.org/2.8/en/docs/user_manual/working_with_raster/raster_calculator.html (Accessed on: May 05, 2020)

Ranchin, T., & Wald, L. (2000). Fusion of high spatial and spectral resolution images: The ARSIS concept and its implementation. *Photogrammetric engineering and remote sensing*, *66*(1), 49-61.

Shahdoosti, H. R., & Ghassemian, H. (2014). Fusion of MS and PAN images preserving spectral quality. *IEEE Geoscience and Remote Sensing Letters*, 12(3), 611-615. https://doi.org/10.1109/LGRS.2014.2353135

Snehmani, Gore, A., Ganju, A., Kumar, S., Srivastava, P. K., & RP, H. R. (2017). A comparative analysis of pansharpening techniques on QuickBird and WorldView-3 images. *Geocarto International*, *32*(11), 1268-1284. https://doi.org/10.1080/10106049.2016.1206627

Thomas, C., Ranchin, T., Wald, L., & Chanussot, J. (2008). Synthesis of multispectral images to high spatial resolution: A critical review of fusion methods based on remote sensing physics. *IEEE Transactions on Geoscience and Remote Sensing*, *46*(5), 1301-1312. https://doi.org/10.1109/TGRS.2007.912448

Tu, T. M., Huang, P. S., Hung, C. L., & Chang, C. P. (2004). A fast intensity-hue-saturation fusion technique with spectral adjustment for IKONOS imagery. *IEEE Geoscience and Remote sensing letters*, *1*(4), 309-312. https://doi.org/10.1109/LGRS.2004.834804

Tu, T. M., Su, S. C., Shyu, H. C., & Huang, P. S. (2001). A new look at IHS-like image fusion methods. *Information fusion*, *2*(3), 177-186. https://doi.org/10.1016/S1566-2535(01)00036-7

Vijayaraj, V., O'Hara, C. G., & Younan, N. H. (2004, September). Quality analysis of pansharpened images. In *IGARSS 2004. 2004 IEEE International Geoscience and Remote Sensing Symposium* (Vol. 1). IEEE. https://doi.org/10.1109/IGARSS.2004.1368951

Yuhendra, J., Kuze, H., & Sri Sumantyo, J. (2011). Performance analyzing of high resolution pan-sharpening techniques: increasing image quality for classification using supervised kernel support vector machine. *Research Journal of Information Technology*, *3*(1), 12-23. https://doi.org/10.3923/rjit.2011.12.23

Wald, L. (2000, January). Quality of high resolution synthesised images: Is there a simple criterion?. In *Third conference" Fusion of Earth data: merging point measurements, raster maps and remotely sensed images"* (pp. 99-103). SEE/URISCA.

Wald, L., Ranchin, T., & Mangolini, M. (1997). Fusion of satellite images of different spatial resolutions: Assessing the quality of resulting images. *Photogrammetric engineering and remote sensing*, *63*(6), 691-699.

Wang, Z., & Bovik, A. C. (2002). A universal image quality index. *IEEE signal processing letters*, *9*(3), 81-84. https://doi.org/10.1109/97.995823

Zhang, J. (2010). Multi-source remote sensing data fusion: status and trends. *International Journal of Image and Data Fusion*, *1*(1), 5-24. https://doi.org/10.1080/19479830903561035

Zhang, Y. (2004). System and method for image fusion. *United States Patent Application* No. 20040141659

AIMS AND SCOPE

Geographia Technica / Technical Geography is an international journal for the progress of Scientific Geography.

Geographia Technica is a journal devoted to the publication of all papers on all aspects of the use of technical and quantitative methods in geographical research. It aims at presenting its readers with the latest developments in G.I.S technology, mathematical methods applicable to any field of geography, territorial micro-scalar and laboratory experiments, and the latest developments induced by the measurement techniques to the geographical research.

Geographia Technica is dedicated to all those who understand that nowadays every field of geography can only be described by specific numerical values, variables both of time and space which require the sort of numerical analysis only possible with the aid of technical and quantitative methods offered by powerful computers and dedicated software.

Our understanding of *Geographia Technica* expands the concept of technical methods applied to geography to its broadest sense and for that, papers of different interests such as: G.I.S, Spatial Analysis, Remote Sensing, Cartography or Geostatistics as well as papers which, by promoting the above mentioned directions bring a technical approach in the fields of hydrology, climatology, geomorphology, human geography territorial planning are more than welcomed provided they are of sufficient wide interest and relevance.

Targeted readers:

The publication intends to serve workers in academia, industry, and government.
Students, teachers, researchers and practitioners should benefit form the ideas in the journal.

Indexed by: CLARIVATE ANALYTICS
SCOPUS
GEOBASE
EBSCO
SJR
CABELL